INNOVATIVE DRILLING TECHNOLOGIES FOR ADVANCED MATERIALS

PHD PROJECT SUPERVISOR

PROF. ING. LUIGI NELE

PHD PROGRAM COORDINATOR

PROF. ING. ANDREA D'ANNA

PHD CANDIDATE

ING. ILARIA IMPROTA

PHD PROGRAMME IN:
PRODUCT ENGINEERING AND INDUSTRIAL PROCESS
XXXIII CYCLE

UNIVERSITÀ DEGLI STUDI DI NAPOLI FEDERICO II
SCUOLA POLITECNICA DELLE SCIENZE DI BASE

CONTENTS

1 INTRODUCTION

Technological innovation, together with the need to identify new materials for the growth of industry and products on the market, has increasingly focused attention on the fabrication and processing of composite materials such as fibre reinforced polymers (FRP).

Nowadays, composite materials are used in various fields, such as aeronautical (wing elements, gaps, aerodynamic brakes, vertical stabilisers, flaps, shoulder blades etc.), automotive (dampers, bumpers, engine parts, doors, Cardan shafts), space (shells of bodies engine, block design nozzle, chamber components, etc.) naval (masts, hulls), medical, design, sports (poles, masts of yachts, boats, catamarans, ski, tennis rackets, badminton rackets, ski poles, fishing rods, etc.), thanks to the numerous advantages attributable to their use [1].

In particular, carbon fibre reinforced polymer (CFRP) composites are among the most widely used composite materials in the aerospace industry, thanks to the high specific mechanical properties offered. These composites combine the fundamental aeronautical requirements of lightness and strength, which have sparked great research interest in improving the properties and the production process of composite materials [2]. CFRP composites can be manufactured in near net shape; however, they often require further machining processes such as drilling, particularly for joining purposes [3]. Fibre orientation plays a fundamental role in CFRP composite materials, affecting the mechanism of chip formation and the quality of the cut surface and making machining of CFRP a challenging task. Proper optimisation of the drilling process can substantially improve CFRP parts quality, which may be affected by several faults generated during the process. In order to simplify the assembly operations and reduce manufacturing costs, efforts are increasingly spent with the aim to optimise CFRP drilling.

1.1 JOINING METHOD IN THE AEROSPACE INDUSRTY

Manufacturing large and complex components parts, such as the wing and fuselage section of aircraft, means to assemble small pasts by using different joining techniques. There are several joining methods, as shown in **Figure 1-1**. For assembling the large composite structures, the conventional methods which are used in industries are mechanical fastening using rivets and bolts, co-consolidation bonding, and chemical bonding by control adhesives [4], [5].

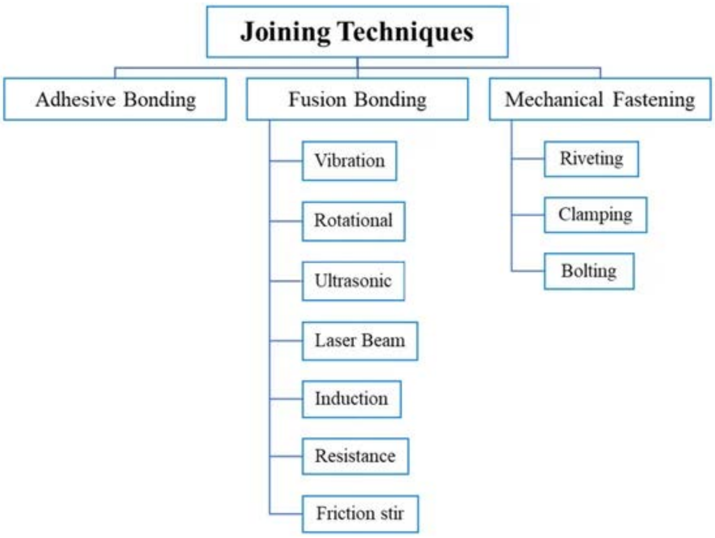

Figure 1-1: Different joining techniques for composite materials and their corresponding methods

Mechanical fastening methods, such as riveting, fasteners and bolting, are the most common method of joining in industries. This method is more efficient for metal joining compared to the polymer composites [6]. The advantages of using mechanical fasteners are that no surface preparation required, they are easy to inspect, and can be easily disassembled except in case of rivet joints.

Adhesive bonded joints are one in which two adherends are bonded together by applying the adhesive between them. With the advances in the polymer joining technology, the performance of adhesives in terms of strength, fatigue life and stiffness, have improved [7]. The principal advantage of adhesive joints is the possibility of bonding together dissimilar materials, and also, the uniform stress distribution and negligible stress concentration. However, adhesive joints also have many disadvantages, such as it requires extensive time for surface preparation and curing, bonding is not as strong as that in the case of mechanical fasteners, and cannot be disassembled [8].

Moreover, adhesive often require a longer curing cycle time, which is not ideal for industrial production. Hybrid joints using both the adhesive and bolted joints are also developed to improve the mechanical properties. Hybrid joints have shown several advantages in terms of load bearing capability and fatigue life [9], [10]. But also, there are several associated disadvantages, such as extensive labour work and longer joining time. Moreover, adhesive bonding, requires extensive surface preparation and high cure times of adhesives, as demonstrated by Fotsing et al. [11], who claim in their study that the density of surface porosities affects the bonding quality.

Another option for joining thermoplastic matrix composites, is the fusion bonding as alternatives to the classic mechanical joints. In fact, a composite laminate is formed by joining itself more laminae on each other, and the use of mechanical joints in the realisation of composite structures involves several problems such as stress concentrations and possible delamination [12], [13].

Fusion bonding, also known as welding, allows to join two or more parts by fusing their contact interfaces; this technique overcomes all problems related to the techniques mentioned above.

Over the years, various welding techniques for thermoplastics matrix composite materials have been proposed and tested, such as resistance [14] , ultrasonic [15]-[17], and electromagnetic induction welding [18], that are reviewed by Stokes [19] and Ageorges et al.[20].

For instance, Yousefpour et al.[21] focused their attention to reviewing the different fusion-bonding methods for thermoplastic composite components, and described the various welding techniques, the effects of processing parameters on weld performance and quality, the advantages/disadvantages of each technique, and the applications.

The principal advantages of fusion bonding technology is the easily automation, that it is ideal for large scale manufacturing process.

Unfortunately, the welding technology is applicable only to thermoplastic matrixes composite, so it is not an alternative for thermosets ones.

1.2 THE CUTTING MECHANISM FOR FIBROUS COMPOSITE MATERIALS

The base mechanisms of material removal for fibrous composite materials are substantially different from those of metals [1]. Composite materials generally comprise a reinforcement phase and a matrix phase and exhibit heterogeneous and anisotropic behaviour, which makes the material removal highly complex [1]-[3]. König [22] showed that fibrous composite materials machining depends on the specific properties and relative content of the reinforcement and the matrix.

Caprino et al. [1] investigated the effect of the tool rake and relief angles and of the depth of cut on the cutting forces when using high-speed steel tools on unidirectional glass fibre reinforced polymers (GFRP). While no wear could be detected on the tool face upon visual examination of the tool surfaces following machining operations, wearing was observed on the tool flank.

In general, for a given orientation of the fibres, the thrust force decreases with increasing the rake angle α (**Figure 1-2**), while by increasing the relief angle γ, lower values of the main cutting force are recorded [1], [23] [24], [25].

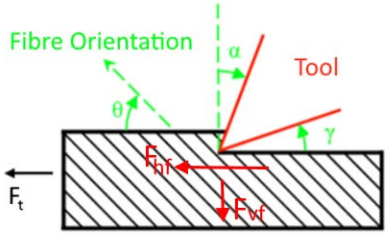

Figure 1-2: Definition of the orientation angle of the fibres and rake angle α and relief angle γ.

In other studies, the unit cutting force was shown to increase with decreasing depth of cut, undergoing the well-known 'size effect' [26], [27].

Tool wear increases proportionally with the volumetric percentage of the reinforcement and the vertical thrust exerted by the tool [28].

Tool wear can also be due to the low thermal conductivity of CFRP composites, which results in extensive heating. The thermal energy generated during the drilling process is absorbed mostly by the tool (50% of the total) for CFRP composites, whereas only 18% of the total thermal energy is absorbed by the tool for metal drilling [29][30].

1.3 DRILLING OF FIBROUS COMPOSITE MATERIALS

Drilling is the main machining process applied to fibrous composite materials, particularly in the aerospace industry, as mechanical joining using rivets or bolts is the universal joining technique for aircraft components. Drilling of CFRP composites is a complex operation compared to metal drilling and it is regulated by numerous factors, such as the cutting parameters (e.g. feed and cutting speed), the material properties (e.g. including fibre volume fraction, fibre orientation, stacking sequence, etc.) and the geometry of the drilling tool [3], [31].

Since composites are non-homogeneous and anisotropic materials, drilling poses many challenges, which can affect the strength and fatigue life of the parts [23]. During the drilling process, the workpiece can be subjected to various types of damage, the most common of which is delamination. Other drilling-induced damages include fibre pull-out, fibre breakage, matrix cracking, and thermal damage [32], [33], which can affect the service life of the component. Delamination is the most relevant damage induced during CFRP drilling [34], [35], and it is considered as the main cause of the substantial reduction in the fatigue strength of CFRP components, which compromises their long-term performance. Two delamination mechanisms, namely peel-up and push-out delamination, have been identified for CFRP laminate drilling and are shown in **Figure 1-4**. Peel-up and push-out delamination occur when the axial forces exerted by the drill bit helix overcome the interlaminar strength of the workpiece [36]. As demonstrated by Davim and Reis [37], the delamination damage grows with increasing cutting speed and feed rate, which increases the thrust force and determines an enlargement of the delamination damage at the hole exit [38].

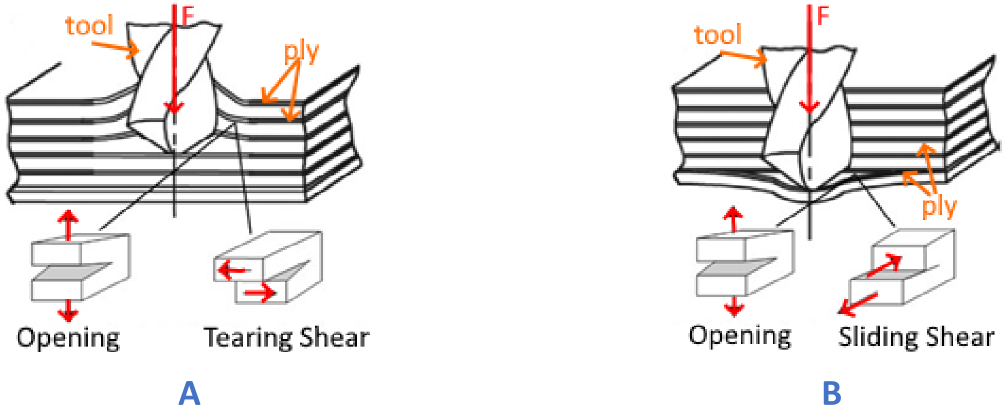

Figure 1-3: Mechanism of delamination in composite laminate drilling: (a) peel-up delamination and (b) push-out delamination. Adapted from Geng et al. [39]**.**

For traditional CFRP components drilling approaches, push-out delamination can occur if the axial load acting on the workpiece exceeds a threshold value, according to the linear elastic fracture model [36], [40]. The axial load represents a work equal to the sum of the energy required to deform the last laminate ply and the energy required to generate a new fracture surface [41]. The axial load evaluation refers to a concentrated load at the centre of the last laminate ply [27].

The geometry of the drilling tool, in particular the rake angle, has been shown to significantly affect delamination, as it determines the distribution of the cutting forces that the tool exerts on the workpiece [37]. In order to minimise delamination, twist drills with a point angle of 120° are typically used. Furthermore, while the extent of push-out delamination can be reduced by 45% by using drilling tools with point angles of 85°, tools with 140° point angles are required for minimal peel-up delamination [38].

1.4 ANALYSIS OF THE PROCESS PARAMETERS

The effect of the tool geometry and technological parameters on the drilling of CFRP composite materials has been widely studied in the literature. On the one hand, a comparison of the shear force data available in the literature is highly challenging due to the multiplicity of operating parameters. On the other hand, some considerations can be made to support the choice of the appropriate tool geometry and cutting parameters.

The cutting mechanism and the relative effect of cutting parameters on delamination during CFRP drilling have been largely investigated in the literature, identifying a critical thrust force below which no damage occurs [42]–[44]. It was observed that the thrust force is strongly dependent on the feed rate, probably due to higher undeformed chip thickness at higher feed rates; the delamination is a function of both feed and spindle speed; the effect of feed is amplified at higher rotational speeds[42].

The specific structural, thermal, and abrasive characteristics of CFRPs require a careful choice of the geometry and the material of the tool, which depends on the type of reinforcement used. The traditional drill bit, which is generally employed for metal drilling, is still used for composite materials drilling; however, this tool undergoes rapid tool wear and induces delamination in composite laminates.

The magnitude of the measured thrust force and torque varies during different drilling stages process, and the extent of such variations, as well as the overall process quality, depending on the process parameters (*e.g.* the geometric features of the drilling tools, the rotational speed, or the feed rate) and the tool wear. Representative graphs for the measured thrust force and torque during the drilling process for the twist drill are shown in Figure 1-4. Positive values for the thrust force represent a compression action exerted by the drilling tool on the workpiece as the cutting edge engages with the workpiece, the thrust force increases (zones 1-3 in Figure 1-4). Once the tool is completely involved in the workpiece, the thrust force remains almost constant to decrease sharply when the tool leaves the first laminate (zone 4 in Figure 1-4). An increase in the thrust force is observed when the tool is engaged with the second laminate (zone 5 in Figure 1-4), followed by a rapid decrease when the tool leaves the material (zones 6-7 in Figure 1-4). A similar trend can be observed for the torque: a rapid and linear increase in the measured torque occurs when an increasing portion of the cutting edge becomes involved in the workpiece (zone 1 in Figure 1-4). The increasing friction between the side surfaces of the tool and the inside of the hole causes a change of slope in the curve (zone 2 in Figure 1-5); as the drilling proceeds, the contact area between the tool and the material increases, which induces an increase in the torque (zones 3-5 in Figure 1-5). A rapid decrease of the torque observed when the tool ruptures the bottom surface of the hole (zone 6 in Figure 1-5), followed by a slighter decrease due to the tool-material friction until the torque reaches a constant value (zone 7 in Figure 1-5). The measured thrust force and torque were different for the twist tool and the step tool, which could be due to their different geometries [45].

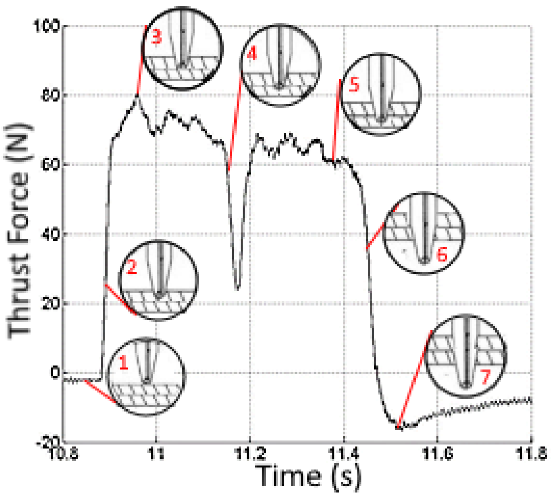

Figure 1-4: Thrust force value in CFRP-CFRP stack drilling with the twist tool.

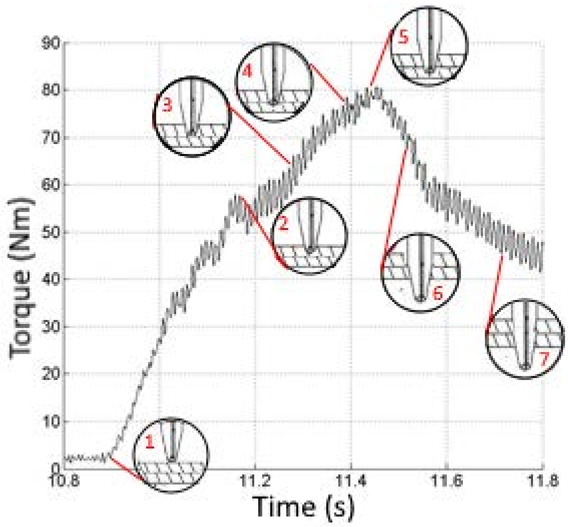

Figure 1-5: Torque value in CFRP-CFRP stack drilling with the twist tool.

The measured maximum thrust force and torque values depend on the number of holes made, the chosen cutting parameters, and the tool geometry. In particular, an increase in the measured thrust force and torque was observed as the number of drilled holes increased [45].

The effect of the drilling parameters on the measured thrust force, and the torque was evaluated in [45]. In this case, a custom-made drilling apparatus that enables detection and monitoring of the thrust force was used (Figure 1-6). Especially a CNC machining centre was equipped with two Kistler piezoelectric load cells to detect the thrust force and the torque that the tool exerts on the workpiece.

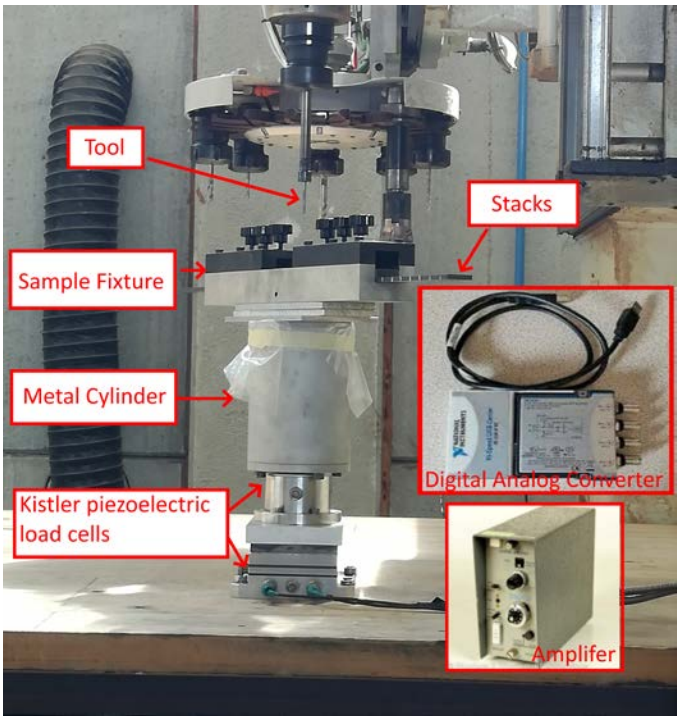

Figure 1-6: Equipped CNC machining centre.

Tool state and hole quality assessment, advanced signal processing based on signal conditioning and feature extraction was applied to the multiple sensor signals acquired through the monitoring system to find the correlations between sensorial data.

1.4.1 DELAMINATION FACTOR

As mentioned above, delamination can occur around the drilled hole at the top and the bottom of the laminate, and the push-out delamination is generally more severe than the peel-up delamination [46]. An important parameter to consider is the Delamination Factor (F_d), which is defined as the ratio between the maximum diameter of the circle encompassing the delamination zone (D_{MAX}) and the nominal hole diameter (D_0), as indicated in **Eq. 1-1**:

$$F_d = \frac{D_{MAX}}{D_0} \qquad \text{Eq. 1-1}$$

However, this parameter only accounts for the extent of delamination along the radius, without considering the total delamination area, as shown in **Figure 1-7**. Therefore, this parameter is not fully representative of the quality of the drilled hole.

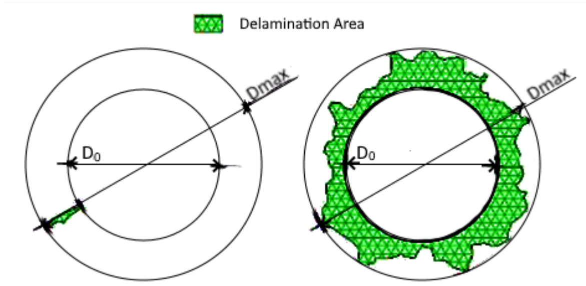

Figure 1-7: Example of two delamination patterns characterised by the same Dmax values but different delaminated areas, Ad. Adapted from [47].

Alternative delamination parameters have been proposed in the literature. For example, J.P. Davim et al. [48] introduced an adjusted delamination factor (F_{da}), calculated as:

$$F_{da} = \alpha \frac{D_{max}}{D_0} + \beta \frac{A_{max}}{A_0} \qquad \text{Eq. 1-2}$$

where the first and the second parts of **Eq. 1-2** represent the crack size (F_d) and the damaged area, respectively, β is the ratio between the damaged area (A_d) and the area corresponding to D_{max} (A_{max}) minus the nominal hole area (A_0), and α is the complement to 1 of β.

In order to determine the quality of the drilled holes, Caggiano *et al.* [47] developed a MatLab-based image analysis procedure able to extract the F_d and F_{da} parameters from the images of drilled holes. The developed image analysis procedure could identify the perimeter, the perimeter best-fit circumference (based on the mean squared error algorithm), and the delaminated area of the drilled holes (**Figure 1-8** and **Figure 1-9**).

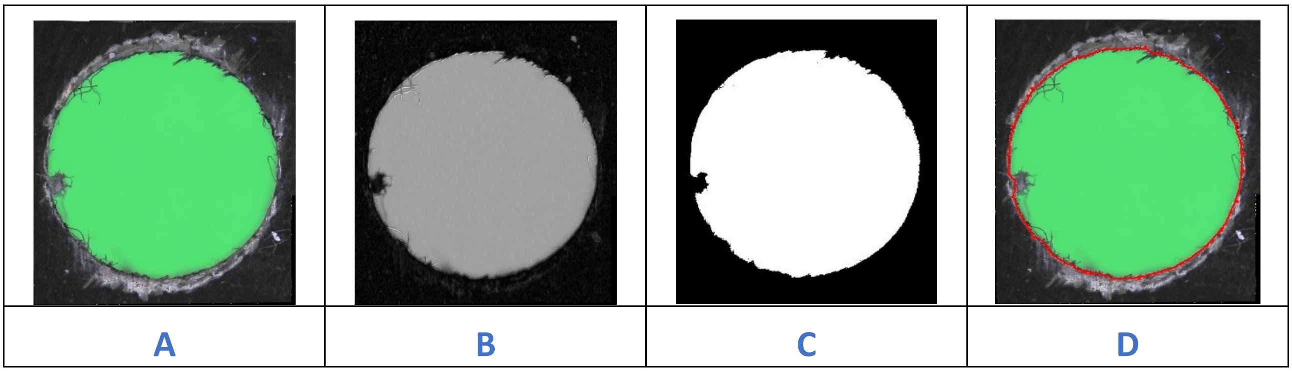

Figure 1-8: An image analysis procedure was developed in Matlab to extract the Fd parameters.

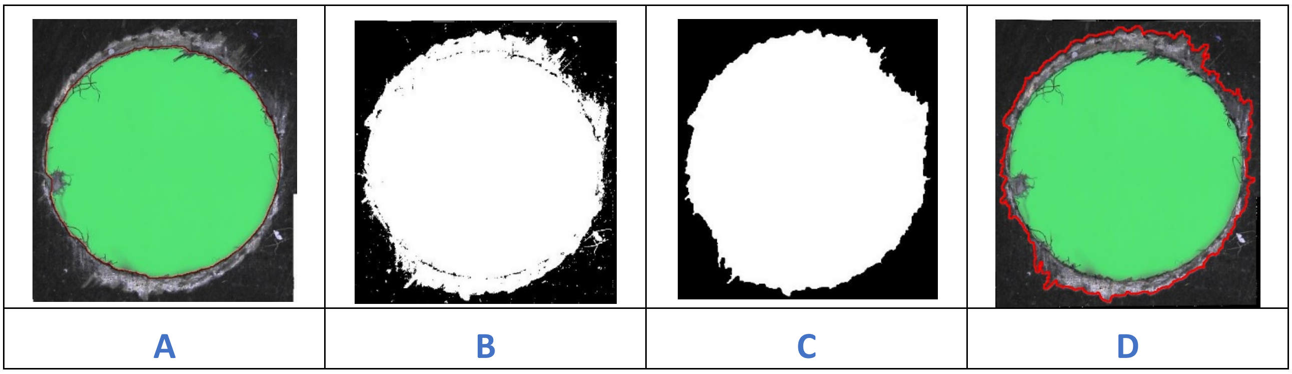

Figure 1-9: An image analysis procedure was developed in Matlab to extract the Fda parameters.

The extracted delaminated areas for holes n. 10, 20, 30, 40, 50, and 60 (drilling parameters: 6000 rpm and 0.20 mm/rev) are shown in Figure 1-10. Push-out delamination preferentially oriented along the 45° direction, which is consistent with the most external plies of the CFRP laminate stacking sequence, could be observed.

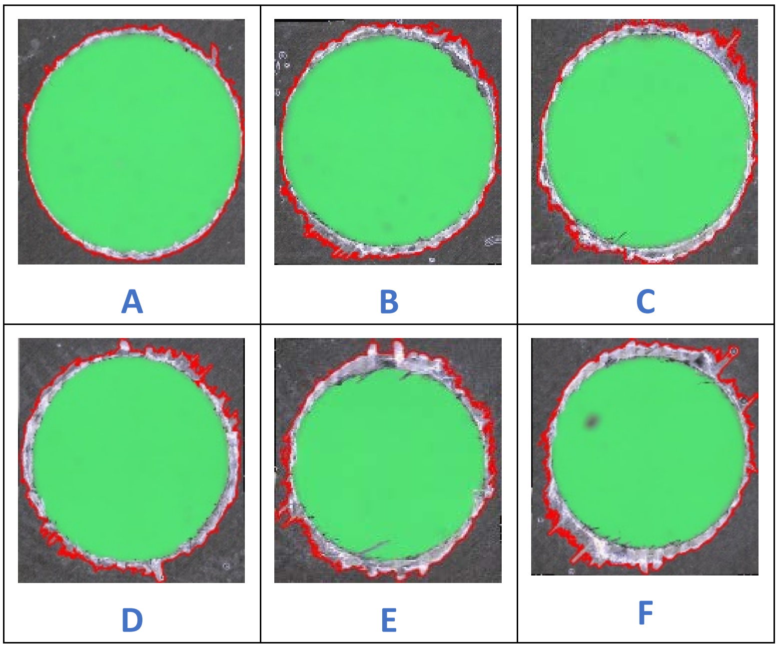

Figure 1-10: Outlined delaminated area at the exit of holes n. (A) 10, (B) 20, (C) 30, (D) 40, (E) 50 and (F) 60 drilled at 6000 rpm – 0.20 mm/rev [49].

The extracted F_d and F_{da} parameters at the hole entry were independent of the number of drilled holes, which suggests that progressive tool wear does not affect delamination at the hole entry, **Figure 1-11A**, (*i.e.* peel-up delamination). However, tool wear was shown to affect delamination at the hole exit, **Figure 1-11B** (*i.e.* push-out delamination) as the extracted F_d and F_{da} parameters increased with an increasing number of drilled holes. [50]

The measurements of the delamination factors are also influenced by the spot defects that can arise on the material in a random way, and that appear due to the very nature of the material, something that we do not find instead for the drilling of metallic materials. For this reason, the graph shown presents irregular values for some holes, while maintaining an increasing trend.

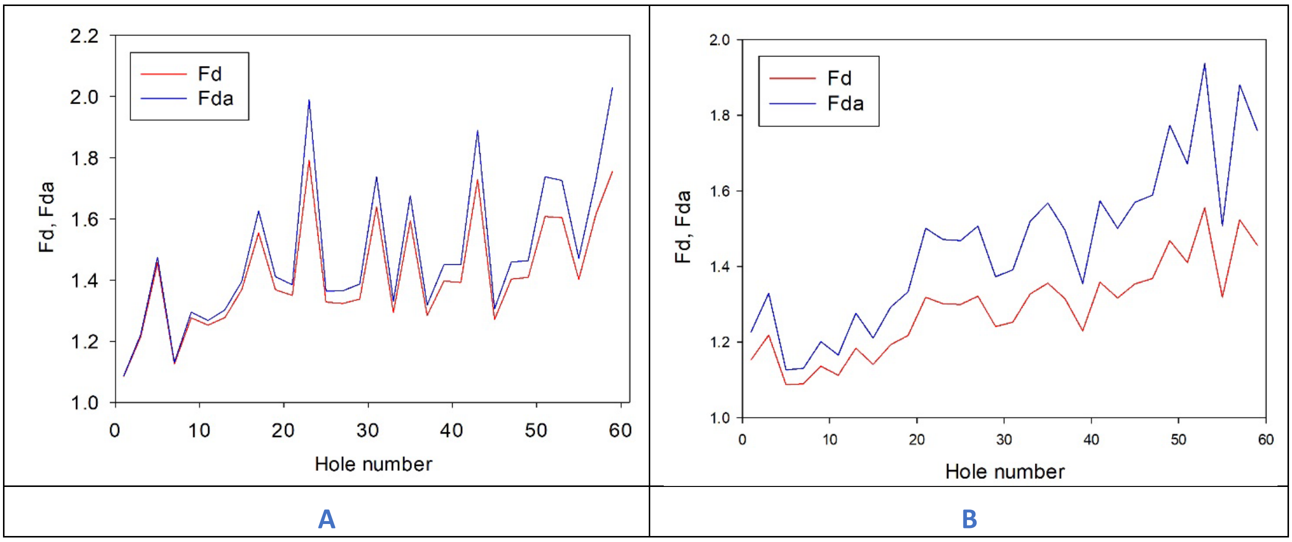

Figure 1-11: Fd and Fda parameters measured at hole exit vs hole number for 60 consecutive holes drilled 6000 rpm – 0.20 mm/rev, hole entry(A) and hole exit (B). [49]

The correlation between these results and the wear values on the tool were studied in **Chapter 4**.

In previous works to this thesis, ultrasound tests were performed in which the delamination inside the hole was evaluated. [51], [52]

1.5 DRILLING OF FIBROUS COMPOSITE MATERIALS: TOOL WEAR

As outlined above, one of the main challenges associated with CFRP components drilling is the extensive tool wear; for example, an HSS drill bit can drill up to 100 holes in a steel workpiece, but less than 10 holes in a CFRP workpiece before tool wear occurs [53].

Wear is the advanced removal material from the surface of the tool upon drilling and is due to the chemical properties of the material, to the onset of high temperatures, and to the high stress undergone by the tool and the workpiece [54]–[56]. Tool wear can significantly alter the shape and dimensions of the tool.

Tool wear can also be caused by:

- abrasion wear, which is due to the sliding surface with different surface stiffness and roughness;
- adhesion wear, which originates from the high contact pressures between the chip and the tool and causes welding of the protrusions of the contacting surfaces;

- diffusion wear, which occurs because of the mutual solubility of the contacting materials and results in the migration of atoms through the tool-chip interface.

The combined effect of mechanical and thermal stresses can induce:

- chipping, which is the removal of metal particles around the cutting edge due to impact or excessive pressure;
- plastic deformation, which is the reduction of the plastic sliding tension of the tool material, with its consequent deformation, due to the high temperatures originating in the cutting area.

Tool wear can occur at the tool rank, resulting in the formation of a cavity due to diffusion wear or at the tool flank, which is characterised by streaks parallel to the cutting direction due to abrasion phenomena. Tool wear can also occur at the tool margin of the chisel edge [53], [57], [58]. Figure 1-12 A shows the tool wear occurring on a twist drill bit at hole n.1 and hole n.93.

Although tool wear can develop in various areas of the tool, one of the most widely used parameters to quantify tool wear refers to the wear occurring at the side of the tool.

Two indices can be calculated, namely, VB_{max} and VB, which are the maximum and the average value of the wear lip width, respectively, as schematically shown in Figure 1-12 B and Figure 1-12 C.

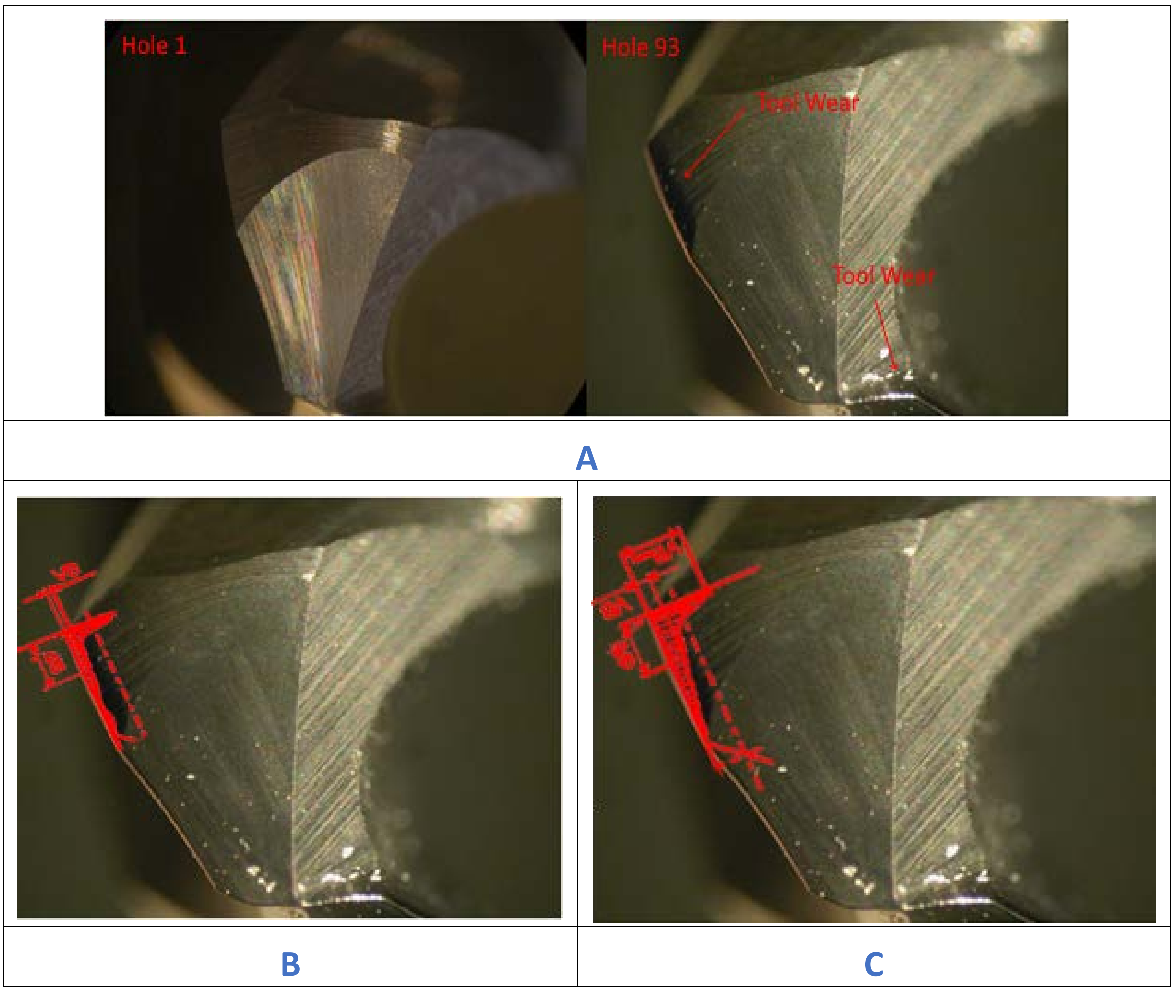

Figure 1-12: (A) Wear that can develop on twist drill bits at hole n.1 and hole n.93; (B) Schematic of the VB (C) and VB_{max} indices used for the analysis of tool wear.

As an example, Figure 1-13 shows the behaviour of the measured VB_{max} and VB as a function of the number of drilled holes when a twist drill bit operating at 6000 rpm and 0.20 mm/rev is used.

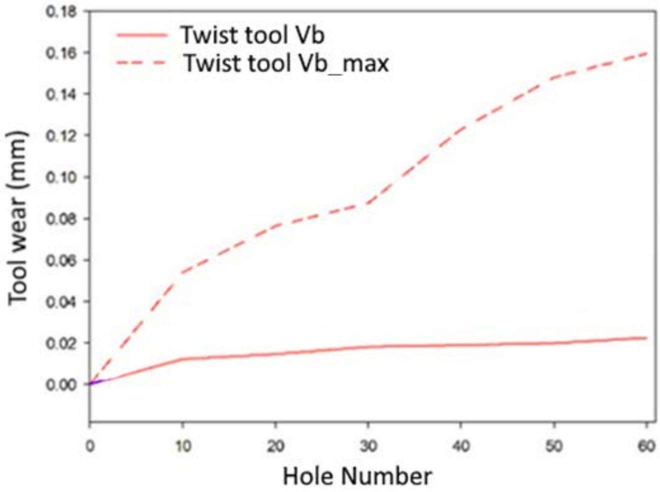

Figure 1-13: VB and VBmax parameters measured every 10 holes for a twist tool operating at 6000 rpm – 0.20 mm/rev. Adapted from [49].

1.6 GEOMETRIC FEATURES OF THE DRILLED HOLES

The drilling process is subject, especially in the aeronautical field, to severe limitations, in terms of geometric features. It must ensure the creation of quality holes, with functional requirements; as a consequence, it is necessary to check and define valid tolerance fields for various characteristics, by current regulations, such as:

1. Diameter of the hole
2. Angularity of the hole
3. Depth of the countersink
4. Surface characteristics

1. The first features define the dimensional tolerance, or the variation allowed between the nominal and the real size, based on the functionality of the element.
Dimensional issues are related to the hole diameter, which should stay within the specified tolerance range; in the aeronautical sector, tight ranges are set (≤ 0.0762 mm) [59].

2. Angularity, on the other hand, defines the hole's shape and orientation limits, focusing attention on the axis of the hole itself (**Figure 1-14**); the maximum angular deviation of the drilling axis must not exceed ± 2° for aeronautical structures.

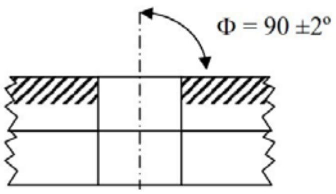

Figure 1-14: Angularity requirement.

3. The countersinking is made to allow the connecting parts' housing; in particular, fillet relief indicates a chamfer required for connecting members with protruding heads.

For connecting devices with protruding head, there are two ways to realise the fillet relief:

• Making a fillet radius around the hole;

• Making a fillet relief around the hole.

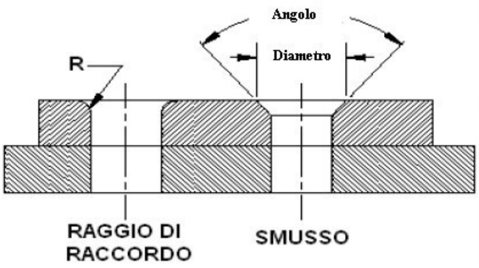

Figure 1-15: Countersinking of holes in the aeronautical field.

The tolerance of 100° countersinks is ± 1°; the countersink can be eccentric to the axis of the hole already made within 0.003 " max. The concentricity of the countersink axis to the axis of the hole must be at most 0.002" (0.050 mm). The axis of the countersink must be parallel to the axis of the hole with a tolerance of ± 0.5°.

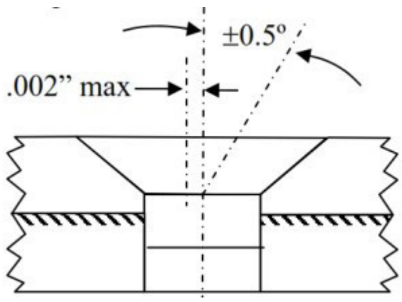

Figure 1-16: Tolerances countersinks in the aeronautical field.

4. Finally, compliance with the surface characteristics is based on the imposition of limits both on the surface finish and on the different types of damage that may occur during processing, and in particular about delamination.
The surface finish is an essential parameter in the processing of composite materials; in fact, limits are imposed by the different fields of application; in particular, in the aeronautical field, the limit usually imposed is Ra=3 μm.
Figure 1-17 reports the maximum fibre delamination values allowed on CFRP.
The letters W and D indicate the maximum acceptable dimensions of fibre delamination or tearing for a given diameter.

Hole Size (inch)	GRAPHITE FABRIC "D" Max [1] (inch) (mm)	GRAPHITE FABRIC "W" Max (inch) (mm)	GRAPHITE TAPE "D" Max (inch) (mm)	GRAPHITE TAPE "W" Max (inch) (mm)
5/32	0.007 (0.178)	0.030 (0.762)	0.014 (0.356)	0.100 (2.54)
3/16	0.007 (0.178)	0.030 (0.762)	0.014 (0.356)	0.100 (2.54)
1/4	0.007 (0.178)	0.040 (1.016)	0.014 (0.356)	0.100 (2.54)
5/16	0.007 (0.178)	0.040 (1.016)	0.014 (0.356)	0.120 (3.05)
3/8	0.007 (0.178)	0.040 (1.016)	0.014 (0.356)	0.120 (3.05)
7/16	0.007 (0.178)	0.040 (1.016)	0.014 (0.356)	0.150 (3.81)
>1/2	0.007 (0.178)	0.040 (1.016)	0.014 (0.356)	0.150 (3.81)

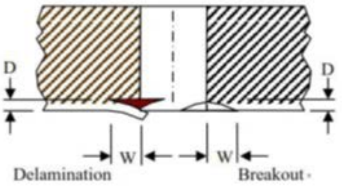

Figure 1-17: Examples of tolerances imposed on hole delamination.

1.6.1 DIMENSIONAL ANALYSIS OF THE DRILLED HOLES

The hole size is strongly affected by the drilling conditions, including feed rate, spindle speed and tool wear level. The role of feed rate on the average hole size was related to the undeformed chip thickness and the cutting force during the process [60], [61]. On the other hand, increasing the spindle speed yields an increase in the average hole size that can be attributed to the thermal expansion of the tool at higher speeds [61].

Ashraf et al. carried out a dimensional analysis of the drilled holes showing good agreement with these findings (Figure 1-18). The average hole diameter decreased as the feed rate increased; more specifically, the hole diameter was reduced by approximately 4.7 µm per feed increments of 0.1 mm/rev (drill diameter:9.525 mm, feed rate: 0.15 mm/rev).

The effect of the feed rate and the torque on the average hole diameter is shown in Figure 1-18.

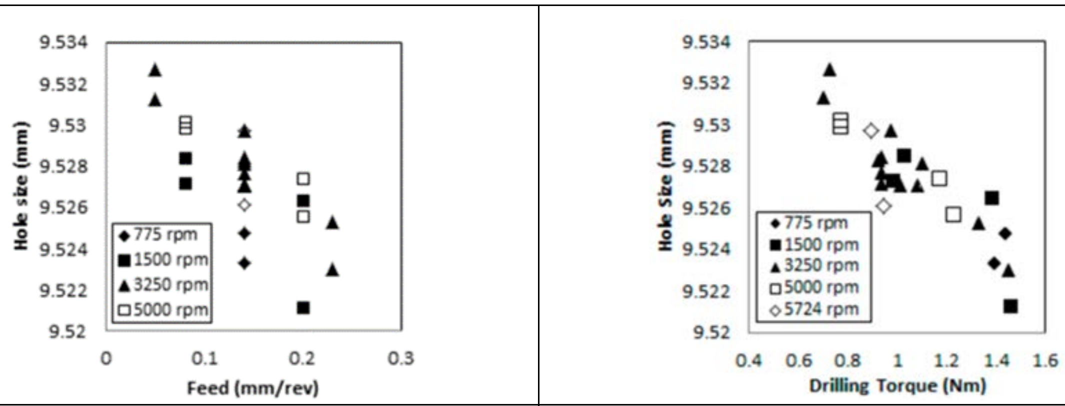

A | B

Figure 1-18: Effects of (a) feed rate and (b) maximum torque on the average hole diameter (drill diameter = 9.525 mm) [62].

The average hole roundness also depends on the drilling conditions, as shown in Figure 1-19 [63].

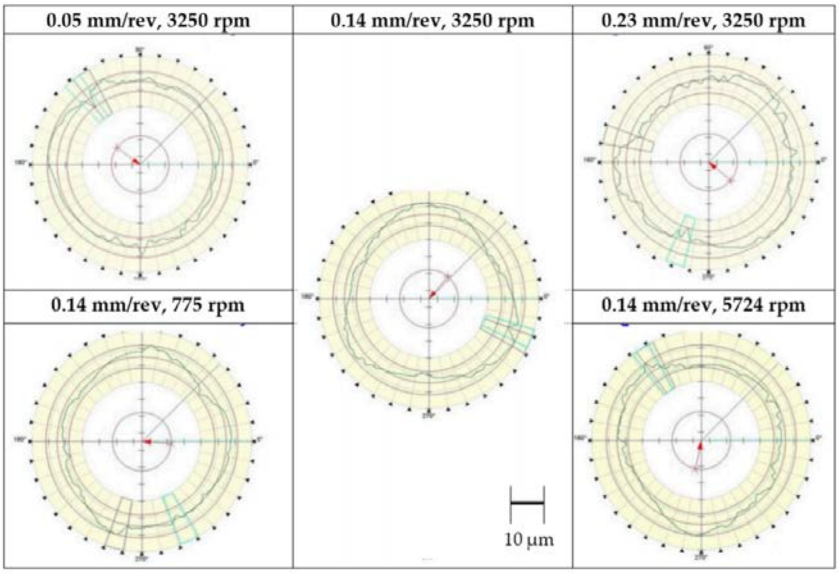

Figure 1-19: Hole roundness profiles in the middle of the holes [62].

In order to assess the quality of the drilled holes, a surface finish analysis is also required. The surface finish inside the drilled holes depends on the extent of tool wear, and various studies have focused on establishing an evaluation procedure that allows a comprehensive assessment of the defect with a surface scan [64], [65]. However, the correct evaluation of the surface finish for composite materials poses many challenges, as various ply-specific defects arise upon drilling due to the ply arrangement.

1.7 SURFACE FINISH ANALYSIS

Confocal microscopy can be used to obtain volumetric scans of the internal surface of the drilled hole and to examine the surface roughness. An example of such surface scans along four different orientations of the laminate plies is shown in Figure 1-20. For a given reference direction, the images show the internal surface of the hole according to the orientation of fibres.

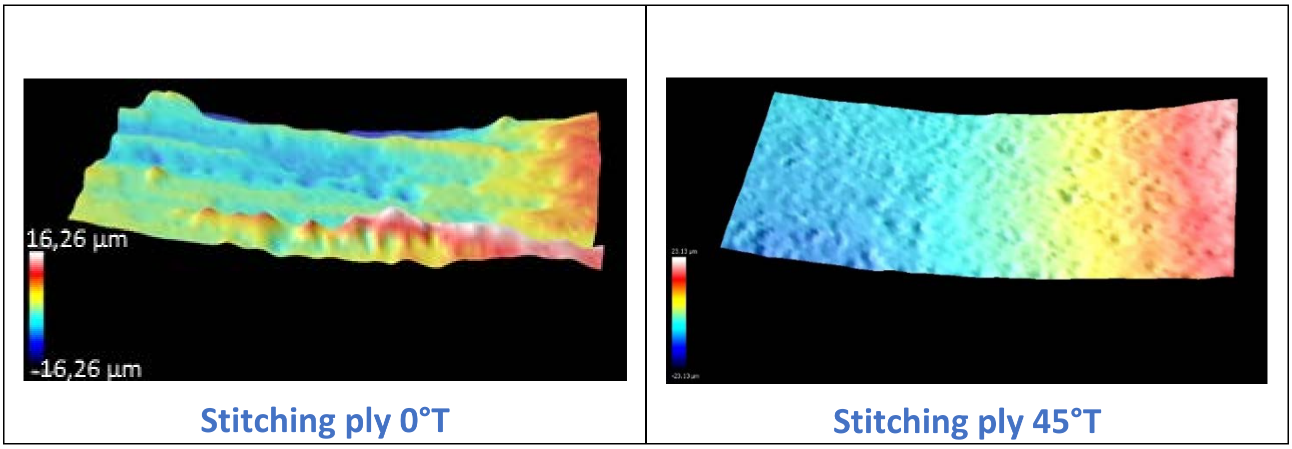

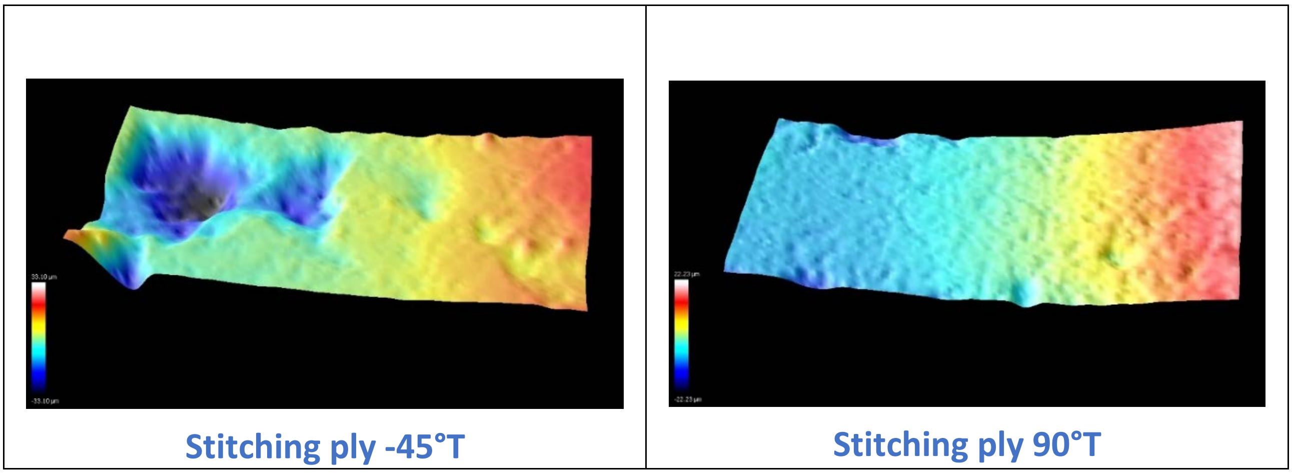

Figure 1-20: Scan with confocal microscopy for the single ply of the laminate.

Figure 1-21 shows the variation of the inner surface of the holes with an increasing number of holes. It can be observed that hole no. 13 (Figure 1-21 A) displays fewer imperfections on both the top and the bottom stack laminates compared to hole no. 93 (Figure 1-21 B).

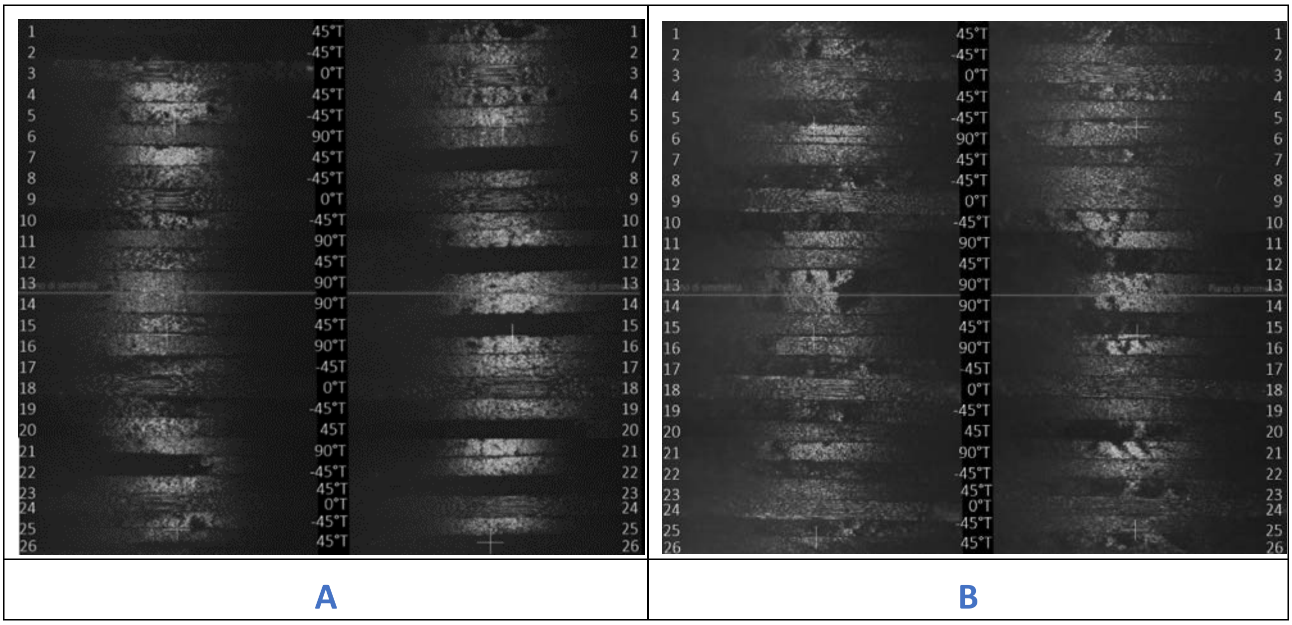

Figure 1-21: Microscopic images at 5x magnification of the inner surface of hole no. 13(A), top and bottom stack laminates hole no. 93 (B), top and bottom stack laminates, produced at 6000 rpm, 0.2 mm/rev.

1.8 AIM OF THE THESIS

This thesis discusses the influence of tool geometry and technological parameters on thrust force, torque and tool wear and their role in delamination and final part quality. These aspects will be illustrated with particular reference to the drilling of CFRP composites, widely employed in the aerospace industry and extensively investigated in the scientific literature.

The opportunity to find a correlation between the sensor data acquired and the hole quality parameter established by the aerospace industry is an excellent strategy for production at zero defect.

This is an opportunity for improving the drilling process automation, with higher productivity and a reduction of the scarps.

The solution proposed in this thesis is based on real-time monitoring temperature and the relative quality hole.

This automation supports the development of a future Smart Factory in the framework Industry 4.0; the autonomy decisional systems are supported by a sensor advanced monitoring of the physical process.

To this aim, three different experimental campaigns were carried out:

1. The first campaign investigates the possibility of using a new method for studying the real-time control of the drilling process using temperature analysis.
2. The second campaign is based on statistical methods of linear regression to find the optimum of the drilling process; the results elaborated with Minitab (Data Analysis, Statistical & Process Improvement Tools) will be used for the process control and inserted in an intelligent system.
3. The third campaign is based on the study of internal surface analysis of the hole after the drilling operation. This parameter has a straight correlation with the tool wear; indeed, the idea to evaluate with a correct solution the surface finish of the composite materials and the possibility to obtain the complete view of the hole defect with a simple superficial scan is very interesting.

Finally, a new drilling process for the composite materials, the drill-mill process, was studied to eliminate the delamination defect, typical of the drilling process.
For this aim, different tool types were developed and characterized.

In order to avoid rapid tool wear, various combinations of tool material and geometry were investigated. To investigate how the variation of the tool parameters affects the quality of the hole, in this work, CFRP/CFRP and Al2024-O/CFRP stacks were drilled using tools with different geometries and cutting parameters. The workpiece material comprised a stack of two CFRP laminates made of CYCOM 977-2 epoxy matrix and Toray T300 carbon fibres, each made up of 26 prepreg unidirectional plies with stacking sequence [±452/0/904/0/90/02]s and total laminate thickness of 5 mm. The vacuum bag containing the CFRP laminates was prepared via hand lay-up and cured in an autoclave. The surface texture of the laminates on the bag side was irregular compared to the mould side.

1. For the first group of drilling experiments, two CFRP laminates were stacked with the bag sides in contact and drilled together to reproduce the aerospace industry's most challenging drilling conditions. In this case, 60 consecutive holes were drilled by the same tool for each testing condition in order to evaluate the tool wear effect.
2. For the second group of drilling experiments, the drilling tests were conducted with the Al sheet on the top of the stack and the CFRP laminate on the bottom to avoid damages due to the aluminium chip. The irregular CFRP side was placed in the middle to test the severest drilling condition. In these tests, 30 consecutive holes were drilled by the same tool for each testing condition in order to evaluate the tool wear effect.

BAG SIDE

MOULD SIDE

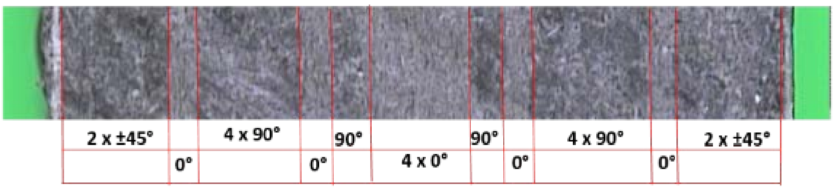

3.

A

B

Figure 2-1: (A) The sequence of layers in the sectioned CFRP laminate. (B) CFRP Stacks used in the test.

BAG SIDE

MOULD SIDE

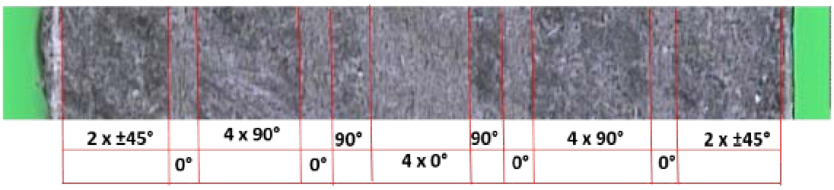

Al2024-O

CFRP

A

B

Figure 2-2: (A) The sequence of layers in the sectioned CFRP laminate. (B) Al/CFRP Stacks used in the test.

The chemical composition of the Aluminium 2024 alloys and the main physical, mechanical and thermal properties are outlined in Table 2-1 and Table 2-2.

Element	**Weight [%]**
Aluminium, Al	Balanced
Copper, Cu	3.80 - 4.90
Magnesium, Mg	1.20 - 1.80
Manganese, Mn	0.30 - 0.90
Silicon, Si	0.50
Iron, Fe	0.50
Zinc, Zn	0.25
Titanium, Ti	0.15
Chromium, Cr	0.10

Table 2-1: Chemical composition of the Aluminium 2024 alloy.

Property	**Value**
Density [g/cm^3]	2.78
Melting point [°C]	510
Ultimate tensile strength [MPa]	220
Elastic modulus [GPa]	70 - 80
Poisson's ratio	0.33
Thermal expansion in the range 20 – 100°C [µm/m°C]	22.8
Thermal conductivity at 25°C [W/mK]	193

Table 2-2: Physical, mechanical and thermal properties of the Aluminium 2024 alloy.

In the tests conducted on Al/CFRP stacks, aluminium was drilled first to prevent aluminium chips from ruining the CFRP hole, and the laminates were, as in CFRP/CFRP drilling, overlapped with the irregular part of the CFRP between them to test the severest condition.

Two drilling tools, the properties of which are described below, were used:

- Traditional Twist drill: a two-flute twist drill made of tungsten carbide (WC), Ø6.35 mm, which features a 120° point angle and 20° helix angle (**TTD6**) (Figure 2-3 A);
- Traditional Twist drill: a two-flute twist drill made of tungsten carbide (WC), Ø4.9 mm, which features a 120° point angle 20° helix angle (**TTD4**) (Figure 2-3 B);

- Innovative Step drill: a two-flute step drill made of tungsten carbide (WC). Diameter increases from 4.95 mm to 6.35 mm in two steps with sharp elliptical margins. The point angle is 125° and 30° helix angle (**ISD6**) (Figure 2-3 C).
- Innovative Step drill: a two-flute step drill made of tungsten carbide (WC). Diameter increases from 3.5 mm to 4.9 mm in two steps with sharp elliptical margins. The point angle is 125° and 30° helix angle (**ISD6**) (Figure 2-3 D).

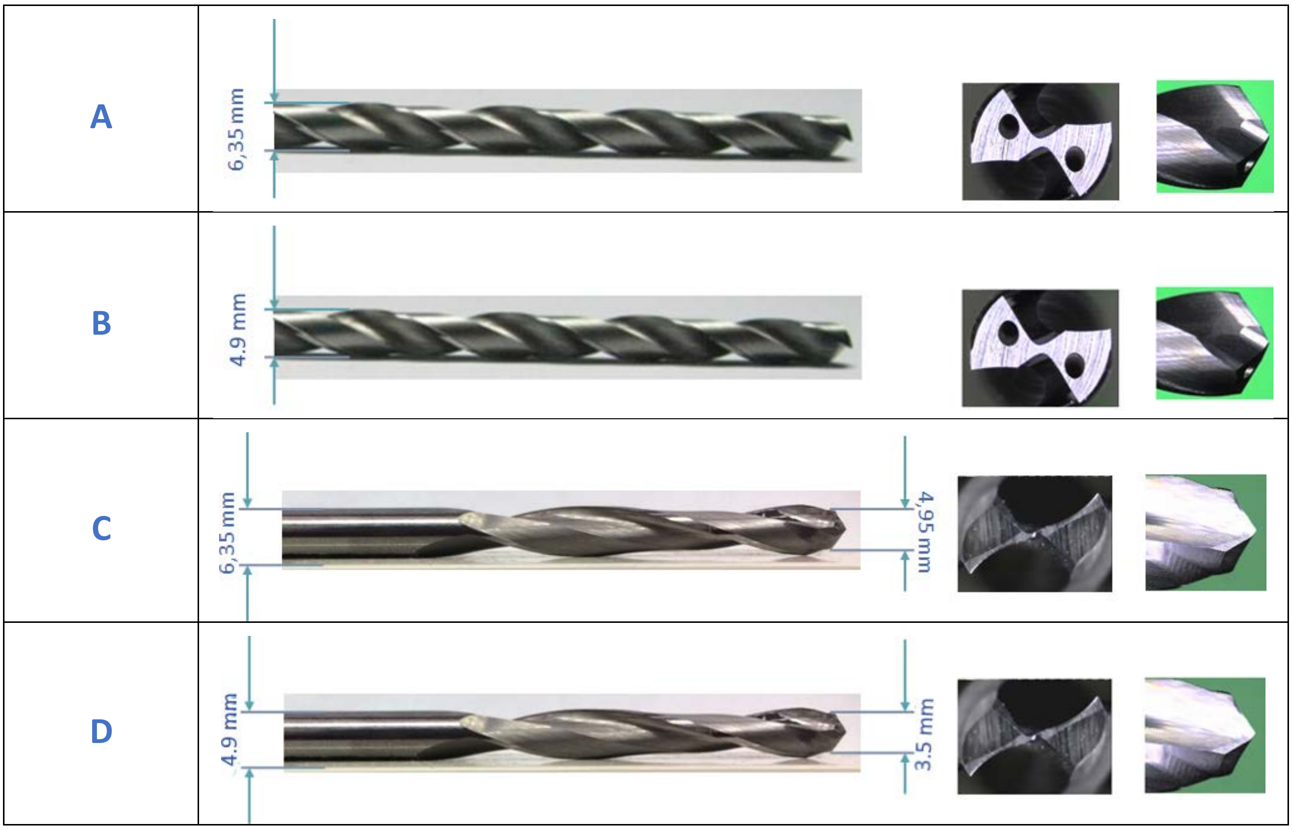

Figure 2-3: Front and side view of (A) the twist drill and (B) the step drill.

2.1 THRUST FORCE AND TORQUE ANALYSIS IN STACKS DRILLING PROCESS

The values of force and torque and the quality of the process depend significantly on the tool wear and, then, on the process parameters. Figure 2-4 and Figure 2-5 show the trend, respectively, of the force and the torque vs time.

Qualitative trend of both force and torque is the same for the tests, and it increases after each machining. The positive vertical thrust force represents a compression action exerted by the tool on the piece. As the edge of the cutting edge engages, the trend of the thrust force is increasing, with a very high angular coefficient first, mainly dependent on the thrust exerted by the transversal cutting edge, then lower because it only depends on the lateral actions. When the tool is completely involved in the workpiece, the thrust remains almost constant. The force value decreases when the tool leaves the first composite panel making up the package and then increases once in contact with the stack's second panel. The value is almost constant when the tool is completely sunk in the second composite panel and then decreases when it leaves the material.

Figure 2-4 shows seven zones: from the first one to the second one, a progressive increase of the force is verified, until the achievement of a constant value for all the duration of the first laminate of the stacks. Zone 3 is the peaks of force during the drilling. Zone 4 shows a decrease of thrust force due to the overlap of the laminate; in fact, the passage of the tool from one laminate to another is responsible for reducing the recorded value of thrust force. Similarly to the previous zones, zone 5 is localised by constant force values. Zones 6 and 7 show a notable decrease of force when the cutting edge reaches the end of the second laminate of the stack.

Instead, Figure 2-5 shows, zone 1, signal torque growing rapidly and linearly due to an increasing part of the cutting edge involved in the process. Zone 2 changes slope of the line due to increasing friction between side surfaces of the tool and inside of the hole; as drilling proceeds, the contact area between the tool and material increases and, therefore, the torque increases, how shown in zone 3-5. When the tool breaks the bottom surface of the hole, zone 6, the only remaining component is the one linked to friction, so there is an initial decrease until a constant value, how shown in zone 7.

The measured thrust force and torque were different for the twist tool and the step tool, which could be due to their different geometries.

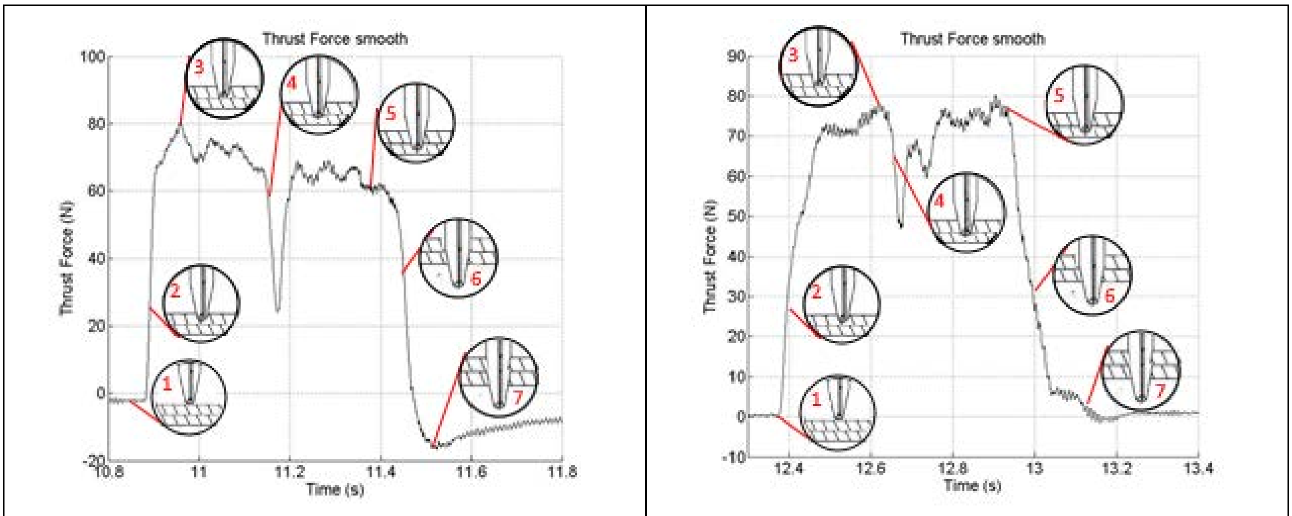

A	B

Figure 2-4: Force value in a drilling machine process in the stack CFRP-CFRP for TTD(A) and ISD(B).

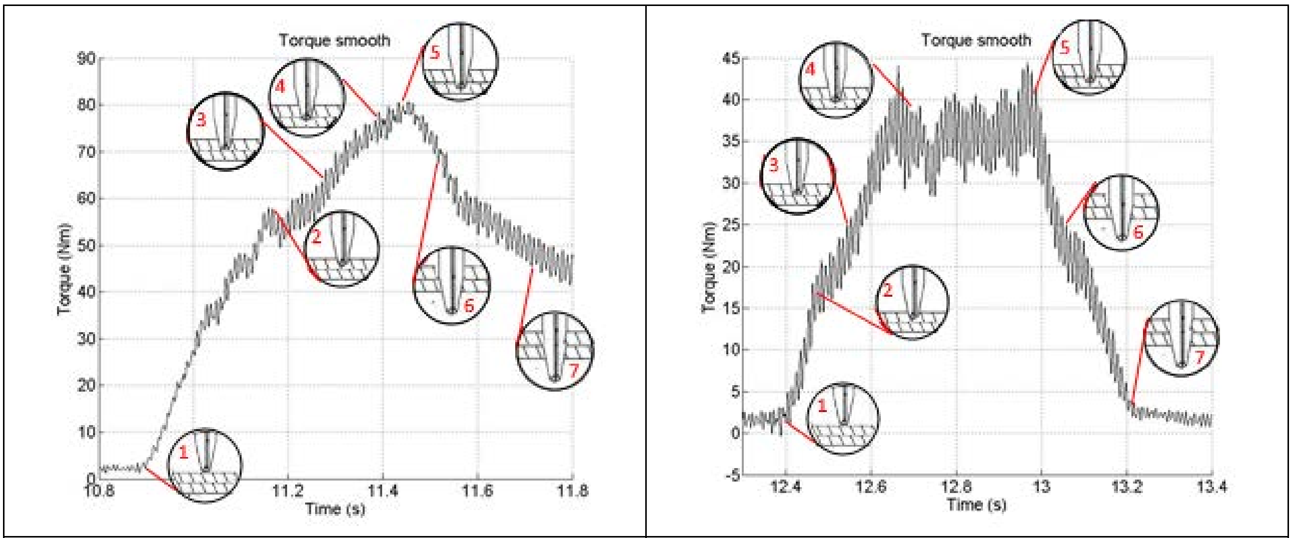

A	B

Figure 2-5: Torque value in a drilling machine process in the stack CFRP-CFRP TTD(A) and ISD(B).

Wear increase implies an increase of thrust force and torque and a worsening of the drilling quality. The tool wear depends on the its material and the process parameters. During the drilling, the wear caused the increasing temperature. The numerosity of the holes and the wear zone depend on the tool material. For example, the traditional tools of tungsten carbide show higher strength, and this allows manufacturing a higher number of holes. The set of low feed rates implies the limited duration of the tool due to more top working time and a consequent increase of the temperature. On the contrary, the criticalities for the carbide tools are high velocity and feed. The wear for these tools is lower, localised near the flank, and it increases with an exponential law with the feed rate.

The recorded force and torque values depend significantly on the number of holes made, on the cutting parameters chosen and on the type of tool used. In all cases, there is a significant increase in both vertical thrust force and torque as the number of holes made increases. Figure 2-6 and Figure 2-7 show that the force and the torque change with the rise in the number of holes.

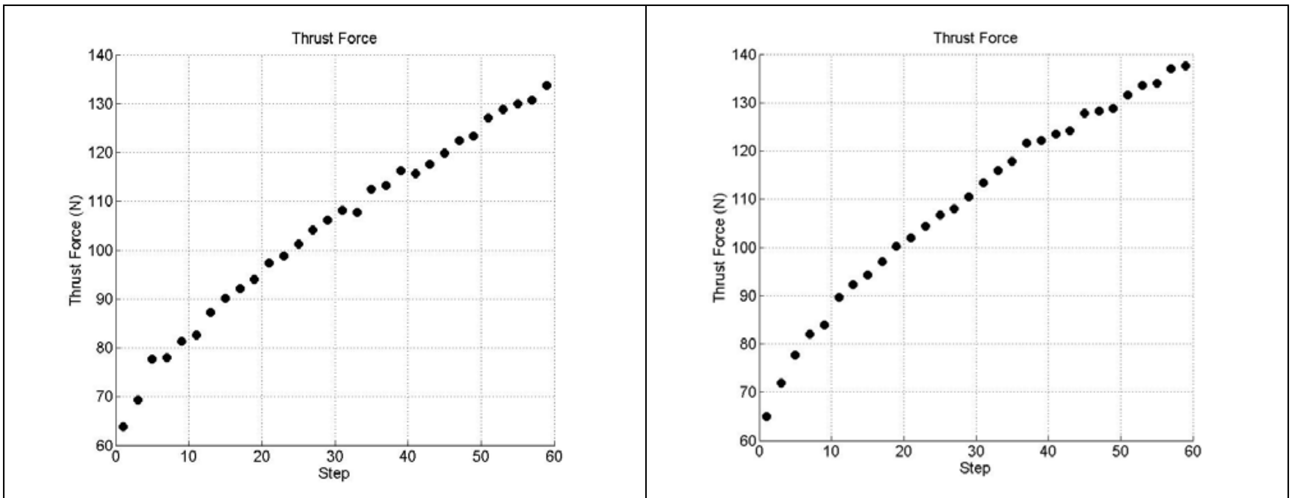

A	B

Figure 2-6: Measured Thrust Force max vs hole number for 60 consecutive holes drilled by the (A) TTD (B) ISD at 6000 rpm – 0.20 mm/rev.

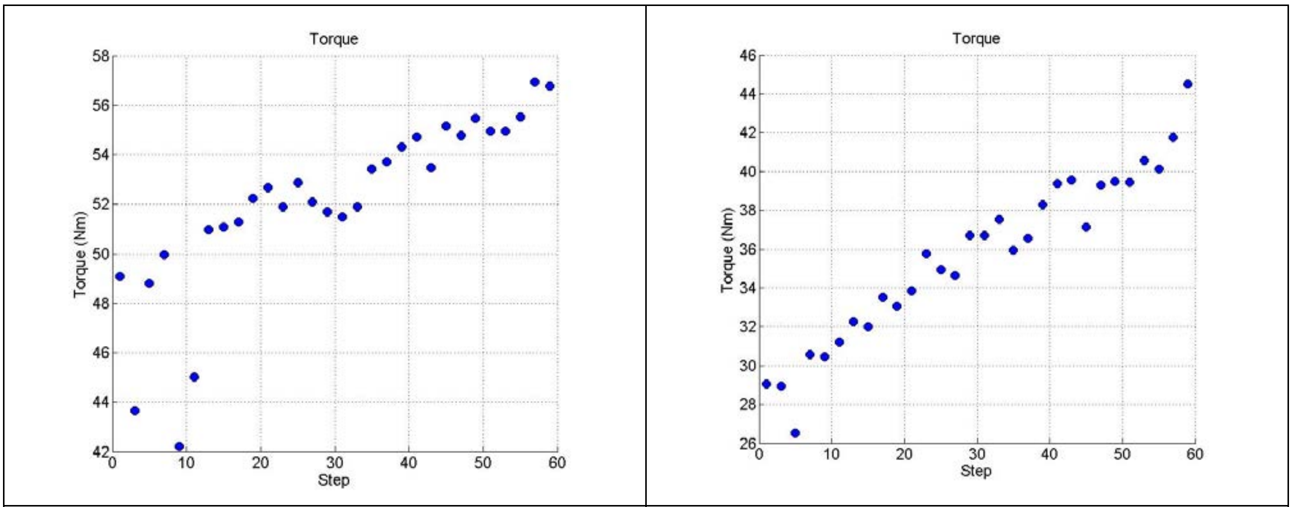

A	B

Figure 2-7: Measured Torque max vs hole number for 60 consecutive holes drilled by the ((A) TTD (B) ISD at 6000 rpm – 0.20 mm/rev.

Furthermore, changing the drilling parameters results in different force and torque. Parameters are chosen on characteristics tool, type material.

A system is required for monitoring and acquiring the signals. The sensory signals were conditioned during the drilling tests to eliminate the noise and portions not related to the actual processing, as shown in Figure 2-8, which shows the progress of the feed force, for hole no. 6 in operating conditions 6000 rpm – 0.15 mm/rev in stacks CFRP/CFRP.

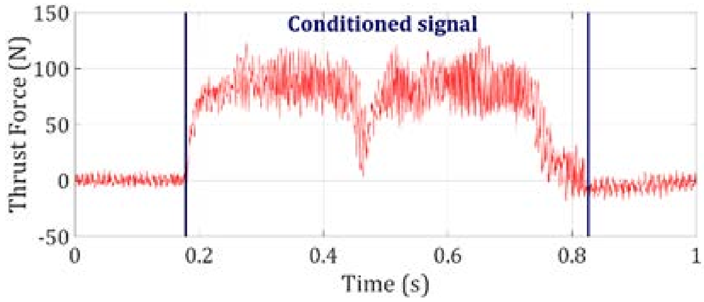

Figure 2-8: Signal relating to the thrust force recorder at 6000 rpm – 0.15 mm/rev.

The drilling of the Al/CFRP stacks is characterised by an increase of the force and the torque during the processing of the metal compared to the composite; this difference can worsen the quality of the holes.

Thrust force and torque increase with the feed rate due to the greater influence of the arrangement fibres. In CFRP, thrust force decreases with feed motion since the rise of temperature reduces the shear strength of the resin; on the contrary, for aluminium, the increase of velocity implies an increase of the thrust force (Figure 2-9).

The velocity also influences the chip's formation: small chips are generated when low values of the velocity are set. But a slighter influence of the mandrel velocity is found. The chip of aluminium's dimension can influence the hole quality; then, it is essential to reduce their sizes and help the removal.

For the same hole, the thrust force has a growing trend until reaching a constant value; the first peak is related to drill aluminium; when it starts to drill, CFRP laminate has a lower and constant force. At the end of the drilling, the force assumes a value equal to zero when the tool exits the laminate (Figure 2-9).

The consideration of the trend of the torque is similar to the trend of the thrust force.

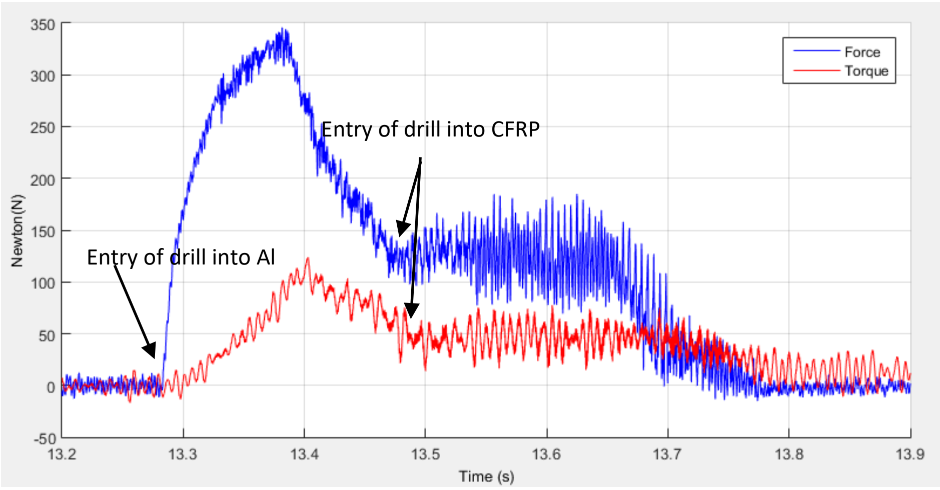

Figure 2-9: Signal of thrust force (blue line) and torque (red line) in the drilling machine process of Al/CFRP Stacks.

A CNC machining centre was equipped with two Kistler piezoelectric load cells to detect the torque and the vertical force that the tool exerts on the workpiece. The load cell generates a d.d.p. proportional to the recorded force; by means of an amplifier (Kistler; model: type 5007), each voltage signal is then amplified. A Hi-Speed USB Carrier acquisition card, type NI USB-9162, receives the amplified signal recorded by a PC using the Vibration Basic Analyzer (Wintek 2006) -Rel software. 1.0 B, and finally processed through the Matlab program. Figure 2-10 shows the equipment where the sample fixture is positioned up to the thrust force and torque sensors.

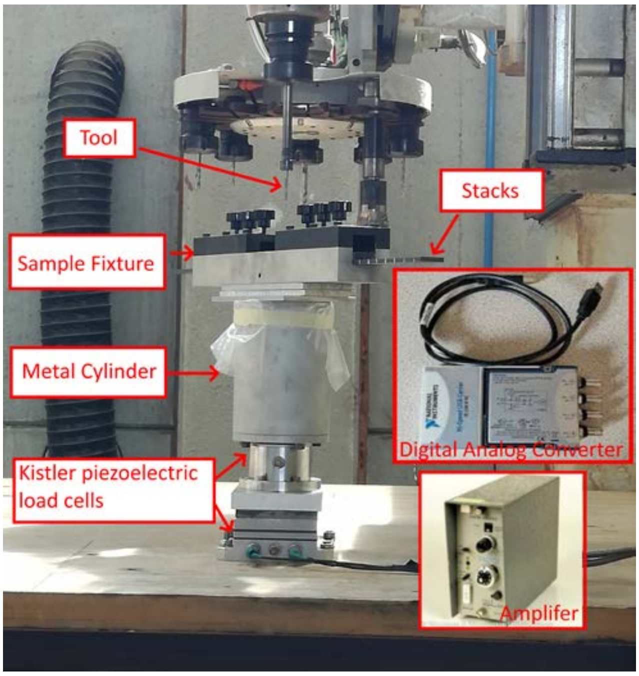

Figure 2-10: Equipment.

To study the influence of the drilling process parameters, as close as possible to those of the actual operating conditions on the aeronautical structures' assembly sites were chosen.

The study of the drilling process is essential to verify dimensional tolerances imposed by the specific sector. It deems necessary to carry out appropriate dimensional analyses of the holes. Furthermore, it is important to monitor the dependence on the cutting parameters chosen, the type of tool used, and the degree of wear of the tool itself.

2.2 PROCESS PARAMETERS

The drilling process involves two basic motions [66]:

- The primary (or cutting) motion represents the rotation around the tool axis. The cutting speed V_t is measurable by the following relation:

$$V_t = \frac{\pi * n * D}{1000} \qquad \text{Eq. 2-1}$$

where:
D is the bit diameter;
n is the spindle speed.

- The second motion is called the feed motion (V_a). It is obtained from the motion of the tool perpendicular to the workpiece. The feed of the main spindle is calculated as follows:

$$V_a = f_r * n \qquad \text{Eq. 2-2}$$

where f_r is the feed per revolution.

The feed rate (f) or forward ratio is the ratio between forwarding speed *Fs* and spindle speed:

$$f = \frac{V_a}{n} \quad \text{Eq. 2-3}$$

Figure 2-11 shows the characteristic parameters of drilling.

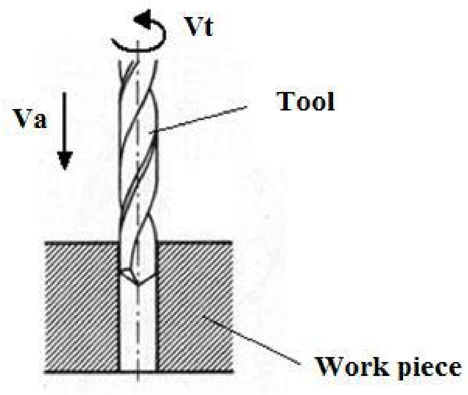

Figure 2-11: Drilling basic motions.

For the success of the drilling operations, it is essential to know these parameters and their combination.

Different fibres' orientations constitute the laminates of composite materials. They acquire anisotropy and inhomogeneity properties, making it light and strong and hard to be machined [67].

Drilling is a particularly hostile operation for composite laminates because highly concentrated efforts and vibrations generated during such processing may cause widespread damage. Such damages cause problems from an aesthetical point of view, but they can also compromise finished mechanical properties.

Table 2-3 and Table 2-4 show the nomenclature of the tool and the parameters for the study of this thesis.

For all the tests, three repetitions were carried out, and the results were averaged.

STACK	TOOL	DIAMETER [MM]	TEST NAME	SPINDLE SPEED [RPM]	FEED RATE [MM/REV]
CFRP /CFRP	TTD	4.9	CFRP-TTD1	2700	0.11
CFRP /CFRP	TTD	4.9	CFRP-TTD2	6000	0.2
CFRP /CFRP	TTD	4.9	CFRP-TTD3	7500	0.2
CFRP /CFRP	ISD	4.9	CFRP-ISD1	2700	0.11
CFRP /CFRP	ISD	4.9	CFRP-ISD2	6000	0.2
CFRP /CFRP	ISD	4.9	CFRP-ISD3	7500	0.2
CFRP /CFRP	TTD	6.35	CFRP-T1	2700	0.11
CFRP /CFRP	TTD	6.35	CFRP-T2	6000	0.2
CFRP /CFRP	TTD	6.35	CFRP-T3	7500	0.2
CFRP /CFRP	TTD	6.35	CFRP-I1	2700	0.11
CFRP /CFRP	TTD	6.35	CFRP-I2	6000	0.2
CFRP /CFRP	TTD	6.35	CFRP-I3	7500	0.2

Table 2-3: Test names and corresponding process parameters combinations for the tool used to CFRP/CFRP stack.

STACK	TOOL	DIAMETER [MM]	TEST NAME	SPINDLE SPEED [RPM]	FEED RATE [MM/REV]
AL/CFRP	TTD	4.9	TTD1	2700	0.11
AL/CFRP	TTD	4.9	TTD2	6000	0.2
AL/CFRP	TTD	4.9	TTD3	7500	0.2
AL/CFRP	TTD			9000	0.11
AL/CFRP	ISD			2700	0.11
AL/CFRP	ISD			6000	0.2
AL/CFRP	ISD			7500	0.2
AL/CFRP	ISD	4.9	ISD1	9000	0.11
AL/CFRP	TTD	6.35	T1	3000	0.05
AL/CFRP	TTD	6.35	T2	3000	0.10
AL/CFRP	TTD	6.35	T3	3000	0.15
AL/CFRP	TTD	6.35	T4	4500	0.05
AL/CFRP	TTD	6.35	T5	4500	0.10
AL/CFRP	TTD	6.35	T6	4500	0.15
AL/CFRP	TTD	6.35	T7	6000	0.05
AL/CFRP	TTD	6.35	T8	6000	0.10
AL/CFRP	TTD	6.35	T9	6000	0.15
AL/CFRP	ISD	6.35	I1	2700	0.11
AL/CFRP	ISD	6.35	I2	6000	0.2
AL/CFRP	ISD	6.35	I3	7500	0.2

Table 2-4: Test names and corresponding process parameters combinations for the tool used to CFRP/CFRP stack.

3 TEMPERATURE ANALYSIS

The interest in temperature analysis is due to the possibility of process control in the industrial field by measuring the temperature.

It is necessary to measure the process temperature to proceed with a correct study of the phenomenon linked to heat transmission.

The choice of a correct thermal camera is fundamental to measuring the real temperature. This tool is based on three essential characteristics:

- Temperature range to be acquired: make sure that the entire process is thermally monitored; for this reason, it is necessary to make sure to define, with a previous study, the temperature range to which the material is subjected during processing and consequently proceed with the choice of a thermal imager that ensures the display of this range.

- Choice of acquisition frequency: acquisition frequencies that are too low cannot monitor a sufficient number of frames to ensure that the maximum temperature reached during the process has been acquired. This temperature becomes necessary if you want to study the phenomena to which the material on which the mechanical machining is taking place is subject and on the tool chosen. In order not to miss important information, it is necessary to know the processing speed and to choose a thermal imaging camera with the appropriate capture rate capabilities. A good thermal imaging camera should have, depending on the processing speed, an acquisition frequency of at least 80 Hz, for the drilling process.

- Lens: the lens of the thermal imager can also play a fundamental role in its choice. More performing lens can allow you to place the camera at the desired distance without losing information due to poor focus.

The choice of a correct processed area is significant. In addition, the presence of thermal phenomena is more critical to collocate the thermal camera. Finally, this study could also affect the camera's size, as large cameras are not easily positioned inside a machine tool.

The temperature is an important parameter for I.A. for data processing and machine control; since the temperature is a measurable parameter during the machining. It is easy to think of being able to send a signal to the machine tool in order to automatically modify some machining parameters or indicate the need to replace the worn device without the need to stop the machine from checking the material. This information can be given to the machine downstream of an accurate study of the process, which allows defining all the quality parameters.

3.1 AIM OF THERMAL ANALYSIS

A correlation between the increase in temperature and the wear of the tip itself is studied.

Is possible to demonstrate how the increased temperature due to tool wears favours the onset of delamination at the exit hole. Temperature data acquisitions were performed using an Infrared Optris PI 450 camera, shown in **Figure 3-1 A**, with 80 Hz framerate and an optical resolution of 382 x 288 pixels providing real-time thermographic monitoring. This infrared camera offers a temperature range from -20°C to 900°C. The spectral range is from 7.5 to 13 µm. The Optris PI Connect software allows the acquisition of videos and instant recordings, from which it is possible to extrapolate the data relating to the area to examine.

The Optris PI Connect software allows capturing videos, instantaneous pictures and temperature profiles from which the required data are extracted along with a selected direction or within an area of desired geometry inside the field of view, shown in **Figure 3-1 B**.

The characteristic emission value for this type of CFRP material, commonly used in the literature, is 0.85 (measured according to the procedure of ASTM E 1933 standard [68]); therefore, this coefficient was set in the software.

In the tests, the camera was placed inside a metal cylinder under the laminates fixture, as shown in **Figure 2-10.** The cylinder protected with a film to prevent powder generated during the drilling process from infiltrating and causing an alteration in investigation temperature [69]. The acquisition date is corresponding to the moment when the tip comes out of the laminate during drilling.

The processing of the data acquired through the thermographic camera software makes possible to record a temperature/time diagram for each hole drilled. Temperature measurements were carried out only for odd number holes to speed up data acquisition; this choice is possible because of the temperature difference between a hole and the next one of few degrees.

Figure 3-2 shows the Optris PI Connect software interface that allows the acquisition field's choice for the temperature measurement.

	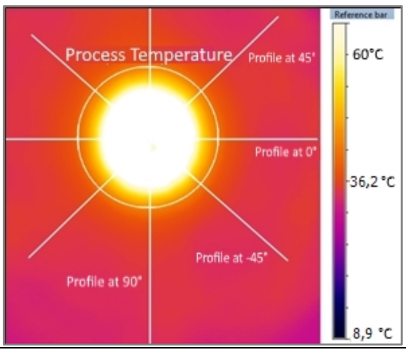
A	**B**

Figure 3-1: (A) Temocamera Optris PI 450; (B) Four directions (0°, ±45° and 90°) of inquired temperature.

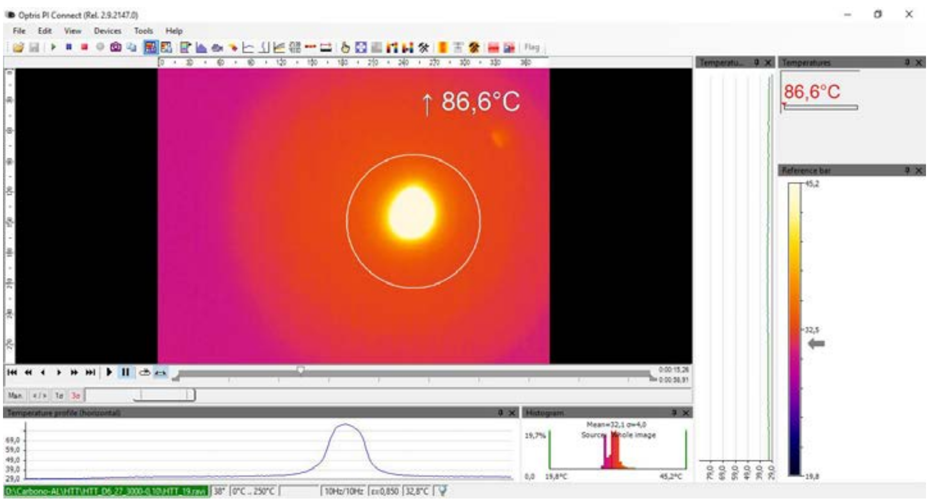

Figure 3-2: Software Optris PI Connect: graphic interface.

From the processing of the data acquired through the software, it was possible to obtain a temperature/time diagram related to the single hole.

These graphs were subsequently developed.

In the following paragraphs, therefore, the graphs are related to:

a) Temperature trend as a function of time, obtained for holes 1-29-59 for the CFRP / CFRP stacks, and graphs of the temperature trend as a function of time for holes 1-15-29 regarding the Al / CFRP stacks.

b) The trend of the maximum temperature reached inside the individual holes, reporting the temperatures of only the odd holes for the single tool used;

c) The cooling time trend reached for the number of odd holes for the single tool used.

d) Results obtained from the data analysis, reporting in a summary table that compares **TTD** and **ISD** tool:

   - the maximum temperature reached in the first hole; **T_MAX _1**
   - the absolute maximum temperature reached during the acquisitions from hole 1 to the last hole; **T_MAX _N**
   - the difference between the minimum and maximum temperature values; **Delta_T**
   - The highest cooling time encountered during processing; **(Cooling Time max)**
   - The lowest cooling time encountered during processing; **(Cooling Time min)**
   - The difference between the highest and the lowest cooling time encountered during washing. **(Delta Cooling Time)**

3.2 CFRP/CFRP STACKS – DIAMETER TOOL 4.9 MM

This paragraph shows the **trends of the maximum temperature** in the area around the hole. Graphs temperature/time are detected by the thermo-camera during the CFRP/CFRP stack drilling process. A comparison was made between the curves obtained from the data analysis for holes n. 1-29-59 for the two different tools with a nominal diameter tool of 4.9 mm.

All tests were carried out under standard conditions of temperature and pressure.

Afterwards, the **maximum temperature** (**T_MAX**) and the **cooling time** acquired in a single drill were reported and, finally, the data from the different tools were compared.

3.2.1 PARAMETER: CFRP-TTD1/CFRP-ISD1

The data acquired via the thermographic camera were suitably post-processed to obtain a temperature/time diagram describing the temperature trend during the drilling of each hole.

Figure 3-7 shows the trends for the number of 1-29-59 holes for TTD and ISD tools.

The traditional tool graph has a slower cooling phase, during which the laminate is subjected to high temperature for a longer time.

The reason is that the traditional tool is a twist drill; when the flank ultimately enters the laminate, the full drill diameter gets in contact with the inner hole wall. In this case, the heat generated during the process cannot dissipate. Instead, an innovative tool has two-step geometry with increasing diameters; hence, the first drill bit step removed the material but heated the near materials. The second drill bit step high-temperature material removed as chip material.

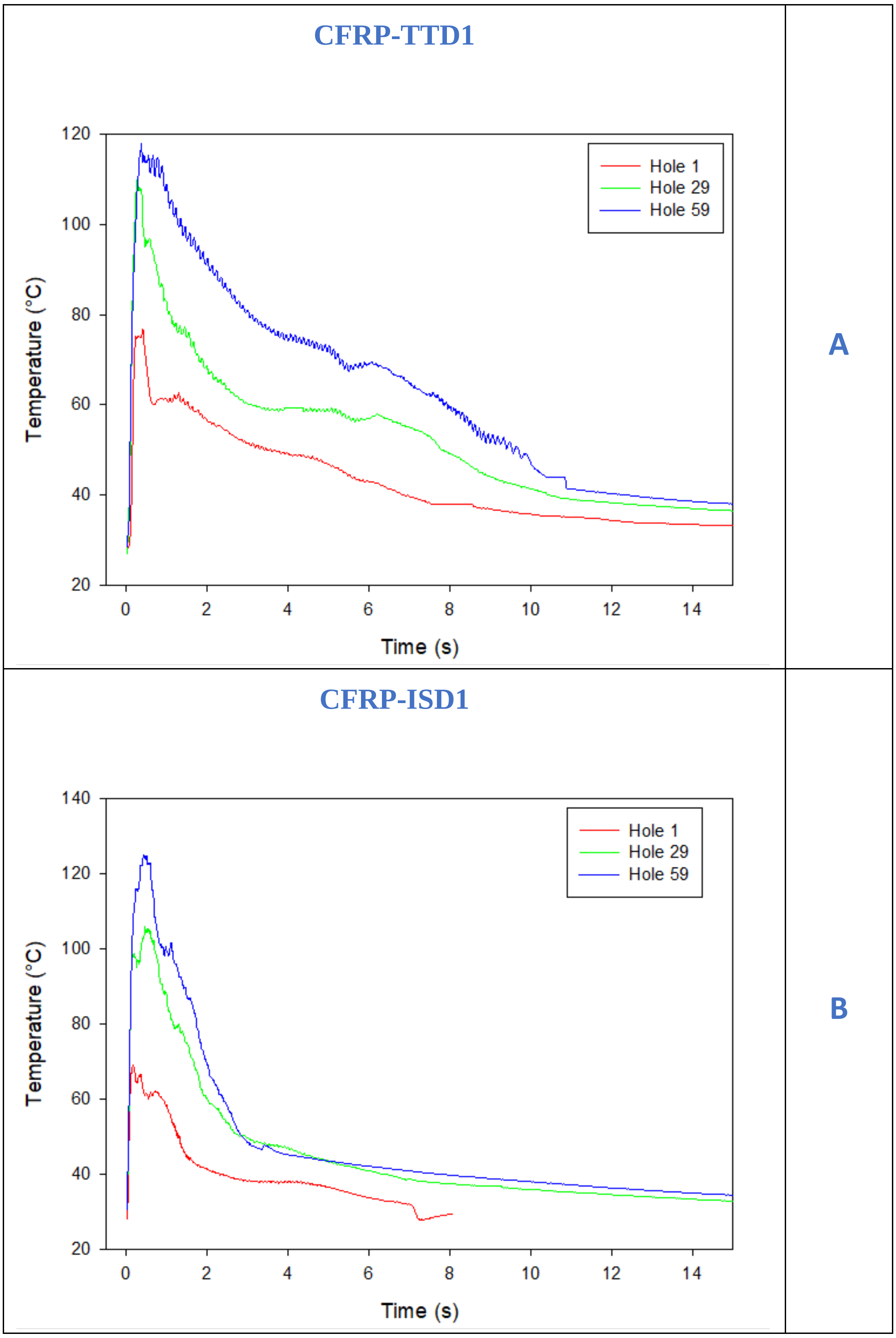

Figure 3-3: Temperature trend for the holes n. 1-29-59 for TTD (A) end ISD (B) tool, parameter 2700 rpm and 0.11 mm/rev.

The maximum temperature, **T_MAX** is reported in Figure 3-4A. The trends show that with CFRP-TTD1, the maximum temperature is high but constant with the increasing number of the hole. Indeed, ISD has a lower temperature in the first 30 holes but has a fitting curve with higher slope, compared to CFRP-TTD1.

The cooling times of the specimens (time from the maximum and the room temperature), are shown in Figure 3-4 B. CFRP-ISD1 reached a higher cooling time of the laminate during all tests than CFRP-TTD1, but the CFRP-TTD1 tool has a fitting curve with higher slope, compared to CFRP-ISD1. As a matter of fact, with CFRP-TTD1, hole no. 59 cools down in 13.5 s, with ISD, and it cools down in 8.1 s. On the other hand, holes no. 1 have a cooling time difference of 2.5 s between the different tool. In particular, with CFRP-TTD1, hole no. 1 cools down in 6.5 s, with CFRP-ISD1, and it cools down in 4.0 s.

All tests show a growing trend of the cooling time with the increasing number of holes.

The results obtained are reported in a summary (Table 7-1) that compares the CFRP-TTD1 and CFRP-ISD1tool.

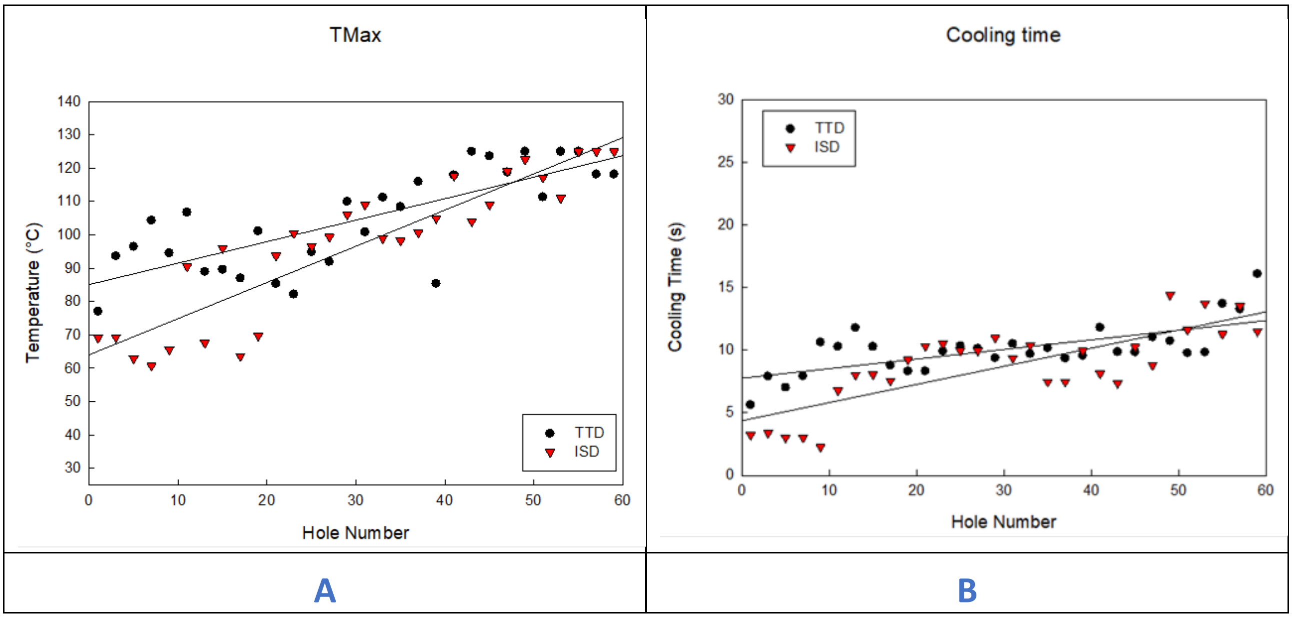

Figure 3-4: Measured T_MAX vs Hole Number(A) and Cooling time VS hole number (B) for 60 consecutive odd holes drilled by the TTD and ISD tools, parameter 2700 rpm and 0.11 mm/rev.

	T_MAX_1 [°C]	T_MAX_N [°C]	DELTA_T [°C]	COOLING TIME MIN [S]	COOLING TIME MAX [S]	DELTA COOLING TIME [S]
CFRP-TTD1	77	124	47	6.5	13.5	6.9
CFRP-ISD1	61	124	63	4.0	8.1	4.1

Table 3-1: Comparison of the results obtained during stack drilling of CFRP / CFRP by the TTD and ISD tools, parameter 2700 rpm and 0.11 mm/rev.

3.2.2 PARAMETER: CFRP-TTD2/CFRP-ISD2

The data acquired via the thermographic camera were suitably post-processed to obtain a temperature/time diagram describing the temperature trend during the drilling of each hole.

Figure 3-5 shows the trends for the number of 1-29-59 holes for TTD and ISD tools. The shape of this graph is similar to parameter 2700 rpm and 2700 0.11 mm/rev. The difference is mostly in CFRP-ISD2, where the trends have shown a more rapid decrease and a tighter peak.

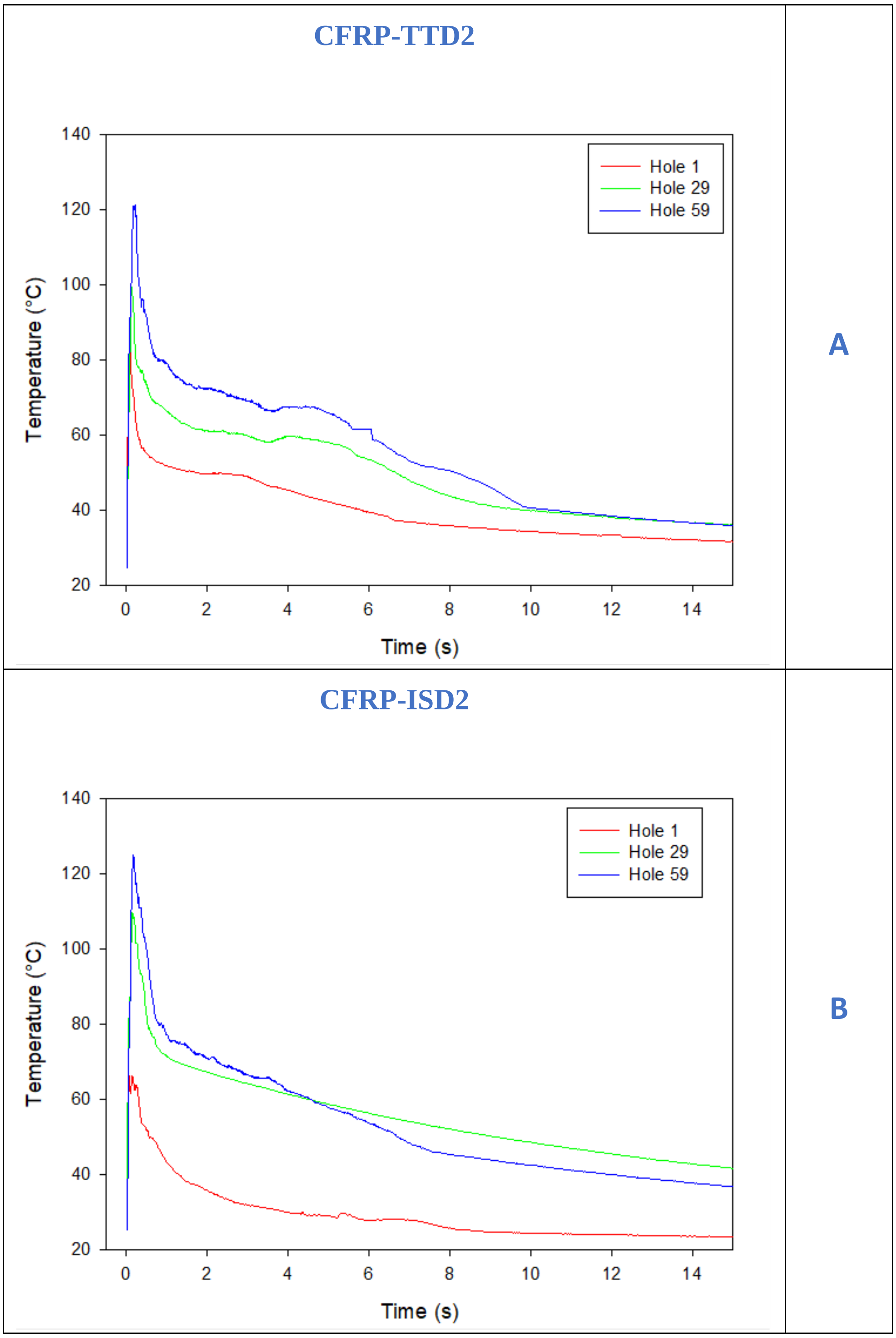

Figure 3-5: Temperature trend for the holes n. 1-29-59 for TTD (A) end ISD (B) tool, parameter 6000 rpm and 0.2 mm/rev.

The maximum temperature, T_MAX, reached during drilling, is attested in **Figure 3-6 A**. The trends show that with CFRP-TTD2, the maximum temperature is high but constant with the increasing number of the hole. Indeed, CFRP-ISD2 has a lower temperature in the first 10 holes but has a higher increment of slope with respect to CFRP-TTD2. Indeed, the DELTA_T for the CFRP-ISD2 is 61°C and for CFRP-TTD2 is 48°C, a difference of 13°C.

The cooling times of the specimens are shown in **Figure 3-6 B**. CFRP-ISD2 presents a lower cooling time during the first 20 holes than CFRP-TTD2, but the CFRP-ISD2 tool has a fitting curve similar respect to CFRP-TTD2. As a matter of fact, with CFRP-TTD2, hole no. 59 cools down in 16.1 s, with CFRP-ISD2, and it cools down in 14.4 s. On the other hand, holes no. 1 have a cooling time difference of 3.3 s between the different tool. In particular, with CFRP-TTD2, hole no. 1 cools down in 5.6 s, with CFRP-ISD2, and it cools down in 2.3 s.

All tests show a growing trend of the cooling time with the increasing number of holes.

The results obtained are reported in a summary (**Table 3-2**) that compares the CFRP-TTD2 and CFRP-ISD2 tool.

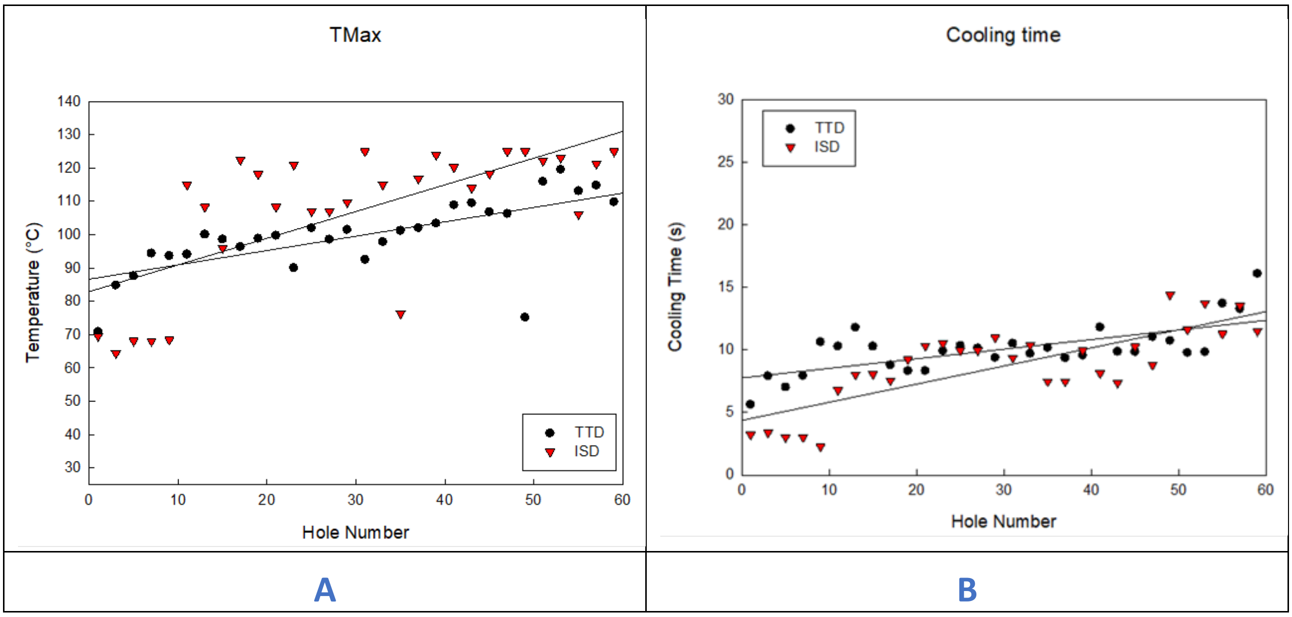

Figure 3-6: Measured T_MAX vs Hole Number (A) and Cooling time VS hole number (B) for 60 consecutive odd holes drilled by the TTD and ISD tools, parameter 6000 rpm and 0.2 mm/rev.

	T_MAX_1 [°C]	T_MAX_N [°C]	DELTA_T [°C]	COOLING TIME MIN [S]	COOLING TIME MAX [S]	DELTA COOLING TIME [S]
CFRP-TTD2	71	119	48	5.6	16.1	10.5
CFRP-ISD2	64	125	61	2.3	14.4	12.1

Table 3-2: Comparison of the results obtained during stack drilling of CFRP / CFRP by the TTD and ISD tools, parameter 6000 rpm and 0.2 mm/rev.

3.2.3 PARAMETER: CFRP-TTD3/CFRP-ISD3

The data acquired via the thermographic camera were suitably post-processed to obtain a temperature/time diagram describing the temperature trend during the drilling of each hole.

Figure 3-7 shows the trends for the number of 1-29-59 holes for TTD and ISD tools.

The traditional tool graph has a slower cooling phase, during which the laminate is subjected to high temperature for a longer time, like parameter 2700 rpm - 0.11 mm/rev and 6000 rpm - 0.2 mm/rev.

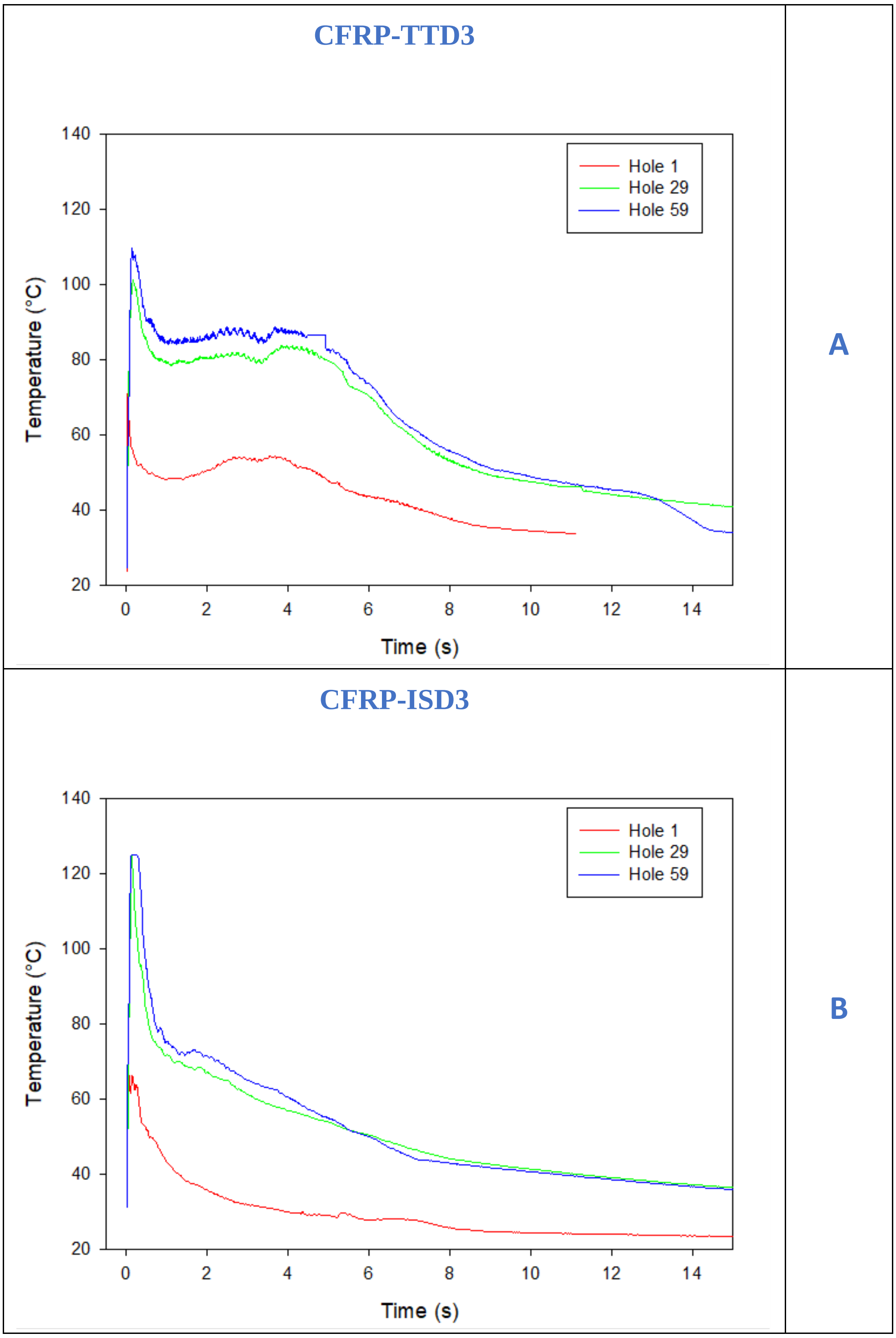

Figure 3-7: Temperature trend for the holes n. 1-29-59 for TTD (A) end ISD (B) tool, parameter 7500 rpm and 0.2 mm/rev.

The maximum temperature, **T_MAX**, is shown in **Figure 3-8 A**. The trends show that with CFRP-TTD3, the maximum temperature is high but constant with the increasing number of the hole. Indeed, CFRP-ISD3 has a lower temperature in the first 10 holes but has a higher increment of slope to CFRP-TTD3. After this instant increase of temperature, CFRP-ISD3 has a constant trend. Indeed, the DELTA_T for the CFRP-ISD3 is 63°C and for CFRP-TTD3 is 40°C, a difference of 13°C.

The cooling times of the specimens are shown in **Figure 3-8 B**. CFRP-ISD3 reached a lower cooling time of the laminate during all tests than CFRP-TTD3 and in the first 10 holes, the time cooling of CFRP-ISD3 is much lower of CFRP-TTD3. As a matter of fact, with CFRP-TTD3, hole no. 59 cools down in 15.4 s, with CFRP-ISD3, and it cools down in 13.2 s. On the other hand, holes no. 1 have a cooling time difference of 5.1 s between the different tool. In particular, with CFRP-TTD3, hole no. 1 cools down in 7.1 s, with CFRP-ISD3, and it cools down in 2.0 s.

All tests show a growing trend of the cooling time with the increasing number of holes.

The results obtained are reported in a summary (**Table 3-3**) that compares the CFRP-TTD3 and CFRP-ISD3 tool.

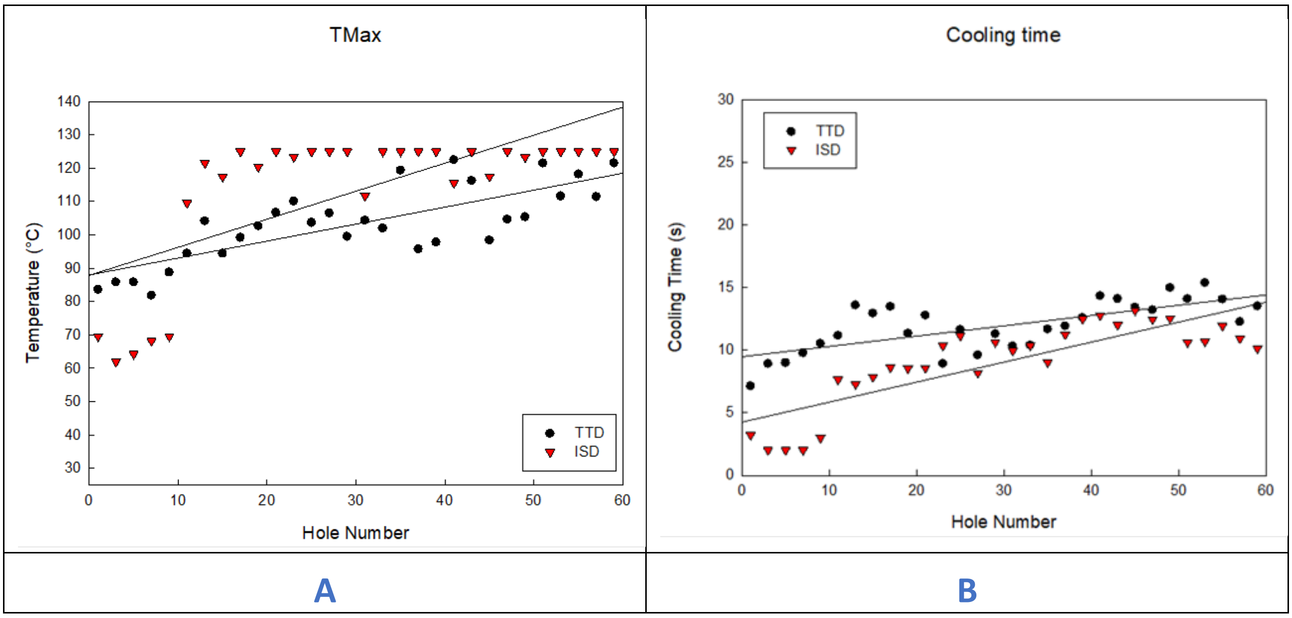

Figure 3-8: Measured T_MAX vs Hole Number(A) and Cooling time VS hole number (B) for 60 consecutive odd holes drilled by the TTD and ISD tools, parameter 7500 rpm and 0.2 mm/rev.

	T_MAX_1 [°C]	T_MAX_N [°C]	DELTA_T [°C]	COOLING TIME MIN [S]	COOLING TIME MAX [S]	DELTA COOLING TIME [S]
CFRP-TTD3	82	122	40	7.1	15.4	8.3
CFRP-ISD3	62	125	63	2.0	13.2	11.2

Table 3-3: Comparison of the results obtained during stack drilling of CFRP / CFRP by the TTD and ISD tools, parameter 7500 rpm and 0.2 mm/rev.

3.3 CFRP/CFRP STACKS – DIAMETER TOOL 6.35 MM

This paragraph shows the **trends of the maximum temperature** in the area around the hole. Graphs temperature/time are detected by the thermo-camera during the CFRP/CFRP stack drilling process. A comparison was made between the curves obtained from the data analysis for holes n. 1-29-59 for the two different tools with a nominal diameter tool of 6.35 mm.

All tests were carried out under the standard condition of temperature and pressure.

Afterwards, the **maximum temperature** (**T_MAX**) and the **cooling time** acquired in a single drill were reported and, finally, the data from the different tools were compared.

3.3.1 PARAMETER: CFRP-T1/CFRP-I1

The data acquired via the thermographic camera were suitably post-processed to obtain a temperature/time diagram describing the temperature trend during each hole's drilling.

Figure 3-9 shows the trends for the number of 1-29-59 holes for TTD and ISD tools.

The traditional tool graph has a slower cooling phase, during which the laminate is subjected to high temperature for a longer time, as seen in the previous paragraph.

For slower parameters, in the CFRP-I1 graph, a decrease and an increase in the maximum recorded temperature are observed after the temperature peak. However, as seen in the above paragraphs, the subsequent temperature increase after the maximum peak is no longer visible with the increasing speed rate.

The maximum temperature, **T_MAX**, reached during drilling, is attested in Figure 3-10 A. The trends show that with CFRP-T1, the maximum temperature is high and constant with the increasing number of the hole. CFRP-I1 has a lower temperature but has a fitting curve with higher slope, compared to CFRP-T1. A slight difference in values during processing between the different tools was noticed.

The specimens cooling times are shown in Figure 3-10 B. CFRP-I1 reached a higher cooling time of the laminate during all tests than CFRP-T1, as the result with the same parameter but with different diameter. As a matter of fact, with CFRP-T1, hole no. 59 cools down in 44.2 s, with CFRP-I1, and it cools down in 46.4 s. On the other hand, holes no. 1 have a cooling time difference of 7.4 s between the different tool. In particular, with CFRP-T1, hole no. 1 cools down in 12.7 s, with CFRP-I1, and it cools down in 20.1 s.

All tests show a growing trend of the cooling time with the increasing number of holes.

The results obtained are reported in a summary (Table 3-4) that compares the CFRP-T1 and CFRP-I1 tool.

CFRP-T1

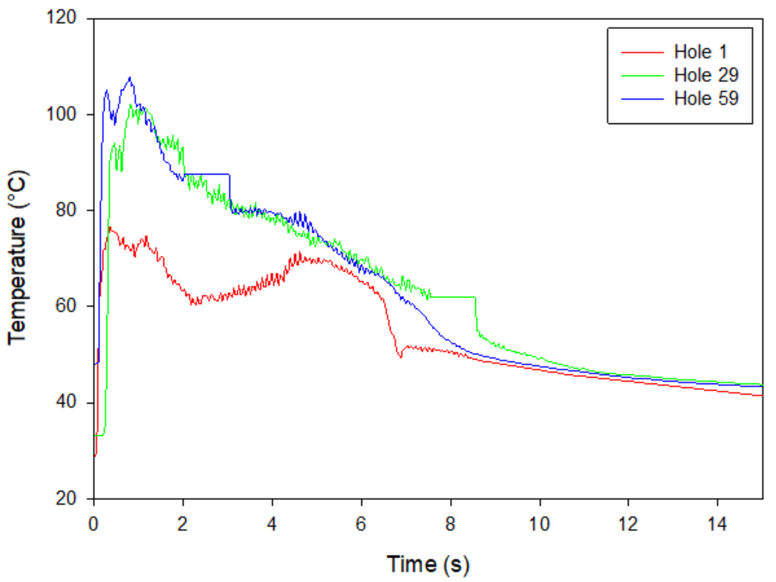

A

CFRP-I1

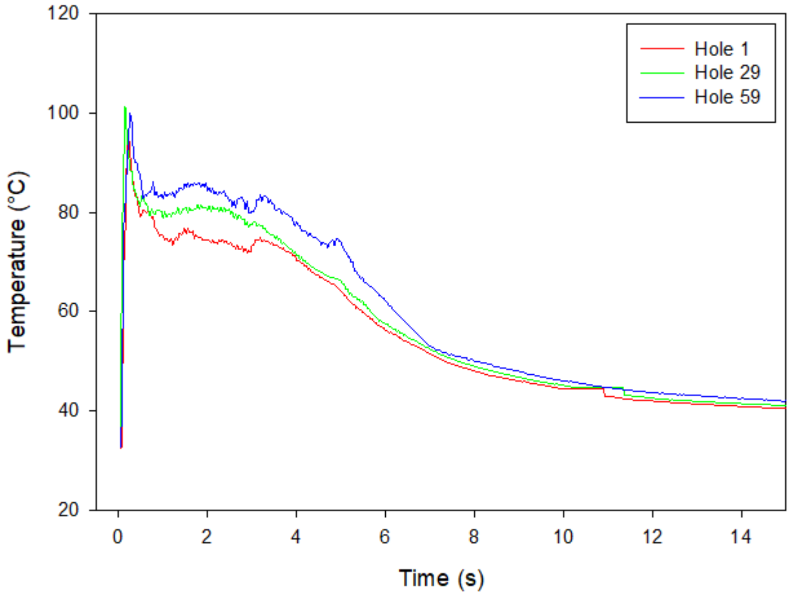

B

Figure 3-9: Temperature trend for the holes n. 1-29-59 for TTD (A) end ISD (B) tool, parameter 2700 rpm and 0.11 mm/rev.

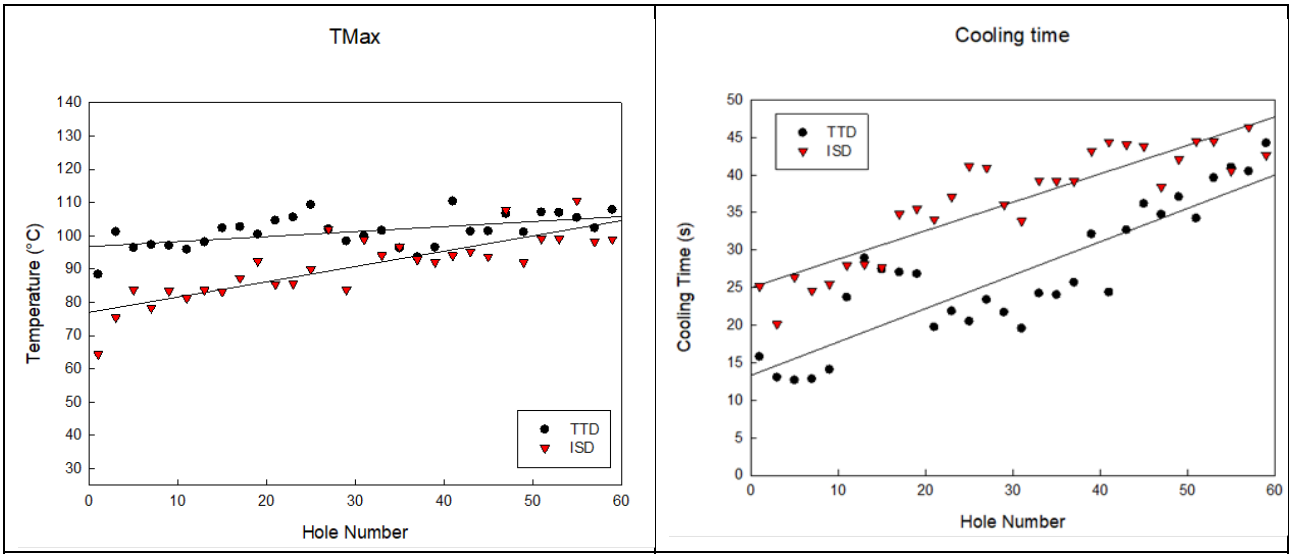

A	B

Figure 3-10: Measured T_MAX vs Hole Number(A) and Cooling time VS hole number (B) for 60 consecutive odd holes drilled by the TTD and ISD tools, parameter 2700 rpm and 0.11 mm/rev.

	T_MAX_1 [°C]	T_MAX_N [°C]	DELTA_T [°C]	COOLING TIME MIN [S]	COOLING TIME MAX [S]	DELTA COOLING TIME [S]
CFRP-T1	88	110	22	12.7	44.2	31.6
CFRP-I1	64	110	46	20.1	46.4	26.3

Table 3-4: Comparison of the results obtained during stack drilling of CFRP / CFRP by the TTD and ISD tools, parameter 2700 rpm and 0.11 mm/rev.

3.3.2 PARAMETER: CFRP-T2/CFRP-I2

The data acquired via the thermographic camera were suitably post-processed to obtain a temperature/time diagram describing the temperature trend during the drilling of each hole.

Figure 3-11 shows the trends for the number of 1-29-59 holes for TTD and ISD tools.

The traditional tool graph has a slower cooling phase, during which the laminate is subjected to high temperature for a longer time.

The maximum temperature, **T_MAX**, reached during drilling, is attested in Figure 3-12 A. The trends show that with CFRP-T2, the maximum temperature exceeds 100°C from the first holes and then remains almost constant while using CFRP-I2. The temperature exceeds 100°C only after hole no. 40.

The cooling times of the specimens are shown in Figure 3-12 B. CFRP-T2 reached a higher cooling time of the laminate during all tests than CFRP-I2, but the CFRP-I2 tool has a fitting curve with higher slope respect to CFRP-T2. As a matter of fact, with CFRP-T2, hole no. 59 cools down in 20.6 s, with CFRP-I2, and it cools down in 17.5 s. On the other hand, holes no. 1 have a cooling time difference of 3.1 s between the different tool. In particular, with CFRP-T2, hole no. 1 cools down in 11.7 s, with CFRP-I2, and it cools down in 4.8 s.

All tests show a growing trend of the cooling time with the increasing number of holes.

The results obtained are reported in a summary (Table 3-5) that compares the CFRP-T2 and CFRP-I2 tool.

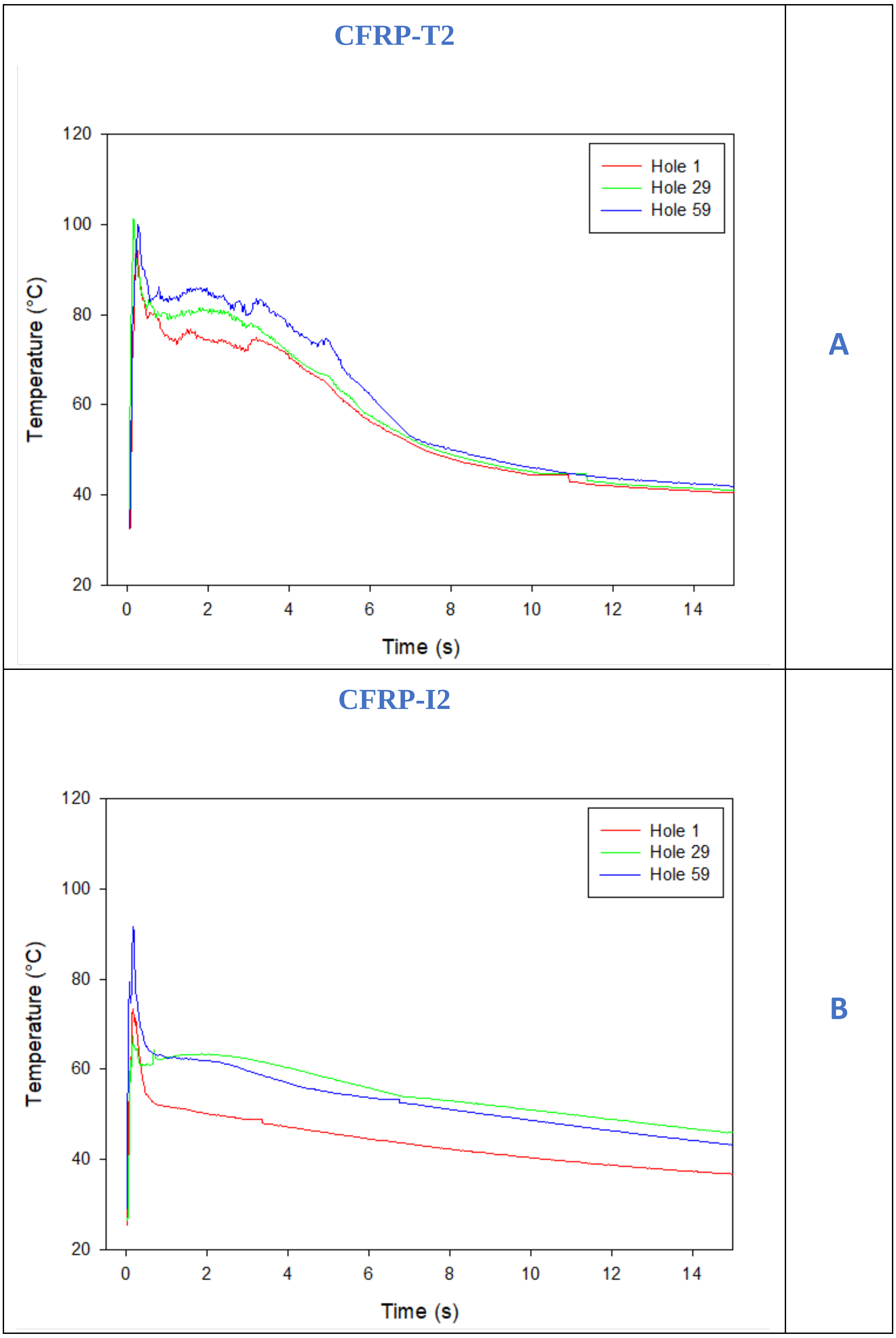

Figure 3-11: Temperature trend for the holes n. 1-29-59 for TTD (A) end CFRP-I2 (B) tool, parameter 6000 rpm and 0.2 mm/rev.

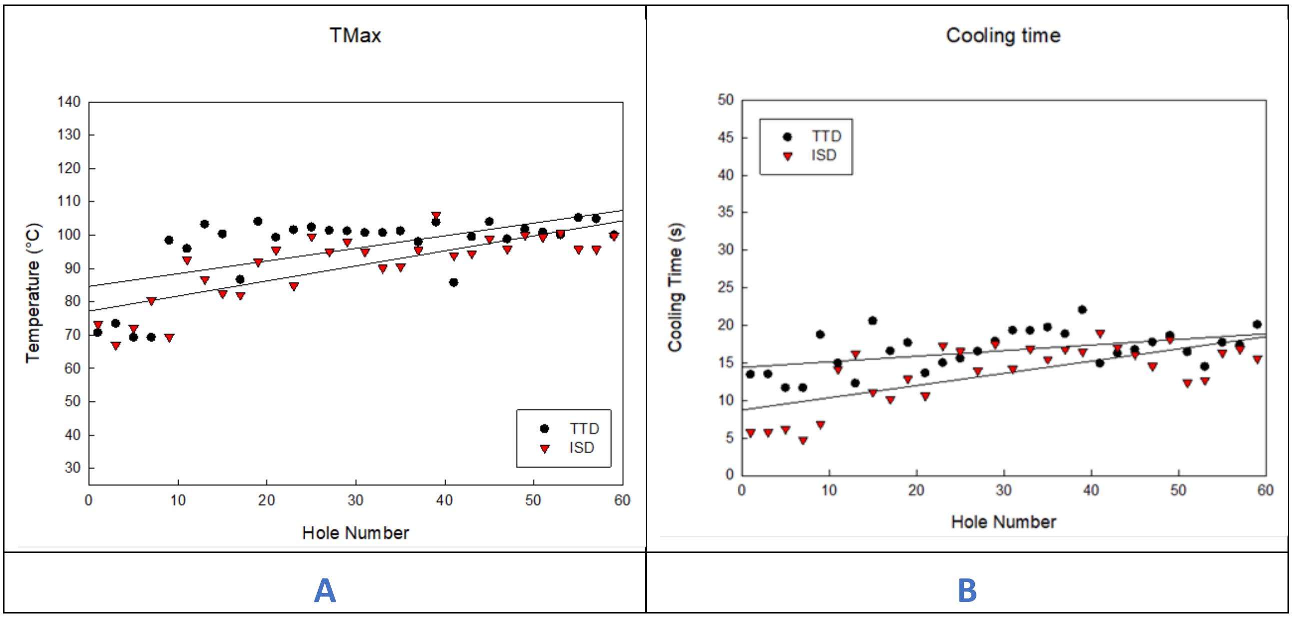

Figure 3-12: Measured T_MAX vs Hole Number(A) and Cooling time VS hole number (B) for 60 consecutive odd holes drilled by the TTD and ISD tools, parameter 6000 rpm and 0.2 mm/rev.

	T_MAX_1 [°C]	T_MAX_N [°C]	DELTA_T [°C]	COOLING TIME MIN [S]	COOLING TIME MAX [S]	DELTA COOLING TIME [S]
CFRP-T2	69	105	36	11.7	20.6	8.9
CFRP-I2	67	106	39	4.8	17.5	12.7

Table 3-5: Comparison of the results obtained during stack drilling of CFRP / CFRP by the TTD and ISD tools, parameter 6000 rpm and 0.2 mm/rev.

3.3.3 PARAMETER: CFRP-T3/CFRP-I3

The data acquired via the thermographic camera were suitably post-processed to obtain a temperature/time diagram describing the temperature trend during the drilling of each hole.

Figure 3-13 shows the trends for the number of 1-29-59 holes for TTD and ISD tools.

The maximum temperature, **T_MAX**, reached during drilling, is attested in **Figure 3-14 A.** The trends show that with CFRP-T3, the maximum temperature is lower with the increasing number of the hole. CFRP-I3 has a higher temperature but a similar fitting curve to CFRP-T3. Not notice an excessive difference in values during processing between the different tool. There are many degrees of difference between the T_MAX of the first and last hole in both tools.

The cooling times of the specimens are shown in **Figure 3-14 B**. CFRP-I3 reached a lower cooling time for the first 20 holes, but the CFRP-I3 tool has a fitting curve with higher slope respect to CFRP-T3. As a matter of fact, with CFRP-T3, hole no. 59 cools down in 22.6 s, with CFRP-I3, and it cools down in 21.4 s. On the other hand, holes no. 1 have a cooling time difference of 3.1 s between the different tool. In particular, with CFRP-T3, hole no. 1 cools down in 14.5 s, with CFRP-I3, and it cools down in 8.6 s.

All tests show a growing trend of the cooling time with the increasing number of holes.

The results obtained are reported in a summary (Table 3-6) that compares the CFRP-T3 and CFRP-I3 tool.

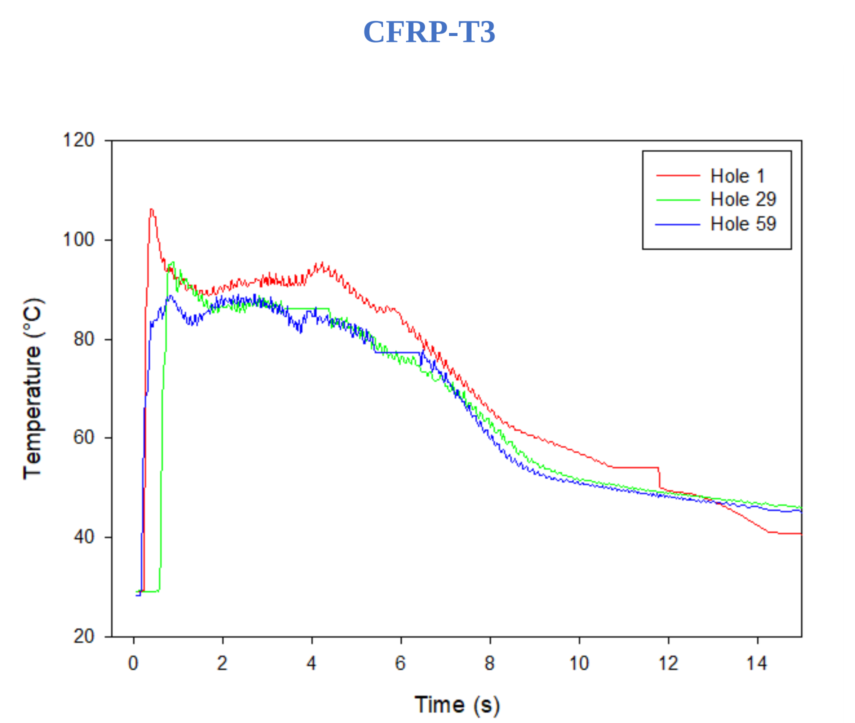

A

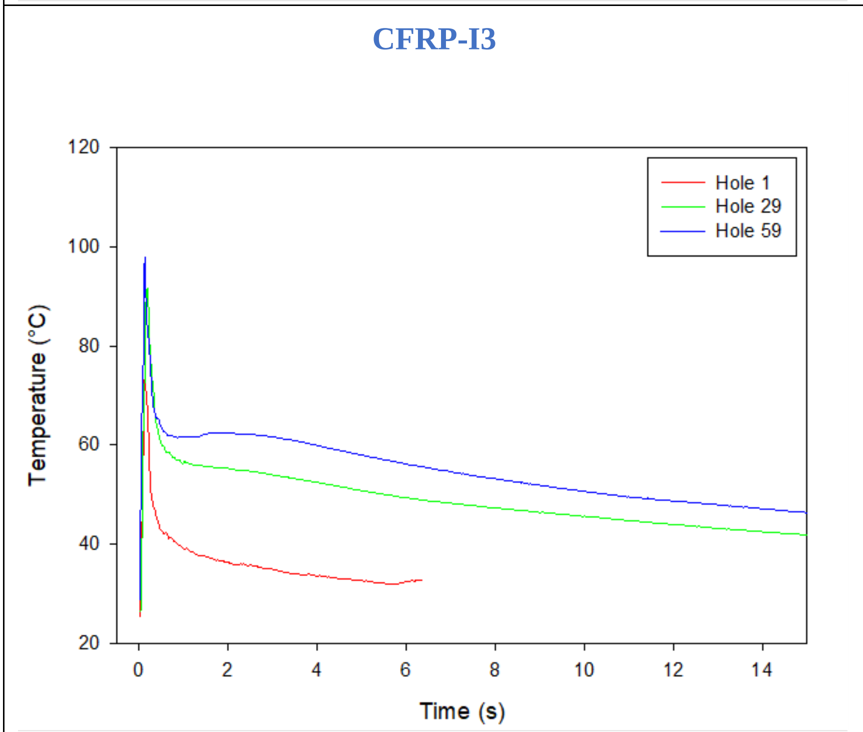

B

Figure 3-13: Temperature trend for the holes n. 1-29-59 for TTD (A) end ISD (B) tool, parameter 7500 rpm and 0.2 mm/rev.

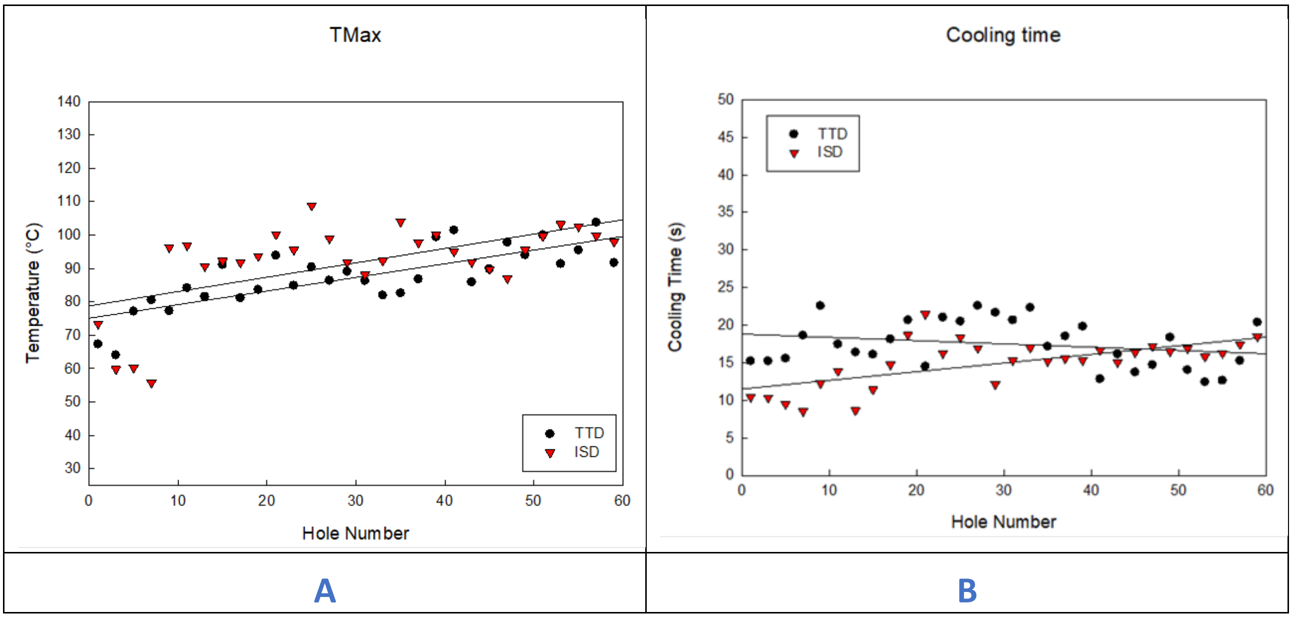

Figure 3-14: Measured T_MAX vs Hole Number(A) and Cooling time VS hole number (B) for 60 consecutive odd holes drilled by the TTD and ISD tools, parameter 7500 rpm and 0.11 mm/rev.

	T_MAX_1 [°C]	T_MAX_N [°C]	DELTA_T [°C]	COOLING TIME MIN [S]	COOLING TIME MAX [S]	DELTA COOLING TIME [S]
CFRP-T3	64	104	40	14.5	22.6	8.1
CFRP-I3	56	109	53	8.6	21.4	12.9

Table 3-6: Comparison of the results obtained during stack drilling of CFRP / CFRP by the TTD and ISD tools, parameter 7500 rpm and 0.11 mm/rev.

3.4 AL/CFRP STACKS– DIAMETER TOOL 4.9 MM

This paragraph shows the **trends of the maximum temperature** in the area around the hole. Graphs temperature/time are detected by the thermo-camera during the Al/CFRP stack drilling process. A comparison was made between the data obtained from the data analysis tools with a nominal diameter tool of 4.9 mm.

For this test, the ISD tools did not return useful results with these parameters for drilling Al/CFRP stacks, except with 9000 rpm and 0.11 mm/rev. For this set, the TTD tools did not return useful results. Table 3-7 shows the parameter used for this combination of diameter tool and materials stacks. Table 3-8 shows the number hole with the tool's cracking during the drilling of Al/CFRP stacks.

All tests were carried out under the standard condition of temperature and pressure.

Afterwards, the **maximum temperature** (T_MAX) and the **cooling time** acquired in a single drill were reported and, finally, the data from the different tools were compared.

TOOL	TEST NAME	SPINDLE SPEED [RPM]	FEED RATE [MM/REV]
TTD	TTD1	2700	0.11
TTD	TTD2	6000	0.2
TTD	TTD3	7500	0.2
ISD	ISD1	9000	0.11

Table 3-7: Test names and corresponding process parameters combinations.

TOOL	SPINDLE SPEED [RPM]	FEED RATE [MM/REV]	NUMBER HOLE OF TOOL CRACKING
ISD	2700	0.11	5
ISD	6000	0.2	5
ISD	7500	0.2	1
TTD	9000	0.11	1

Table 3-8: Number hole with the tool's cracking during the drilling of Al / CFRP stacks.

3.4.1 PARAMETER: TTD1/TTD2/TTD3

This paragraph will compare the different parameter studied with TTD.

The data acquired via the thermographic camera were suitably post-processed to obtain a temperature/time diagram describing the temperature trend during the drilling of each hole.

The maximum temperature, **T_MAX**, reached during drilling, is attested in Figure 3-15 A. All the parameters combination have a similar and constant trend. In fact, TTD1 has the major **DELTA_T** (of 20°C), and TTD3 has the minor **DELTA_T** (9°C) respect all parameters. The temperature range is 60-90°C, an intermediate range that respects the corresponding parameters of the CFRP/CFRP stacks' drilling parameters.

The cooling times of the specimens are shown in Figure 3-15 B. TTD1 and TTD2 reached a lower cooling time for the first hole, but this feature incresead for the following ones. TTD3 kept a constant cooling time during the drilling process whit a DELTA cooling time of 4.7 s, a difference of TTD1 and TTD2 with 10.0 s and 9.1 s.

Compared to the values found for the CFRP/CFRP stacks, the lower temperature and cooling time values are due to aluminium, which helps the composite to dissipate heat faster.

The results obtained are reported in a summary (Table 3-9) that compares the tool.

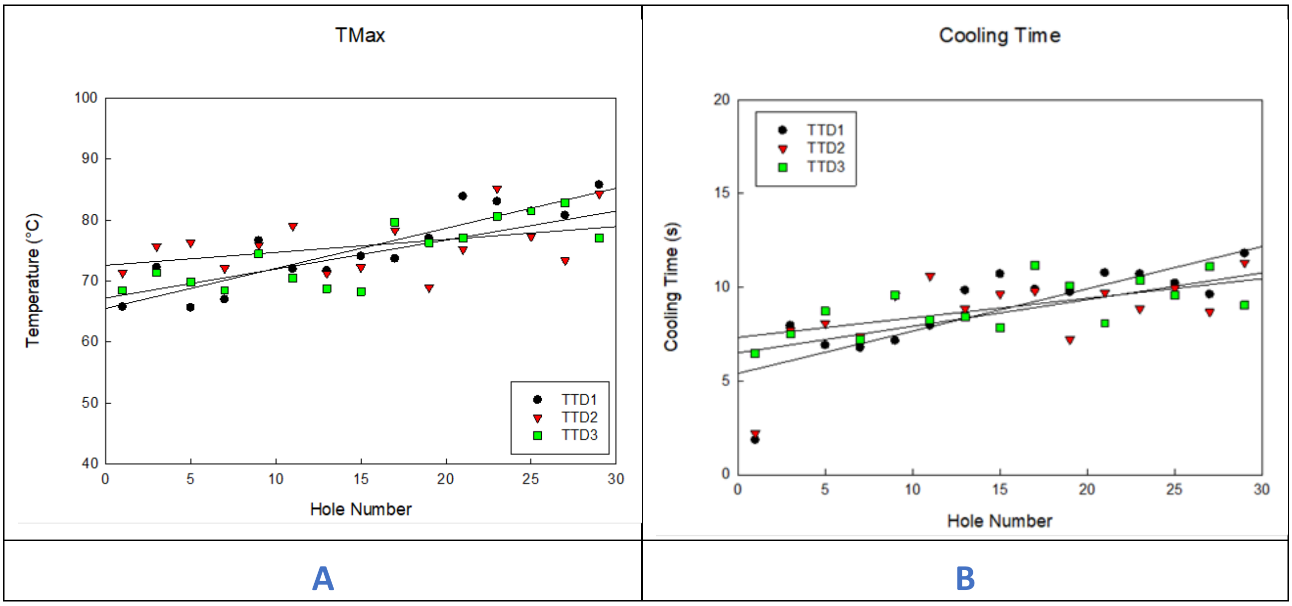

Figure 3-15: Measured T_MAX vs Hole Number(A) and Cooling time VS hole number (B) for 30 consecutive odd holes drilled by the TTD1, TTD2 and TTD3 tools.

	T_MAX_1 [°C]	T_MAX_N [°C]	DELTA_T [°C]	COOLING TIME MIN [S]	COOLING TIME MAX [S]	DELTA COOLING TIME [S]
TTD1	66	86	20	1.9	11.8	10.0
TTD2	71	84	13	2.2	11.3	9.1
TTD3	68	77	9	6.5	11.2	4.7

Table 3-9: Comparison of the results obtained during stack drilling of Al / CFRP by the TTD1, TTD2 and TTD3 tools.

3.4.2 PARAMETER: ISD1

From the innovative tool's characterisation, it was not possible to obtain results comparable to those obtained with TTD as the tool broke during drilling.

Therefore, it was decided to increase the rotation speed to 9000 rpm and modify the feed speed by pruning it to 0.11 mm/rev. These parameters are more suitable for drilling this type of stack of the tool designed.

The data acquired via the thermographic camera were suitably post-processed to obtain a temperature/time diagram describing the temperature trend during the drilling of each hole.

The maximum temperature, **T_MAX**, reached during drilling, is attested in Figure 3-16 A. ISD has a higher temperature respect fitting curve to TTD. There are the same degrees of difference between the T_MAX of the first and last hole in both tools (**DELTA_T** is 26°C), but the temperature range is 80-110°C.

The cooling times of the specimens are shown in Figure 3-16 B. ISD reached a lower cooling time than TTD tools. As a matter of fact, with TTD, hole no. 1 cools down in 1.1 s and hole no. 29 cools down in 7.0 s, with a DELTA cooling time of 5.6 s.

All tests show a growing trend of the cooling time with the increasing number of holes.

The results obtained are reported in a summary (Table 3-10).

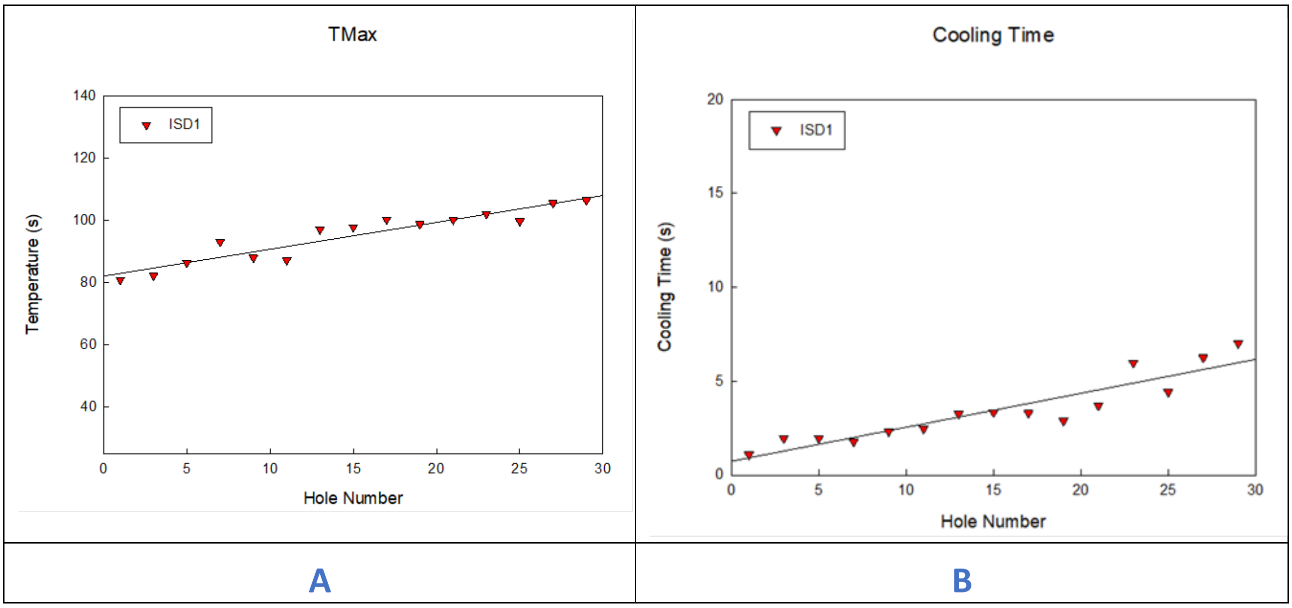

Figure 3-16: Measured T_MAX vs Hole Number(A) and Cooling time VS hole number (B) for 30 consecutive odd holes drilled by the TTD and ISD tools (null), parameter 2700 rpm and 0.11 mm/rev.

	T_MAX_1 [°C]	T_MAX_N [°C]	DELTA_T [°C]	COOLING TIME MIN [S]	COOLING TIME MAX [S]	DELTA COOLING TIME [S]
ISD1	81	106	26	0.11	7.0	5.9

Table 3-10: Comparison of the results obtained during stack drilling of CFRP / CFRP by the TTD and ISD tools, parameter 7500 rpm and 0.11 mm/rev.

3.5 AL/CFRP STACKS– DIAMETER TOOL 6.35 MM

This paragraph shows the **trends of the maximum temperature** in the area around the hole. Graphs temperature/time are detected by the thermo-camera during the Al/CFRP stack drilling process. A comparison was made between the data obtained from the data analysis tools with a nominal diameter tool of 6.35 mm.

For this test, it was decided to use a different set of parameters for the TTD tools to deepen, based on the knowledge of the previous tests, more accurately the best drilling parameters. For ISD, instead, we proceeded with the parameters used for drilling the Al / CFRP stacks.

Table 3-11 shows the parameter used for this combination of diameter tool and materials stacks.

All tests were carried out under the standard condition of temperature and pressure.

Afterwards, the **maximum temperature** (T_MAX) and the **cooling time** acquired in a single drill were reported and, finally, the data from the different tools were compared.

TOOL	TEST NAME	SPINDLE SPEED [RPM]	FEED RATE [MM/REV]
TTD	T1	3000	0.05
TTD	T2	3000	0.10
TTD	T3	3000	0.15
TTD	T4	4500	0.05
TTD	T5	4500	0.10
TTD	T6	4500	0.15
TTD	T7	6000	0.05
TTD	T8	6000	0.10
TTD	T9	6000	0.15
ISD	I1	2700	0.11
ISD	I2	6000	0.2
ISD	I3	7500	0.2

Table 3-11: Test names and corresponding process parameters combinations.

3.5.1 PARAMETER: T1/T2/T3

By setting the spindle speed at 3000 rpm, higher **T_MAX** is reached at lower feed rates; this is because the dwelling time of the tool inside the stack is longer and the heat is transferred by conduction; the temperature reached in the last hole of T3 is 80°C, lower than the first hole of T1 and T2.

The cooling times are shown in **Figure 3-17 A**. T1 reached a higher **T_MAX**, as the laminate's cooling time is slower than T2 and T3, as shows in **Figure 3-17 B**. With T1, the laminate's cooling is slower than T2 and T3; as a matter of fact, with T1, hole no. 29 cools down in 40.4 s, with T2 and T3 cool down in 17.0 s and 21.0 s, respectively.

All tests show a growing trend of the cooling time with the increasing number of holes. The results obtained are reported in **Table 3-12**.

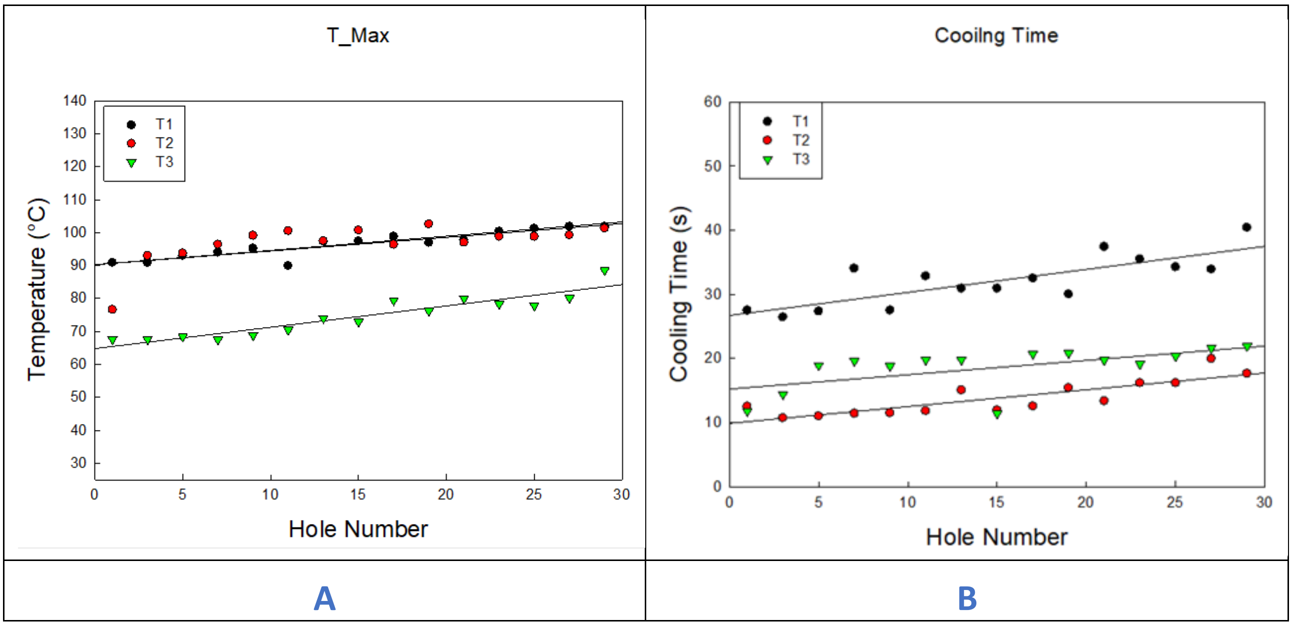

Figure 3-17: Measured T_MAX vs Hole Number(A) and Cooling time VS hole number (B) for T1, T2, and T3 tests.

	T_MAX_1 [°C]	T_MAX_N [°C]	DELTA_T [°C]	COOLING TIME MIN [S]	COOLING TIME MAX [S]	DELTA COOLING TIME [S]
TTD1	90	102	12	26.4	40.4	14.0
TTD2	77	103	26	10.7	20.0	9.2
TTD3	67	89	21	11.4	21.9	10.5

Table 3-12: Comparison of the results obtained during stack drilling of Al / CFRP by the T1, T2 and T3 tools.

3.5.2 PARAMETER: T4/T5/T6

Figure 3-18 A shows the maximum temperature, **T_MAX**, reached during drilling of all odd number holes, where the rotation speed is set at 4500 rpm; as for 3000 rpm, the lower Tmax values occur at higher feed rates, with the difference that test T5 starts from lower temperatures up to similar values of T4; the temperature of the last hole of test T6 is 19°C and 13°C lower than the last hole of T4 and T5, respectively.

Similar results to T2 and T3 tests were also found for cooling time in Figure 3-18 B for T4, T5 and T6, where test T4 has the fitting curve's greatest slope. With T4, the laminate's cooling is slower than T5 and T6; as a matter of fact, with T4, hole no. 29 cools down in 14.6 s, with T5 and T6 cool down in 7.5 s and 6.6 s, respectively.
All tests show a growing trend of the cooling time with the increasing number of holes.

The results obtained are reported in a summary (Table 3-13).

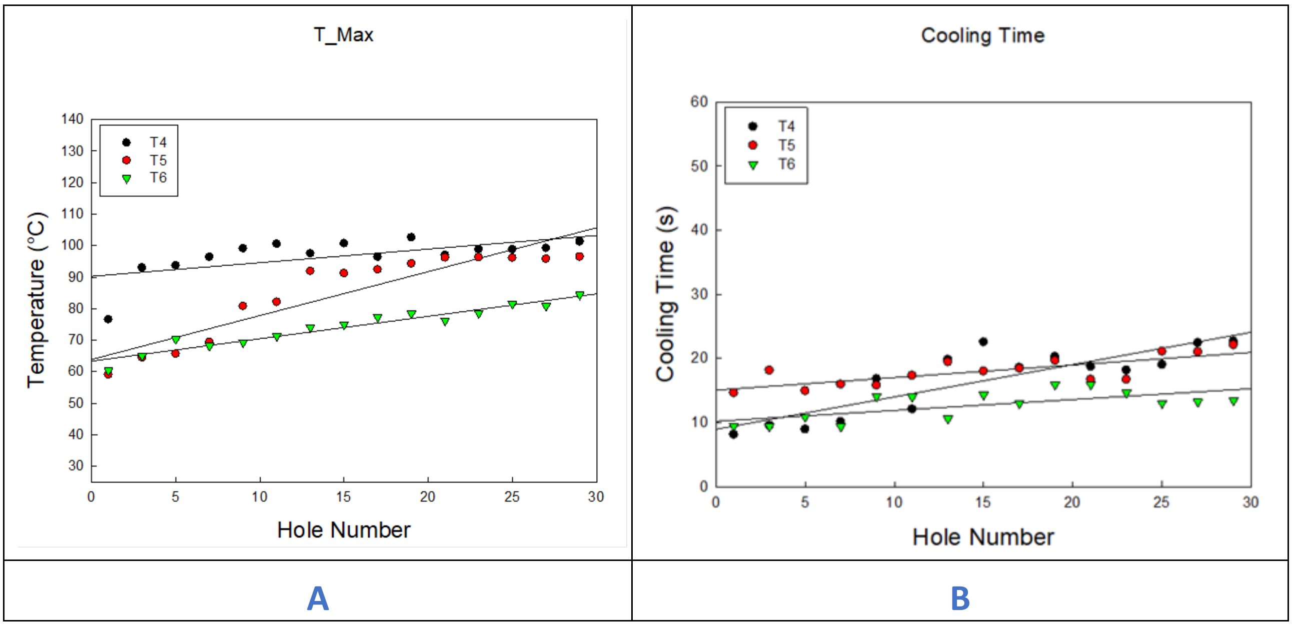

Figure 3-18: Measured T_MAX vs Hole Number(A) and Cooling time VS hole number (B) for tests T4, T5 and T6.

	T_MAX_1 [°C]	T_MAX_N [°C]	DELTA_T [°C]	COOLING TIME MIN [S]	COOLING TIME MAX [S]	DELTA COOLING TIME [S]
T4	77	103	26	8.1	22.7	14.6
T5	59	97	37	14.6	22.1	7.5
T6	60	84	24	9.4	15.9	6.6

Table 3-13: Comparison of the results obtained during stack drilling of Al / CFRP by the T4, T5 and T6 tools.

3.5.1 PARAMETER: T7/T8/T9

For this parameter combination, it was not possible to complete the test. Indeed with T8 and T9, it was a break of the tool at the first hole. For these reasons, this paragraph only reports the result of T7.

Figure 3-19 A shows the results of T7; it was observed how the **T_MAX** is comparable to T3 and T6. In this case, the lowest temperatures found are not due to the feed rate but due to the higher rotational speed and forced convection.

Instead, Figure 3-19 B shows that the higher rotation speed does not affect greatly the cooling speed in drilling with T7: the cooling speed does not exceed 10.7 s, and it shows a constant trend.

All tests show a growing trend of the cooling time with the increasing number of holes.

The results obtained are reported in a summary (Table 3-14).

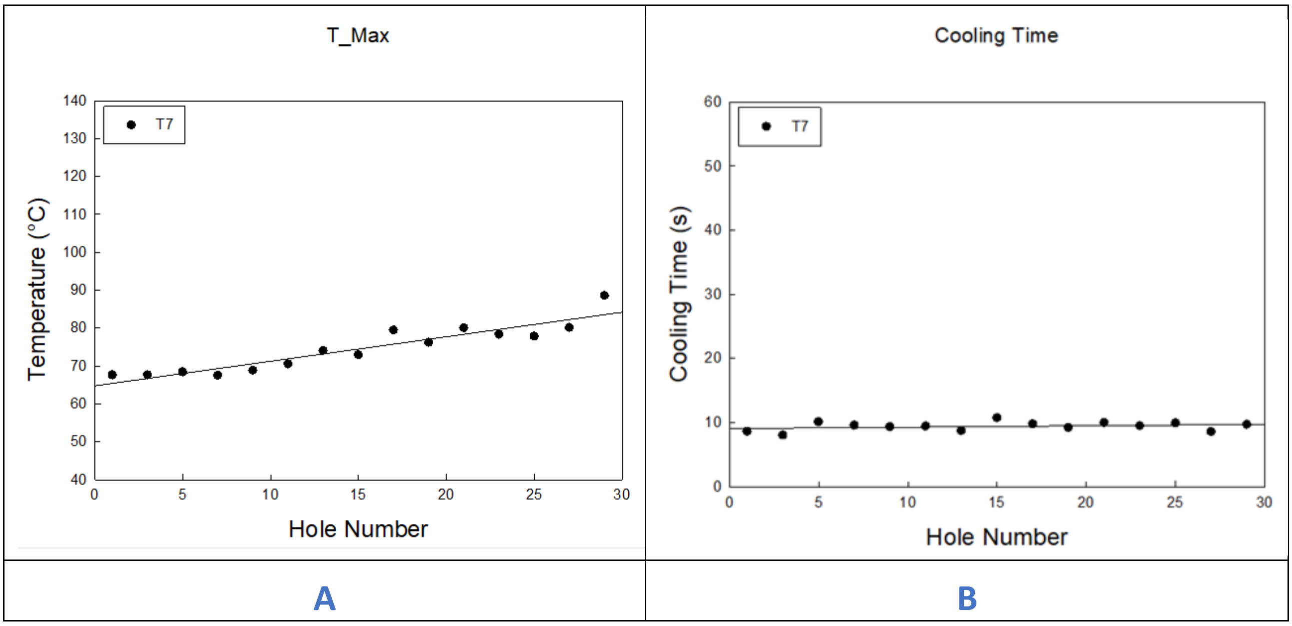

Figure 3-19: Measured T_MAX vs Hole Number(A) and Cooling time VS hole number (B) for tests T7, T8 and T9.

	T_MAX_1 [°C]	T_MAX_N [°C]	DELTA_T [°C]	COOLING TIME MIN [S]	COOLING TIME MAX [S]	DELTA COOLING TIME [S]
T7	67	88	21	8.0	10.7	2.7
T8	-	-	-	-	-	-
T9	-	-	-	-	-	-

Table 3-14: Comparison of the results obtained during stack drilling of Al / CFRP by the T7, T8 and T9 tools.

3.5.2 PARAMETER: I1/I2/I3

The data acquired via the thermographic camera were suitably post-processed to obtain a temperature/time diagram describing the temperature trend during the drilling of each hole.

From the innovative tool's characterisation, it was not possible to obtain results comparable to those obtained with TTD as the tool broke during drilling. The tests studied are reported in Table 3-11.

Figure 3-20 A shows the maximum temperature, **T_MAX**, reached during drilling of all odd number holes; the lower Tmax values occur at lower feed rates. The last hole of test I1 is 13°C and 16°C lower than the last hole of I2 and I3, respectively.

The cooling times of the specimens are shown in Figure 3-20 B. I1 reached a lower cooling time for the first 20 holes, but the I1 tool has a fitting curve with higher slope, compared to I2 and I3. As a matter of fact, with I2 and I3, hole no. 59 cools down in 2.26 s, with ISD, and it cools down in 2.14 s. On the other hand, holes no. 1 have a cooling time difference of 3.1 s between the different tool. In particular, with TTD, hole no. 1 cools down in 9.1 s and 9.5 s respectively, with I1, it cools down in 14.5 s.

All tests show a growing trend of the cooling time with the increasing number of holes. The results obtained are reported in a summary (Table 3-15) that compares ISD tool.

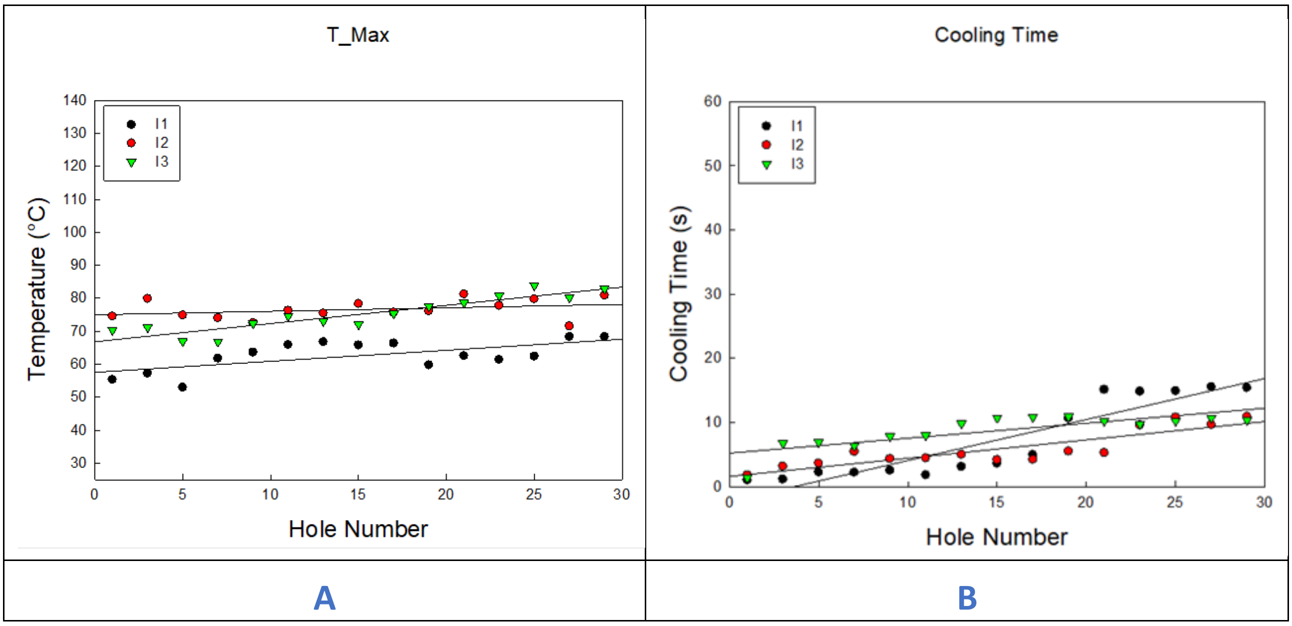

Figure 3-20: Measured T_MAX vs Hole Number(A) and Cooling time VS hole number (B) for 30 consecutive odd holes drilled by the I1, I2 and I3 tools.

	T_MAX_1 [°C]	T_MAX_N [°C]	DELTA_T [°C]	COOLING TIME MIN [S]	COOLING TIME MAX [S]	DELTA COOLING TIME [S]
I1	53	68	15	1.0	15.5	14.5
I2	72	81	10	1.8	10.9	9.1
I3	67	84	17	1.4	10.9	9.5

Table 3-15: Comparison of the results obtained during stack drilling of CFRP / CFRP by the I1, I2 and I3 tools.

3.6 TEMPERATURE 2-D ANALYSIS

Since delamination has a 45° preferential direction, as studied by Canturri et al. [70], it was chosen to investigate the hole temperature along this direction. This study verifies the heat diffusion in the laminate; the heat distribution of heat in hole no. 1 and hole no. 29 with T1, T2, T3, T4, T5, T6, T7 (T8 and T9 are not reported, due to the tool breakage) is reported in Table 3-11, relative to the stacks Al/CFRP [71], [72].

3.6.1 CHARACTERIZATION OF TEMPERATURE IN DRILLING

Figure 3-21 shows the images acquired via a thermographic camera at different times during the drilling process. From Figure 3-21 (a), the tool leaves the CFRP laminate, and Tmax belongs to the tool. The tool is drilling, Figure 3-21 (b-c), the temperature inside the selected area continues to rise up to a maximum. Then, the temperature decreases, Figure 3-21 (d-e-f), while the tool continues to go down, rotating around its axis and cooling down by forced convection, while the heat diffuses inside the material by conduction.

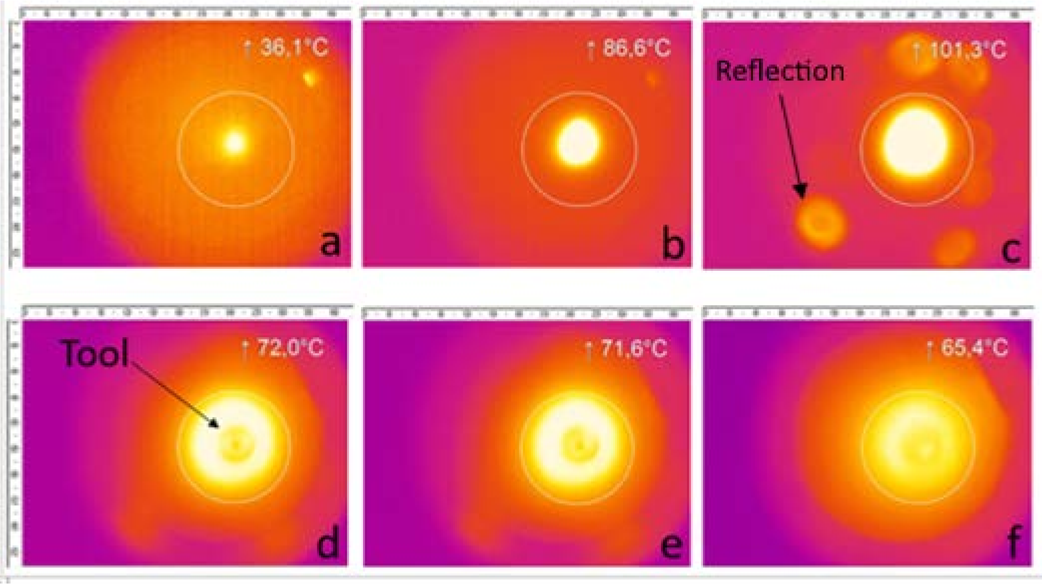

Figure 3-21: Process temperature in a single hole (test T2, hole n. 19).

All the experimental tests' temperature profiles were extrapolated every 0.1 s from the temperature maps along a horizontal line passing through the hole's centre. The temperature profiles show the different instants of time during the drilling process until the tool feed motion is stopped after complete stack perforation; the phase goes back of the tool up from the laminate was not taken into account.

The temperature profiles of test T1, T2 and T3 are shown in Figure 3-22 Figure 3-23 Figure 3-24. In all the temperature profiles, it is possible to highlight three different phases. Phase 1, indicated by the red lines, is monotonically increasing. Phase 2, represented by the green lines, is monotonically increasing: in this phase, the heat begins to diffuse inside the laminate, and the maximum temperature is reached, which is recorded inside the laminate. Finally, phase 3, indicated by the blue lines, is monotonically decreasing: in this phase, the heat begins to diffuse, and the tool is outside the laminate. A modification of the shape of the profiles is observed comparing hole no. 1 and hole no. 29 of both test T1 and test T2; moreover, the blue curves are more distant from each other because there is a lower cooling rate. These results are due to tool wear; as a matter of fact, the higher the tool's wear, the greater the profiles' shape change.

On the other hand, test T3, reported in Figure 3-24, shows a lower change in the profile shape from hole no. 1 to hole no. 29. The irregularity of the curves is due to the metal cylinder's reflection, which interferes with heat detection in the area.

Hole 1 of test T1 and hole 29 of test T3 show an additional phase, indicated by orange lines, which is monotonically increasing and is due to the chips that determine a longer dwelling time at high temperature although they do not affect the overall maximum temperature.

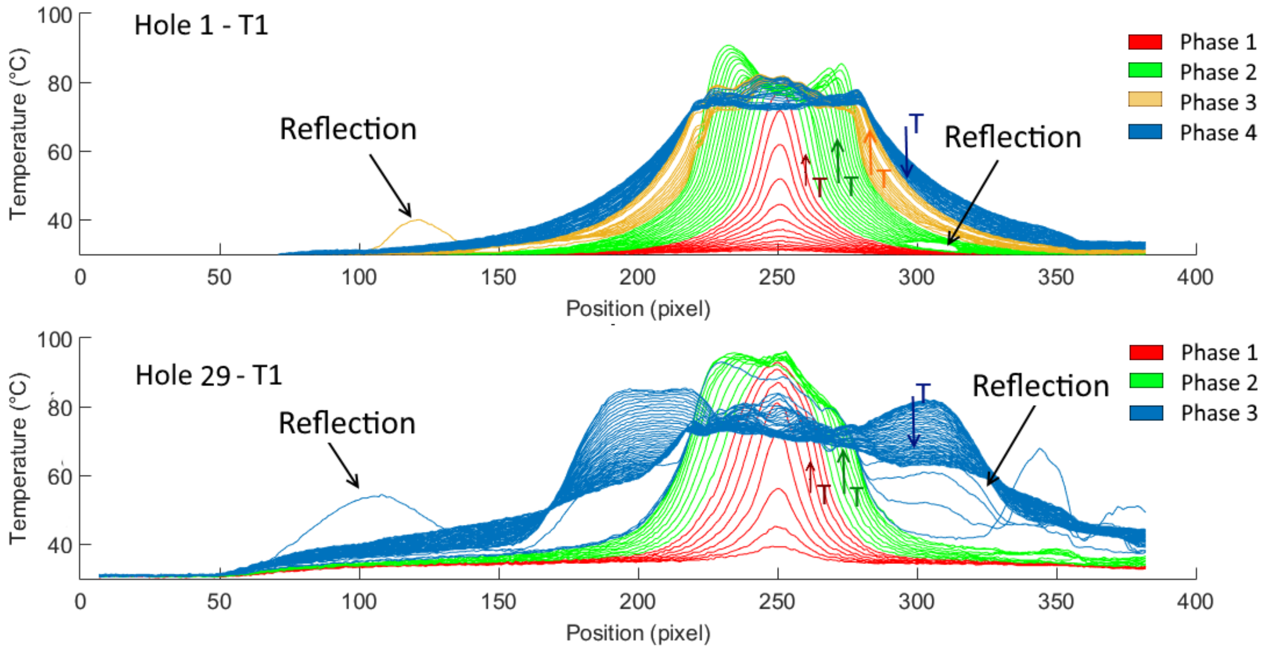

Figure 3-22: Temperature profiles for hole no. 1 and hole no. 29, test T1.

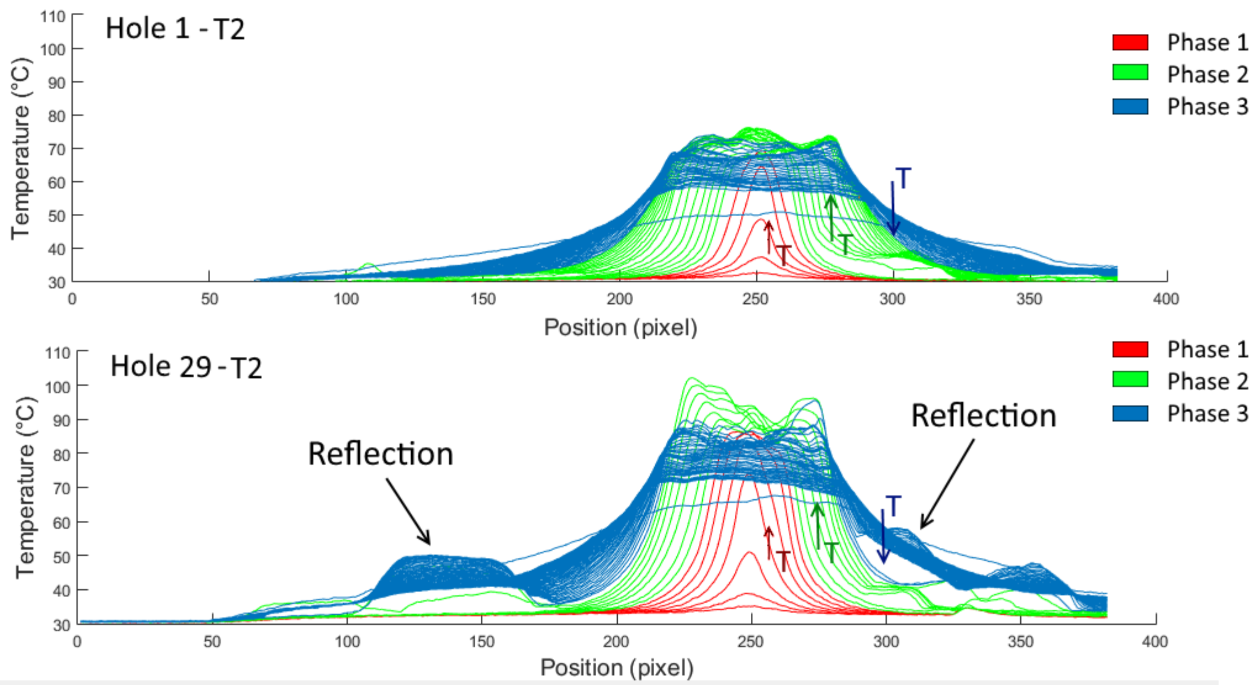

Figure 3-23: Temperature profiles for hole no. 1 and hole no. 29, test T2.

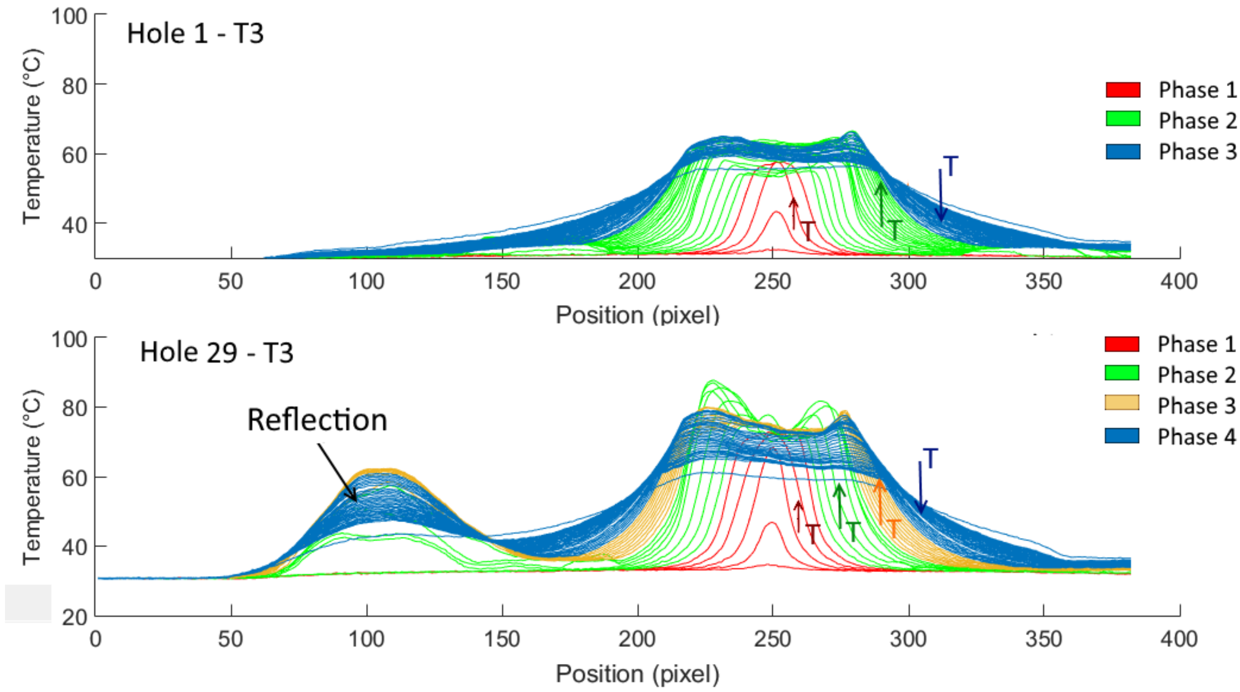

Figure 3-24: Temperature profiles for hole no. 1 and hole no. 29, test T3.

Figure 3-25 Figure 3-26 and Figure 3-27 reported the different time instants' temperature profile during the drilling process for T4, T5 and T6, respectively.

A modification of the profiles' shape is observed comparing hole no. 1 and hole no. 29 of T4, T5 and T6. With the increase of feed rate, the blue curves are more distant from each other because there is a lower cooling rate for hole no. 29. These results, particularly for T6, are due to a lower tool wear; furthermore, the tool had in contact with material lower time, and it had minor friction. On the other hand, test T3, reported in Figure 3-27, shows a minor change in the profile shape from hole no. 1 to hole no. 29.

As a matter of fact, the higher the tool's wear, the greater the profiles' shape change.

The irregularity of the curves is due to the metal cylinder's reflection, which interferes with heat detection in the area.

Hole no. 1 of test T4 (Figure 3-25) and hole no. 1 and no. 29 of test T6 (Figure 3-26) show an additional phase, indicated by orange lines, which is monotonically increasing and is due to the chips that determine a longer dwelling time at high temperature although they do not affect the overall maximum temperature.

For T5, a greater change of shape to T4 and T6 is observed; this result agrees with the analysis of T_MAX.

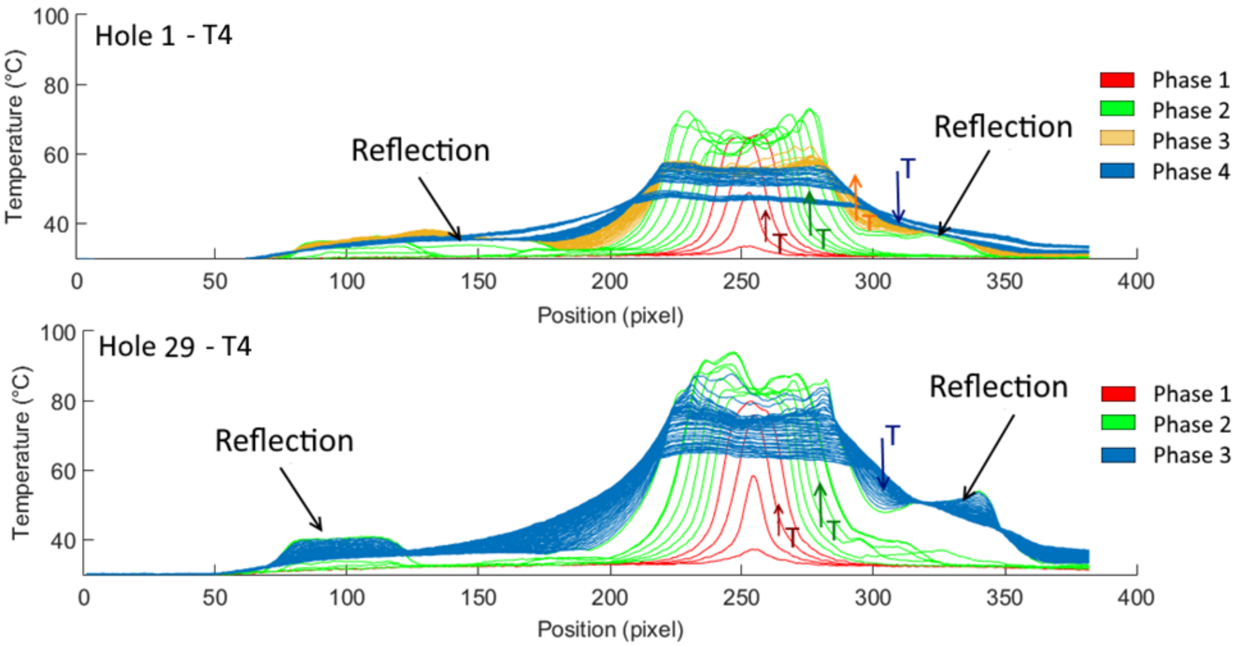

Figure 3-25: Temperature profiles for hole no. 1 and hole no. 29, test T4.

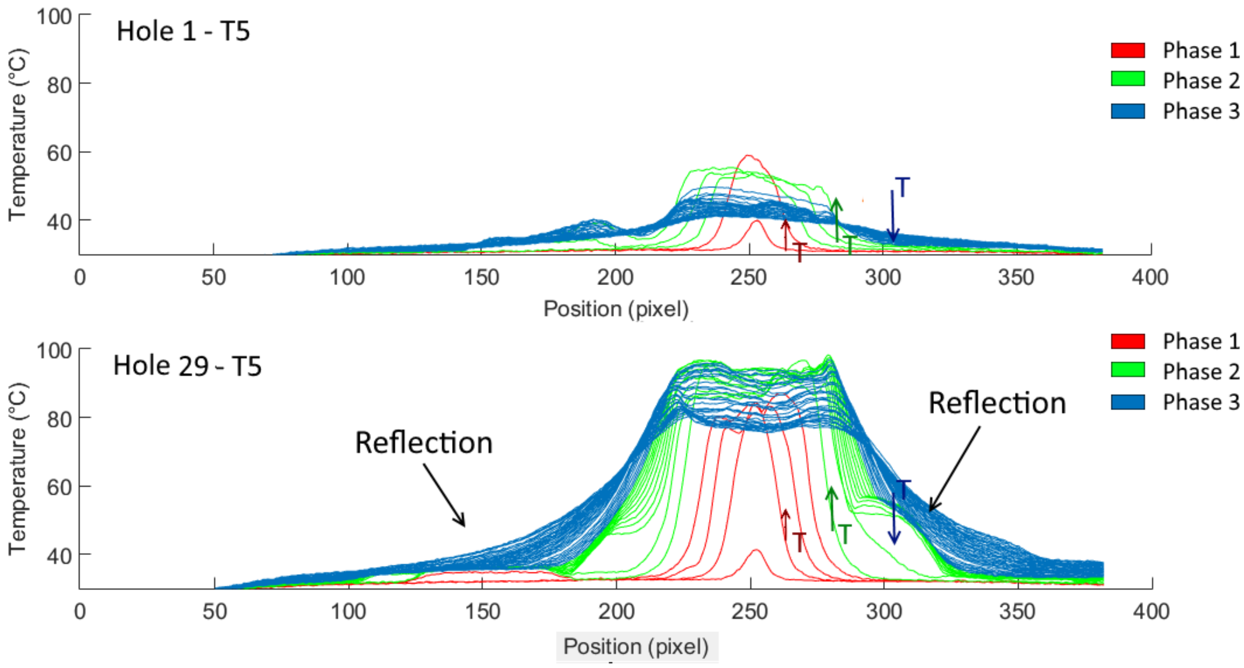

Figure 3-26: Temperature profiles for hole no. 1 and hole no. 29, test T5.

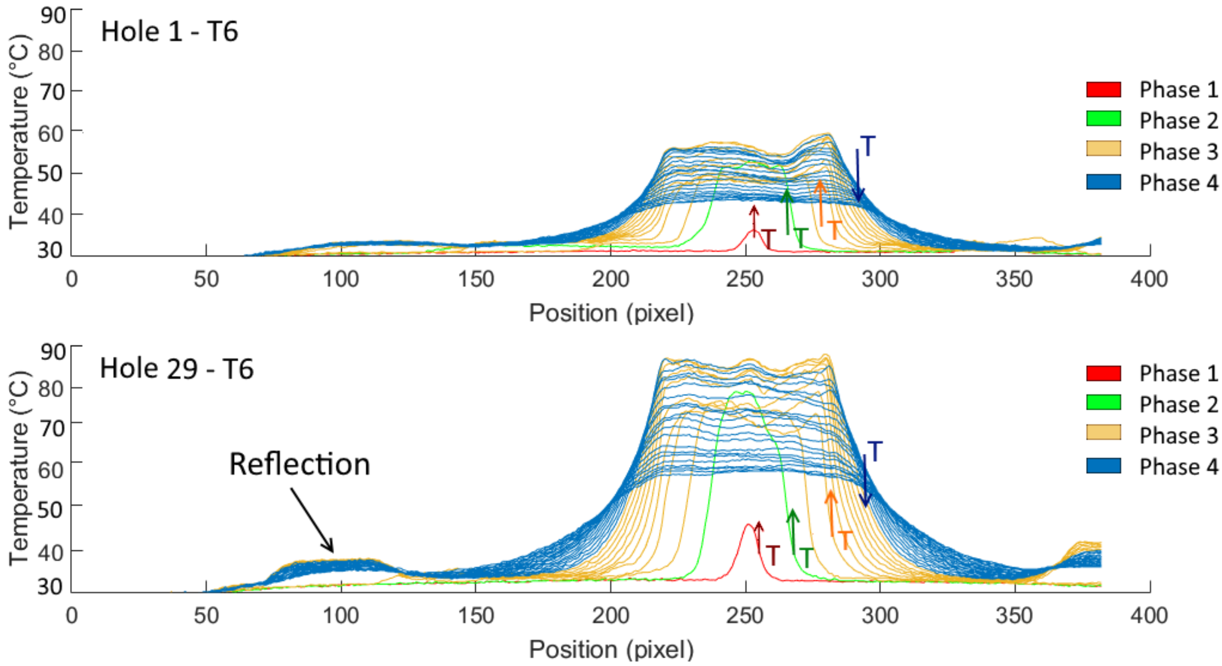

Figure 3-27: Temperature profiles for hole no. 1 and hole no. 29, test T6.

Figure 3-28 reported the different temperature profiles during the drilling process for T7.

In this case, by comparing hole no. 1 and no. 29, differences of the profiles' shape are not observed. With the difference of other parameters, the blue curves did not change the distance between hole no. 1 and hole no. 29. These results are due to the fact that the tool was in contact with the material for lower time, and there was less friction. The irregularity of the curves is due to the metal cylinder's reflection, which interferes with heat detection in the area.

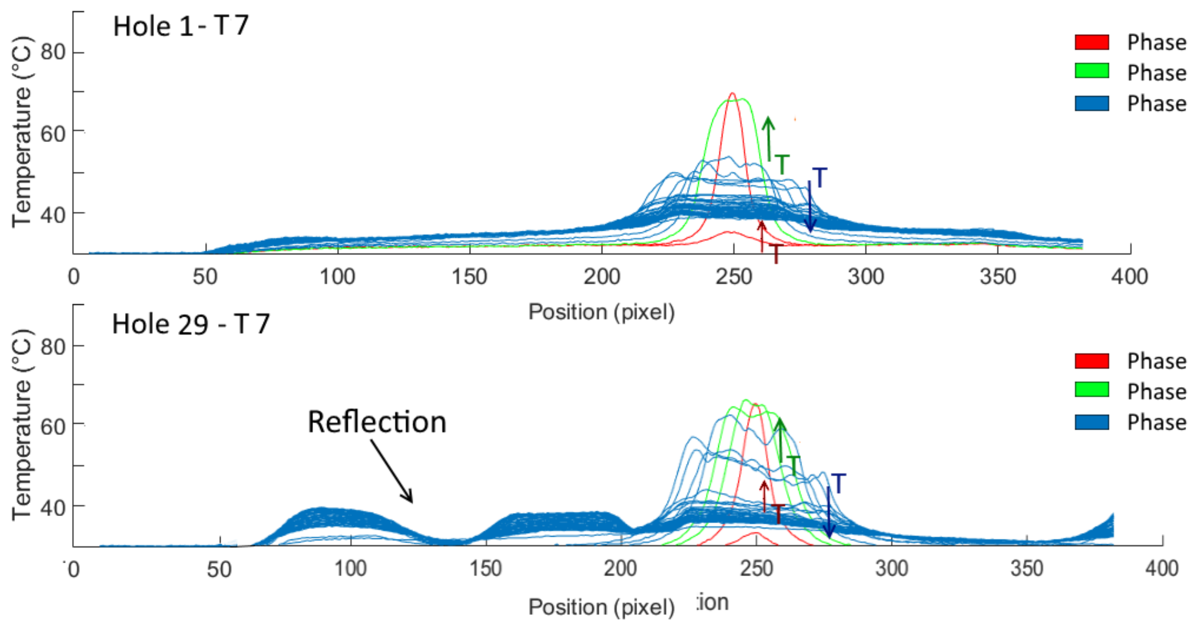

Figure 3-28: Temperature profiles for hole no. 1 and hole no. 29, test T7.

4 DRILLING OF COMPOSITE MATERIALS: GEOMETRY PARAMETERS

Several studies have dwelt on drilling the composite material using different tool geometries to understand how it influenced the delamination. The difference between the different geometries is due to the different distribution of the cutting forces exchanged between tool and piece. It has shown that delamination, especially at the hole's exit, was significantly dependent on the tool's rake angle and the cutting edge [73].

Carbide twist drills provide better performance than those obtained from twist drills but made of high-speed steel (HSS) and from the four-edged carbide tool. The carbide drills are also the optimal choice for drilling CFRP as the tool's progressive wear is significantly reduced. Subsequently, to reduce delamination to a minimum, it was always decided to use twist drills but no longer with cutting edge angle 85° but 120°. Several studies have highlighted that peel-up and push-down are influenced differently by the chosen tip angle, forward speed, and rotation speed. For example, using drills with a tip angle of 85°, push-down delamination reduced by 45%, and this also allows a reduction in the angle of the cutting edge. Instead of the peel-up delamination, remarkable results have obtained by using tip angles equal to 140° instead of 118°; this, however, was in contrast with the results obtained in terms of thrust force since a lower tip angle led to a lower level of force [74].

4.1 DRILLED HOLE QUALITY PARAMETERS

Different types of damages can interest during the drilling of the CFRP/CFRP stacks.

Delamination may occur around the drilled hole at both the top and the bottom of the laminate. The push-out delamination is generally more severe than peel-up delamination [46].

The most common parameter is the Delamination Factor (F_d); it is defined as the ratio between the maximum diameter of the circle encompassing the delamination zone (D_{MAX}) and the nominal hole diameter (D_0), as indicated in **Eq. 4-1**:

$$F_d = \frac{D_{MAX}}{D_0} \qquad \text{Eq. 4-1}$$

However, this parameter does not consider the total area damaged, as shown in **Figure 4-1**, but only the maximum extent of delamination in the radial direction. Therefore, this parameter is not fully representative of the hole quality.

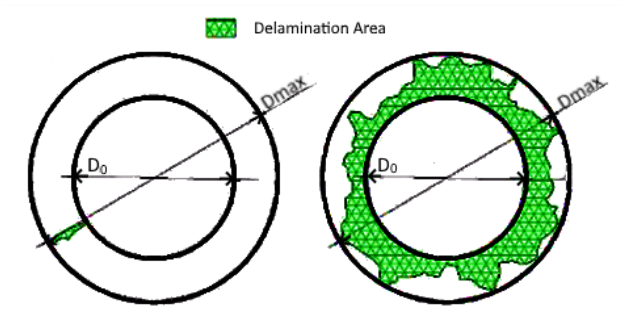

Figure 4-1: Example of two diverse delamination patterns characterised by the same Dmax values but the different extent of delaminated area, Ad.

Alternative delamination characteristic parameters have proposed in the literature. J.P. Davim et al. [48] presented the adjusted delamination factor (F_{da}) calculated through Eq. 4-2.

$$F_{da} = \alpha \frac{D_{max}}{D_0} + \beta \frac{A_{max}}{A_0} \qquad \text{Eq. 4-2}$$

The first part of Eq. 4-2 represents the crack size (Fd), and the second part represents the damaged area. The parameters α and β used as weights; in particular, β is the ratio between the damaged area (A_d) and the area corresponding to D_{max} (A_{max}) minus the nominal hole area (A_0), and the parameter α is the ones' complement of β.

An image analysis procedure was developed in Matlab to extract the quality mentioned above parameters from the drilled holes' acquired images. The procedure shown in Figure 4-2 and Figure 4-3 consists of two main steps focused on identifying the perimeter of the hole (and the parameters related to the circumference that best fits the perimeter based on the mean squared error algorithm) and the delaminated area [59].

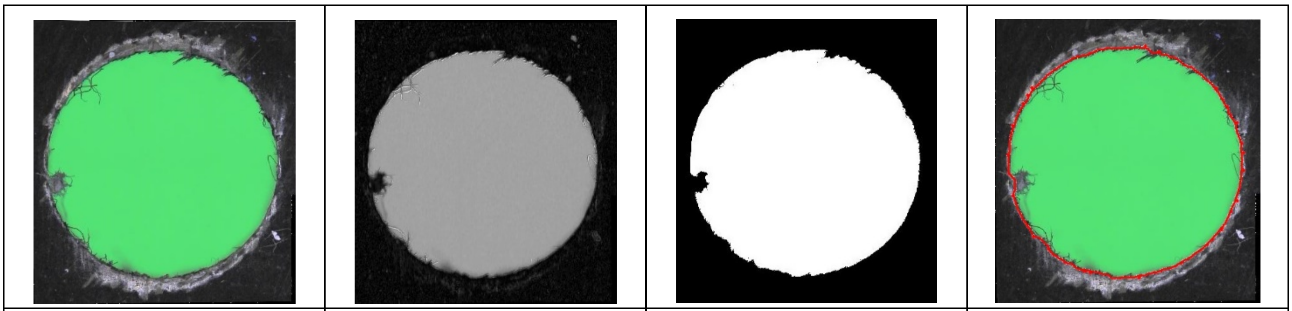

A	B	C	D

Figure 4-2: An image analysis procedure was developed in Matlab to extract the Fd parameters.

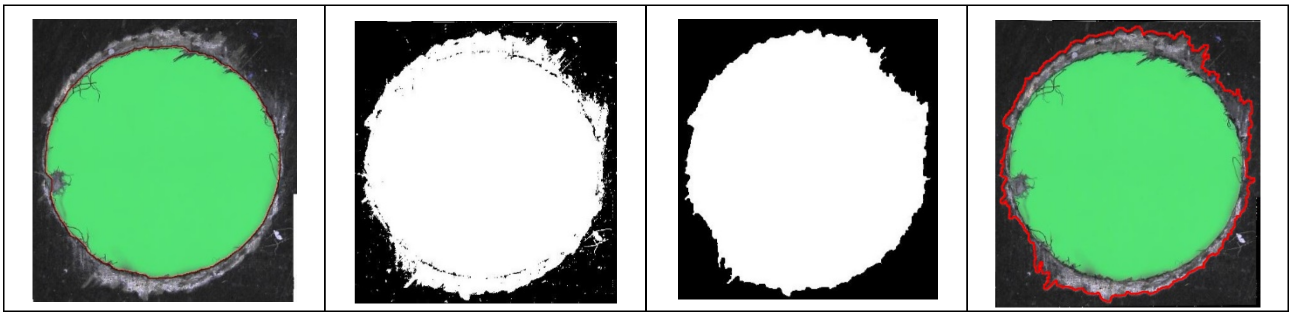

A	B	C	D

Figure 4-3: An image analysis procedure was developed in Matlab to extract the Fda parameters.

Figure 4-4 shows that the traditional tool generates a push out delamination oriented in a preferential direction (45°) consistent with the most external plies of the CFRP laminates stacking sequence. Similar results were obtained with the innovative tool.

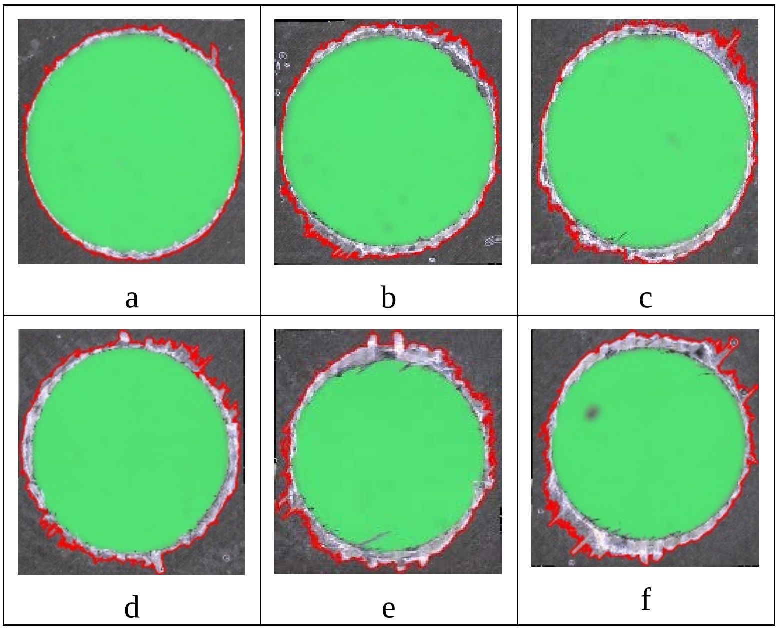

Figure 4-4: Outlined delaminated area at exit of holes no. (a) 10, (b) 20, (c) 30, (d) 40, (e) 50 and (f) 60 drilled by TTD tool at 6000 rpm – 0.20 mm/rev.

In the test, neither F_d nor F_{da} show any positive or negative trend of delamination at hole entry with an increasing number of holes; therefore, they seem less correlated to tool wear progression. The same behaviour was found for all the tests performed; for this reason, the following sections only refer to the hole exit (push out delamination). The F_d and F_{da} values evaluated at the hole exit for the TTD and ISD tool holes drilled. Figure 4-5 shows that *Fd* and *Fda* show an increase with a higher number of holes due to increased tool wear during the drilling process.

The ISD shows a slightly increasing trend with a more significant gap between F_d and F_{da}, which denotes more considerable hole damage than the traditional tool.

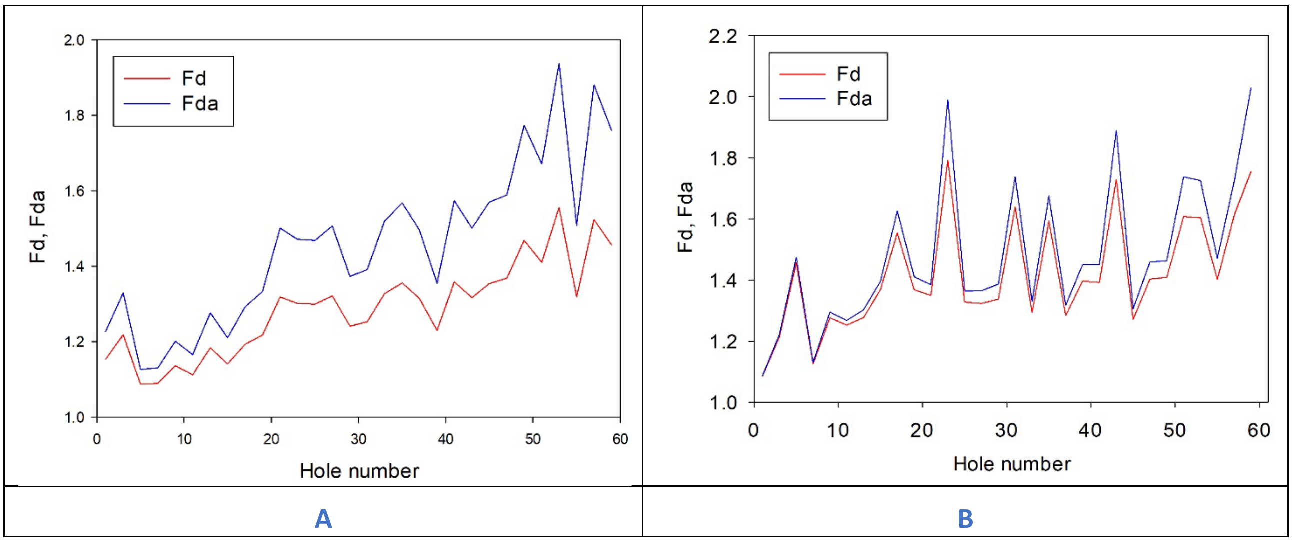

Figure 4-5: Fd and Fda parameters measured at hole exit vs hole number for 60 consecutive holes drilled by the traditional (A) and the innovative (B) tool at 6000 rpm – 0.20 mm/rev.

4.2 DIMENSIONAL ANALYSIS

Dimensional issues are related to the hole diameter, which should stay within the specified tolerance range; in the aeronautical sector, it is often ≤ 0.0762 mm [49].

The hole diameter was measured by "Marposs quick digit" dial gauge with an aluminium body with a polyamide front shell. The measuring range is 12.5 mm, with a resolution of 0.001 mm. It has a liquid crystal display and the possibility of rotating the display up to 270° and a measuring stem in hardened and ground stainless steel. The device has an M1 probe (Figure 4-6); the probe has a steel cylindrical body and two spheres of 1.5 mm diameter stick out from two opposite sides; when it is inserted into the hole, the two spheres approach and push a piston that rises to a height proportional to the hole diameter that is readable on the tool display.

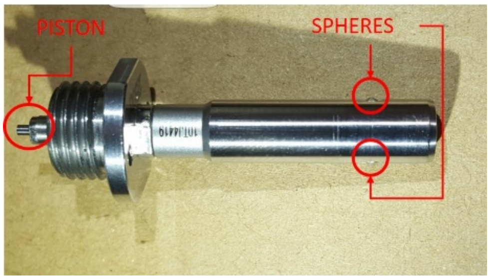

Figure 4-6: Marposs quick digit' M1 probe.

It is necessary to evaluate the measurement on four angles of a single hole, to evaluate both the average size of the single hole and the presence of any circularity error.

The inner side of each hole is measured at half laminate thickness along with four directions (0°, ±45°, and 90°) so as observed in Figure 4-7. These values are essential to evaluate roundness hole, used spider graph, while the diameter is calculated as their arithmetic average.

The results confirmed that the reduction of diameter is correlated with the wear's increase in the drilling process with the traditional and innovative tool.

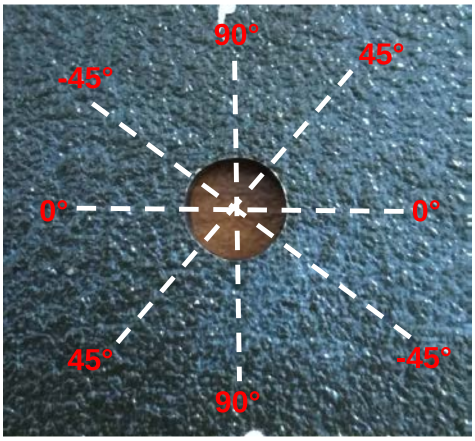

Figure 4-7: Four directions (0°, ±45° and 90°) of diameter measurement.

4.3 CFRP/CFRP STACKS – DIAMETER TOOL 4.9 MM

This paragraph compares the measures of the diameters of the holes obtained with a nominal diameter tool of 4.9 mm during the CFRP/CFRP stack drilling process.

Spider graphs are used for comparison of the roundness of the hole of stacks A and B. With this type of graph, it was possible to observe the difference in dimension between the stacks. (In the graph, the unit of measure is the mm).

Successively, the mean diameters of the holes for both tools were compared. This feature has a strong correlation with the wear. As regards the dimensional errors that affect the CFRP drilled holes, it is known from the literature that the hole diameter is generally reduced with an increasing number of holes; this behaviour is confirmed by the measurements, always showing a decreasing trend of the measured hole diameter for 60 consecutive holes drilled with different parameter.

The parameters used are the same in the study of the temperature of Chapter 3.

All test were carried out three times, and the results were mediated between them.

4.3.1 PARAMETER: 2700 RPM - 0.11 MM/REV

The data acquired via dial gauge were suitably post-processed to obtain a spider diagram describing the measurement of diameter during each hole's drilling.
Figure 4-8 shows the dimensional analysis for the number of 1-30-60 holes for TTD and ISD tools for stack A and stack B (Figure 2-1).

Figure 4-8 A shows the TTD hole, and it shows that stack B holes are smaller than the respective hole of stack A, except the hole no. 60, where the green lines relative to the last hole are overlapped. Moreover, the holes are not asymmetrical. Figure 4-8 B shows the ISD hole; from the figure stack B holes are smaller than the respective ones of stack A. Moreover, the holes are asymmetrical, in particular for stacks B.

Figure 4-9 shows the hole diameter measured from hole no. 1 to no. 60 drilled by TTD and ISD tools. The upper and lower limits for the measurement are also reported in the graph (the up limit is 4.849 mm, and the low limit is 4.925 mm). These are technological limits.

Figure 4-9 A shows the TTD hole diameter Hole A and Hole B have a constant tend, but the measurement translated from the low limit. In stack A, the first hole has a quick diminution of diameter; successively, the size is constant. Figure 4-9 B shows the ISD hole diameter. Hole A and Hole B have a constant value, but the measurement translated from the up limit. In both tools, the trend is decreasing.

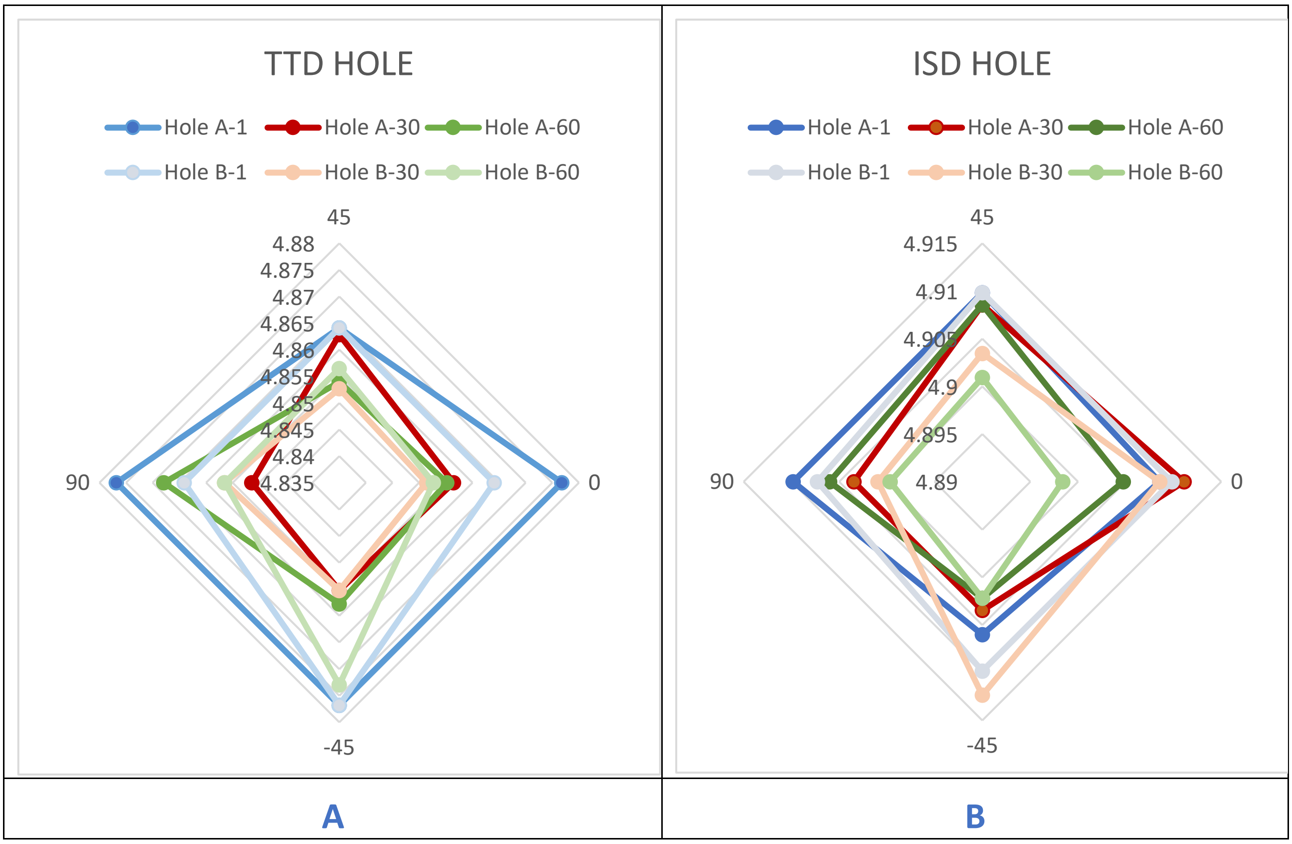

Figure 4-8: Dimensional analysis for the number of 1-30-60 holes for TTD (A) and ISD (B) tools, parameter 2700 rpm and 0.11 mm/rev (unit of measure in mm).

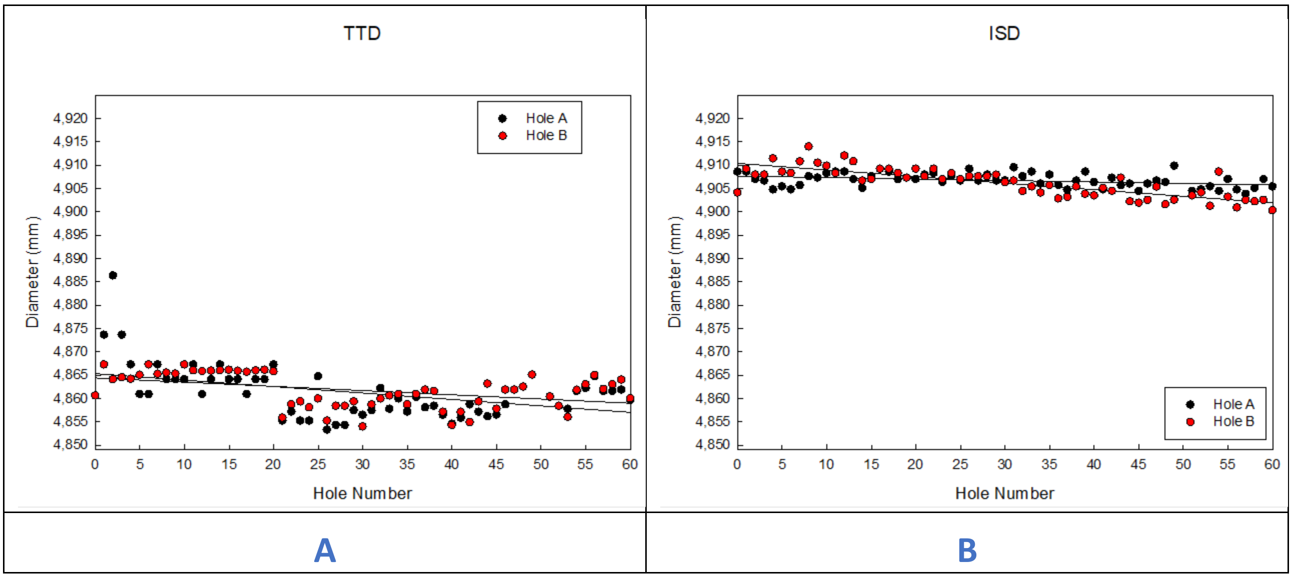

Figure 4-9: Hole diameter measured from hole no. 1 to no. 60 and stacks A and B drilled by TTD (A) and ISD (B) tools, parameter 2700 rpm and 0.11 mm/rev.

4.3.2 PARAMETER: 6000 RPM - 0.2 MM/REV

The data acquired via dial gauge were suitably post-processed to obtain a spider diagram describing the measurement of diameter during each hole's drilling.
Figure 4-10 shows the dimensional analysis for the number of 1-30-60 holes for TTD and ISD tools for stack A and stack B (Figure 2-1).

Figure 4-10 A shows the TTD hole, and stack B holes are smaller than the respective hole of stack A, except the hole no. 60, where the green lines relative to the last hole are in the counter of the light green line. Moreover, the holes are asymmetrical. Figure 4-10 B shows the ISD hole, and the stack B holes are smaller than the respective hole of stack A. Moreover, that the holes are asymmetrical, in particular for stacks B.

Figure 4-11 shows the hole diameter measured from hole no. 1 to no. 60 drilled by TTD and ISD tools. The upper and lower limits for the measurement are also reported in the graph (the up limit is 4.849 mm, and the low limit is 4.925 mm). These are technological limits.

Figure 4-11 A shows the TTD hole diameter. Hole A and Hole B have a constant trend, but the measurement translated from the low limit. In stack B, the first hole has a quick diminution of diameter; successively, the size is constant. Figure 4-11 B shows the ISD hole diameter. Stack A and stack B holes have a constant value, but the B ones are higher. In both tools, the trend is decreasing.

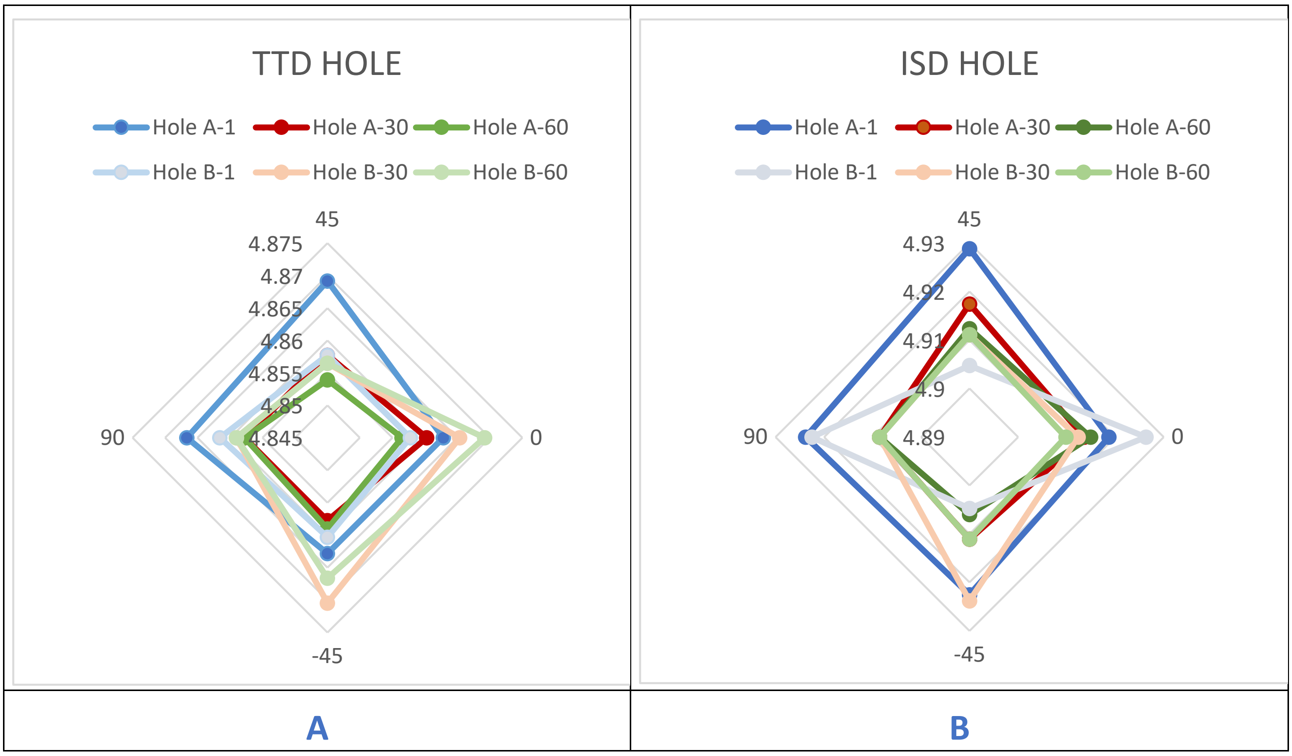

Figure 4-10: Dimensional analysis for the number of 1-30-60 holes for TTD (A) and ISD (B) tools, parameter 6000 rpm and 0.2 mm/rev (unit of measure in mm).

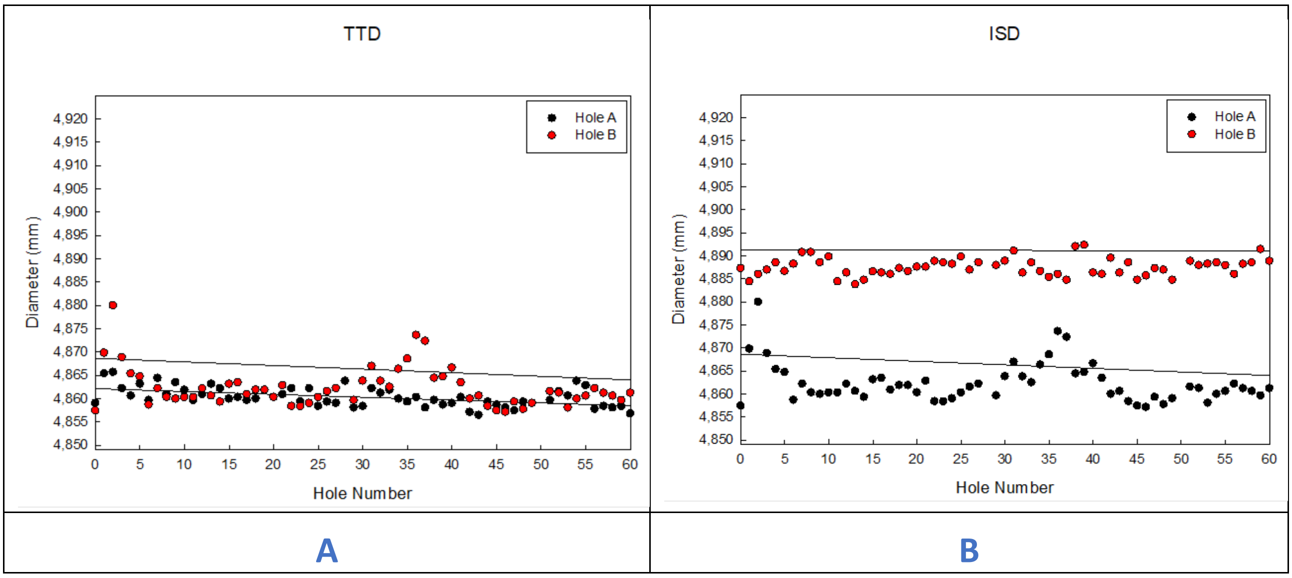

Figure 4-11: Hole diameter measured from hole no. 1 to no. 60 and stacks A and B drilled by TTD (A) and ISD (B) tools, parameter 6000 rpm and 0.2 mm/rev.

4.3.3 PARAMETER: 7500 RPM - 0.2 MM/REV

The data acquired via dial gauge were suitably post-processed to obtain a spider diagram describing the measurement of diameter during each hole's drilling.
Figure 4-12 shows the dimensional analysis for the number of 1-30-60 holes for TTD and ISD tools for stack A and stack B (Figure 2-1).

Figure 4-12 A shows the TTD hole, and holes' stack A are smaller than the respective hole of stack B, except the hole no. 60. Moreover, the holes are asymmetrical Figure 4-12 B shows the ISD hole, and holes' stack A have a similar size to the respective hole of stack B. Moreover, the holes are asymmetrical.

Figure 4-13 shows the hole diameter measured from hole no. 1 to no. 60 drilled by TTD and ISD tools. The upper and lower limits for the measurement are also reported in the graph (the up limit is 4.849 mm, and the low limit is 4.925 mm). These are technological limits.

Figure 4-13 A shows the TTD hole diameter. Holes A and Holes B have a constant trend, but stack B holes are bigger than the respective hole of stack A. Figure 4-13 B shows the ISD hole diameter. Hole A and Hole B have a constant value, but the measurement translated from the up limit. In both tools, the trend is decreasing. In stack A and B, the first holes (up to hole no. 10) have a quick diminution of diameter; successively, the size is constant.

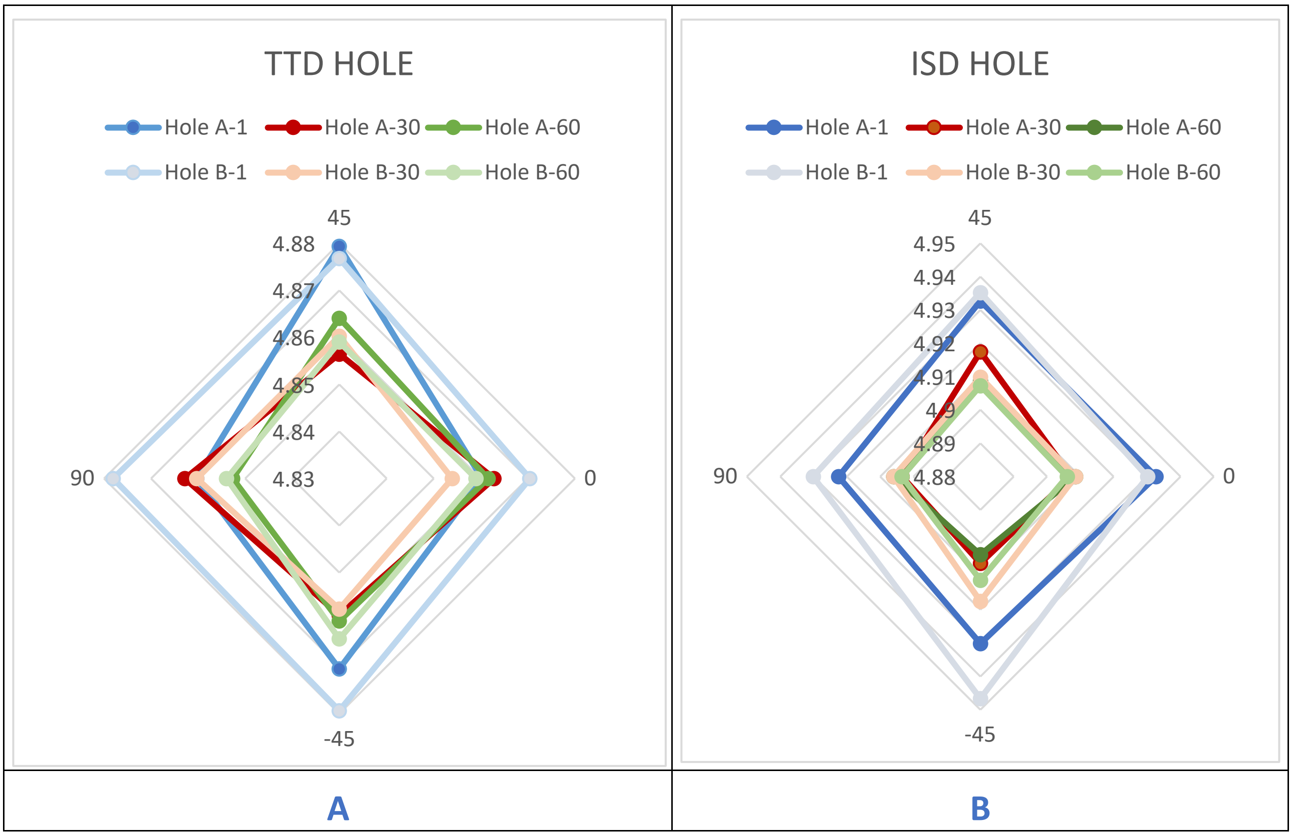

Figure 4-12: Dimensional analysis for the number of 1-30-60 holes for TTD (A) and ISD (B) tools, parameter 7500 rpm and 0.2 mm/rev (unit of measure in mm).

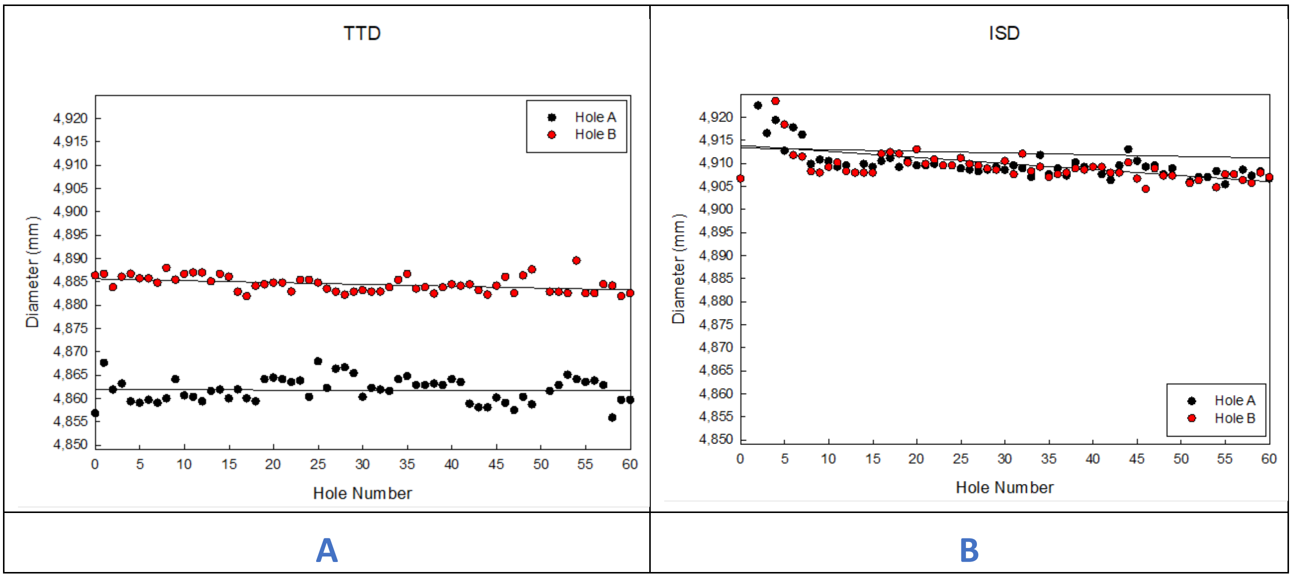

Figure 4-13: Hole diameter measured from hole no. 1 to no. 60 and stacks A and B drilled by TTD (A) and ISD (B) tools, parameter 7500 rpm and 0.2 mm/rev.

4.4 CFRP/CFRP STACKS – DIAMETER TOOL 6.35 MM

This paragraph shows the comparison of the measurement of the hole obtained from the data analysis tools with a nominal diameter tool of 6.5 mm during the CFRP/CFRP stack drilling process.

Spider graphs are used for comparison of the roundness of the hole of stacks A and B. With this type of graph, it was possible to observe the difference in dimension between the stacks. (In the graph, the unit of measure is the mm).

Successively, the mean diameter of the holes for both tools was compared. This feature has a strong correlation with the wear.

The parameters used are the same in the study of the temperature.

All tests were carried out three times, and the results were mediated between them.

4.4.1 PARAMETER: 2700 RPM - 0.11 MM/REV

The data acquired via dial gauge were suitably post-processed to obtain a spider diagram describing the measurement of diameter during each hole's drilling.
Figure 4-14 shows the dimensional analysis for the number of 1-30-60 holes for ISD tools for stack A and stack B (**Figure 2-1**). With this parameter's choice, the TTD tool gets off of tolerance, and it was not possible to represent the graph.

Figure 4-14 B shows the ISD hole, and that stack B holes are similar to the respective hole of stack A. Moreover, the holes are asymmetrical, in particular for stacks B.

Figure 4-15 shows the hole diameter measured from hole no. 1 to no. 60 drilled by TTD and ISD tools. The upper and lower limits for the measurement are also reported in the graph (the up limit is 6.35 mm, and the low limit is 6.426 mm). These are technological limits.

Figure 4-15 A shows the TTD hole diameter. It observed that hole no. 16, of both the stacks, get off of lower tolerance; indeed, the dial gauge’s tip doesn’t enter the hole, and the measurement was not possible. **Figure 4-15 B** shows the ISD hole diameter. Hole A and Hole B have a decreasing trend; the measurement started with a high value and translated from the up limit to the low limit. In both tools, the trend is decreasing.

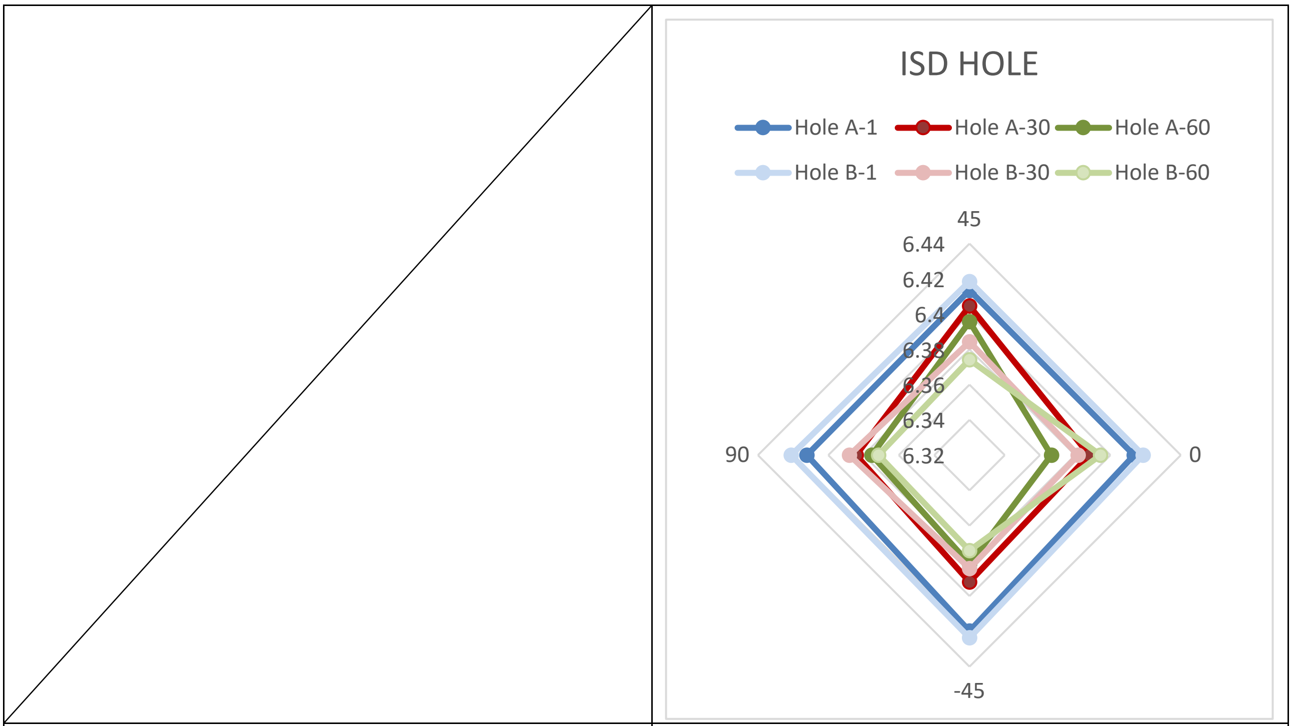

A B

Figure 4-14: Dimensional analysis for the number of 1-30-60 holes for TTD (A) and ISD (B) tools, parameter 2700 rpm and 0.11 mm/rev (unit of measure in mm).

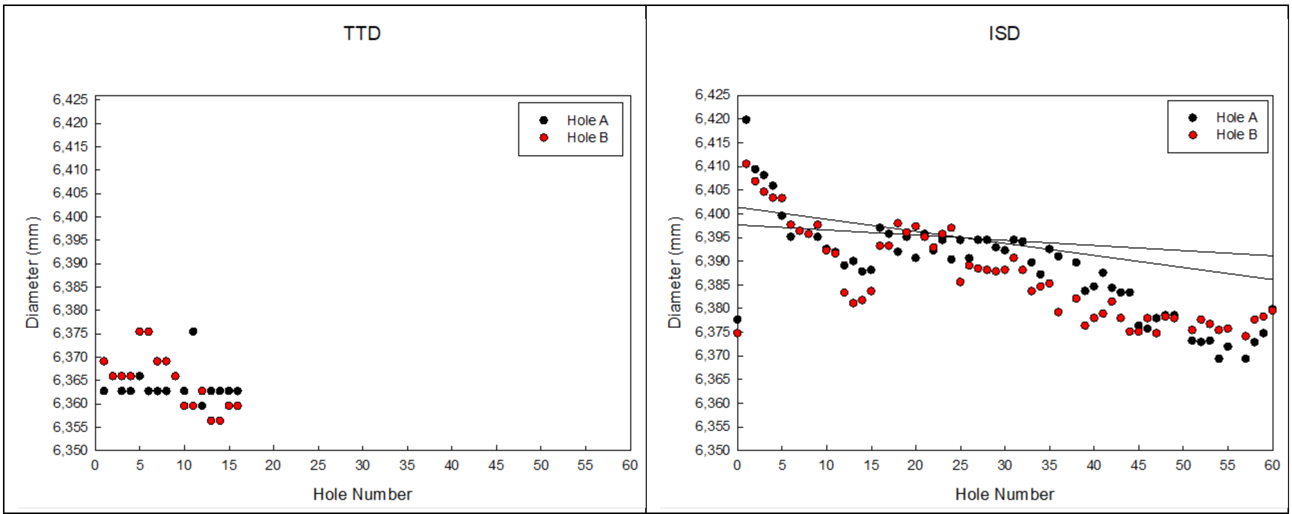

A B

Figure 4-15: Hole diameter measured from hole no. 1 to no. 60 and stacks A and B drilled by TTD (A) and ISD (B) tools, parameter 2700 rpm and 0.11 mm/rev.

4.4.2 PARAMETER: 6000 RPM - 0.2 MM/REV

The data acquired via dial gauge were suitably post-processed to obtain a spider diagram describing the measurement of diameter during each hole's drilling.

Figure 4-16 shows the dimensional analysis for the number of 1-30-60 holes for TTD and ISD tools for stack A and stack B (Figure 2-1).

Figure 4-16 A shows the TTD hole, and holes stack A is similar to the respective hole of stack B. Moreover, the holes are symmetrical. Figure 4-16 B shows the ISD hole, and holes stack A is similar to the respective hole of stack B, but, in this case, the measurement started with a high value and translated from the up limit to the low limit. Moreover, the holes are symmetrical, in particular for stacks B.

Figure 4-17 shows the hole diameter measured from hole no. 1 to no. 60 drilled by TTD and ISD tools. The upper and lower limits for the measurement are also reported in the graph (the up limit is 6.35 mm, and the low limit is 6.426 mm). These are technological limits.

Figure 4-17 A shows the TTD hole diameter. Hole A and Hole B have a constant trend, but stack B holes are bigger than the respective hole of stack hole A. Figure 4-17 B shows the ISD hole diameter. Hole A is similar to Hole B, but In stack A and B, the first holes (up to hole no. 15) have a quick diminution of diameter; successively, the size is decreasing but with a lower slope. In both tools, the trend is decreasing. The interval of value translated from the up limit to the low limit.

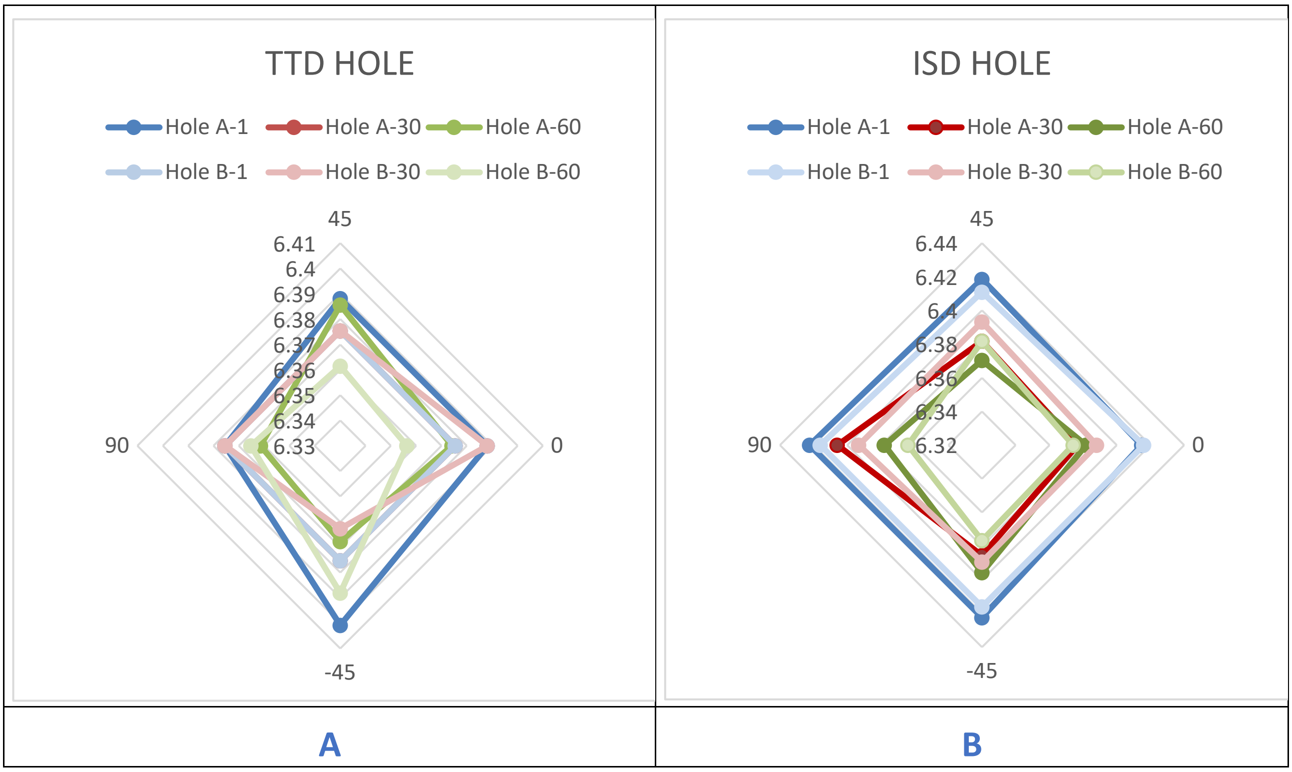

Figure 4-16: Dimensional analysis for the number of 1-30-60 holes for TTD (A) and ISD (B) tools, parameter 6000 rpm and 0.2 mm/rev (unit of measure in mm).

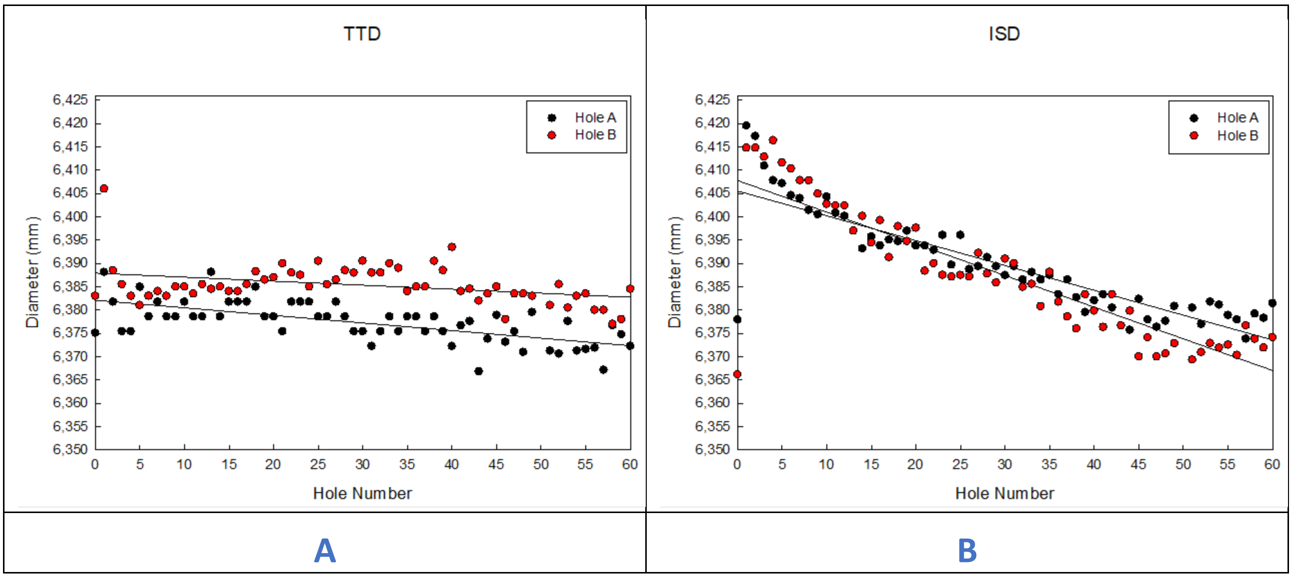

Figure 4-17: Hole diameter measured from hole no. 1 to no. 60 and stacks A and B drilled by TTD (A) and ISD (B) tools, parameter 6000 rpm and 0.2 mm/rev.

4.4.3 PARAMETER: 7500 RPM - 0.2 MM/REV

The data acquired via dial gauge were suitably post-processed to obtain a spider diagram describing the diameter measurement during each hole's drilling.
Figure 4-18 shows the dimensional analysis for the number of 1-30-60 holes for TTD and ISD tools for stack A and stack B (Figure 2-1).

Figure 4-18 A shows the TTD hole, and holes' stack A are similar to the respective hole of stack B, except the hole no. 60, where the green lines relative to the last hole is out of the blu line (relative to the first hole) in one direction. Moreover, the holes are asymmetrical in the direction of -45° and 45°. Figure 4-18 B shows the ISD hole, and stack B holes are smaller than the respective hole of stack A. Moreover, the holes are asymmetrical after hole no. 30; an asymmetry in the 0° and 90° direction is observed.

Figure 4-19 shows the hole diameter measured from hole no. 1 to no. 60 drilled by TTD and ISD tools. The upper and lower limits for the measurement are also reported in the graph (the up limit is 6.35 mm, and the low limit is 6.426 mm). These are technological limits.

Figure 4-19 A shows the TTD hole diameter. Hole A and Hole B have a constant trend, but the measurement translated from the low limit. Figure 4-19 B shows the ISD hole diameter. Hole A and Hole B have a similar trend, but stack holes A are bigger than the respective hole of stack hole B. In both tools, the trend is decreasing, but in stack A and B, the first holes (up to hole no. 15) have a quick diminution of diameter; successively, the size decreases but with a lower slope. The interval of value translated from the up limit to the low limit.

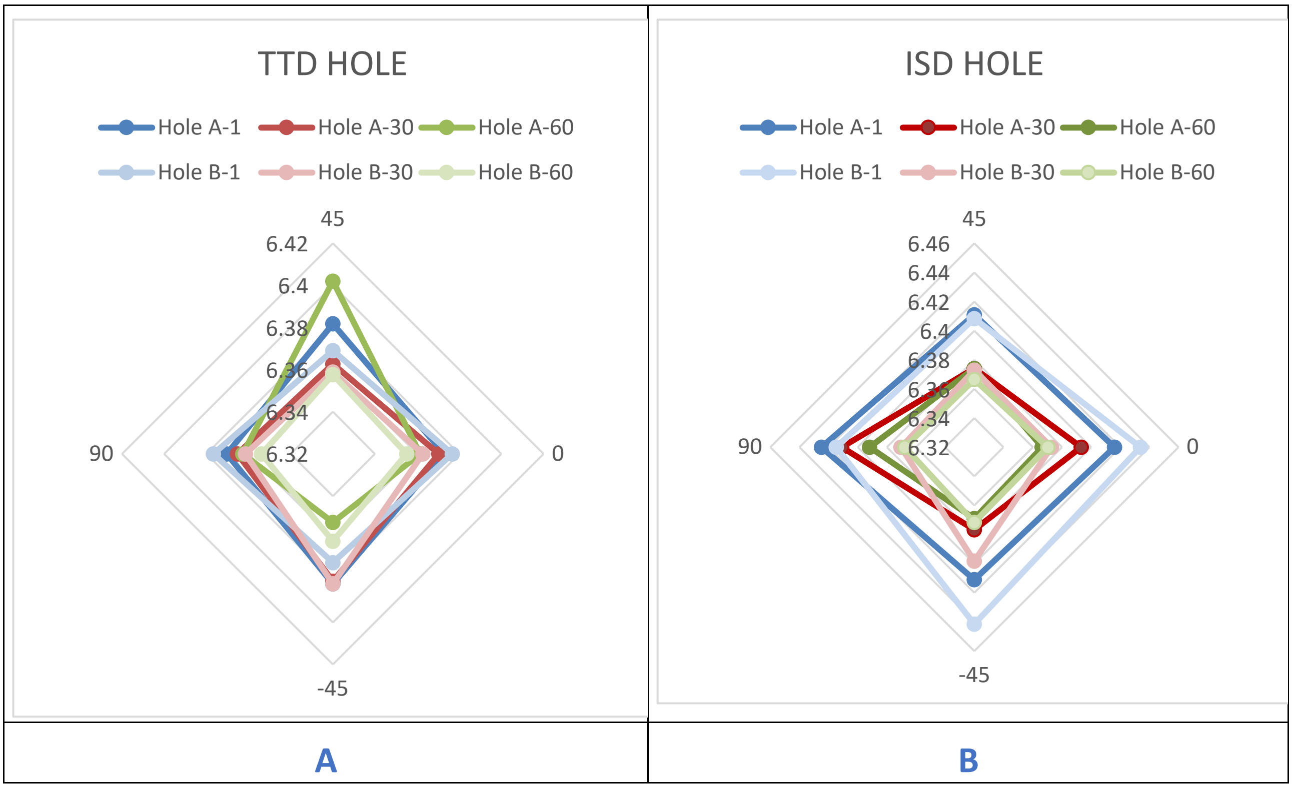

Figure 4-18: Dimensional analysis for the number of 1-30-60 holes for TTD (A) and ISD (B) tools, parameter 7500 rpm and 0.2 mm/rev (unit of measure in mm).

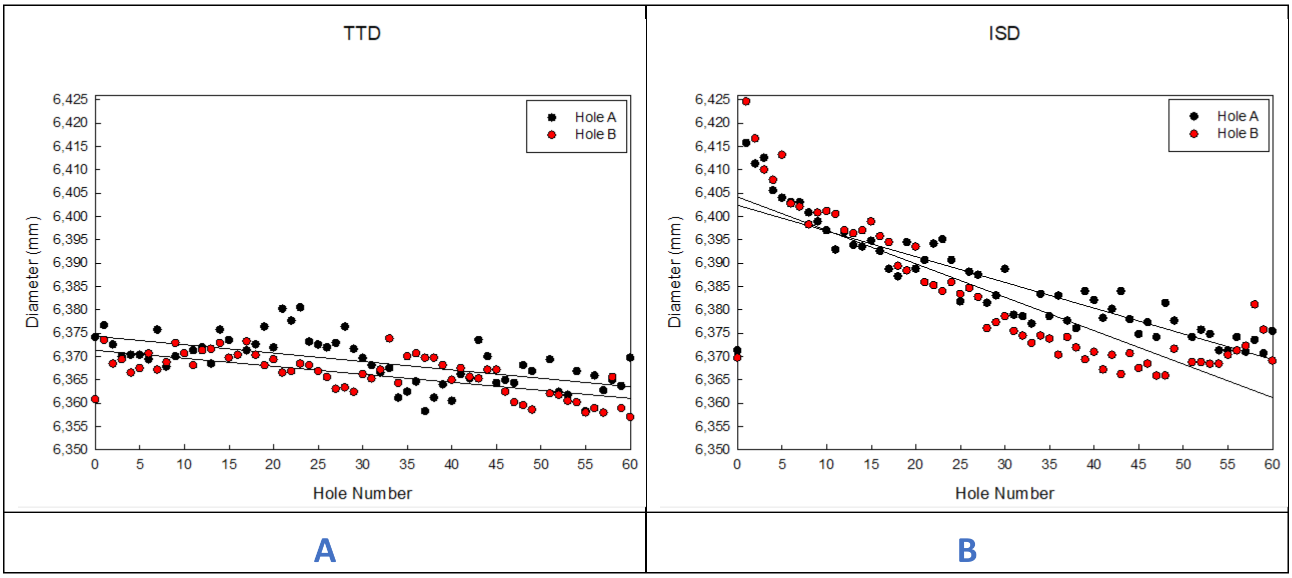

Figure 4-19: Hole diameter measured from hole no. 1 to no. 60 and stacks A and B drilled by TTD (A) and ISD (B) tools, parameter 7500 rpm and 0.2 mm/rev.

4.5 AL/CFRP STACKS – DIAMETER TOOL 4.9 MM

This paragraph shows the comparison of the measurement of the hole obtained from the data analysis tools with a nominal diameter tool of 4.9 mm during the Al/CFRP stack drilling process.

Spider graphs are used for comparison of the eccentricity of the hole of stacks A and B. With this type of graph, it was possible to observe the difference in dimension between the stacks (In the graph, the unit of measure is the mm).

Successively, the mean of the diameter of the hole for both tools was compared. This feature has a strong correlation with the wear. As regards the dimensional errors that affect the CFRP drilled holes, it is known from the literature that the hole diameter is generally reduced with an increasing number of holes; this behaviour is confirmed by the measurements, always showing a decreasing trend of the measured hole diameter for 30 consecutive holes drilled with different parameters.

The parameters used are the same in the study of the temperature of **Chapter 3**.

For this test, the ISD tools did not return useful results for drilling Al/CFRP stacks except with parameters 9000 rpm and 0.11 mm/rev. For this parameter, the TTD tools did not return useful results. **Table 3-7** shows the parameter used for this combination of diameter tool and materials stacks. **Table 3-8** shows the number hole with the tool's cracking during the drilling of Al/CFRP stacks.

All tests were carried out under the standard condition of temperature and pressure.

All test were carried out three times, and the results were mediated between them.

4.5.1 PARAMETER: TTD1/TTD2/TTD3

The data acquired via dial gauge were suitably post-processed to obtain a spider diagram describing the measurement of diameter during each hole's drilling.
Figure 4-20 shows the dimensional analysis for the number of 1-15-30 holes for TTD1, TTD2 and TTD3 for CFRP stack and Al stack (**Figure 2-2**).

Figure 4-20 A shows the TTD1 hole; it is possible to note that oles' stack A is more significant than the respective holes of stack B. Moreover, the holes are symmetrical. **Figure 4-20 B** shows the TTD2 hole; holes' stack A are bigger than the respective ones of stack B. Moreover, the holes are asymmetrical from the first hole; an asymmetry in different directions is observed. **Figure 4-20 C** shows the TTD3 hole and, similarly to TTD1 and TTD2, holes' stack A (relative to Aluminium) is bigger than the respective holes of stack B. Moreover, the holes are symmetrical.

Figure 4-21 shows the hole diameter measured from hole no. 1 to no. 30 drilled by TTD1, TTD2 and TTD3 tools. The upper and lower limits for the measurement are also reported in the graph (the up limit is 4.849 mm, and the low limit is 4.925 mm). These are technological limits.

Figure 4-21 A shows the TTD1 hole diameter. Hole A and Hole B don't have a constant trend, and the measurement is outside the upper limit for the first 15 holes of stack A (relative to Aluminium). **Figure 4-21 B** shows the TTD2 hole diameter. Hole A and Hole B have a very irregular trend; holes B have an upper size than hole A, and their values are near the upper limits. The trend highly decreases for stack A, and the holes' stack B is not constant. **Figure 4-21 C** shows the TTD3 hole diameter. Hole A and Hole B have a similar trend, but stack holes A are bigger than the respective hole of stack hole

B. In both tools, the trend is decreasing. This set of parameters is the only one without measures out of technological limit and has symmetrical holes.

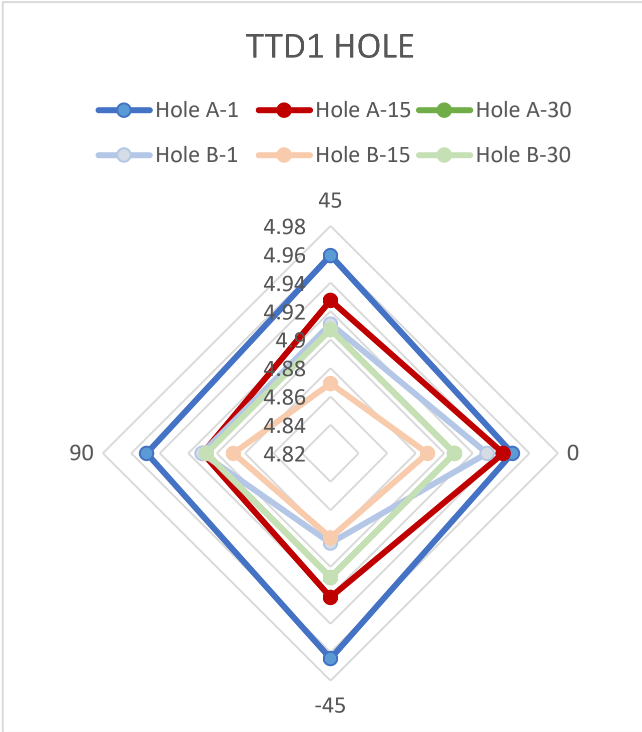

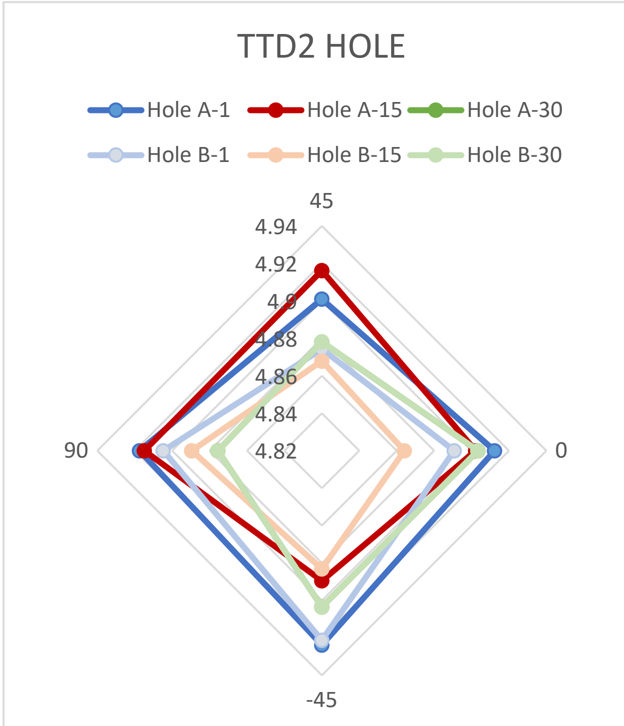

A

B

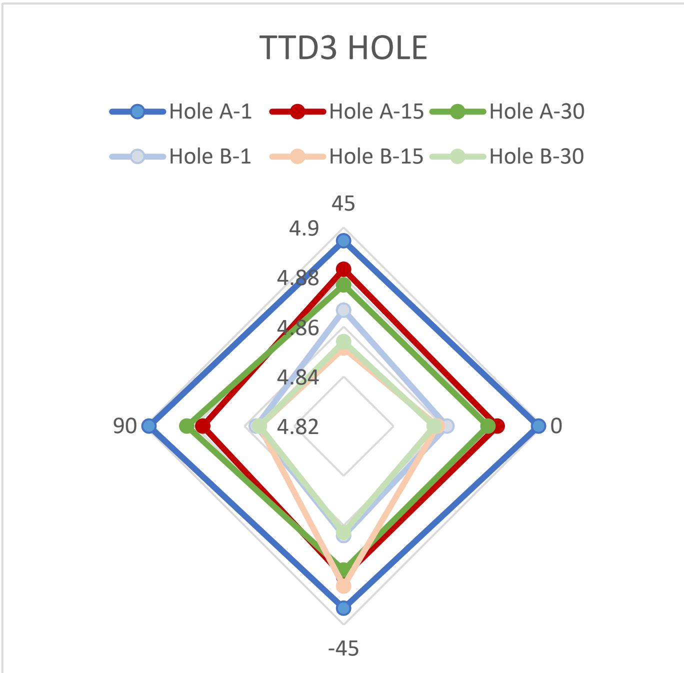

C

Figure 4-20: Dimensional analysis for the number of 1-15-30 holes for TTD1 (A), TTD2(B) and TT3(C) (unit of measure in mm).

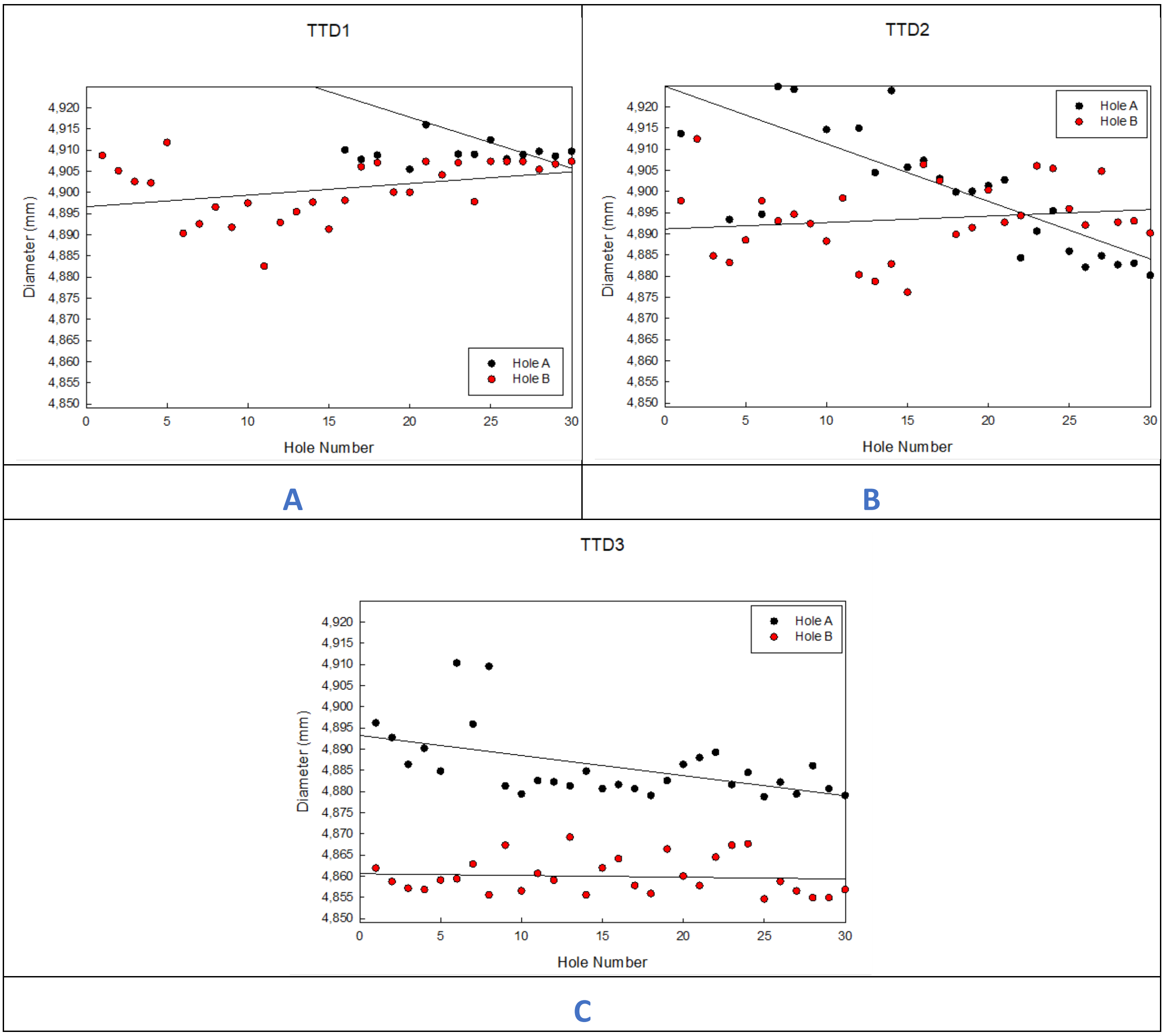

Figure 4-21: Hole diameter measured from hole no. 1 to no. 30 and stacks A and B drilled by TTD1 (A), TTD2(B) and TT3(C).

4.5.2 PARAMETER: ISD1

The data acquired via dial gauge were suitably post-processed to obtain a spider diagram describing the measurement of diameter during each hole's drilling.

Figure 4-22 shows the dimensional analysis for the number of 1-15-30 holes for ISD1 tools for stack A and stack B (Figure 2-2). Holes' stack A are bigger than stack B, except the hole no. 1, where the light blu lines relative to the first hole of stack B is out of the blu line (relative to the first hole of stack A) in all the directions. Moreover, the holes are symmetrical except the hole 30 of stack B along the direction of 0°.

Figure 4-23 shows the hole diameter measured from hole no. 1 to no. 30 drilled by ISD1 tools. The upper and lower limits for the measurement are also reported in the graph (the up limit is 4.849 mm, and the low limit is 4.925 mm). These are technological limits.

Figure 4-23 shows that Hole A and Hole B exceeded the upper limit and it was not possible to analyse the measurement of the graph.

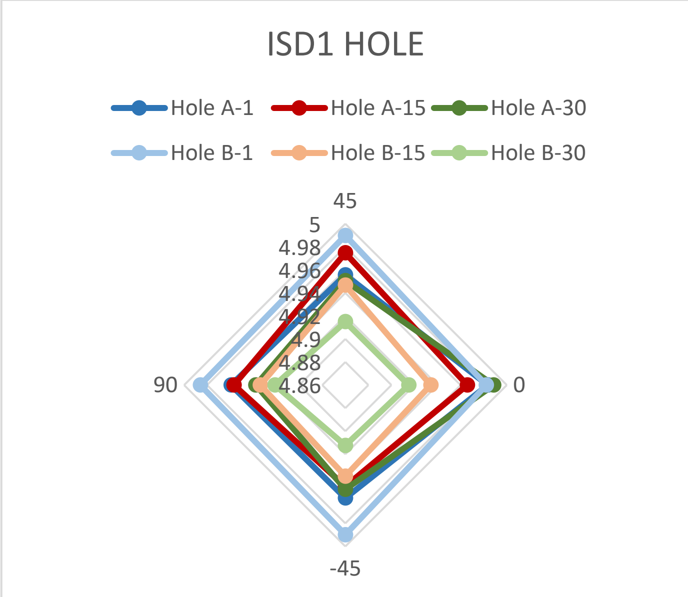

Figure 4-22: Dimensional analysis for the number of 1-15-30 holes for ISD1 (unit of measure in mm).

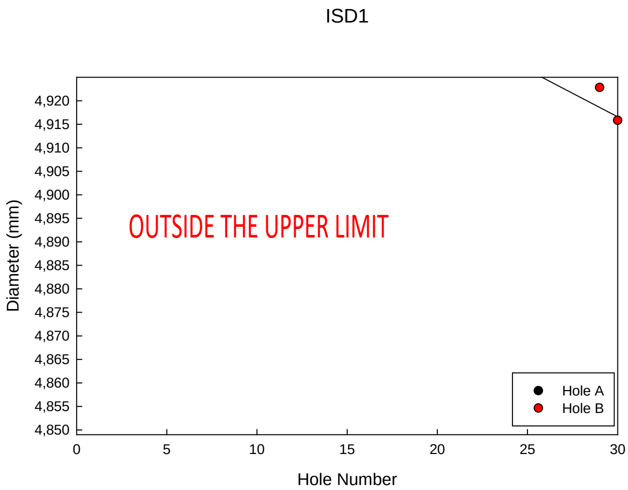

Figure 4-23: Hole diameter measured from hole no. 1 to no. 30 and stacks A and B drilled by ISD1.

4.6 AL/CFRP STACKS – DIAMETER TOOL 6.35 MM

This paragraph shows the comparison of the measurement of the hole obtained from the data analysis tools with a nominal diameter tool of 6.35 mm during the Al/CFRP stack drilling process.

Spider graphs are used for comparison of the eccentricity of the hole of stacks A and B. With this type of graph, it was possible to observe the difference in dimension between the stacks. (In the graph, the unit of measure is the mm).

Successively, the mean of the diameter of the hole for both tools was compared. This feature has a strong correlation with the wear. As regards the dimensional errors that affect the CFRP drilled holes, it is known from the literature that the hole diameter is generally reduced with an increasing number of holes; this behaviour is confirmed by the measurements, always showing a decreasing trend of the measured hole diameter for 30 consecutive holes drilled with different parameter.

The parameters used are the same in the study of the temperature of Chapter 3.

For this test, it was decided to use a different set of parameters for the TTD tools to deepen, based on the knowledge of the previous tests, more accurately the best drilling parameters. For ISD, instead, we proceeded with the parameters used for drilling the Al / CFRP stacks.

Table 3-11 shows the parameter used for this combination of diameter tool and materials stacks.

All tests were carried out under the standard condition of temperature and pressure.

All test were carried out three times, and the results were mediated between them.

4.6.1 PARAMETER: T1/T2/T3

The data acquired via dial gauge were suitably post-processed to obtain a spider diagram describing the measurement of diameter during each hole's drilling.
Figure 4-24 shows the dimensional analysis for the number of 1-15-30 holes for T1, T2 end T3 for CFRP stack and Al stack (Figure 2-2).

Figure 4-24 A doesn't show the T1 hole because the measurement was impossible; furthermore, the dial gauge doesn't enter the hole. Figure 4-24 B shows the T2 hole, and holes' stack A are similar to the respective hole of stack B. Moreover, the holes are symmetrical. Figure 4-24 C shows the T3 hole, and holes' stack A (relative to Aluminium) are greater than the respective holes of stack B. Moreover, the holes are symmetrical, except the hole no. 30, where is an asymmetry along the 45°direction.

Figure 4-25 shows the hole diameter measured from hole no. 1 to no. 30 drilled by T1, T2 and T3 tools. The upper and lower limits for the measurement are also reported in the graph (the up limit is 6.35 mm, and the low limit is 6.426 mm). These are technological limits.

Figure 4-25 A doesn't show the T1 hole because the measurement was impossible. Figure 4-25 B shows the T2 hole diameter. the diameters of holes B are greater than holes A, and their values, for the first five holes, go out the upper limits. The trend is high decreasing for both the stacks. Figure 4-25 C shows the T3 hole diameter. Hole A and Hole B have a similar trend, but holes A are greater than holes hole B; moreover, the first ten holes of stack A go out the upper limits. In both tools, the trend is high decreasing.

	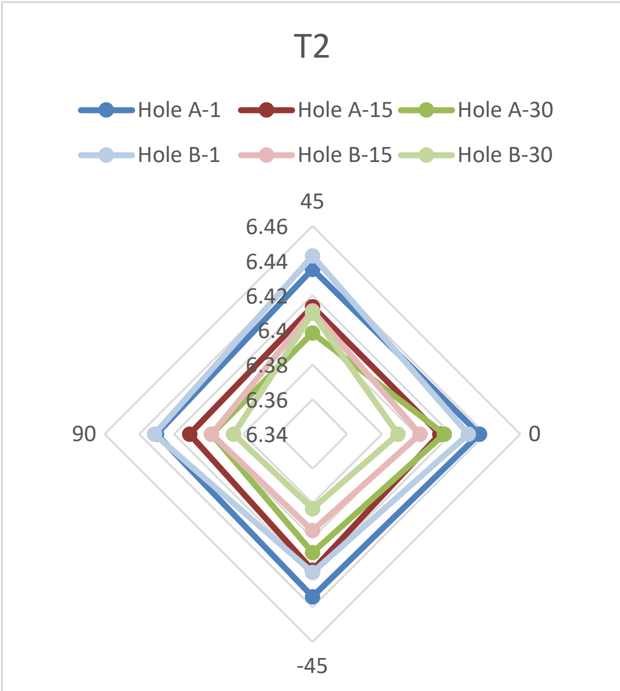
A	**B**

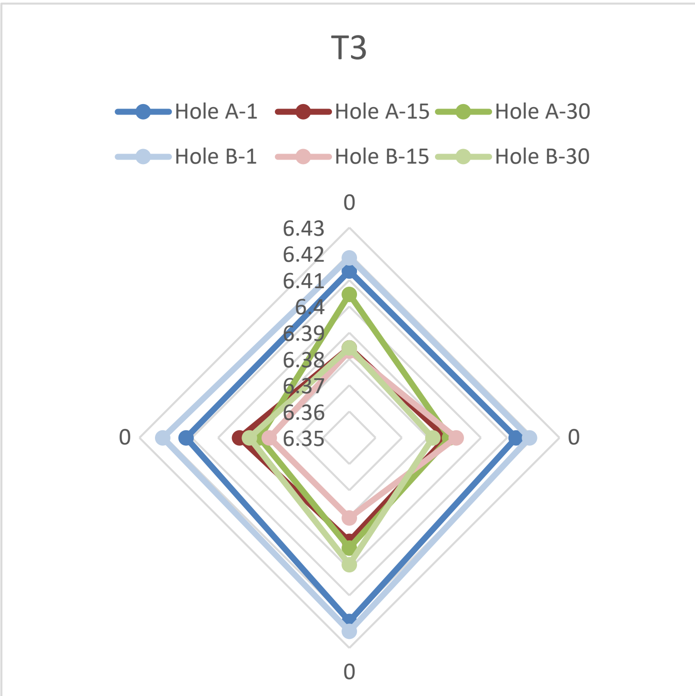

C

Figure 4-24: Dimensional analysis for the number of 1-15-30 holes for T1 (A), T2(B) and T3(C) (unit of measure in mm).

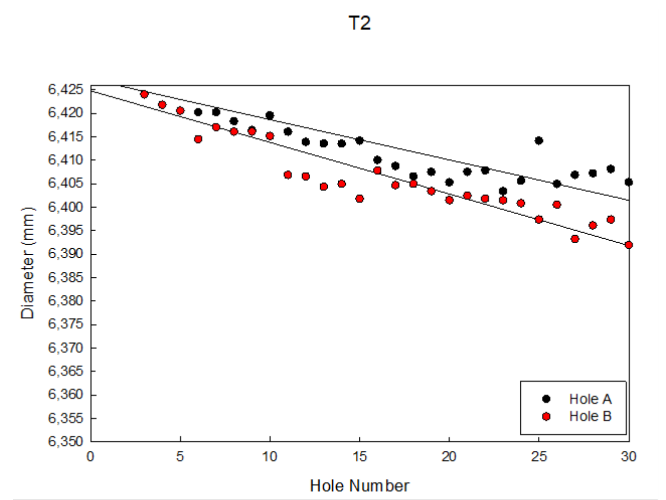

A

B

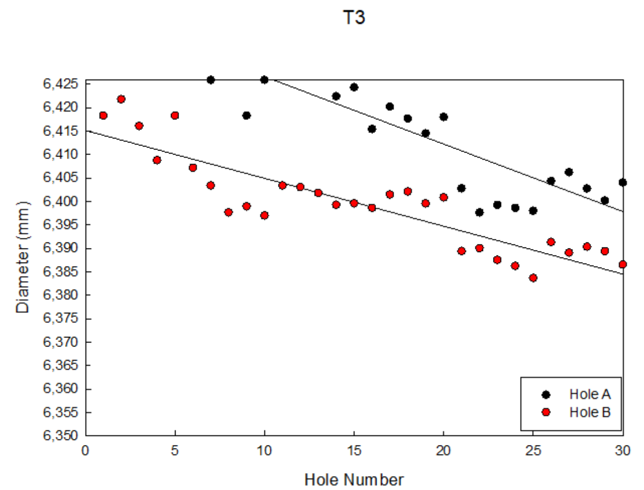

C

Figure 4-25: Hole diameter measured from hole no. 1 to no. 30 and stacks A and B drilled by T1 (A), T2(B) and T3(C).

4.6.2 PARAMETER: T4/T5/T6

The data acquired via dial gauge were suitably post-processed to obtain a spider diagram describing the measurement of diameter during each hole's drilling.

Figure 4-26 shows the dimensional analysis for the number of 1-15-30 holes for T4, T5 end T6 for CFRP stack and Al stack (Figure 2-2).

Figure 4-26 A shows the T4 hole; that holes' stack A is similar to the respective holes of stack B except for the hole no. 30, where B is smaller than A. Moreover, the holes are symmetrical. Figure 4-26 B shows the T5 hole, holes' stack A are bigger than the respective hole of stack B. Moreover, the holes are symmetrical except the hole no. 15 B, where an asymmetry along the -40° direction is observed. Figure 4-26 C shows the T6 hole, and the values are not constant and the holes are asymmetrical.

Figure 4-27 shows the hole diameter measured from hole no. 1 to no. 30 drilled by T4, T5 end T6 tools. The upper and lower limits for the measurement are also reported in the graph (the up limit is 6.35 mm, and the low limit is 6.426 mm). These are technological limits. Figure 4-27 A shows the T4 hole diameter. Hole A and hole B have a decreasing trend, and the A is bigger than B. Figure 4-27 B shows the T4 hole diameter. Hole A and hole B have a similar trend; holes A have a similar size to hole B, and their values are near the upper limits. The trend is high, decreasing for stack A and B. Figure 4-27 C shows the T6 hole diameter. Hole A and Hole B have a very irregular trend, but hole A has a similar size to hole B.

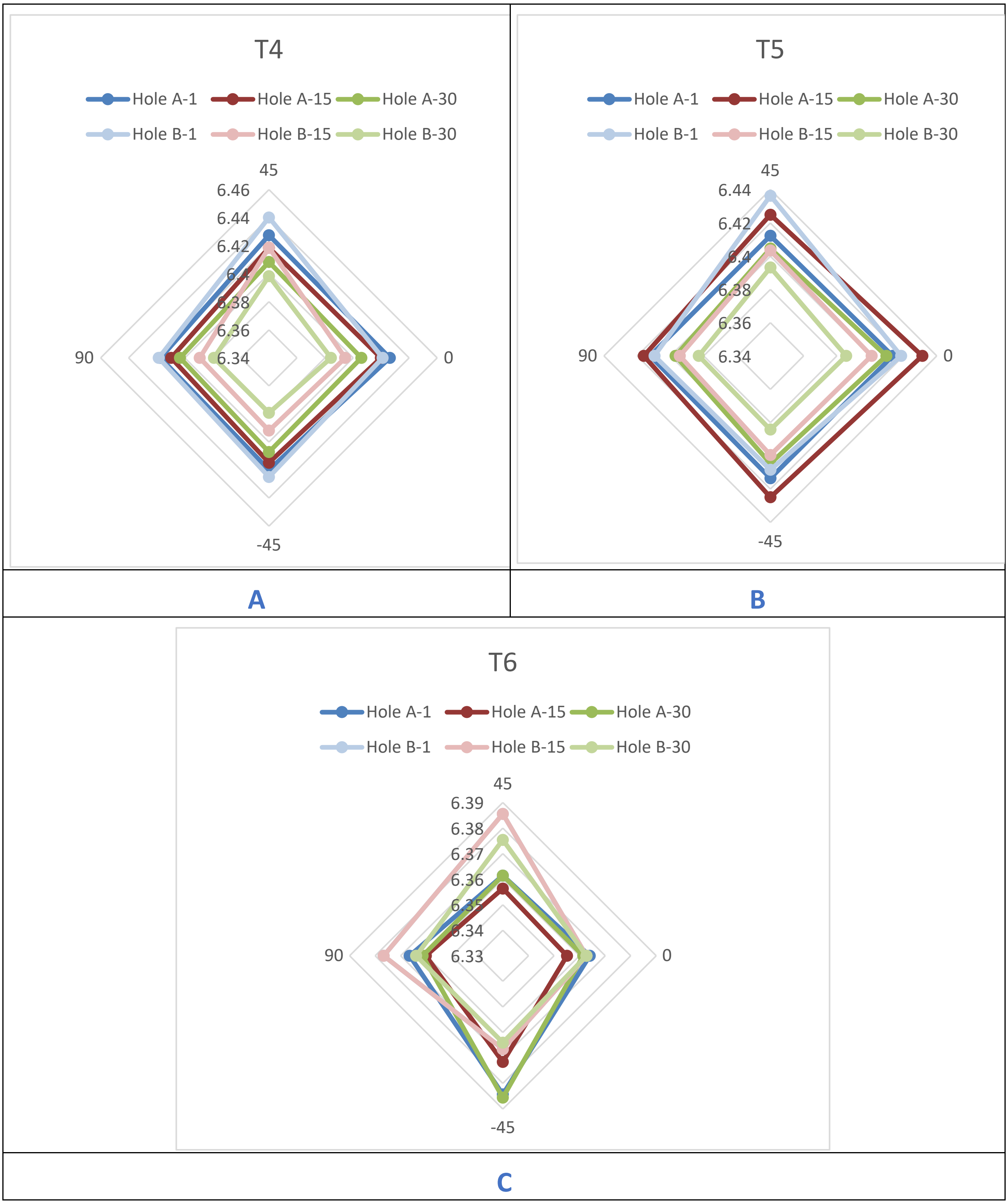

Figure 4-26: Dimensional analysis for the number of 1-15-30 holes for T4 (A), T5(B) and T6(C) (unit of measure in mm).

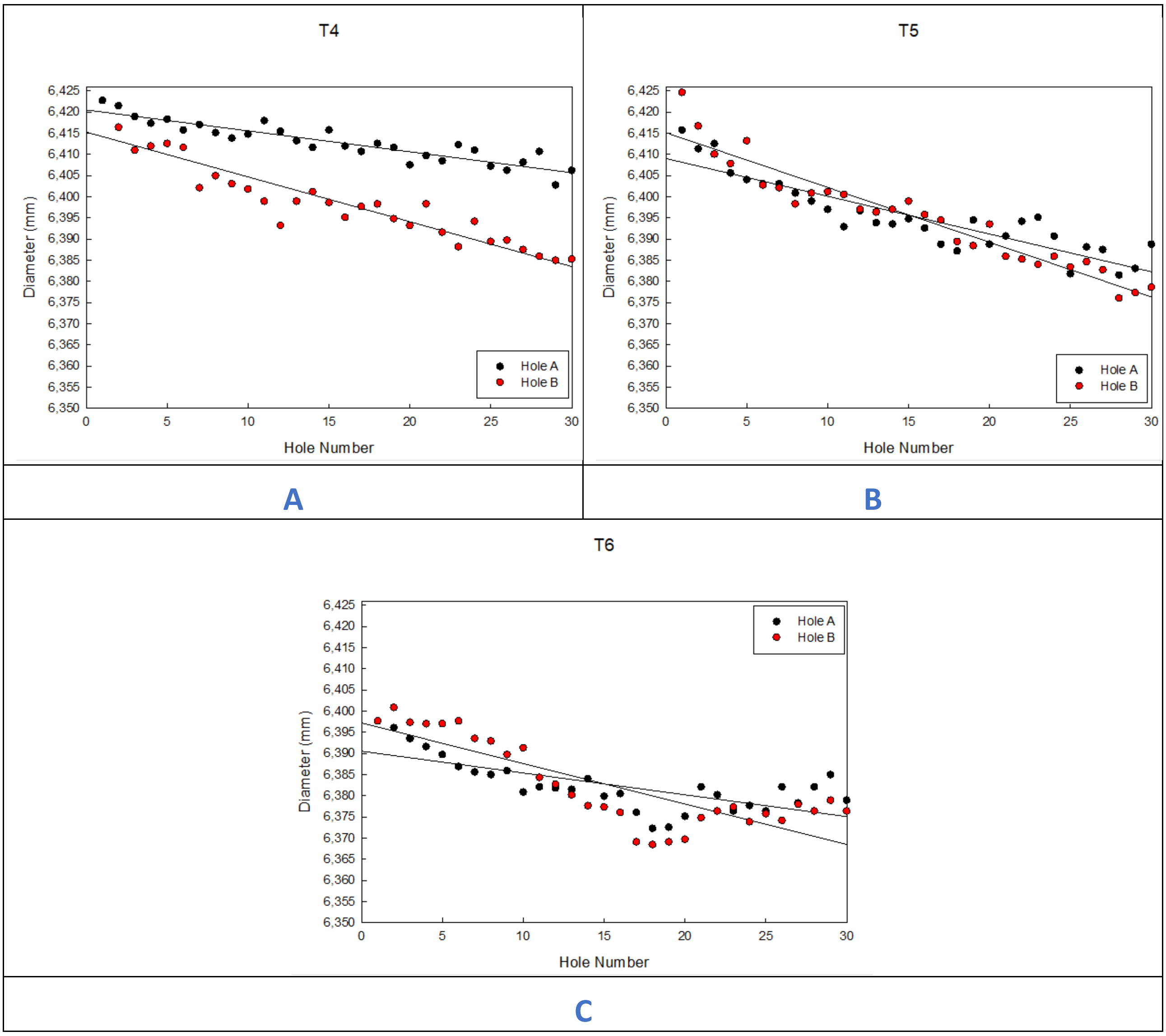

Figure 4-27: Hole diameter measured from hole no. 1 to no. 30 and stacks A and B drilled by T4 (A), T5(B) and T6(C).

4.6.3 PARAMETER: T7/T8/T9

For this parameter combination, it was not possible to complete the test. Indeed with T8 and T9, it was a break of the tool at the first hole. For these reasons, this paragraph only reports the result of T7.

The data acquired via dial gauge were suitably post-processed to obtain a spider diagram describing the measurement of diameter during each hole's drilling.

Figure 4-28 shows the dimensional analysis for the number of 1-15-30 holes for T7 for CFRP stack and Al stack (Figure 2-2). Holes' stack A is more significant than the respective holes of stack B, excepted to hole no. 1, where the holes' sizes are similar. Moreover, the holes are symmetrical for the fist hole A and B, but successively the holes are asymmetrical.

Figure 4-29 shows the hole diameter measured from hole no. 1 to no. 30 drilled by the T7 tool. The upper and lower limits for the measurement are also reported in the graph (the up limit is 6.35 mm, and the low limit is 6.426 mm). These are technological limits. Hole A and B have a decreasing trend, which is more significant for the first stack.

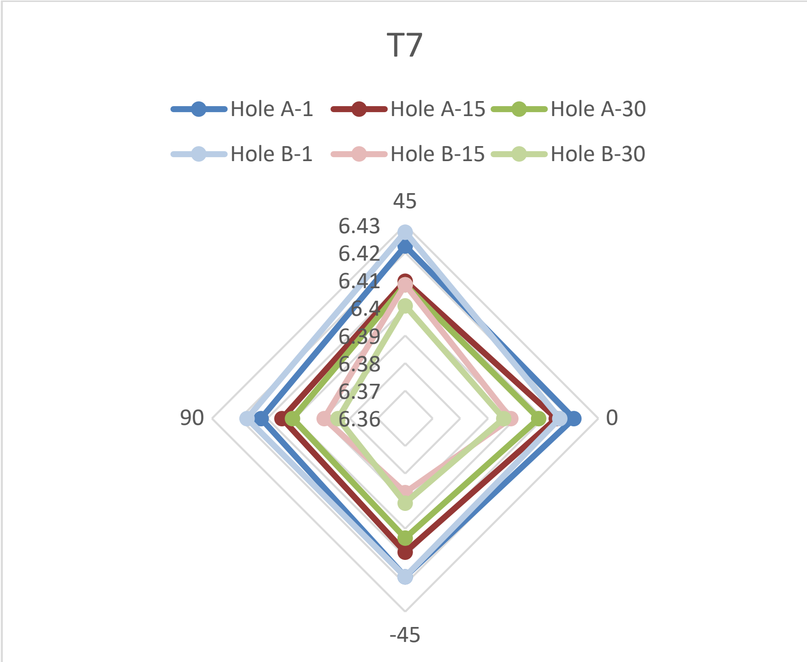

Figure 4-28: Dimensional analysis for the number of 1-15-30 holes for T7.

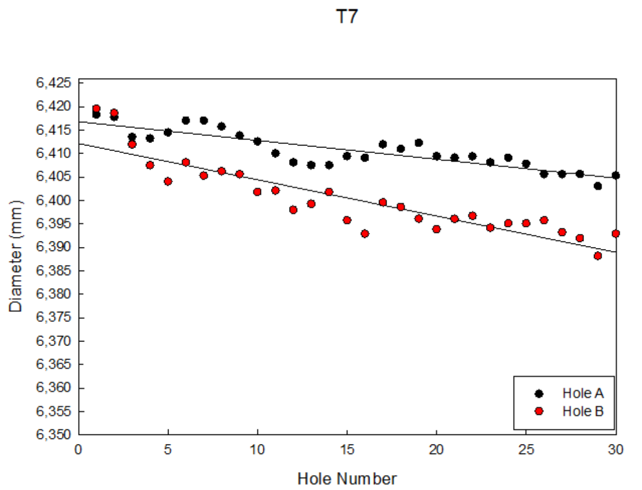

Figure 4-29: Hole diameter measured from hole no. 1 to no. 30 and stacks A and B drilled by T7.

4.6.4 PARAMETER I1/I2/I3

The data acquired via dial gauge were suitably post-processed to obtain a spider diagram describing the measurement of diameter during each hole's drilling.

Figure 4-30 shows the dimensional analysis for the number of 1-15-30 holes for I1, I2 end I3 for CFRP stack and Al stack (Figure 2-2).

Figure 4-30 A shows the I1 hole, and holes' stack A is bigger than the respective holes of stack B except for hole no. 1, where the size of A and B are similar. Moreover, the holes are symmetrical except the hole no. 30, especially no. 30 B that has an asymmetry along the 45° direction. Figure 4-30 B shows the I2 hole, stack holes A are bigger than the respective hole of stack holes B except for hole no. 1, where the size of A and B are similar, as I1. Moreover, holes B are asymmetrical (except the first hole) along the 45° direction. Figure 4-30 C shows the I3 hole, and, holes' stack A (relative to

Aluminium) is similar to the respective holes of stack B, except the hole no. 1, where the stack holes B is bigger than stack hole A. Moreover, the holes are asymmetrical from the first holes.
Figure 4-31 shows the hole diameter measured from hole no. 1 to no. 30 drilled by I1, I2 and I3 tools. The upper and lower limits for the measurement are also reported in the graph (the up limit is 6.35 mm, and the low limit is 6.426 mm). These are technological limits. Figure 4-31 A shows the I1 hole diameter. Hole A and hole B have a higher decreasing trend and similar value. Figure 4-31 B shows the I2 hole diameter. Hole A has a higher decreasing trend than Hole B; moreover, holes B have a bigger size than hole A. Figure 4-31 C shows the I3 hole diameter. Hole A and Hole B have a similar trend. In both tools, the trend is decreasing.

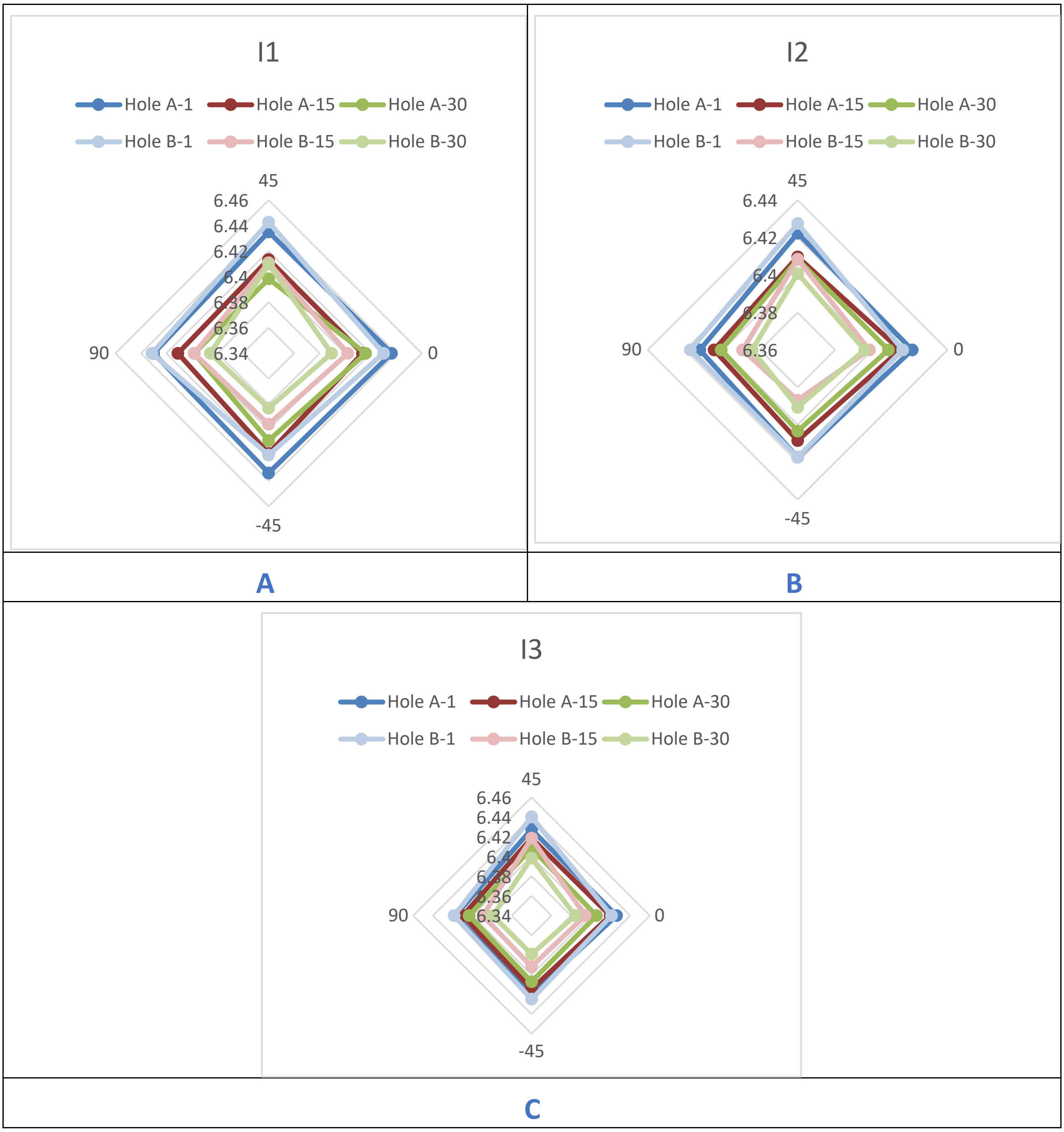

Figure 4-30: Dimensional analysis for the number of 1-15-30 holes for I1 (A), I2(B) and I3(C) (unit of measure in mm).

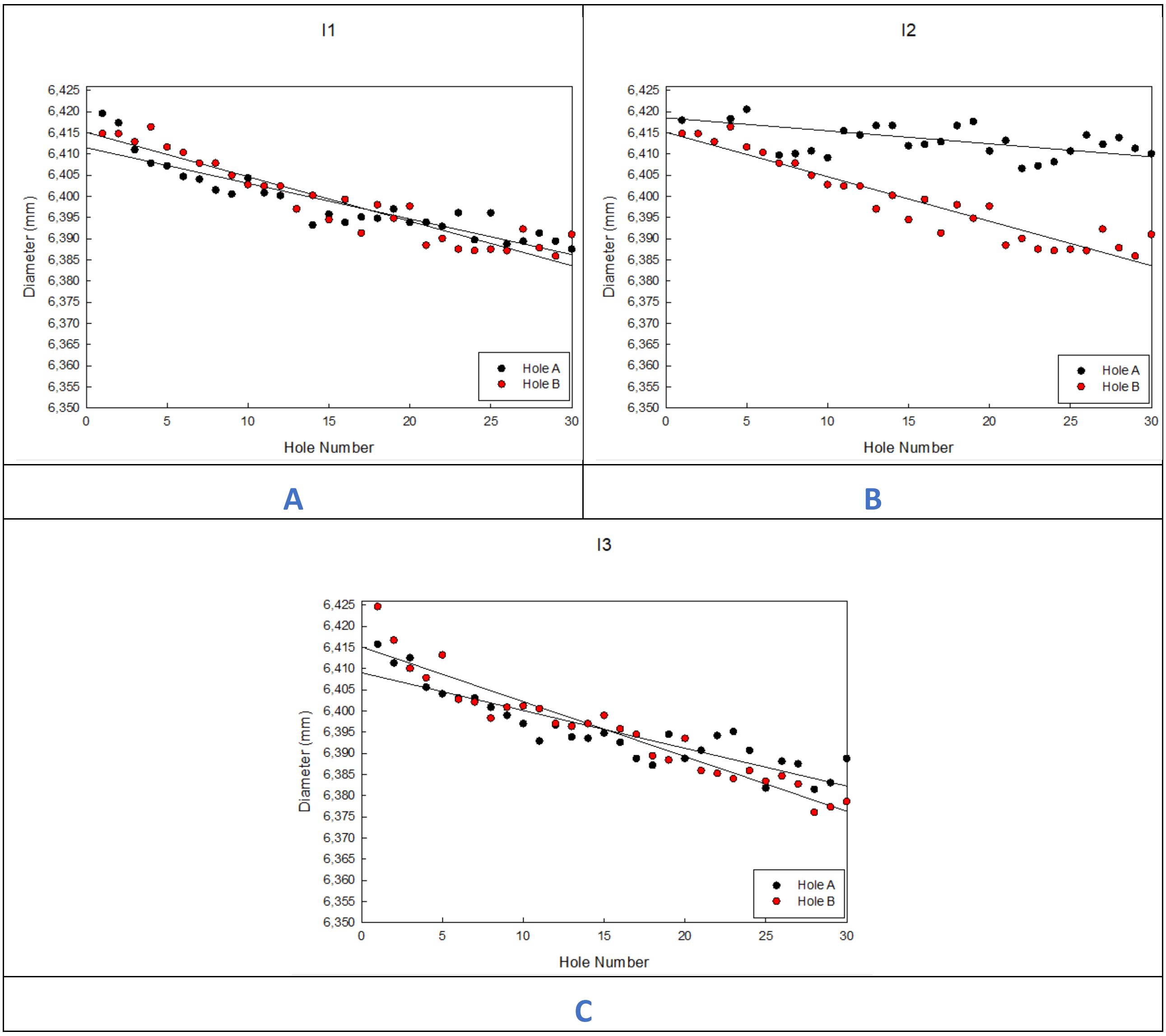

Figure 4-31: Hole diameter measured from hole no. 1 to no. 30 and stacks A and B drilled by I1 (A), I2(B) and I3(C).

5 SURFACE FINISHING ANALYSIS

The surface finishing inside the holes after the drilling operations is a highly correlated parameter with tool wear; the idea of being able to evaluate in the right way the surface finishing of composite materials and the possibility of obtaining a complete view of the defects inside the holes with a simple surface scan occupies many studies [64], [75]. However, this parameter is difficult to read after drilling operations because of the characteristic defects caused by the ply's arrangement. Moreover, each ply has characteristic defects.

With the increased roughness, it is possible to evaluate how the parameters influence the holes' quality [65]. After the acquisition of the data obtained from the roughness tester, various parameters of surface roughness were evaluated and, subsequently [76], the 3D images of the surfaces were studied to observe the morphology of the internal hole and to compare these images with the microscopy analysis using deep learning procedure [77].

The results were compared to study a new visual recognition method of CFRP laminate defects [78].

5.1 INTERNAL SURFACE ANALYSIS

In this work, the internal roughness of holes it is determined on stacks CFRP/CFRP with three different tools and two different parameters, to characterize tools of industrial interest respecting the limits imposed by the application fields [77], [79], [80].

The roughness parameters were reported:

Sa (arithmetical mean height)

Sa expresses, as an absolute value, the difference in the height of each point compared to the arithmetical mean of the surface.

$$Sa = \frac{1}{A}\iint_A |Z(x,y)|dxdy \quad \text{Eq. 5-1}$$

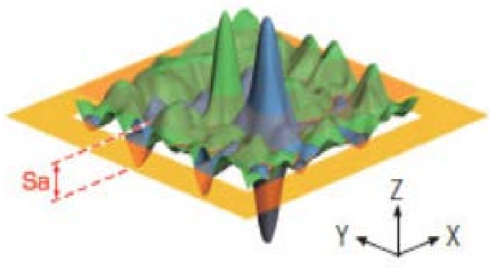

Sq (Root mean squared height)

Sq represents the root mean square value of ordinate values within the defined area.

$$Sa = \sqrt{\frac{1}{A}\iint_A Z^2(x,y)dxdy} \quad \text{Eq. 5-2}$$

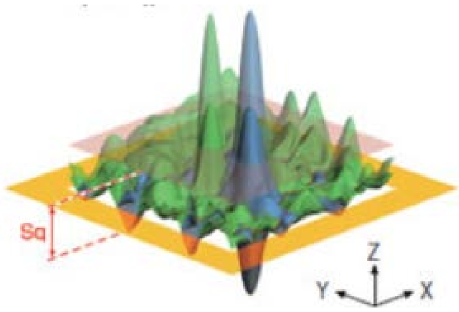

Sz (Maximum height)

Sz is defined as the sum of the largest peak height value (*Sp*) and the largest pit depth value (*Sv*) within the defined area.

$$Sz = Sp + Sv \quad \text{Eq. 5-3}$$

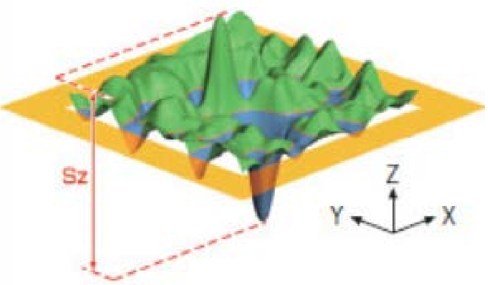

Ssk (Skewness)

Ssk values represent the degree of symmetry of peaks and valleys about the average surface as the centre.

Ssk<0: Height distribution is skewed above the mean plane.

Ssk=0: Height distribution (peaks and pits) is symmetrical around the mean plane.

Ssk>0: Height distribution is skewed below the mean plane.

$$Sa = \frac{1}{Sq^3}\left(\sqrt{\frac{1}{A}\iint_A Z^3(x,y)dxdy}\right) \quad \text{Eq. 5-4}$$

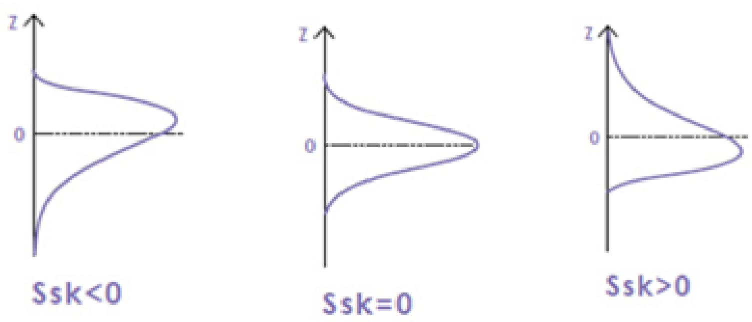

Sku (Kurtosis)

Sku value is a measure of the sharpness of the roughness profile.

Sku<3: Height distribution is skewed above the mean plane.

Sku=3: Height distribution is normal (Sharp portions and indented portions co-exist).

Sku>3: Height distribution is spiked.

$$Sa = \frac{1}{Sq^4}\left(\sqrt{\frac{1}{A}\iint_A Z^4(x,y)dxdy}\right) \qquad \textbf{Eq. 5-5}$$

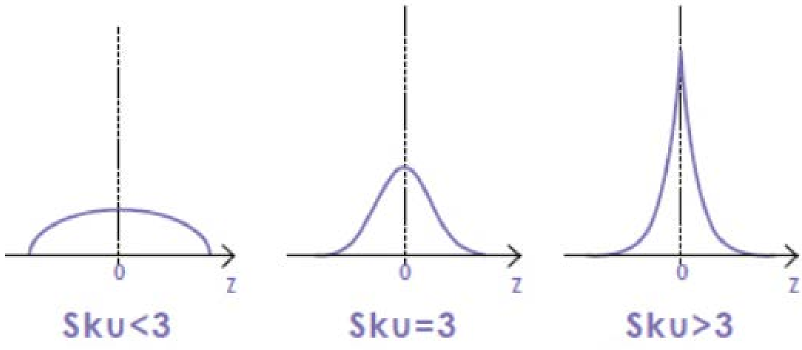

With the increase of the roughness, it is possible to evaluate how the geometry of the tool and the parameters chosen influence the quality of the holes [81]; in particular, three geometries will be evaluated with two different working parameters [82], [83].

In this work, the internal roughness of holes made on Al/CFRP stacks is determined with different parameters [47], [84], [85].

5.2 ROUGHNESS CHARACTERIZATION OF HOLE QUALITY IN DRILLING OF AL/CFRP STACKS.

The composite material used for the test is the same as described in **Chapter 2** and shown in **Figure 2-1**.

Experimental drilling tests were carried out on stacks made of CFRP laminate (thickness 5 mm) and Al sheet (thickness 2.5 mm); the CFRP laminate comprises 26 CFRP prepreg plies made of CYCOM 977-2 epoxy matrix and Toray T300 carbon fibres.

Laminates were fabricated by hand lay-up and autoclave curing with stacking sequence $[\pm45_2/0/90_4/0/90/0_2]_s$. To accurately reproduce the severest drilling conditions in the aerospace industry, the two laminates were stacked and drilled together, with the Al on the top and the CFRP on the bottom with the bag side in contact. The drilling bit is a traditional two-flute twist drill made of tungsten carbide (WC), Ø6.35 mm, which features a 125° point angle.

Image and roughness analysis was conducted every 5 holes on 30 consecutive holes made by the same cutting tool; the analysis was repeated with different cutting conditions.

Table 3-11 shows the parameter used for this combination of diameter tool and materials stacks.

Tests were also performed with the parameters 6000 rpm - 0.10 mm/rev and 6000 rpm - 0.15 mm/rev; in these cases, a catastrophic tool failure occurred that did not allow to make other considerations for these parameters except that they are too pushed for drilling of Al/CFRP stacks.

5.2.1 ROUGHNESS MEASUREMENT PROCEDURE

The 3D roughness measurements were conducted using a Talysurf S3F roughness tester produced by Taylor Hobson. The size of each generated surface is 512x512 points with steps along y-direction of 0.1 mm and the sample area was set at 4x3.5 mm^2. In order to avoid the rotation of the samples during the roughness measurements, they were cut and fixed inside a clamping device, shown in Figure 5-1 A.

The data acquired in the cylindrical samples, shown in Figure 5-1 B, were processed to obtain flat surfaces, to reduce the inaccuracies.

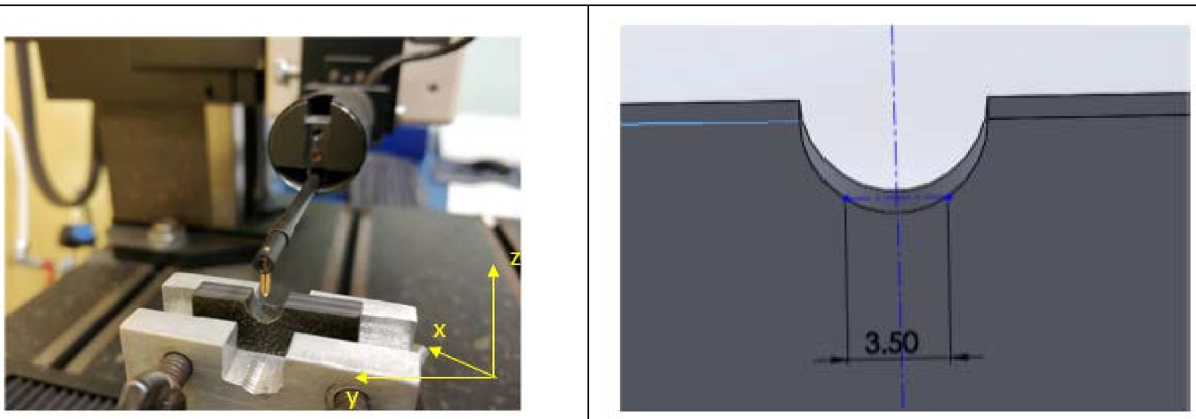

A	B

Figure 5-1: Setup employed for roughness measurement (A) and area of measurement (B).

The micro-roughness measurements need to be filtered to eliminate any contribution due to macro-roughness and to the confirmation of the device under test because the sample may not be perfectly flat. The size of each generated surface is 512x512 points with the steps in the x and y direction of 0.1 mm.

Suppression of the shape of the surface with a fifth-degree polynomial proceeded. A point fill operation is required for interpolation and three-point levelling and gives roughness values measured with a Gaussian filter and a cut-off of 80 µm.

Figure 5-2 A-B show an image of surface hole no. 1 at T1 and a surface after being filtered of the same hole.

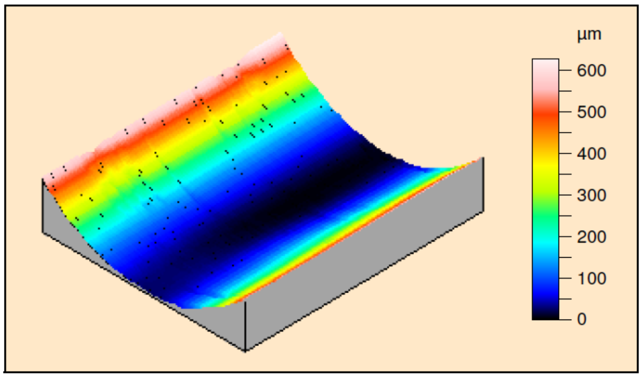	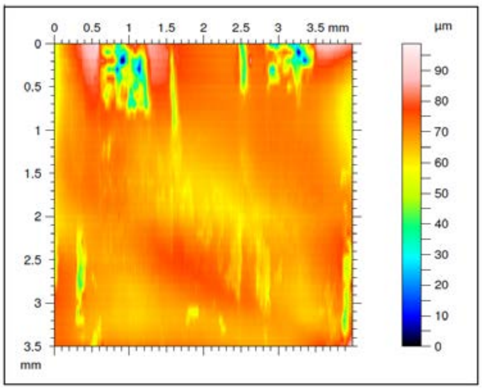
A	**B**

Figure 5-2: A surface image of hole no. 1 of test T1 (A) and a surface example after being filtered of hole no. 1 at T1(B).

After the acquisition of the data obtained from the roughness tester, the following surface roughness parameters were evaluated: Sa (arithmetical mean height), Sq (Root mean square height), Sz (Maximum height), Ssk (Skewness), Sku (Kurtosis).

Roughness measurements have allowed, through the use of Sa, Sq, Sku and Ssk, to obtain a quantitative evaluation of the damage caused by drilling.

Subsequently, the 3D images of the surfaces were also studied to observe the morphology of the inner surface of the hole and to compare these images with the roughness values.

The roughness values have been studied every 5 holes.

Images are acquired by TESA VISIO 200 optical machine and processed in Matlab to reconstruct the inner surface of the CFRP hole from the images (Figure 5-3) to validate the surface reconstructed by the roughness tester.

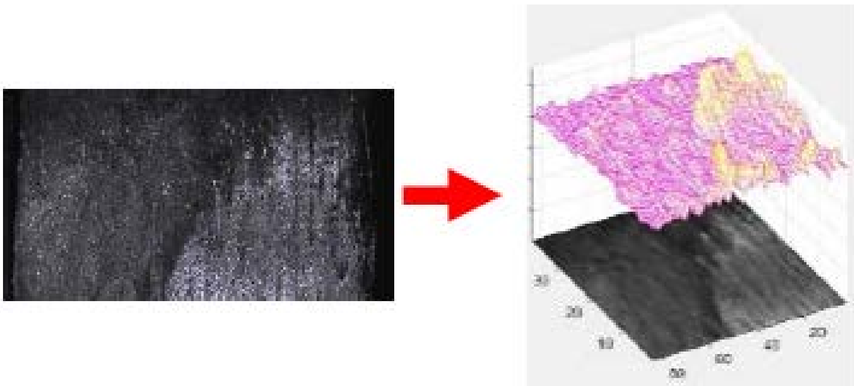

Figure 5-3: Hole image acquired by TESA VISIO 200 and MATLAB 3D surface reconstruction (Tool T1 / Hole no. 15).

5.2.2 ROUGHNESS SURFACE

Figure 5-4 shows the trend of the Sa parameter during the whole working cycle. From a visual examination, it is immediately noticeable that T7 differs more than the other values; moreover, it has higher Sa values starting from the first hole. T2 and T3 show a better trend than the others; from hole no. 1 at the end of the processing, it remains relatively constant.

In T4, hole no. 1 shows a high Sa value, which then decreases during processing. This trend indicates that Sa is not a sufficient parameter to evaluate the whole drilling process; therefore, it is essential to evaluate other parameters. T1, T4 and T6 have a low Sa value, which is constant during processing, except for hole no. 30.

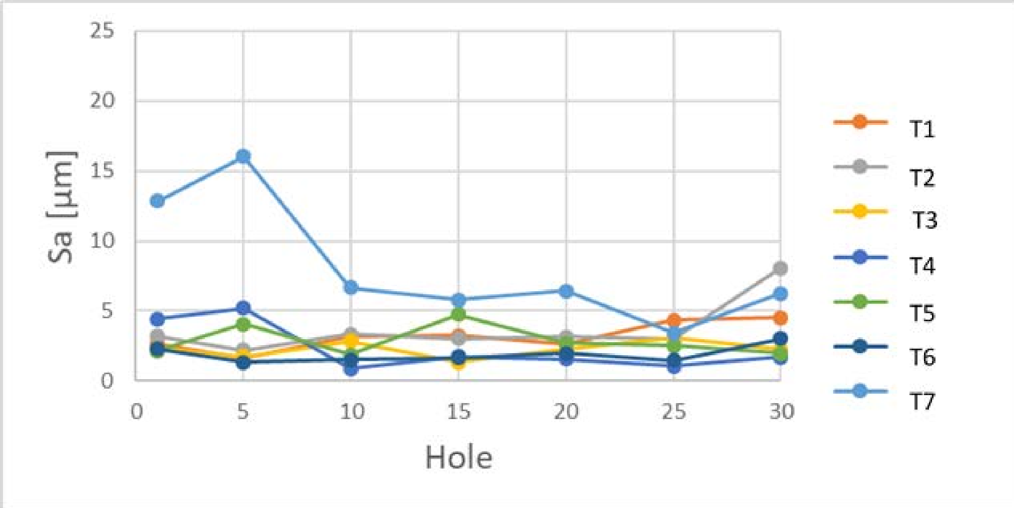

Figure 5-4: Values of Sa relative to the holes obtained with the drilling process.

Figure 5-5 shows the trend of the Sq parameter. Sa and Sq trends are similar; this confirms that the Sa data are correct.

Sq is based on the mean square deviation while Sa evaluates the average line; Sq is then fundamental because it gives information about the number of peaks and valleys.

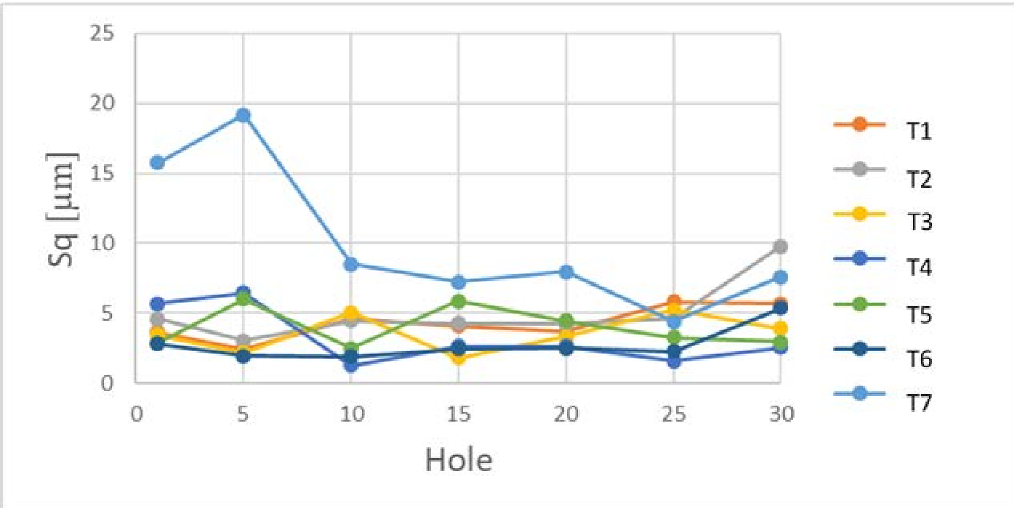

Figure 5-5: Values of Sq relative to the holes obtained with the drilling process.

Sz shown in Figure 5-6 gives us the maximum height found between the lowest valley and the highest peak. Sz is fundamental. The parameters with 3000 rpm are lower than the others. This means that the difference between the highest peak and the lowest valley is small, and therefore we can say that they have probably the best surfaces.

T4 starts with high values that remain unaffected and shows considerable alternation between peaks and valleys.

T5 has a very irregular Sz. Such a situation is not preferable because the more irregular it is, the more difficult it is to predict what happens as the work progresses.

T6 has a constant trend up to hole no. 25 already found for Sa and Sq. This hole is a particularly deep hole or a hight peak that affects the overall roughness.

T7 remains high and irregular, particularly in hole no. 5, where we find particularly high value.

If in a single point we have a particularly high peak, it does not mean that it is a parameter to be completely rejected because if all the surface is flat but has a point that alters the measurement, it does not mean that it discarded, but we must evaluate how much this defect goes to affect the quality of the hole.

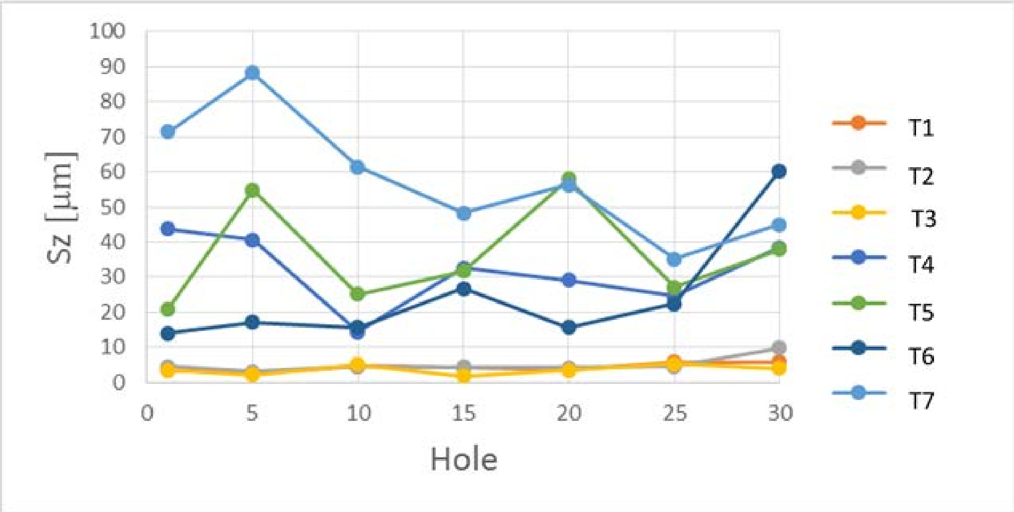

Figure 5-6: Values of Sz relative to the holes obtained with the drilling process.

The parameter Sku shown in **Figure 5-8** is a measure of the distribution of the heights of the peaks and valleys that we find within our surface. It is a dimensionless parameter that goes from -3 to 3. The more the value deviates from zero, the greater the depth of the peak or valley in question. For example, in the case of T1, the distribution is fairly homogeneous between peaks and valleys except for hole no. 5, where concentrated defect. Contrary, T3 has an asymmetrical pattern in many holes, and T4 has very negative asymmetry values.

The analysis agrees with what seen from the analysis of Sa, Sq and Sz parameters.

The parameter Ssk also gives us useful information for evaluating the distribution of peaks and valleys and their symmetry.

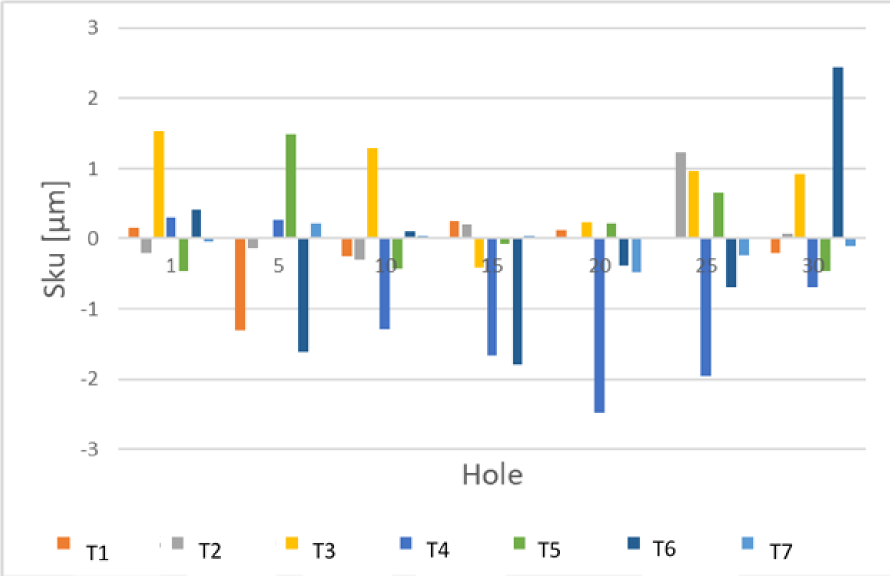

Figure 5-7: Values of Sku relative to the holes obtained with the drilling process.

In **Figure 5-8**, T1 shows defects concentration in hole no. 1 and in hole no. 5. Ssk values decrease with the process progress.

T2 turns out to be the most symmetrical and with lower values.

T3 presents high peaks already from hole no. 1; there is no correspondence with the previous parameters' analysis. The study of Sz T3 had little difference between the lowest valley and the highest peak. Consequently, the only analysis of Sz could not quantify some defects.

T4, T5, T6 start with low values and with the progress of the processing, the value of Ssk increases.

T7 shows symmetry between peaks and valleys; the analysis of the other parameters is not satisfactory. Therefore, the defects are at a precise point, and this consideration is in agreement with Sa and Sz where the first holes have low values, but the roughness was higher; therefore, this time, the 3D analysis is fundamental for a clear vision of the progress of the test.

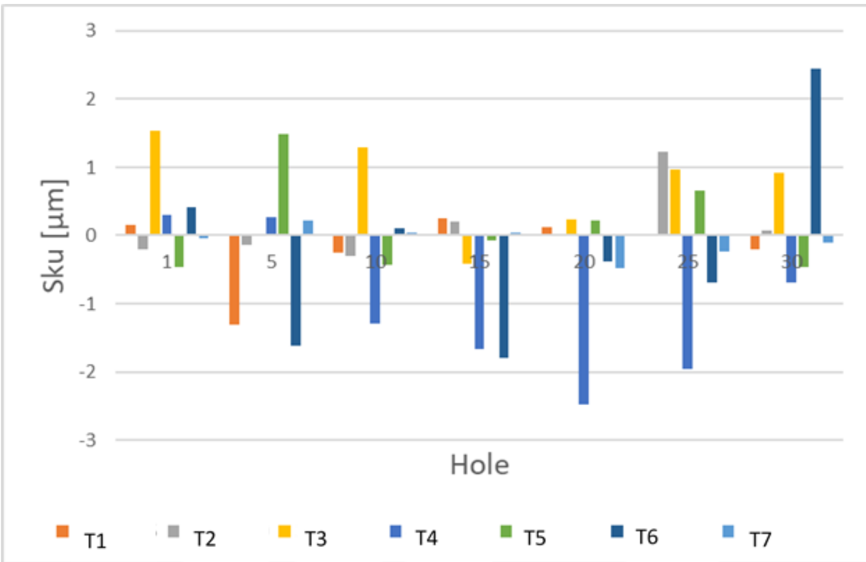

Figure 5-8: Values of Ssk relative to the holes obtained with the drilling process.

5.2.3 IMAGE ANALYSIS OF ROUGHNESS TEST

The analysis of the parameters is fundamental for the visual analysis of the 3D images since by integrating these images into the collected data, and it is possible to have a much clearer view of each test.

Figure 5-9 shows three examples of 3D surfaces obtained with three different parameters; images with the same feed rate were compared. Furthermore, it was found that the internal roughness depends much more on the feed rate than spindle speed; in fact, parameters with the same number of revolutions have surfaces similar to each other. In T1 at hole no. 1, there are peaks, but overall the surface is quite homogeneous and proceeds to see how an oblique defect is formed in the central part that affects the entire surface. This situation is particularly evident in the image of hole no. 25 and hole no. 30. Also, parameter T2 have a situation similar to parameter T1; in fact, find since hole no. 1 the oblique defect that as the processing proceeds, it is amplified up to hole no. 30, where it is particularly marked. We note that these oblique depressions are found in many of the tests carried out. At T6 and T7 from hole no. 1, the surface appears to be irregular.

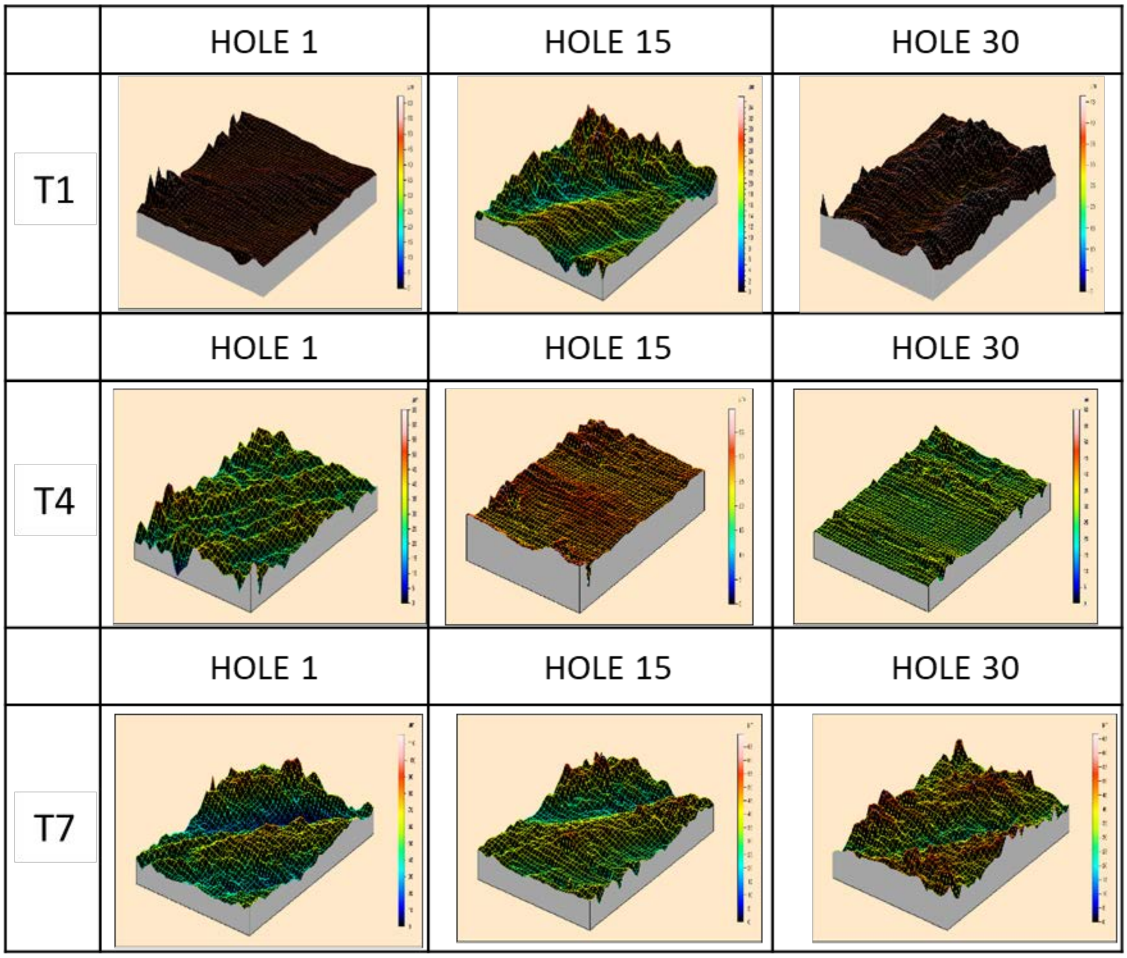

Figure 5-9: 3D Image analysis of roughness test for parameter T1, T4, T7 for holes no. 1, 15 and 30.

As 2D images, shown in **Figure 5-10**, the parameter is the best in T4. In hole no. 1, it is possible to display a decidedly deep peak (42µm), which is no longer detectable at hole no. 5. During the rest of the processing, there are no other peaks or valleys that are significantly deep or high.

Relatively to T1, defects were found starting from hole no. 1; they were present up to hole no. 30. In this case, it is likely the work progresses, a surface portion detached and therefore, from the analysis of the 2D images, the surface is regular.

T7 is particularly influenced by the presence of defects. From hole no. 1, it is clear that these defects affect the entire surface. Moreover, from the visual analysis, it can be deduced that as the processing proceeds, the defects develop obliquely. Worth noting is the valley visible at hole no. 30, which reaches modest values of depth and height (Max depth = 42.4 µm; Height = 49 µm).

T4 shows the most uniform results. There are no particularly significant peaks and valleys. The maximum depth and height values are very similar throughout the entire process.

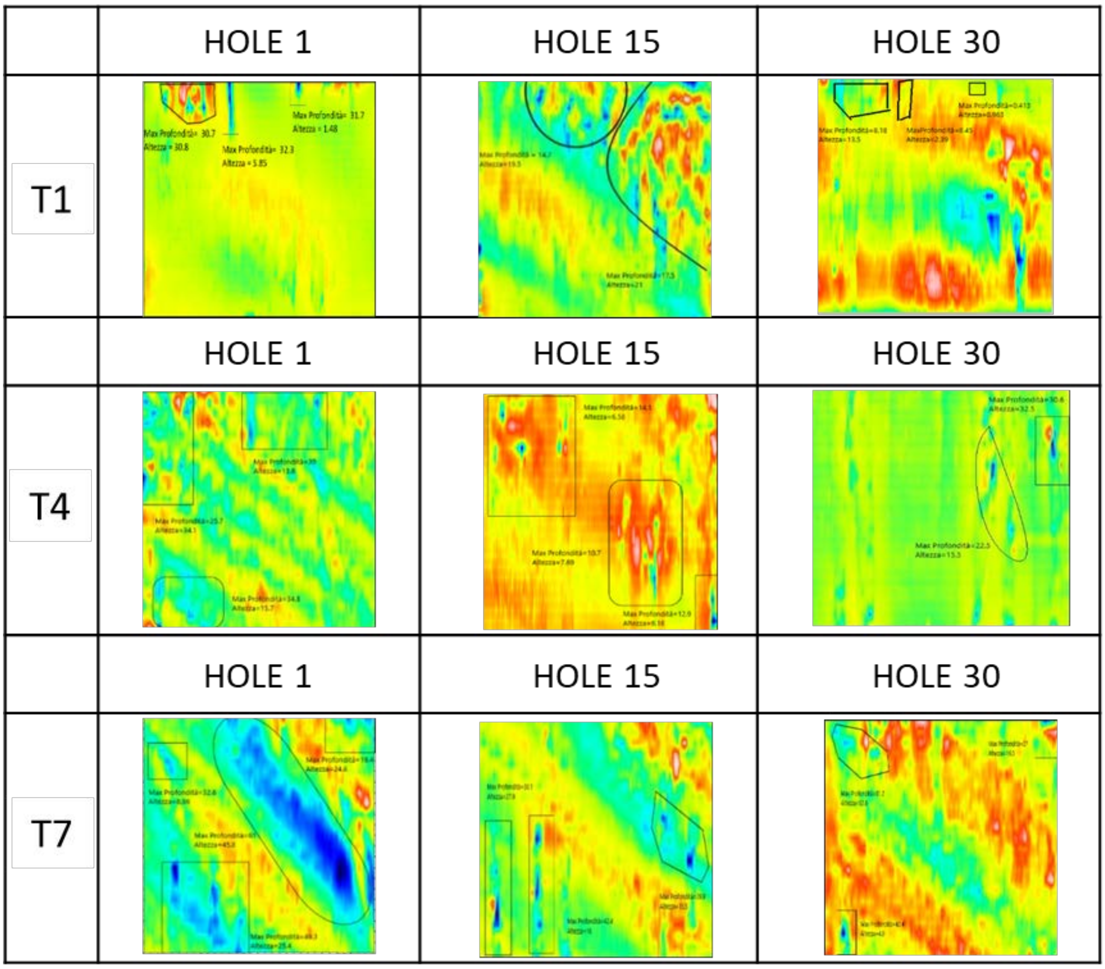

Figure 5-10: 2D Image analysis of roughness test for parameter T1, T4, T7 for holes no. 1, 15 and 30.

Appendix I and **Appendix II** show the complete results relative to all the test.

5.2.4 REAL IMAGE ANALYSIS

Images acquired by TESA VISIO 200 were compared to the 2D images produced by the roughness tester; some of the results are shown in **Figure 5-11**.

<table>
<tr><th>Tool
[name/hole]</th><th>TESA VISIO 200 images</th><th>Roughness Tester</th></tr>
<tr><td>T1/ hole 1</td><td>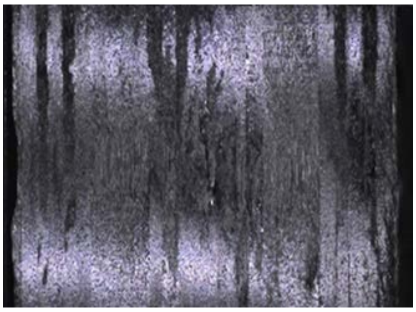</td><td>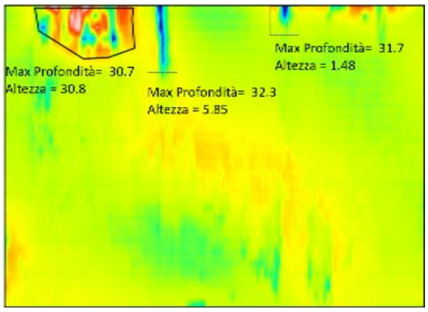</td></tr>
<tr><td>T1/ hole 15</td><td></td><td>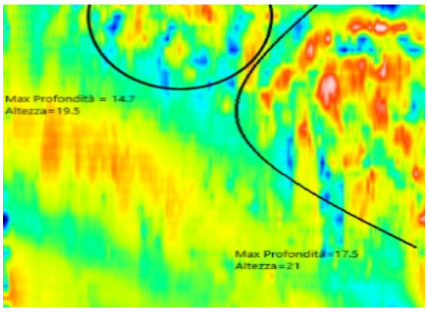</td></tr>
<tr><td>T1/ hole 30</td><td>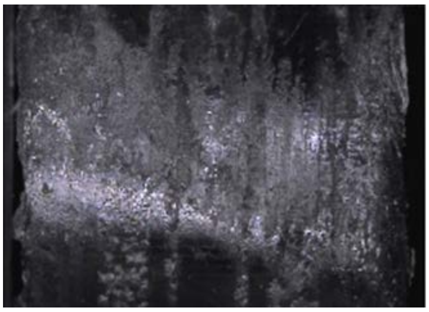</td><td>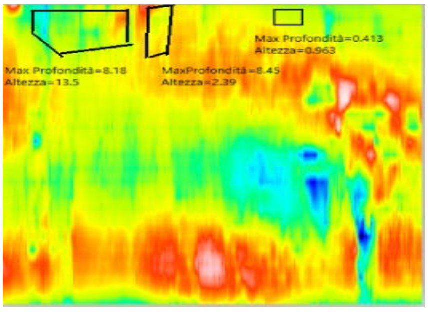</td></tr>
<tr><td>T4/ hole 1</td><td></td><td>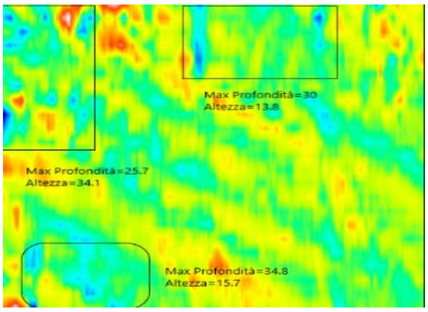</td></tr>
<tr><td>T4/ hole 15</td><td>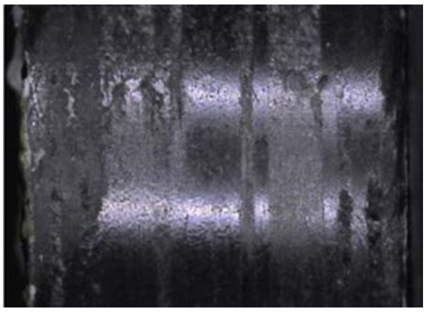</td><td>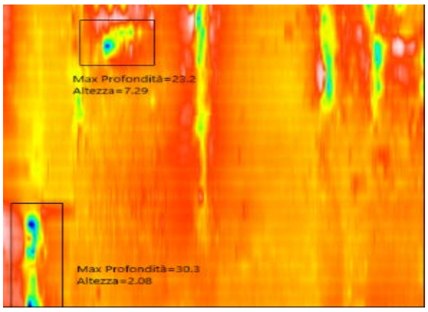</td></tr>
</table>

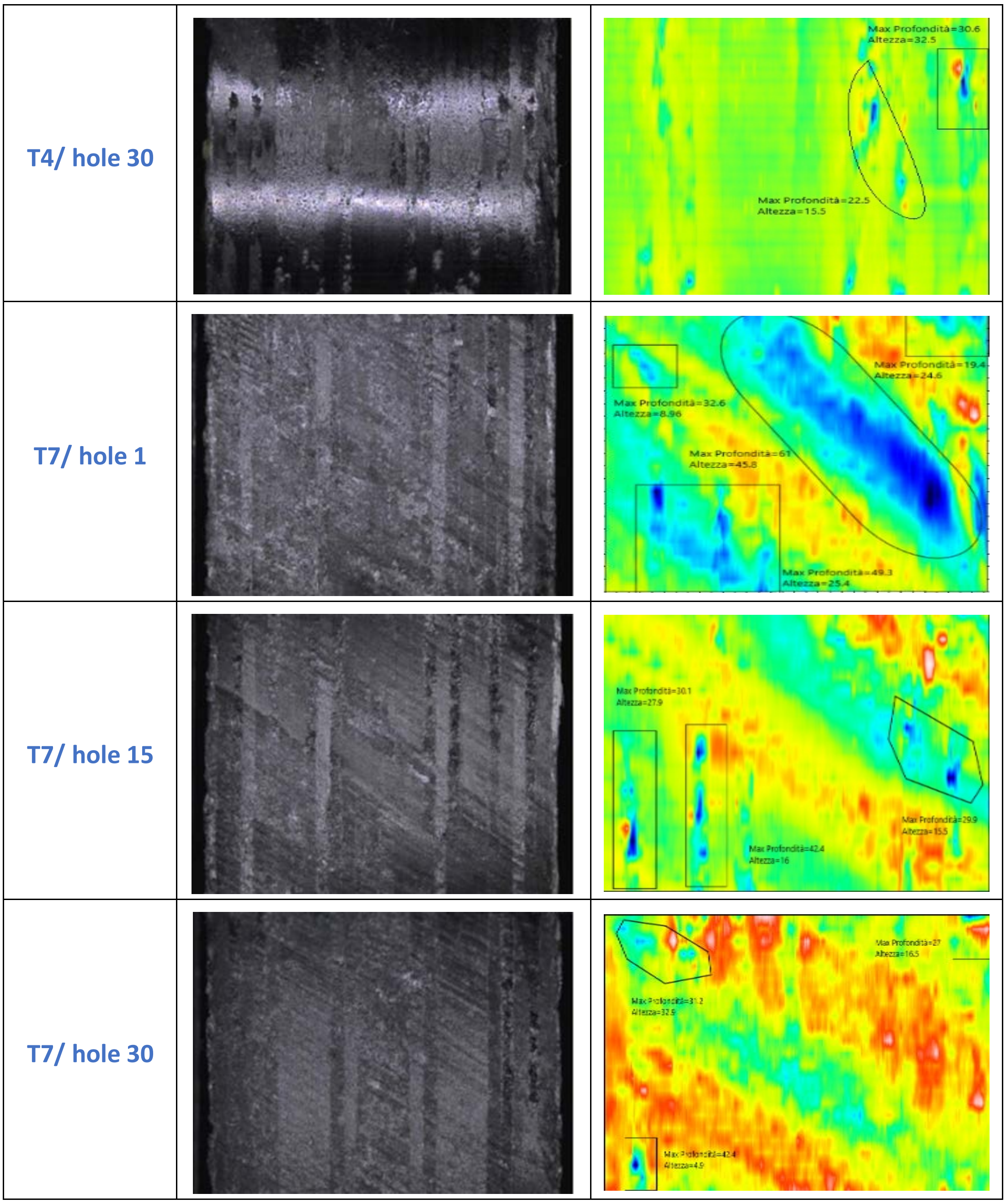

Figure 5-11: Comparison between images of the hole and 2D roughness tester.

5.2.5 DEEP LEARNING SURFACE

In the 2D images produced by the roughness tester, areas that show a response in the images acquired with the microscope have been circled. The areas with higher roughness are, in fact, those that are most damaged under the microscope inspection; the roughness meter also manages to identify oblique lines due to drilling and the layers with a different inclination of the fibres.

Finally, an image analysis procedure was implemented in Matlab to reconstruct the surface of the CFRP inner hole to validate the above discussed.

The results are shown in **Figure 5-12**.

In T1, the correspondence between the peaks presents inside hole no. 1, and those in the corresponding figure. With the increase in defects inside the hole, there is an increase in matches. For example, in hole no. 15, there is the perfect correspondence of the removed surface. Similar considerations can also be made on the other holes.

Tool [name/hole]	MATLAB elaboration	Roughness Tester
T1/ hole 1	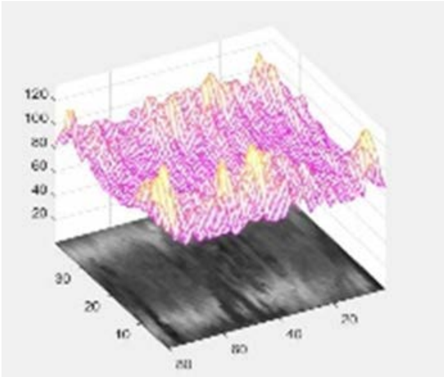	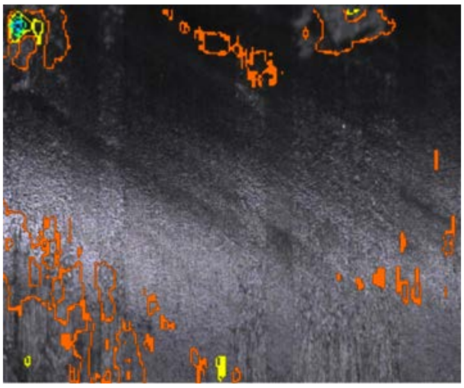
T1/ hole 30	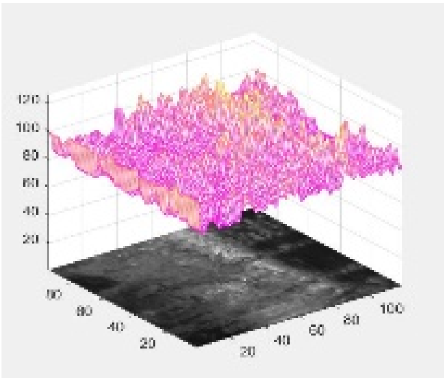	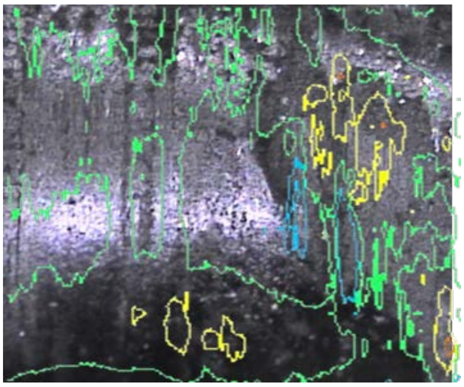
T4/ hole 1	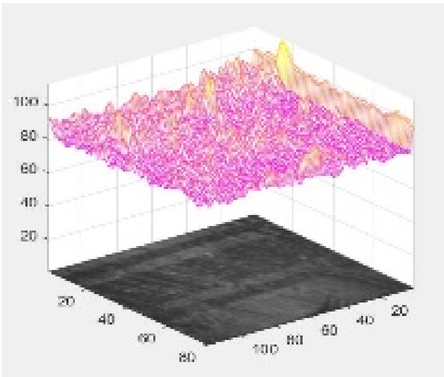	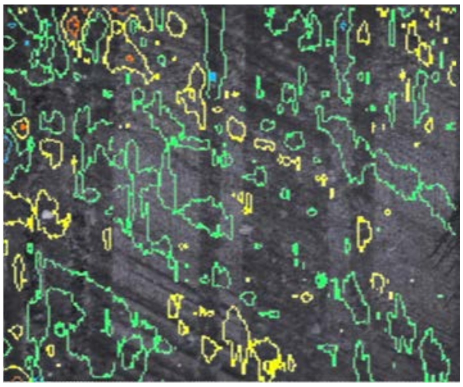
T4/ hole 30	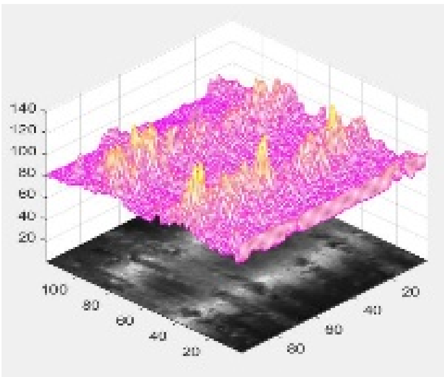	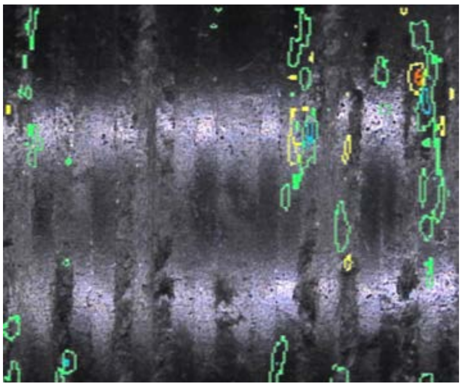

T7/ hole 1	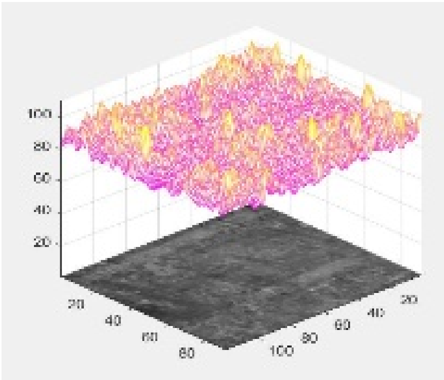	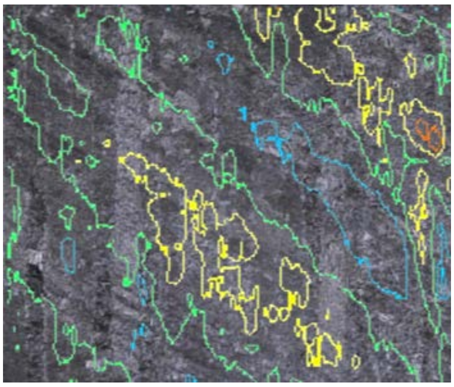
T7/ hole 30	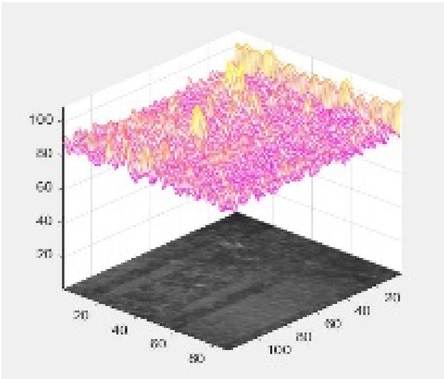	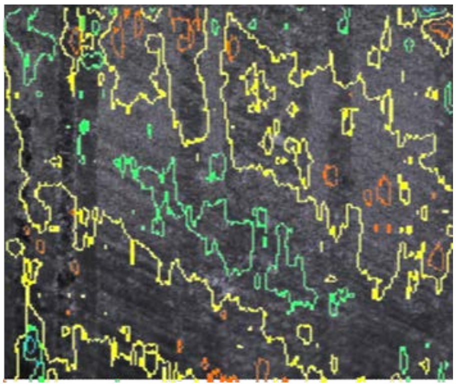

Figure 5-12: Comparison between Matlab elaboration and roughness tester.

5.2.6 CONCLUSIONS

This work made it possible to evaluate the surface roughness of CFRP holes drilled on Al/CFRP stacks to characterize the best processing parameter and study the roughness measurements' reliability inside a composite material.

The surface images of the holes from the microscope and the roughness test were compared to find new, more reliable and faster techniques for studying roughness in composite materials.

In particular, it emerged that:

- The internal roughness depends on the spindle speed rather than the feed rate; parameters with the same spindle speed have similar surfaces.
- The analysis of the surfaces detected under the microscope shows a good correspondence with the roughness tester's images, pushing the research towards new survey techniques.
- 3000 rpm and 0.10 mm/rev and 4500 rpm and 0.05 mm/rev are the best parameters combinations; the holes' surface does not show significant peaks or valleys.
- 6000 rpm and 0.05 mm/rev determine defects. From hole no. 1, they affect the entire surface.
- The most common defect in the surfaces is the matrix's failure, which causes a local increase in roughness. Furthermore, the presence of oblique surfaces due to the cutting of the material is common; this aspect can represent the aim of future studies.

6 STATISTICAL ANALYSIS

Drilling is, therefore, a process by which automation and control are of particular interest in modern industrial evolution.

The opportunity to find an adequate correlation between the acquired sensor data and the quality parameters of the holes established by the aerospace industry is very tempting from a zero-defect production perspective. This would allow greater automation of the drilling process, allowing higher productivity and reducing the percentage of waste, optimising tool replacement strategy based on real-time temperature monitoring and hole quality evaluation. This automation can support developing an "intelligent" factory of the future in the Industry 4.0 framework, where autonomous decision-making systems supported by advanced sensor monitoring of physical processes.

In wear processes, we must focus on reliability problems; that is, the change in quality over time. This type of study is a compromise between instantaneous performances and the ability to keep them at acceptable levels for a sufficiently long time. Therefore, necessary to introduce terms into the method multi-objective to minimise the expected deterioration in performance [86], [87].
Many experiments have to perform and analyse mathematical models to understand the effects of parameters in the machining process.
In this thesis, an approach based on analysis of variance (ANOVA) is used to identify each parameter's contribution in the process.

Moreover, a regression model was developed for correlating the interactions of drilling parameters such as drill bit diameter, spindle speed and feed rate and their effects on responses such as thrust force, torque, temperature and tool wear during drilling of CFRP.

6.1 FIRST ANOVA ANALYSIS

An experimental analysis was conducted to study how the variation of a process or tool parameter affects the quality of the hole.

Tests were conducted with the same tool by varying the cutting parameters and varying the diameter of the tool but keeping the cutting parameters fixed for CFRP/CFRP stacks.

The material is a composite consisting of unidirectional prepreg sheets, with thermosetting epoxy resin matrix and carbon fibres, made using an autoclave manufacturing process according to the following lay-up as shown in **Chapter 2**.

Following the results obtained from the experimental tests, some considerations can be made on how the parameters mutually influence each other in the drilling process.

Two kinds of tools are considered:
- **1** = TTD;
- **2** = ISD.

Two different diameters for each tip:

- **1** = Nominal Diameter Tool 4.9 mm;
- **2** = Nominal Diameter Tool 6.35 mm.

Two different process parameter conditions:

- **1** = Feed rate 0.2 mm /rev; spindle speed 6000 rpm;
- **2** = Feed rate 0.2 mm /rev; spindle speed 7500 rpm.

Experimentally 60 holes were made, and the values of force, torque, temperature, dimensional analysis on the hole of the upper stack, dimensional analysis on the hole of the lower stack, average wear (Vb mean) of the drill bit were calculated for each.
The data distribution is as follows; **Figure 6-1** shows the histogram of the frequencies of the results for force, moment and temperature and an approximation to a gaussian distribution. The mean and standard deviation values for force, torque and temperature are shown on the right.
The number of detections is 56 when it should be 480; this was done to reduce the number of data managed. In fact, all the values of force, moment and temperature for the 60 holes were not taken into the data analysis but for 7 characteristic holes, namely: the first, the tenth, the twentieth, the thirtieth, the fortieth, the fiftieth, the sixty.

Through an Anova analysis performed on the Minitab software, it was possible to understand how by varying the process conditions, the average responses of the parameters vary.

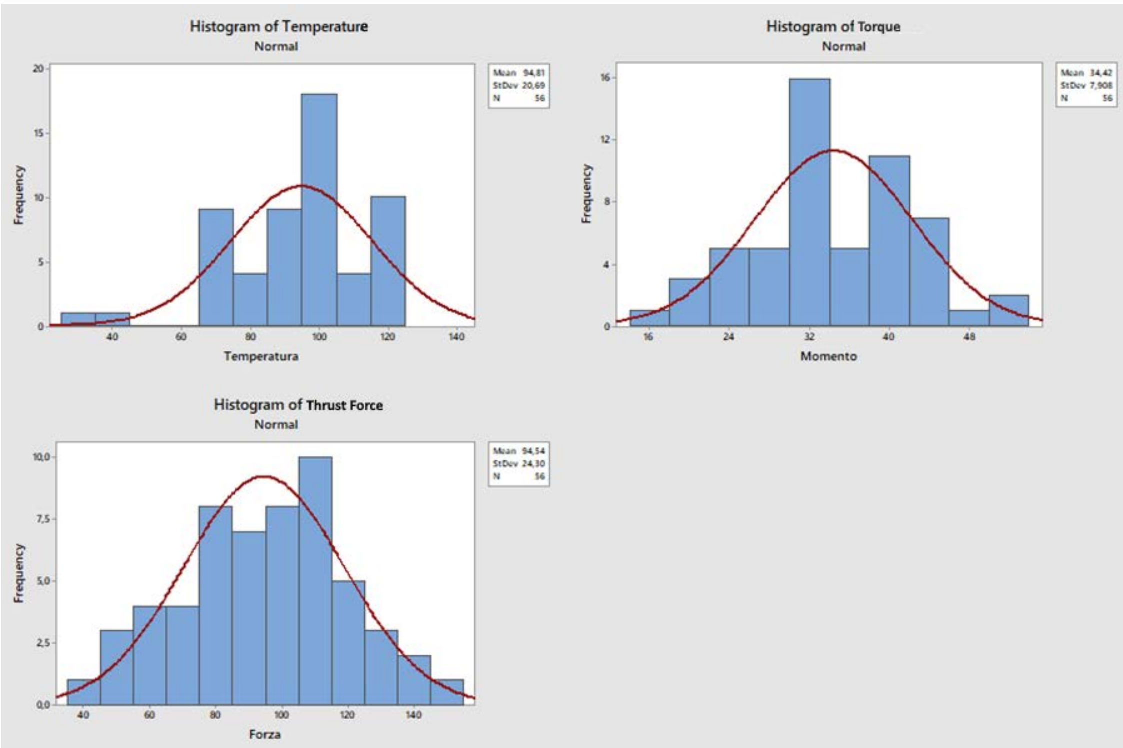

Figure 6-1: Result distribution.

6.1.1 MAIN EFFECT PLOT

The Main Effect Plot function present in the Minitab menu allows us to observe how the variation in the process changes when the parameters change.

It was proceeding with the statistical analysis, it was decided to evaluate which is the best parameter for the chosen tool.

First, consider the thrust force response, shown in **Figure 6-2**. The axial force is very influential on the success of the hole, especially on the wear generated on the tool.

From the study of the graph, it is possible to understand how influential a parameter is; indeed, if there is a greater "gap" between the values 1 and 2, also understood as the angular coefficient of the blue segment, it can be deduced that that parameter is very influential on the response that is being considered.

It can be seen on the left how the average thrust force decreases as the spindle speed is increased from 6000 rpm to 7500 rpm.

By observing the slopes of the segments, how the variation of the parameters of advancement and rotation of the process have a lower impact on the force, since the gap is small, compared to that relating to the geometry of the tool; in fact, using the innovative tip (at parts of spindle speed and feed rate) the average thrust force increases.

On the other hand, the diameter is the parameter that most affects the average response of the detected force; indeed, the average force increases passing from a diameter of 4.9 mm to one of 6.35 mm.

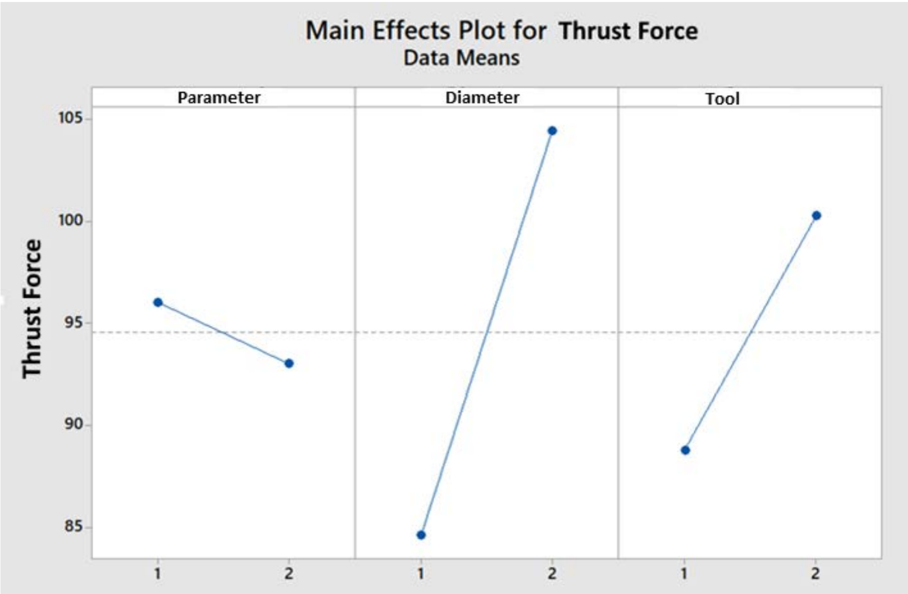

Legend:

Parameter

1= 6000 rpm - 0.2 mm/rev

2= 7500 rpm - 0.2 mm/rev

Diameter

1= 4.9 mm;

2= 6.35 mm;

*fixed 6000 rpm-0.2 mm/rev

Tool

1= TTD;

2= ISD;

*fixed 6000 rpm-0.2 mm/rev

Figure 6-2: Main effect plot for Thrust Force.

Figure 6-3 shows the main effects plot for the torque. The average response is strongly influenced when the tool kind and the diameter are changed (keeping the cutting parameters constant). Passing from a TTD to an ISD, the average torque is lower; instead passing from 4.9 mm to one of 6.35 mm diameter, there is an increase in the torque with a large gap.

The variation of the process parameters does not greatly influence the response.

Figure 6-4 shows the main effect plot for the temperature. It is not very influenced by the change of the tool kind but is very influenced by the variation of the size, passing from the smaller diameter to the larger one, the average temperature is much lower.

Even by changing the process parameters, there is a variation in the response; indeed, using a higher rotation speed shows that the average temperature is lower.

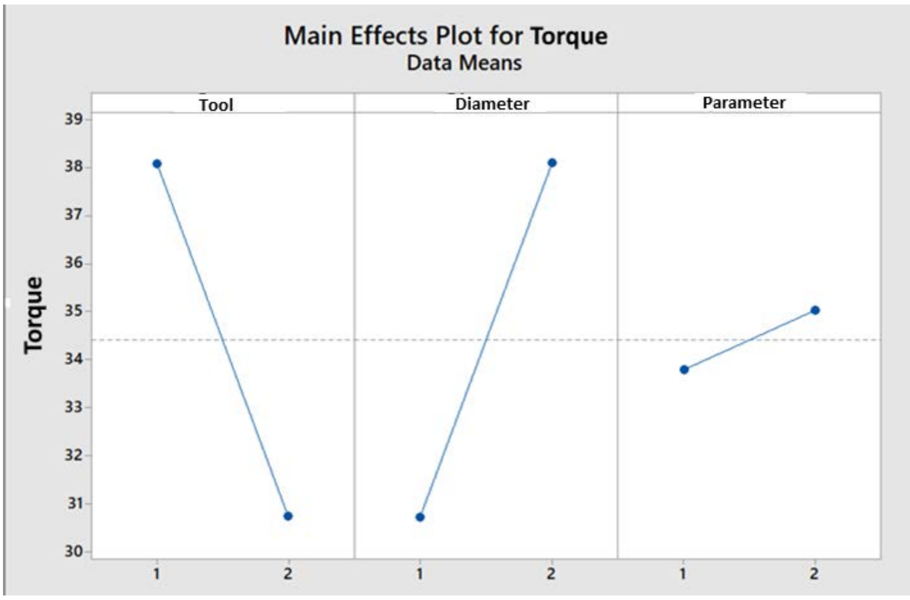

Legend:

Parameter

1= 6000 rpm - 0.2 mm/rev

2= 7500 rpm - 0.2 mm/rev

Diameter

1= 4.9 mm;

2= 6.35 mm;

*fixed 6000 rpm-0.2 mm/rev

Tool

1= TTD;

2= ISD;

*fixed 6000 rpm-0.2 mm/rev

Figure 6-3: Main effect plot for Torque.

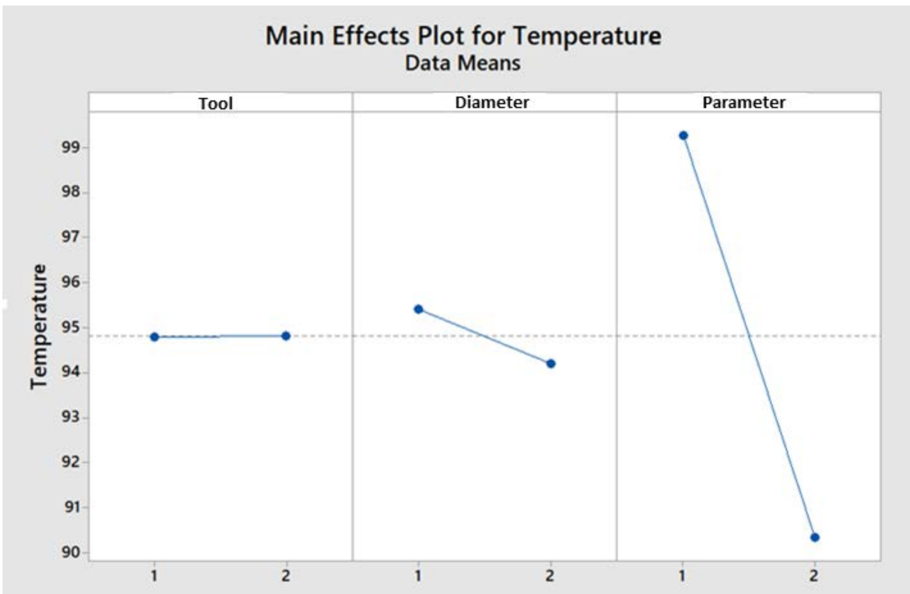

Legend:

Parameter

1= 6000 rpm - 0.2 mm/rev

2= 7500 rpm - 0.2 mm/rev

Diameter

1= 4.9 mm;

2= 6.35 mm;

*fixed 6000 rpm-0.2 mm/rev

Tool

1= TTD;

2= ISD;

*fixed 6000 rpm-0.2 mm/rev

Figure 6-4: Main effect plot for Temperature.

For the dimensional analysis, it is necessary to refer to the measurement on the upper stack and the one on the lower stack; indeed, the experimental tests were carried out by drilling two superimposed specimens to simulate the real drilling conditions in the aeronautical field.

As has been said previously, the tight tolerances in the aeronautical field on the holes push to find optimal parameters that make the hole closer to the project's nominal conditions. The nominal hole conditions are considered an ideal hole diameter of 4.9 mm when drilling with a 4.9 mm drill and an ideal diameter of 6.35 mm when drilling with a 6.35 mm drill.

The considerations will then be treated separately, first studying the dimensional analyses on the hole with a smaller diameter and a larger diameter.

Figure 6-5 shows that the change of parameters does not affect the average response, unlike the tool kind, which instead influences the average response; using an ISD, indeed, the results are on average closer to the ideal diameter that has been set and therefore the drilling process is dimensionally more precise.

If it is considered the hole with the larger diameter, shown in **Figure 6-6**, for both stacks, by switching to the ISD, it is moved away from the ideal conditions of 6.35 mm; the change of parameters, in this case, for the upper stack does not involve differences on the average results. For the lower stack, the increase in the spindle speed shifts the average of the results closer to the target value.

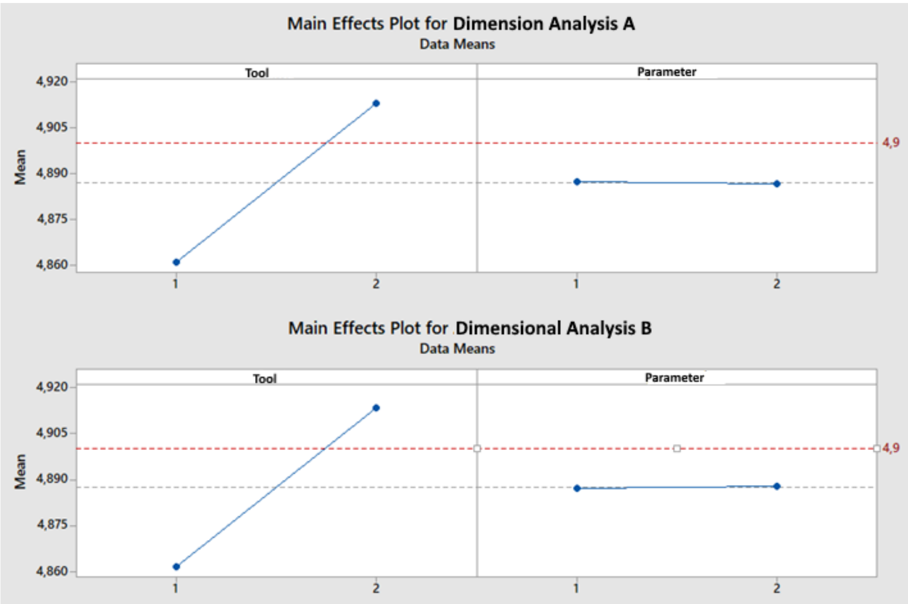

Legenda:

Parameter

1= 6000 rpm - 0.2 mm/rev

2= 7500 rpm - 0.2 mm/rev

Tool

1= TTD; 6000 rpm - 0.2 mm/rev

2= ISD; 6000 rpm - 0.2 mm/rev

Figure 6-5: Main effect plot for dimension analysis for the tool with nominal diameter 4.9 mm.

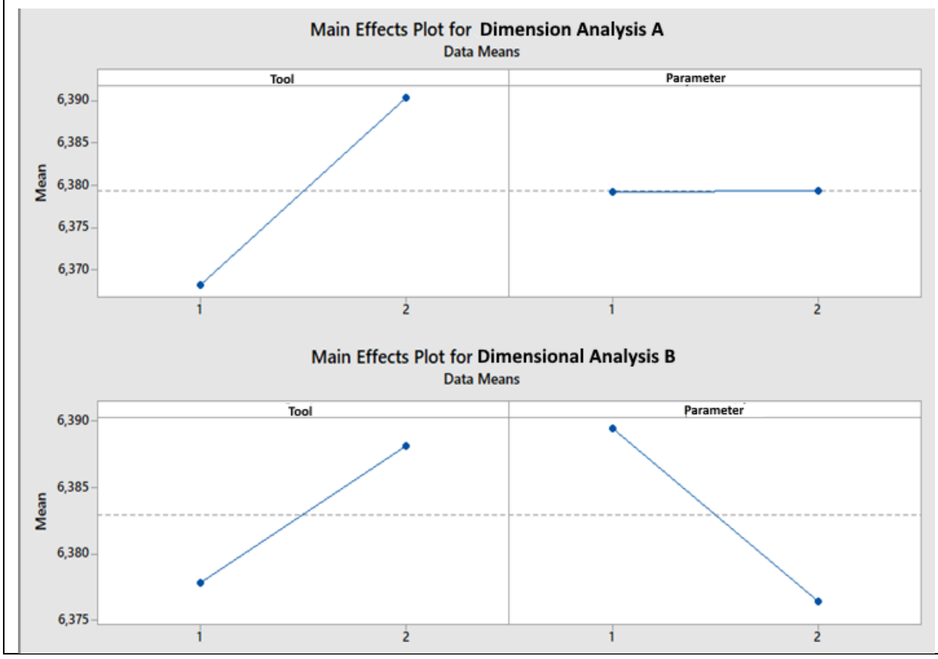

Legenda:

Parameter

1= 6000 rpm - 0.2 mm/rev

2= 7500 rpm - 0.2 mm/rev

Tool

1= TTD; 6000 rpm - 0.2 mm/rev

2= ISD; 6000 rpm - 0.2 mm/rev

Figure 6-6: Main effect plot for dimension analysis for the tool with nominal diameter 6.35 mm.

The consideration made for the diameter variation is better visible in Figure 6-7, where it is shown how the results are distributed; the dotted lines represent the ideal conditions of the holes that have imposed themselves equal to 4.9 mm and 6.35 mm.

The variability of the points associated with the tool change and the process parameters is low; this can be understood from the almost perfectly horizontal lines.

Therefore, it deduced that the change in diameter is not very influential. The considerations made for the upper stack are the same as those for the lower; indeed, the lines that join the results referring to both stacks are superimposable.

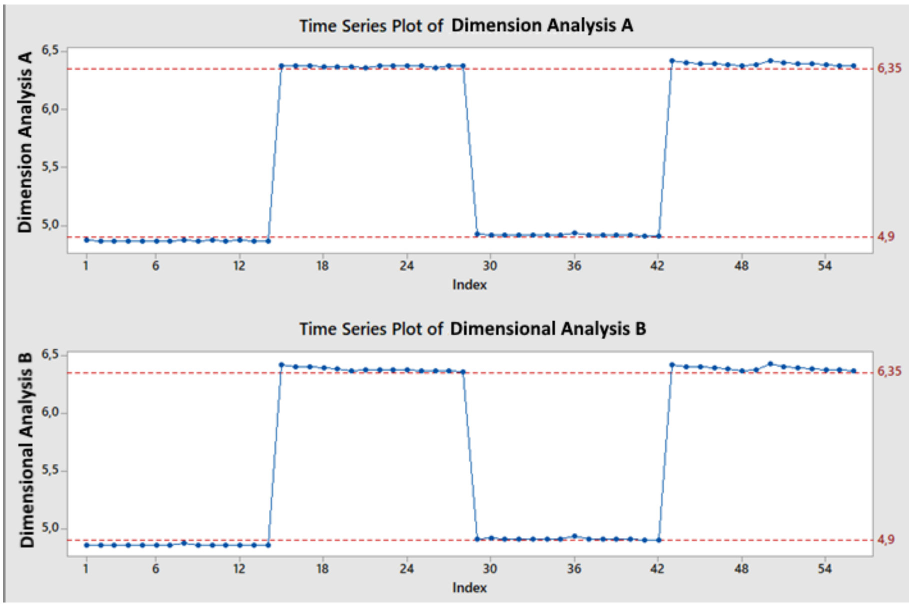

Figure 6-7: Time series plot for dimension analysis.

6.1.2 INTERVAL PLOT

Interval Plot, an additional Minitab function, is used to evaluate the best tool for the process for the chosen parameters. This function allows us to see simultaneously as the parameters vary where the average value of the output in question is found and how wide the interval is in which the result is distributed. Through this function, it will be possible to see the various combinations of parameters simultaneously and, through the average, understand which is the best.

On the abscissa, it is possible to observe how the various parameters can be combined while on the ordinates, the average value of the reliefs considering the parameter in question.

Through the width of the blue segment, it is possible to estimate the maximum and minimum value for each parameter.

It was made considerations for the temperature, force and torque outputs.

From the analysis of Figure 6-8, it is possible to see that the lowest average value for the temperature is obtained when using a TTD with a diameter of 6.35 mm with process parameters of 0.2 mm / rev and spindle speed of 7500 rpm; it is also seen that the maximum temperature reached in the reliefs is also the lowest.

When working with composite materials, we are interested in keeping temperatures low as temperature peaks can damage the resin matrix; therefore, looking at Figure 6-8, the innovative tip gave the worst results when for parameters of 0.2 mm/rev and spindle speed equal to 6000 rpm.

In this case, both with a diameter of 4.9 mm and 6.35 mm, the average temperatures reached during the drilling process are the highest values; in particular when the 4.9 mm drill was used with a feed of 0.2 mm/rev and a spindle speed equal to 7500 rpm the maximum peak temperature of almost 140°C has been reached.

The TTD performed better with the diameter with both diameters and with both process conditions.

As for the torque, Figure 6-9 can be observed.

The ISD performs well both using the 4.9 mm and 6.35 mm diameter; with both process conditions, there are low average values and contained peaks.

The TTD performs worse with 6.35 mm diameter; there are much higher averages, particularly with a feed rate of 0.2 mm/rev and a spindle speed of 6000 rpm where the maximum peak is approximately 52.5 Nm. However, the TTD performs better when using the 4.9 mm diameter; in this case, results are comparable with those of the ISD with both process conditions.

Finally, considering the force, shown in Figure 6-10; the average values are similar, but you can see how the TTD with a diameter of 4.9 mm and with a feed rate of 0.2 mm/rev and a spindle speed of 6000 rpm and the ISD with a diameter of 6.35 mm and a feed rate of 0.2 mm / rev and spindle speed of 7500 rpm gave the worst results.

In both cases, the force generated on average is high, and in these circumstances, high peaks of force equal to about 135 N.

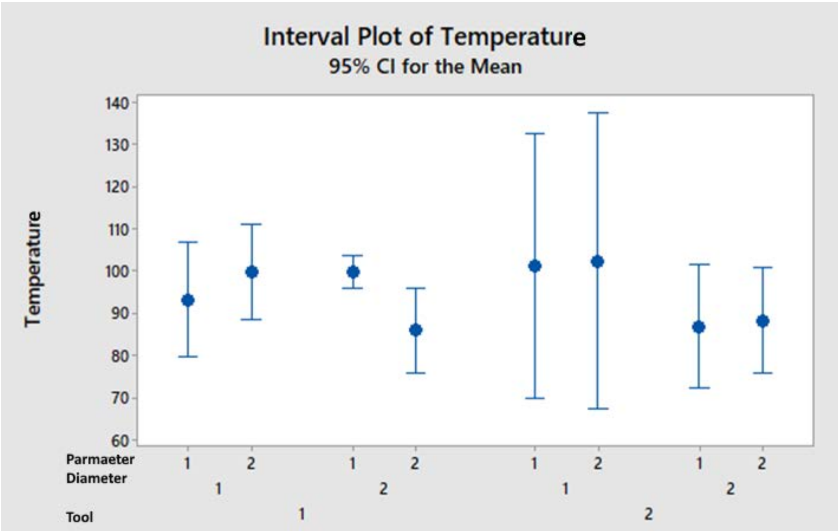

Legend:

Parameter

1= 6000 rpm - 0.2 mm/rev

2= 7500 rpm - 0.2 mm/rev

Diameter

1= 4.9 mm;

2= 6.35 mm;

Tool

1= TTD;

2= ISD;

Figure 6-8: Interval plot of temperature.

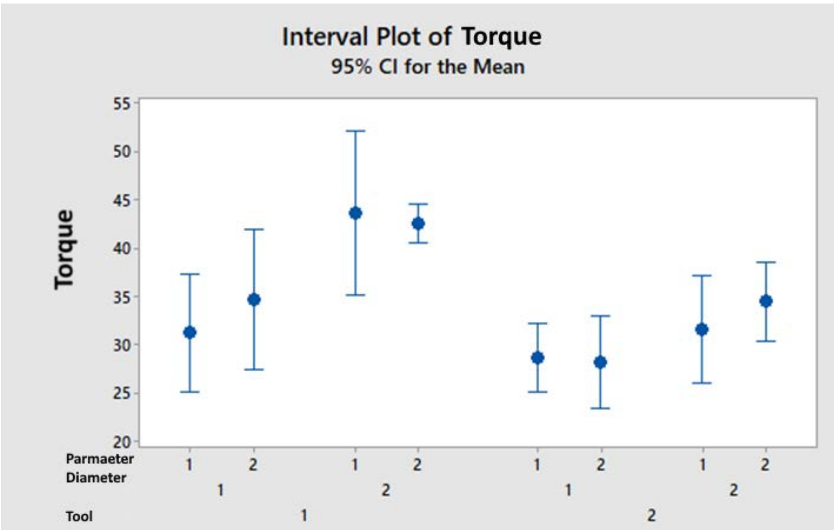

Legend:

Parameter

1= 6000 rpm - 0.2 mm/rev

2= 7500 rpm - 0.2 mm/rev

Diameter

1= 4.9 mm;

2= 6.35 mm;

Tool

1= TTD;

2= ISD;

Figure 6-9: Interval plot of torque.

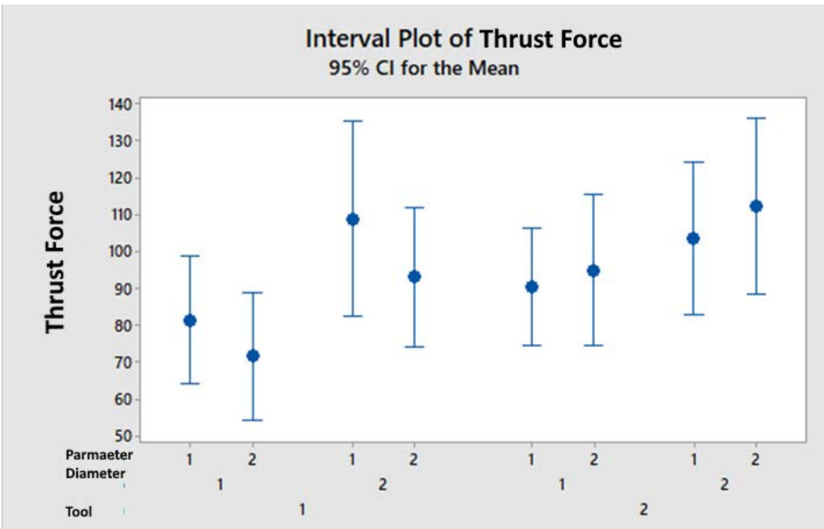

Legend:

Parameter

1= 6000 rpm - 0.2 mm/rev

2= 7500 rpm - 0.2 mm/rev

Diameter

1= 4.9 mm;

2= 6.35 mm;

Tool

1= TTD;

2= ISD;

Figure 6-10: Interval plot of thrust force.

6.1.3 INTERACTION PLOT

Through the Interaction Plot function, it is possible to understand the interaction between factors having force, torque and temperature as output parameters.

If there are parallel lines, there is no interaction between the factors; if there are segments with a great slope, there is a strong interaction.

For the thrust force, shown in **Figure 6-11**, the variation of the process parameters differently influences the kind tool, particularly in the TTD by increasing the spindle speed, the force decreases and in the ISD, on the contrary, the force increases.

Also, as regards the temperature, in **Figure 6-12**, the tool interacts differently with the parameters; indeed, by increasing the spindle speed, the TTD increases in temperature while the ISD reaches significantly lower temperature peaks.

In conclusion, it can be stated after a critical analysis that the traditional drill performs better for these drilling parameters, in particular, the 4.9 mm drill with a feed speed of 0.2 mm/rev and spindle speed of 6000 rpm. This tool provides better results in terms of maximum temperature reached, force and moment generated.

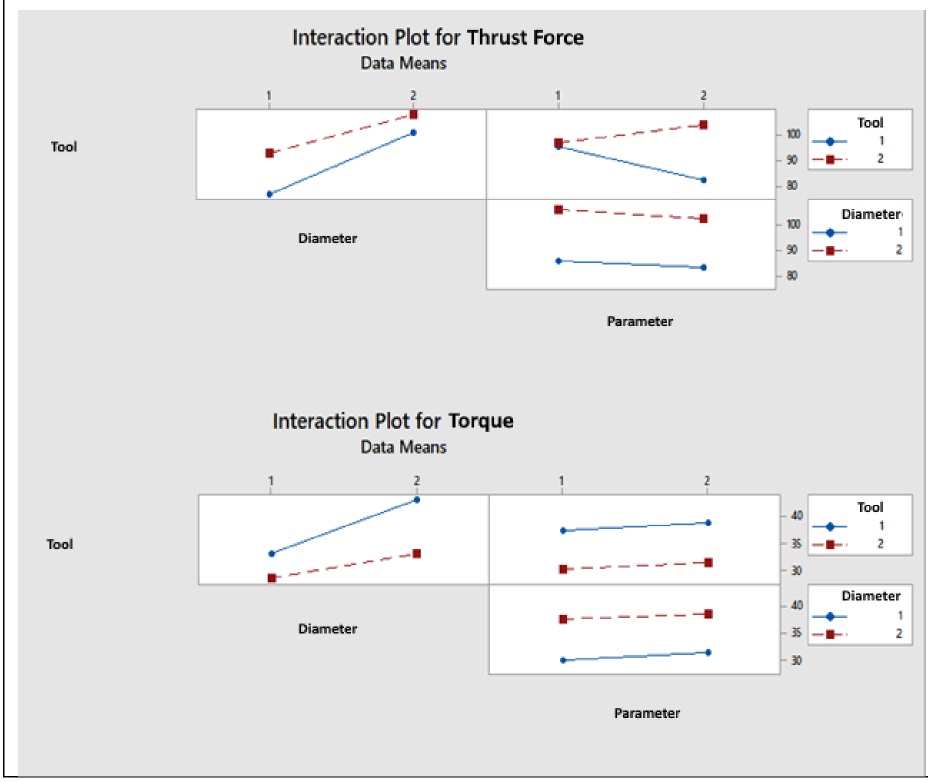

Legend:

Parameter

1= 6000 rpm - 0.2 mm/rev

2= 7500 rpm - 0.2 mm/rev

Diameter

1= 4.9 mm;

2= 6.35 mm;

*fixed 6000 rpm-0.2 mm/rev

Tool

1= TTD;

2= ISD;

*fixed 6000 rpm-0.2 mm/rev

Figure 6-11: Interaction plot for thrust force.

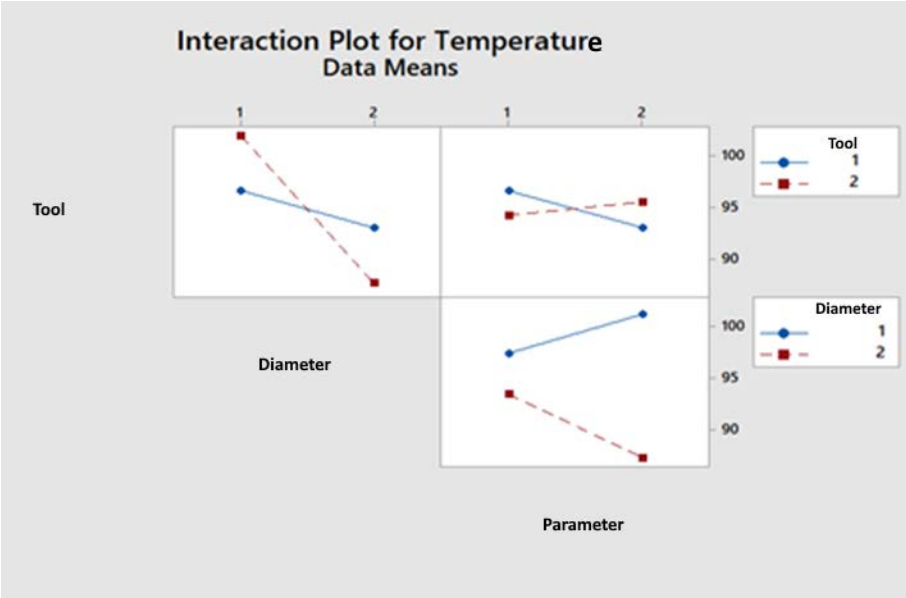

Legend:

Parameter

1= 6000 rpm - 0.2 mm/rev

2= 7500 rpm - 0.2 mm/rev

Diameter

1= 4.9 mm;

2= 6.35 mm;

*fixed 6000 rpm-0.2 mm/rev

Tool

1= TTD;

2= ISD;

*fixed 6000 rpm-0.2 mm/rev

Figure 6-12: Interaction plot for temperature.

6.2 SECOND ANOVA ANALYSIS: A GEOMETRY STUDY

The next step was to fix geometry and analyse the behaviour as the drilling parameters change.

In particular, it was chosen as the reference tool, TTD with a diameter of 6.35 mm, while it was decided to change both the feed rate and the spindle speed.

Following the results obtained from the experimental tests, some considerations can be made on how the parameters mutually influence each other in the drilling process.

Two different feed rate are considered:

- **1** = 0.11 mm/rev;
- **2** = 0.15 mm/rev.

Three different spindle speed conditions:

- **1** = 6000 rpm;
- **2** = 7500 rpm;
- **3** = 9000 rpm.

Also, in this case, the choice of parameters was made to simulate the real drilling conditions on the aeronautical panels.

This study aims to understand, starting from the data obtained thanks to the experimental campaign, which are the optimal process conditions for the kind tool chosen.

Sixty holes were made experimentally and calculated for each:

• the values obtained from the sensory data of thrust force and torque;

• tool wear understood as Vb mean;

• the average dimensional analysis (understood as the average of the measurement on the hole of the upper and lower stack);

• delamination (understood as the ratio between the maximum diameter of the delaminated area and the nominal design diameter of the hole D_{max} / $D_{nominal}$).

Also, in this case, not all the values for 60 holes were considered but for 7 characteristic holes, namely: the first, the tenth, the twentieth, the thirtieth, the fortieth, the fiftieth and sixty. For this study, we will use the same Minitab functions used in the first ANOVA analysis.

6.2.1 MAIN EFFECT PLOT

The Main Effect Plot function present in the Minitab menu allows us to observe how the variation in the process changes when the parameters change.

Figure 6-13 and Figure 6-14 show the change in the feed rate has a greater impact on the thrust force; indeed, while the increase in the feed rate does not affect the average response for the torque, this increase generates a significant increase in the average thrust force.

Also, there is a different response; for the thrust force, the increase in rpm of the spindle speed is negative, while for the torque, this variation is positive.

Moreover, the variation from 2700 rpm to 6000 rpm generates a negligible change in measured average thrust force compared to the passage from 6000 rpm to 9000 rpm.

For the torque, on the contrary, it is the variation from 2700 rpm to 6000 rpm that affects a lot (large range); in particular, there is a moment that on average is much smaller.

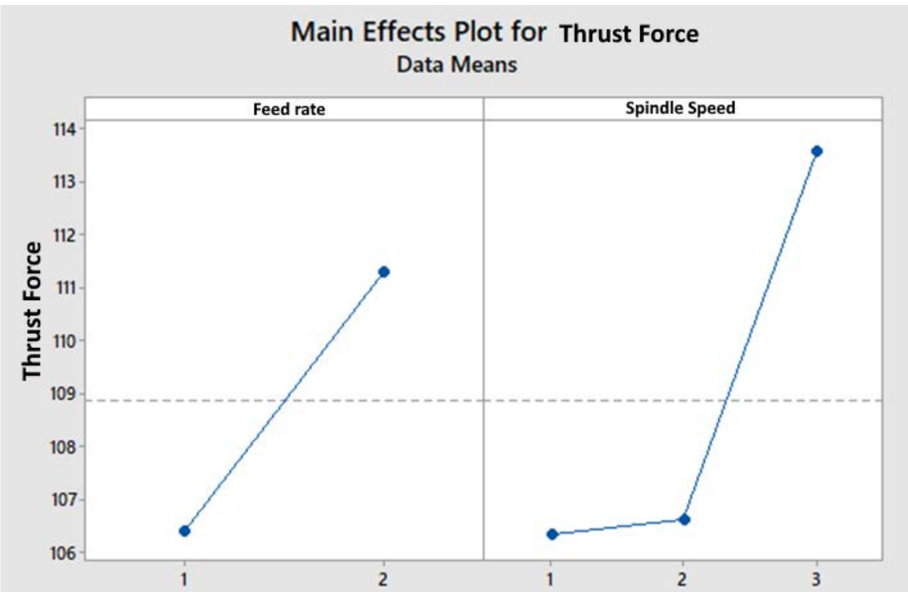

Legend:

Feed rate

1= 0.11 mm/rev

2= 0.15 mm/rev

*fixed 2700 rpm

Spindle speed

1= 2700 rpm

2= 6000 rpm

3= 9000 rpm

*fixed 0.11 mm/rev

Figure 6-13: Main effect Plot for Thrust Force.

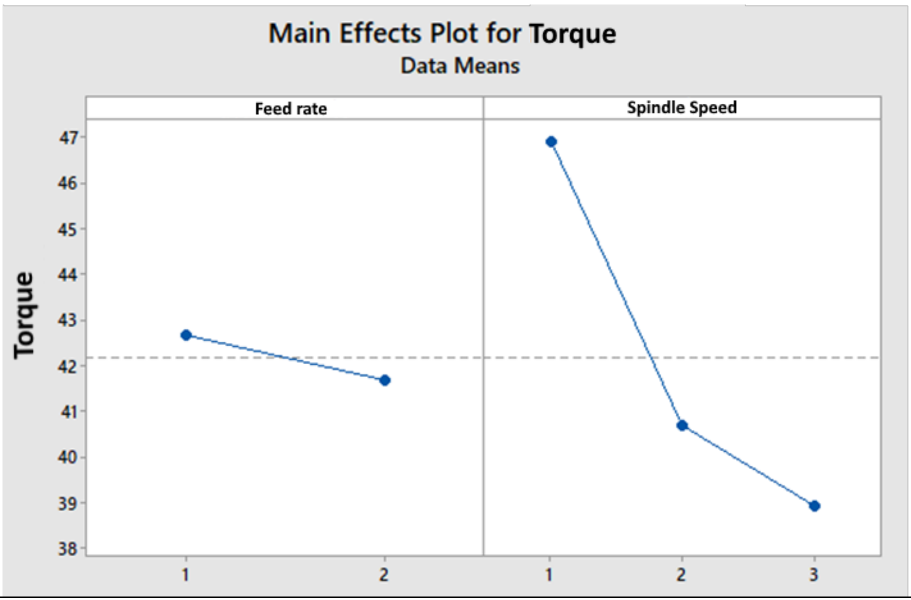

Legend:

Feed rate

1= 0.11 mm/rev

2= 0.15 mm/rev

*fixed 2700 rpm

Spindle speed

1= 2700 rpm

2= 6000 rpm

3= 9000 rpm

*fixed 0.11 mm/rev

Figure 6-14: Main effect Plot for Torque.

6.2.2 INTERVAL PLOT

The Interval Plot function allows us to view the average values and distribution intervals of the results for all combinations of feed rates and rotations. This function is used for the analysis of thrust force and torque for the TTD.

Figure 6-15 shows that the average forces recorded for the holes are higher with a rotation of 9000 rpm; in particular, with a feed of 0.11 mm/rev, there are very high peaks of the force of about 150N.

The force is, on average lower for the holes that have been made with 2700 rpm and 0.11 mm/feed rate; even the peaks are contained; in terms of strength, this is the most suitable process parameter for this tool type.

Figure 6-16 shows that the average torque recorded for the holes are higher for a rotation of 2700 rpm; in particular, with a feed of 0.15 mm/rev, high values are obtained for some holes of about 60 Nm.

The torque, on average, as expected, is lower for higher rotations; the peaks are also contained for both 6000 rpm and 9000 rpm.

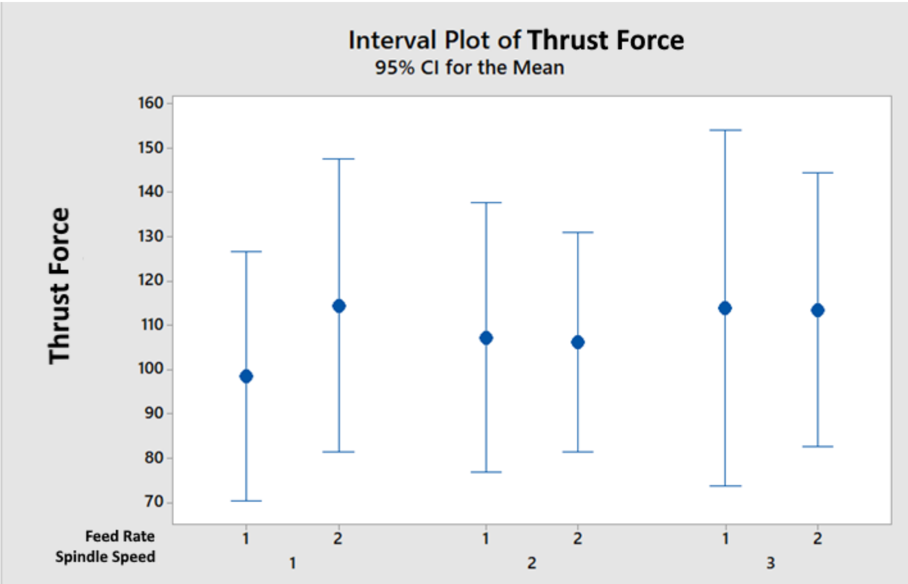

Legend:

Feed rate

1= 0.11 mm/rev

2= 0.15 mm/rev

Spindle speed

1= 2700 rpm

2= 6000 rpm

3= 9000 rpm

Figure 6-15: Interval Plot of thrust force.

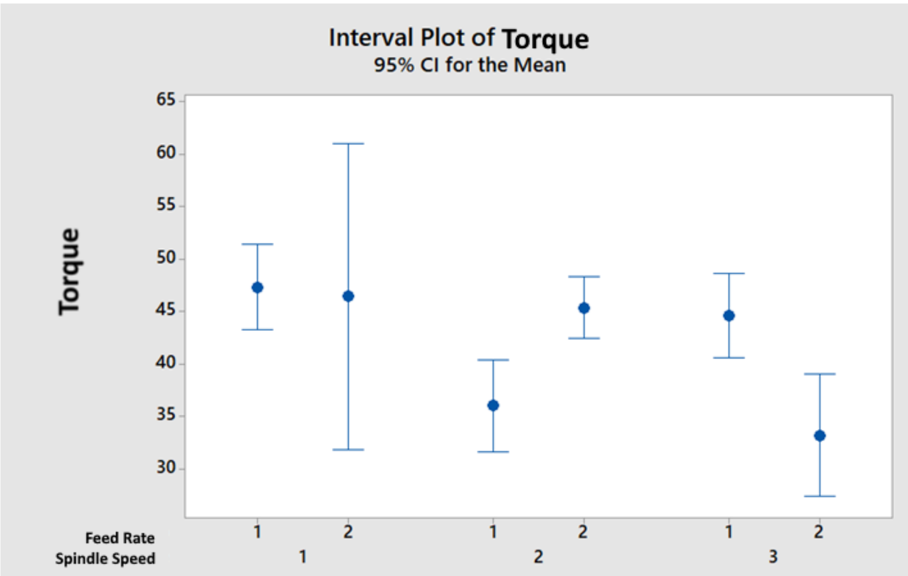

Legend:

Feed rate

1= 0.11 mm/rev

2= 0.15 mm/rev

Spindle speed

1= 2700 rpm

2= 6000 rpm

3= 9000 rpm

Figure 6-16: Interval Plot of torque.

6.2.3 INTERACTION PLOT

It was once again used Minitab function: Interaction Plot. It is to understand how the feed rate and spindle speed influence each other using the average force and the average torque as a target.

For the thrust force, the average response for 6000 rpm and 9000 rpm does not change as the feed rate varies, unlike when there is a process with a low rotation speed; in this case, considering 2700 rpm, the parameters influence each other very much.

It can be seen from Figure 6-17 that in the case of 2700 rpm, the increase in the feed rate greatly affects the response. In particular, it generates an increase in the axial force of more than 10%.

Regarding the moment for low rotations, as shown in Figure 6-18, the response is not affected by the change in forwarding speed, while with rotation speeds of 6000 rpm and 9000 rpm, there are different trends.

For the rotation of 6000 rpm, an increase in speed from 0.11 mm/rev to 0.15 mm/rev is positive in terms of the moment; the average response is indeed more contained, while for the rotation of 9000 rpm, the behaviour is completely opposite.

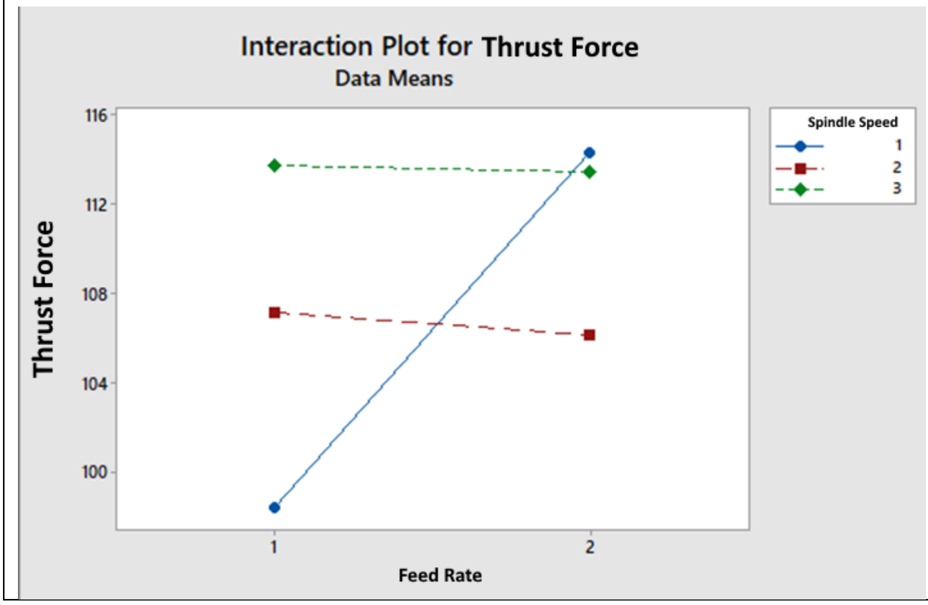

Legend:

Feed rate

1= 0.11 mm/rev

2= 0.15 mm/rev

Spindle speed

1= 2700 rpm

2= 6000 rpm

3= 9000 rpm

Figure 6-17: Interaction plot of thrust force.

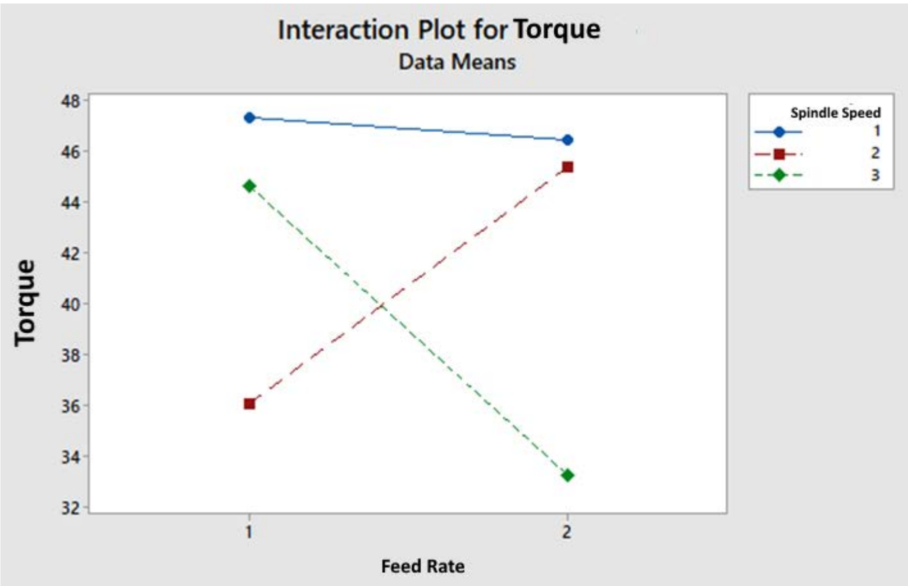

Legend:

Feed rate

1= 0.11 mm/rev

2= 0.15 mm/rev

Spindle speed

1= 2700 rpm

2= 6000 rpm

3= 9000 rpm

Figure 6-18: Interaction plot of torque.

6.3 THIRD ANOVA ANALYSIS: HOLE QUALITY

After focusing on the force and moment generated in the process, we will go on to make considerations purely on the quality of the hole and the goodness of the process.

As control parameters for the quality of the hole, consider:

• **Delamination**: expressed as the ratio between the maximum diameter of the delaminated area and the nominal diameter of the hole.

• **Hole size**: fundamental parameter when you want to ensure that a hole is within the design tolerance range.

• **Roundness**: it is expressed as the ratio between the maximum diameter measured and the minimum diameter.

Instead, the average tool wear is considered a goodness parameter process, calculated as explained in the previous chapter.

In this way, we will study how the average responses of these control parameters vary with the variation of the process conditions, which are once again:

Two different feed rate are considered:

- **1** = 0.11 mm/rev;
- **2** = 0.15 mm/rev.

Three different spindle speed conditions:

- **1** = 6000 rpm;
- **2** = 7500 rpm;
- **3** = 9000 rpm.

The considerations made, in this case, are for a fixed geometry, TTD, with a nominal diameter of 6.35 mm.

6.3.1 ROUNDNESS ANALYSIS

It was analysed the circularity of the hole with Minitab's Main Effect Plot.

As the roundness has been expressed, the closer we get to the '1' value, the more drilling process will guarantee a roundness hole.

Therefore, **Figure 6-19** shows that as the feed speed increases, there are more oval holes.

The best condition in terms of rotation speed is 6000 rpm.

The Interaction Plot in **Figure 6-20** shows the advancement and rotation parameters interact on the roundness output.

When using rotations of 2700 and 6000 rpm, the increase in feed rate has a negative impact as more oval holes are obtained; on the contrary, with 9000 rpm, the increase in feed speed makes the holes on average more round.

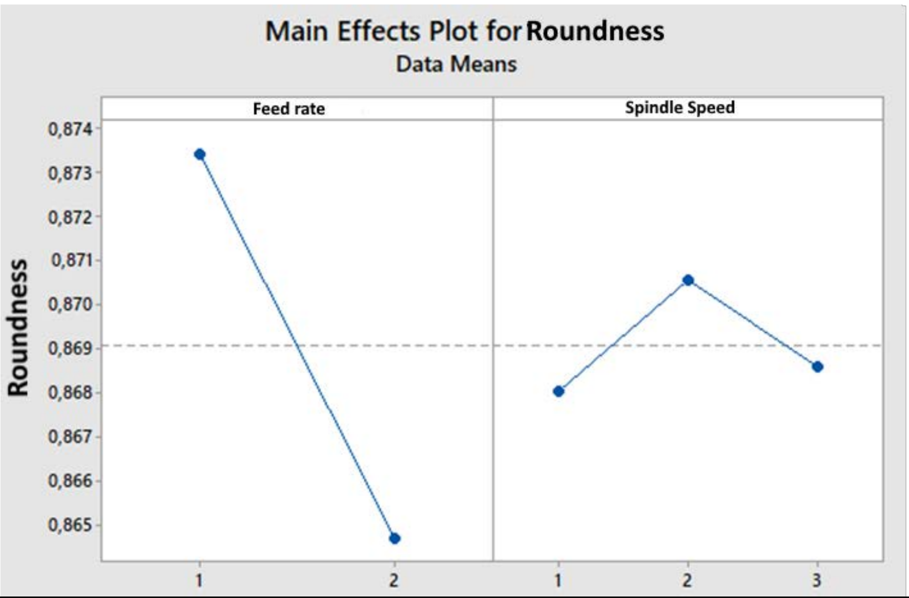

Legend:

Feed rate

1= 0.11 mm/rev - 2700 rpm

2= 0.15 mm/rev - 2700 rpm

Spindle speed

1= 2700 rpm - 0.11 mm/rev

2= 6000 rpm - 0.11 mm/rev

3= 9000 rpm - 0.11 mm/rev

Figure 6-19: Main Effects Plot for roundness.

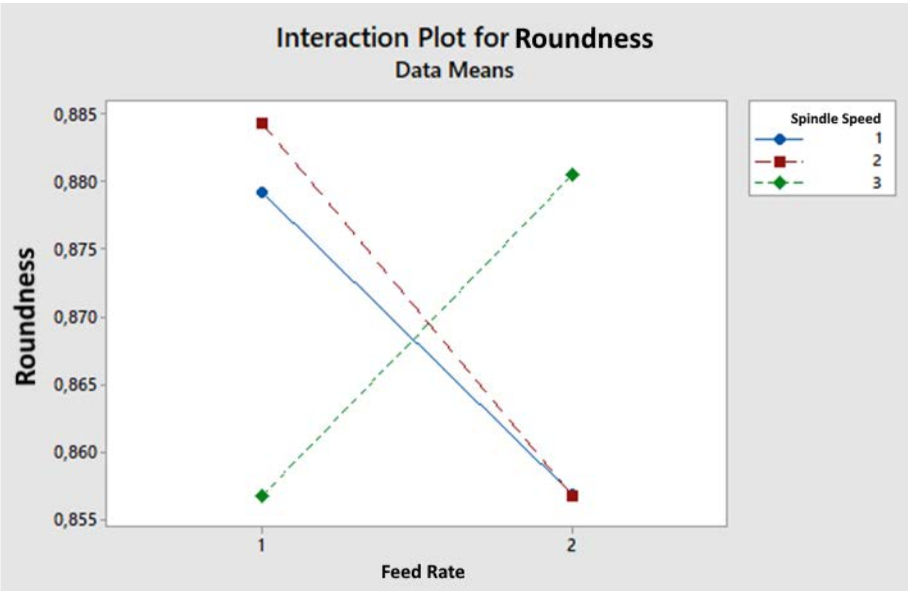

Legend:

Feed rate

1= 0.11 mm/rev - 2700 rpm

2= 0.15 mm/rev - 2700 rpm

Spindle speed

1= 2700 rpm - 0.11 mm/rev

2= 6000 rpm - 0.11 mm/rev

3= 9000 rpm - 0.11 mm/rev

Figure 6-20: Interaction plot for roundness.

6.3.2 DELAMINATION ANALYSIS

Delamination behaves in the opposite way to circularity; in fact, the extension of the delaminated area decreases if the feed speed increases from 0.11 mm/rev to 0.15 mm/rev, as shown in **Figure 6-21**.

For 6000 rpm, where the best holes were obtained for roundness, there are the worst damage responses at the outlet.

The delaminated area, indeed, for this configuration is, on average, much larger than when working with 2700 rpm and 9000 rpm.

Through the Interaction Plot, shown in **Figure 6-22**, it can be seen how the drilling process performed with 6000 rpm is strongly influenced by the change of feed speed; in particular, it is evident that for a feed speed of 0.11 mm/rev, a delaminated area which on average is more than 10 times the nominal diameter.

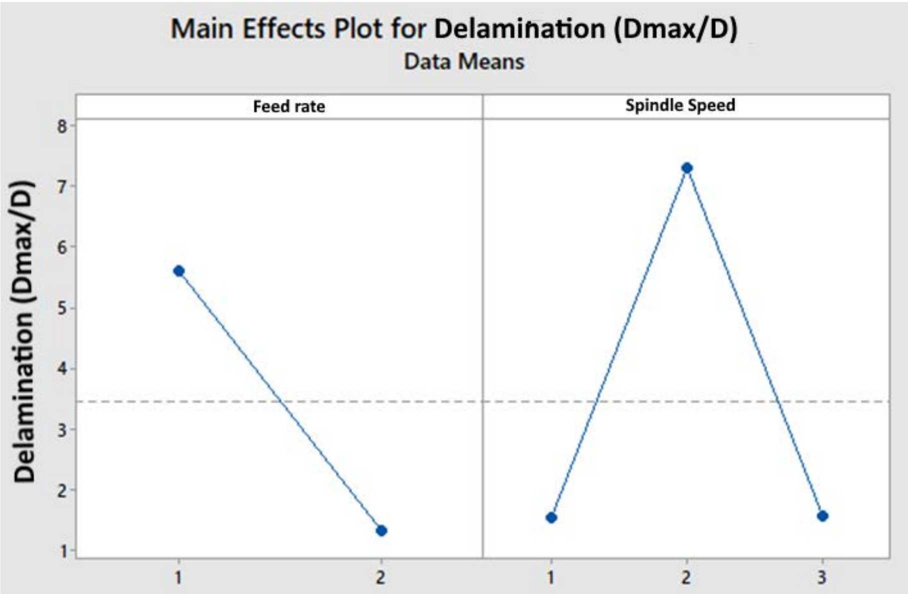

Legend:

Feed rate

1= 0.11 mm/rev - 2700 rpm

2= 0.15 mm/rev - 2700 rpm

Spindle speed

1= 2700 rpm - 0.11 mm/rev

2= 6000 rpm - 0.11 mm/rev

3= 9000 rpm - 0.11 mm/rev

Figure 6-21: Main effects for delamination (Dmax/D).

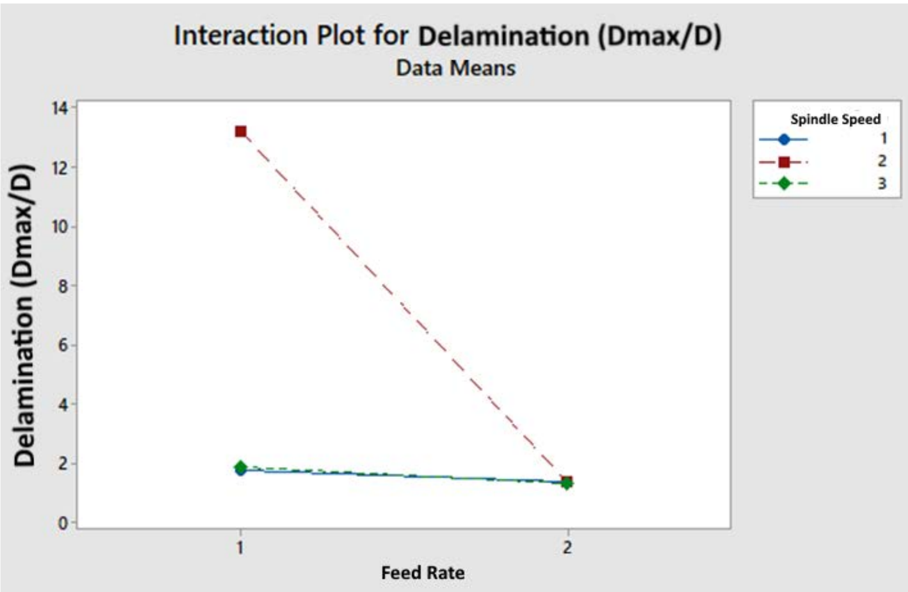

Legend:

Feed rate

1= 0.11 mm/rev

2= 0.15 mm/rev

Spindle speed

1= 2700 rpm

2= 6000 rpm

3= 9000 rpm

Figure 6-22: Interaction plot for delamination (Dmax/D).

6.3.3 DIMENSIONAL HOLE ANALYSIS

Now consider the means of the holes; the measure reported refers to the arithmetic mean between the upper and lower stack measures. Remember that the reference value for the ideal hole is 6.35 mm.

With a feed rate of 0.11 mm/rev, the holes are on average more precise since, as shown in Figure 6-23, it is close to the nominal conditions; drilling with higher speed results in lower accuracies.

When the effect of the spindle speed is taken into consideration, there is a parabola trend with an upward concavity; it can therefore be stated that the optimum process is obtained with intermediate rotation speeds corresponding to 6000 rpm, in such circumstances have holes that on average are closer to the nominal conditions.

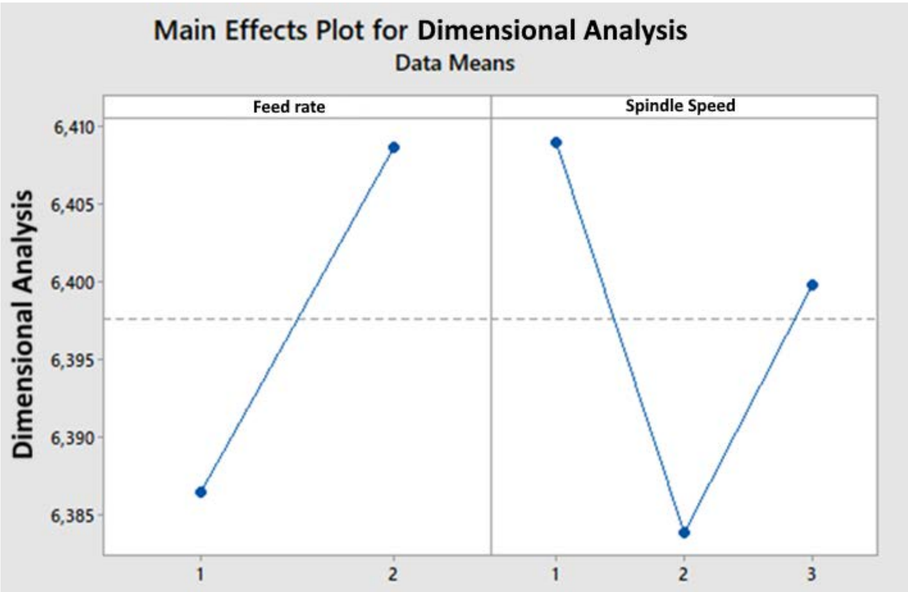

Legend:

Feed rate

1= 0.11 mm/rev - 2700 rpm

2= 0.15 mm/rev - 2700 rpm

Spindle speed

1= 2700 rpm - 0.11 mm/rev

2= 6000 rpm - 0.11 mm/rev

3= 9000 rpm - 0.11 mm/rev

Figure 6-23: Main effects plot for dimensional analysis.

6.3.4 TOOL WEAR ANALYSIS

Finally, it is focused on the wear of the tip.

Figure 6-24 shows how the average tool wear decreases on average when it goes from 0.11 mm/rev to 0.15 mm/rev, while wear is on average more thrust when using the spindle speed equal to 6000 rpm.

Thanks to the Interaction Plot, shown in Figure 6-25 how for higher rotations, 6000 and 9000 rpm, the increase in the feed rate has a positive effect, and indeed the wear is better. Therefore, to obtain less wear during a drilling process, if there is a low spindle speed, a low feed speed must also be set.

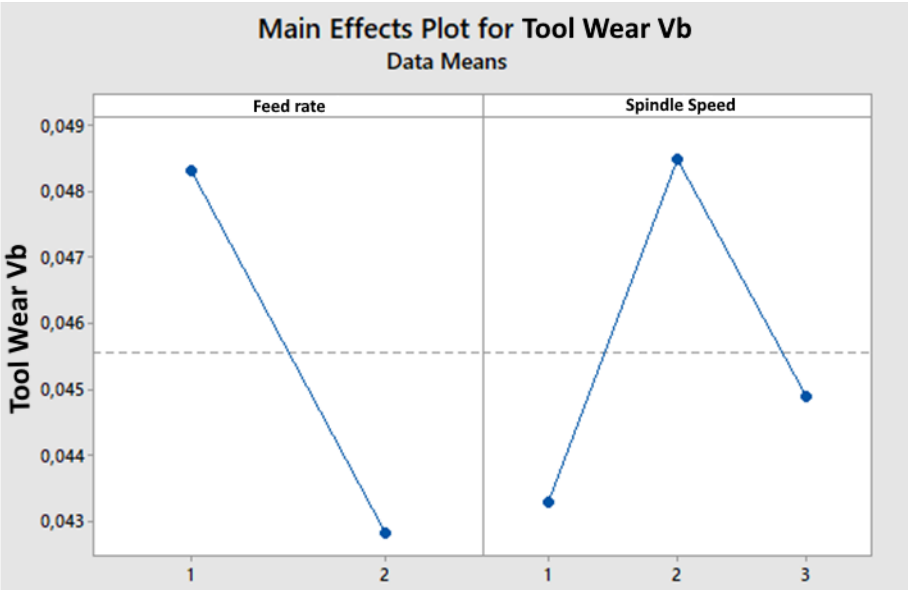

Legend:

Feed rate

1= 0.11 mm/rev - 2700 rpm

2= 0.15 mm/rev - 2700 rpm

Spindle speed

1= 2700 rpm - 0.11 mm/rev

2= 6000 rpm - 0.11 mm/rev

3= 9000 rpm - 0.11 mm/rev

Figure 6-24: Main effects plot for tool wear VB.

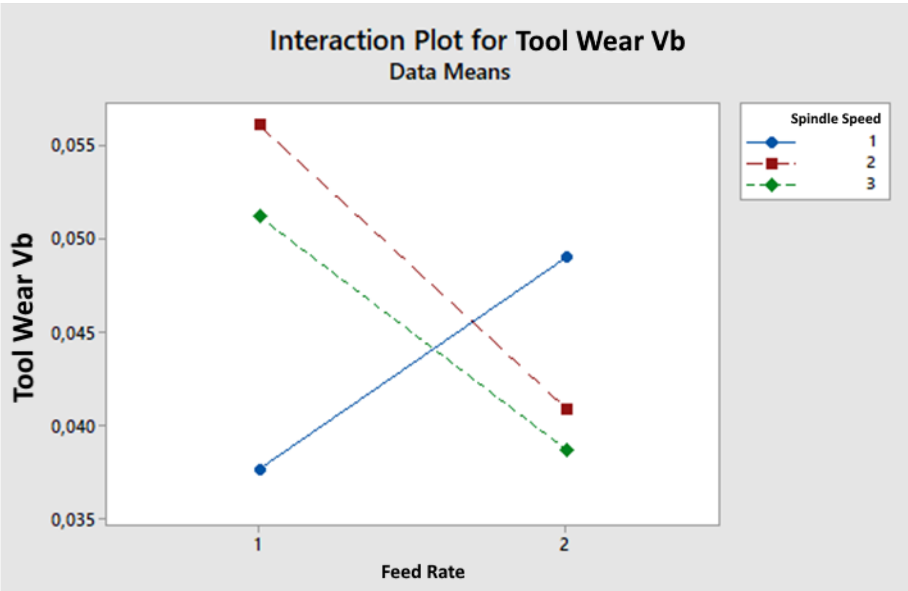

Legend:

Feed rate

1= 0.11 mm/rev - 2700 rpm

2= 0.15 mm/rev - 2700 rpm

Spindle speed

1= 2700 rpm - 0.11 mm/rev

2= 6000 rpm - 0.11 mm/rev

3= 9000 rpm - 0.11 mm/rev

Figure 6-25: Interaction plot for tool wear VB.

6.4 MODEL OF LINEAR REGRESSION FOR THE ESTIMATION OF TOOL WEAR

Regression is a statistical method that allows us to predict the estimated value of a dependent variable given the values of one or more independent variables. In particular, if the relationship is established by a straight line, then the regression is said to be simple linear; if the number of independent variables is more than one, the regression is called multiple.

This statistical method is very useful, but it is also dangerous because it can give answers that do not approximate real behaviours.

In mathematical terms, multiple linear regression assumes a model like the following in Eq. 6-1:

$$\hat{y} = \beta_0 + \beta_1 x_1 + \beta_2 x_2 + \cdots + \beta_n x_n \quad \text{Eq. 6-1}$$

Where:

$\hat{y}$ is the response to the values; it represents the result predicted by the model;

β_0 is the intercept, that is, the value of $\hat{y}$ when the xi are all equal to 0;

β_1 is the coefficient of X1 (the first characteristic);

β_n is the coefficient of Xn (the nth characteristic);

$x_1, x_2 \dots \dots, x_n$ are the independent variables of the model.

The equation explains the relationship between a continuous dependent variable (ŷ) and two or more independent variables ($x_1, x_2 \dots \dots, x_n$). Betas are real numbers and are called the estimated regression coefficients of the model. Note that y is a continuous dependent variable since being the sum of real numbers, it results to be a real number.

Multiple regression analysis is a method used to identify the strength of the effect that independent variables have on a dependent variable.

Understanding how much the dependent variable will change when independent variables are changed allows us to predict the effects or impacts of changes in real situations. Of course, this does not mean that we will know what will happen.

Multiple linear regression is experiencing greater interest in machine learning and artificial intelligence as it allows to obtain performing learning models even in the case of many records to be analyzed.

It was decided to exploit a linear regression model to estimate the tool's behaviour and the material during processing.

As seen, the wear estimate is very difficult and slow as the tip must be extracted from the drill and analysed with the Tesa Visio V-200 optical measuring machine system.

Due to this practical impossibility of measurement, in companies that carry out mechanical processes such as drilling, the tool is changed not after the wear threshold value present in the literature has been reached but after carrying out the number of processes recommended by the manufacturer. This is certainly a practical and fast method based on experience, and the tool is fully exploited.

Therefore, it was decided to relate the axial force generated during the process with the tool wear.

Through Minitab, the thrust forces recorded for the drilling process with a traditional tool with a diameter of 6.35 mm were taken, and the tool wear values were associated with them.

All force records used randomly refer to tests carried out with different combinations of parameters (feed rate: 0.11 mm/rev; 0.15 mm/rev; spidle speed: 2700 rpm; 6000 rpm; 9000 rpm).

Thanks to the “Correlation” function, present in the “Basic Statistics” menu, the degree of correlation between the two variables (force, wear) has been calculated. The correlation coefficient is the measure of the degree of linear association between two variables, from an idea of how one variable changes as the other changes.

This index varies between '-1' and '1'; if positive, it indicates direct proportionality between the variables; if negative, it indicates indirect proportionality between the variables; if '0' indicates no correlation between the variables that have been chosen.

Therefore, observing the correlation between thrust force and tool wear VB, shows in Table 6-1:

Pearson correlation of thrust force and tool wear VB = 0.932
P-Value = 0.000

Table 6-1: Pearson Correlation.

The correlation value is high, indicating a good linear correlation between axial force and tool wear. Furthermore, the null p-value confirms that there is a correlation.

Therefore, the aim is to find a linear function to derive the wear starting from the force measured by the load cell.

The line will look like this:

$$y = a + bx + \epsilon \quad \text{Eq. 6-2}$$

Where ϵ represents the experimental error.

It is very important that the abscissas, i.e. force values calculated experimentally, are distributed randomly and that they cover the entire domain; in this case, the entire range of forces that can be generated during the drilling process.

The outlier values are not considered because they can distort the validity of the model.

The "Regression Fitted Line Plot" function present in the Minitab menu is used to create the linear regression model.

Figure 6-26 was thus obtained where the points obtained experimentally are shown in blue, and the straight line that approximates is shown in red.

In the upper part of the graph, the line equation allows us to calculate the wear value starting from a detected force value.

For the model to make sense, the points must be distributed evenly around the line; moreover, it is of fundamental importance to look at the indices on the right of the graph.

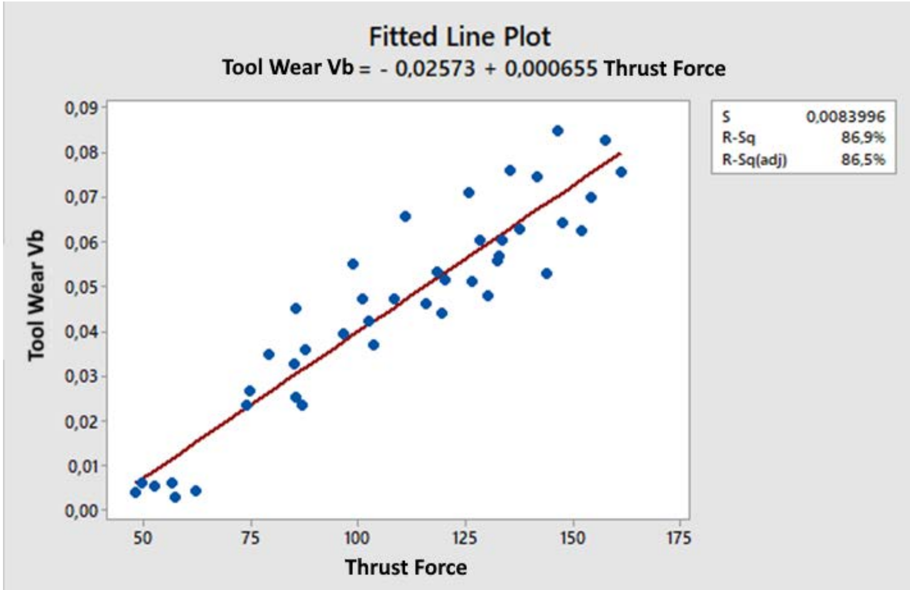

Figure 6-26: Fitted Line Plot.

The **S** index estimates the average variability of the experimental points concerning the straight line; the smaller the **S**, the more accurate the model.

In this case, **S** is 0.0084, so that the line approximates the real behaviour well.

The index **R-Sq** indicates how much the dependent variable **Y** varies in percentage as the independent X varies, **R-Sq(adj)** instead has the same function but also takes into account the number of terms used to generate the model, is used when you want to compare different models that are based on different numbers of terms.

Furthermore, in regression models, it is important to study what happens to the residuals.

The residuals are the difference, understood as the vertical distance, between the empirical point and the model line.

In an ideal and perfect linear regression model, all residuals would be zero since the line, in this case, perfectly intercepts the experimental points.

The validity of a linear regression model is appropriate to study the residuals using Minitab; the relative Figure 6-27 has been plotted.

The residuals must be normally distributed; this can be seen in Figure 6-27 at the top left.

As shown in the histogram at the bottom left, the residuals are normally arranged around the value "0". If this hypothesis is not respected and therefore the residuals arranged randomly, it must be immediately understood that the model is wrong or there is some problem in the experimental data records.

At the top right, the residuals are arranged around zero; in a perfect model, I would see a horizontal line since all residues are zero. However, in a linear regression model, it is to verify that the residuals are quite close to zero and that there is no trend, i.e. the points must be homogeneously arranged above and below zero.

If the trend of the residuals is around zero or densification of points immediately, it must be deduced that the linear model is wrong.

At the bottom right, on the other hand, the experimental points in order of sampling; even here, if the model is correct, you will see a homogeneous arrangement around zero. Downstream of the critical analysis of these residual plots shows that our linear regression model is correct.

Finally, for completeness, it is possible to plot the intervals, shown in Figure 6-28:

• **Confidence Interval (CI)**: interval in which 95% find the average response;

• **Prediction Interval (PI)**: interval in which 95% find the predicted response.

Obviously, the PI always contains the CI.

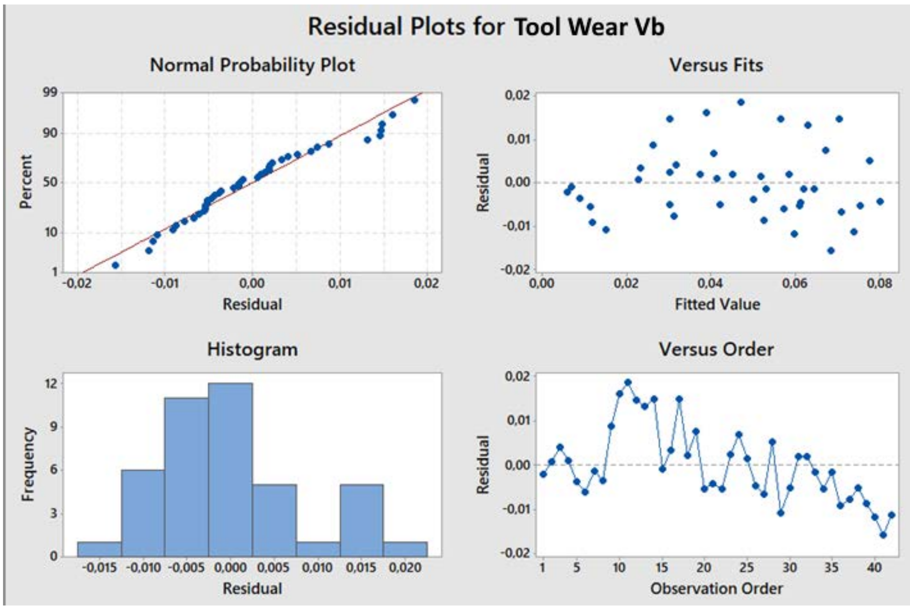

Figure 6-27: Residual Plots for Tool Wear VB.

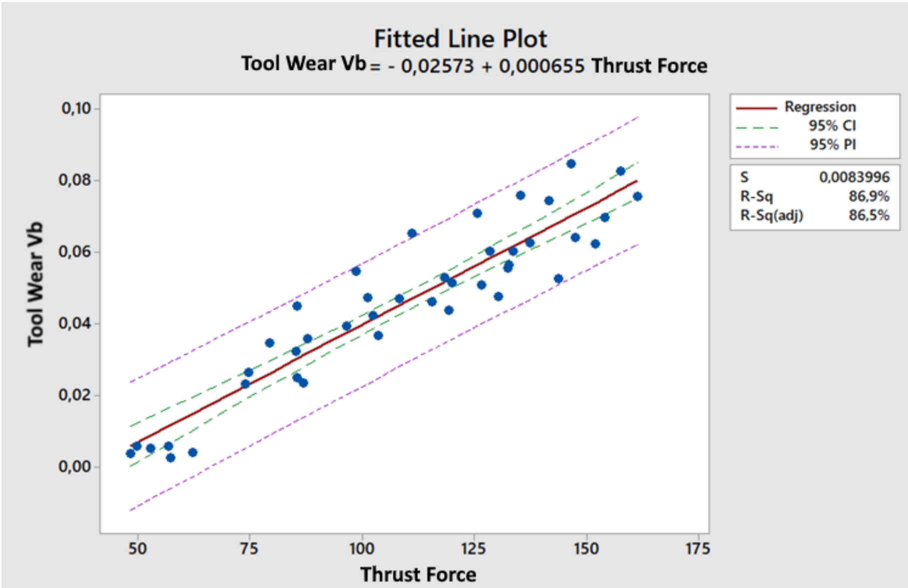

Figure 6-28: Fitted Line Plot VB.

6.5 MODEL OF MULTIPLY REGRESSION FOR THE FOR THE ESTIMATION OF THE TOOL WAER

Finally, we wanted to relate the response parameter, that is, the tool wear, with several independent variables, particularly the feed rate, the spindle speed and the number of the hole.

Reference is always made to a drilling process with a traditional tool with a diameter of 6.35 mm.

360 random records were taken by combining the forwarding speed and rotation parameters and associating each with the wear value recorded with optical control.

The discrete process parameters are 0.11 and 0.15 mm/rev as the feed rate; 2700, 6000, 9000 rpm as spindle speed.

It is referred to as the hole numbering sequence (remember that 60 holes were made in succession for each combination of parameters).

First, we proceed with a correlation analysis between the descriptors; if there is a correlation between descriptors, the model is not reliable.

The correlation between descriptors is called multicollinearity and is a problem that must be solved because it produces a wrong mathematical model.

When there are more descriptors, the correlation must be checked; If there is multicollinearity, Minitab takes a descriptor and eliminates it automatically; if you want to do it by hand, you have to eliminate one a time the one that has the highest coefficient.

In this case, there is no correlation between the various descriptors, so it is possible to calculate a reliable model from data shows in Table 6-2.

	Hole Number	Spindle Speed	Feed Rate
Spindle Speed	0.000		
	1.000		
Feed Rate	-0.000	-0.000	
	1.000	1.000	
Tool Wear	0.863	0.052	-0.163
	0.000	0.322	0.002

Table 6-2: Model.

The regression model with the wear as an output and feed speed, rotation speed, and the hole number as input was created and shows in Table 6-3.

Regression Equation
Tool Wear= 0.03644+0.000936 Hole Number + 0.000010 Spindle Speed - 0.1527 Feed Rate

Table 6-3: Regression equation.

The p-values in the regression show if the descriptor is significant in that specific regression model and not in the physical system in general. When the p-value is zero, it means that that descriptor is significant in the generated model. The spindle speed is the descriptor that affects the least; indeed, its regression coefficient is very low how shows in Table 6-4.

Term	Coef	SE Coef	T-Value	P-Value	VIF
Constant	0.03644	0.00341	10.70	0.000	
Hole Number	0.000936	0.000027	34.20	0.000	1.00
Spindle Speed	0.000000	0.000000	2.08	0.039	1.00
Feed Rate	-0.1527	0.0237	-6.44	0.000	1.00

Table 6-4: Descriptor.

Furthermore, from the correlation analysis, it is possible to deduce how much the succession of holes is significant for wear (correlation coefficient = 0.863); a simple regression model was therefore made that links the dependent variable wear to the independent hole number (Figure 6-29).

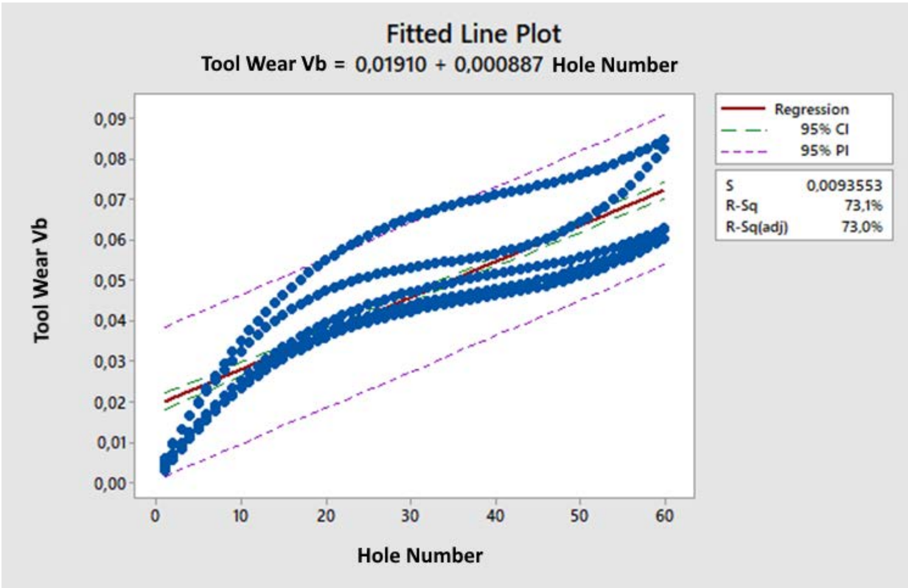

Figure 6-29: Fitted Line Plot VB for the tool wear and hole number.

As shown in Figure 6-29, the linear function does not approximate the experimental points well, so we moved on to a regression model that uses a cubic function.

This model is better, how shown in Figure 6-30; indeed, it has a smaller **S** index and a higher **R-Sq**; through the analysis of the confidence interval and the prediction interval, it is possible to estimate with a good approximation the degree of wear of the tool at the advance of the drilling production process.

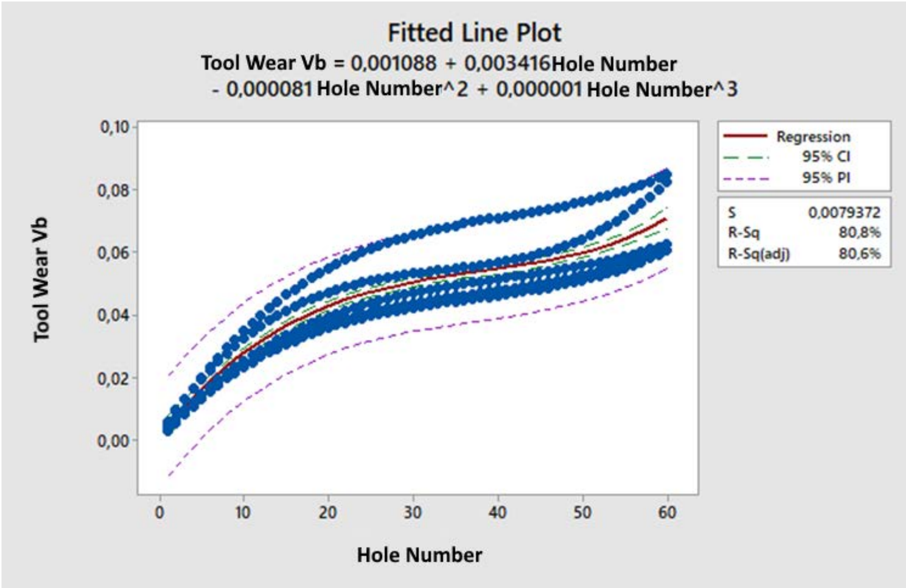

Figure 6-30: Confidence interval and prediction interval for regression with a cubic function.

As previously outlined, the tool's geometry significantly affects the drilling process [37], [88]. The design of tools with better performances in terms of damage reduction, improved hole quality and reduced costs is critical to optimise the drilling process [88]. In order to reduce the extent of delamination and thermal damage, orbital drilling (OD) has been proposed for CFRP components drilling. OD is a circular ramp machining process capable of simultaneously milling with a discontinuous peripheral cut and drilling with a continuous cut along the cutting-edge axis [89]. With this technology, movement along a circular path (X, Y) and axial feed (Z) with a pre-determined step can be performed at the same time (Figure 7-1)[90]. The OD technology is particularly advantageous as it enables drilling holes with different diameters without replacing the tool. Additionally, the orthogonal thrust force exerted on the surface is very low, resulting in holes with superior quality and reduced delamination damage, making this process particularly suitable for CFRP components drilling [91].

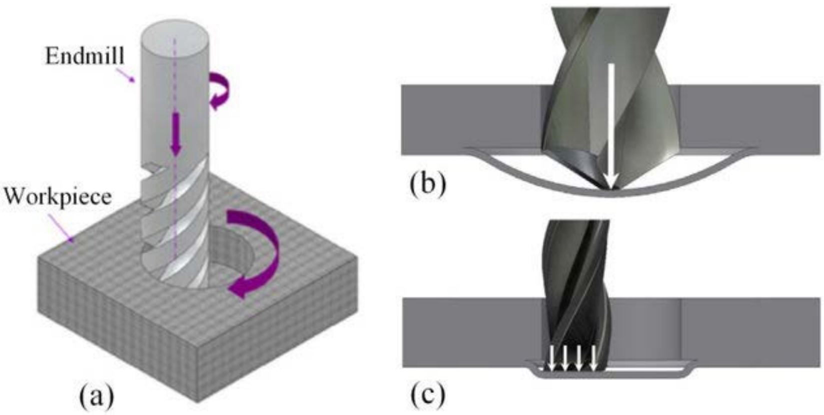

Figure 7-1: Schematics of the OD process(A); Deflection of the last ply in twist drilling (B)and OD(C) [91].

The main drawbacks associated with the use of OD are the difficulties in identifying the correct process parameters and the occurrence of vibration issues. OD operations are carried out by machines, which can exhibit severe forced vibrations leading to a reduced hole quality [92]. For traditional drilling approaches, the axial loading consists of a concentrated load at the centre of the last laminate plies (Figure 7-1 B), while an eccentric distributed axial load acting along the cutting-edge of the mill occurs for OD approaches (Figure 7-1 C) [91].

The OD process is generally characterized by a greater versatility compared to traditional drilling as it allows to obtain holes with different diameters without replacing the tool. This allows the process's high flexibility; however, the type of machining centre and the setting require more attention. Moreover, to realise this drilling process, it is necessary to use at least one three-axis machining centre, and the parameters to be controlled are many.

The parameter process are shown in Figure 7-2, Figure 7-3 and Figure 7-4.

To calculate the tool feed rate V_f, you must first calculate the axial feed of the helix V_{fha}, the tangential feed rate of the cutting edge V_{ft} and the helix's tangential feed rate V_{fht}. Once the helix's angle of inclination is also known, it is possible to calculate the helix's step at a_p *.

All these parameters can be calculated once the axial feed per cutter tooth f_{za} and the tangential feed per tooth f_{zt}, and the diameter of the hole are to be made.

The process consists of a milling peripheral with a discontinuous cut on the edge of the cutting edge and a continuous cut drilling along the cutting edge axis.

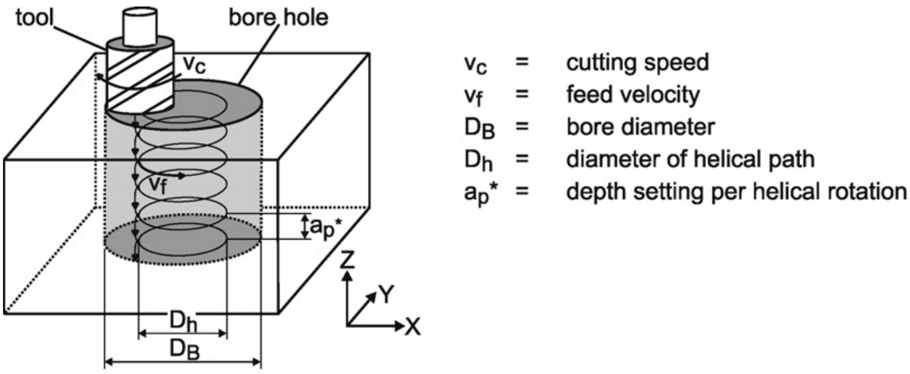

Figure 7-2: Parameter of process OD

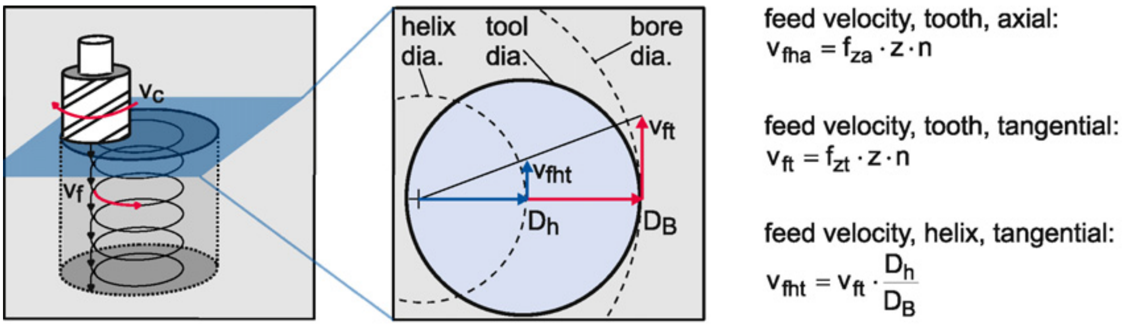

Figure 7-3: Parameter of process OD on the orthogonal axes of the hole

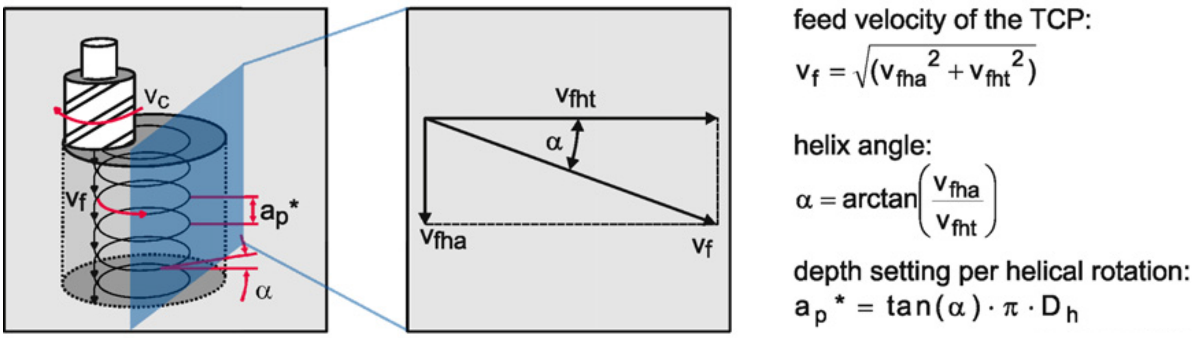

Figure 7-4: Parameter of process OD on the axes of the hole.

With this technique, the orthogonal thrust to the surface is very low with consequent high quality of the hole, especially in composite materials subject to delamination phenomena. Furthermore, this drilling can be carried out in the absence of coolant, making it cleaner and safer.

This type of processing is particularly suitable for applications in the aeronautical field as it allows a reduction in cutting forces and, therefore, a reduction in temperatures which results in a reduction of the polymer matrix of the composite material.

With this technique, the orthogonal thrust to the surface is very low with consequent high quality of the hole, especially in composite materials subject to delamination phenomena. Furthermore, this drilling can be carried out in the absence of coolant, making it cleaner and safer.

This type of processing is particularly suitable for applications in the aeronautical field as it allows a reduction in cutting forces and, therefore, a reduction in temperatures which results in a reduction in the polymer matrix of the composite material.

Furthermore, thanks to a different trajectory than traditional drilling, it is possible to reduce delamination at the entrance and exit.

By the linear elastic fracture mechanics model for conventional drilling of reinforced fibrous materials with a polymeric matrix, the phenomenon of push-out (delamination at the outlet) occurs if the value of the axial load acting on the part being machined exceeds a certain threshold.

The balance of the axial load's work is defined as the total sum of the deformation energy acting on the laminate's last ply and the energy required to form a new fracture surface.

The process was compared with conventional drilling based on the linear elastic model of fracture mechanics.

The linear elastic model of fracture mechanics defines the axial load acting on the last plies at the exit hole, which causes the fracture to propagate and triggers the delamination process.

For evaluating the axial load, reference is generally made to a concentrated load at the centre of the circular element, representing the piece's last ply to be drilled.

For orbital drilling, an energy criterion can be adopted, characterized by applying an eccentric distributed load that acts along the cutter's cutting lip. This model can be expressed by Eq. 7-1:

$$2\pi a \cdot G_{IC} = F_{A,OD}^2 \left(\sum_{i=1}^{i=m} K_{x,i} - \sum_{i=1}^{i=m} K_{u,i} \right) \quad \text{Eq. 7-1}$$

Where:

G_{IC} = Critical energy of propagation of the fracture

m = number of points of the distributed load

$K_{x,i}$ = Deflection of the last ply due to point loads

$K_{u,i}$ = energy stored by the ply due to point loads

a = radius of the circular portion of ply subjected to drilling

M = Bending stiffness due to an eccentric point load

e = Eccentricity of the load

and

$$K_{x,i} = \frac{e}{8\pi M}\left[f\left(\frac{e}{a}\right)\right]$$ Eq. 7-2

$$K_{u,i} = \frac{e}{16\pi M}\left[g\left(\frac{e}{a}\right)\right]$$ Eq. 7-3

So the axial load of the orbital drilling process is:

$$F_{A,OD} = \sqrt{\frac{2\pi a \ \leq G_{IC}}{\left(\sum_{i=1}^{i=m} K_{x,i} - \sum_{i=1}^{i=m} K_{u,i}\right)}}$$ Eq. 7-4

It has been estimated that in the case of traditional drilling, this load is about double that of an orbital drilling process, and the critical threshold value for the delamination of the last ply is greater than about 60% compared to conventional drilling.

This reduction of the axial load corresponds to an increase in tangential loads, totally absent in a conventional drilling process. However, this does not negatively affect the delamination process at the outlet but could affect the entrance's delamination (Peel-Up).

According to bibliographic data, the orbital drilling process leads to a 45% reduction in the axial load and a 100% increase in tangential loads. However, the latter is less harmful and less than 30% of the axial thrust. [91]

Figure 7-7 shows as the spindle speed increases, a progressive reduction of the axial force and tangential loads are obtained; the material that each cutting edge must remove to make the hole is reduced [91].

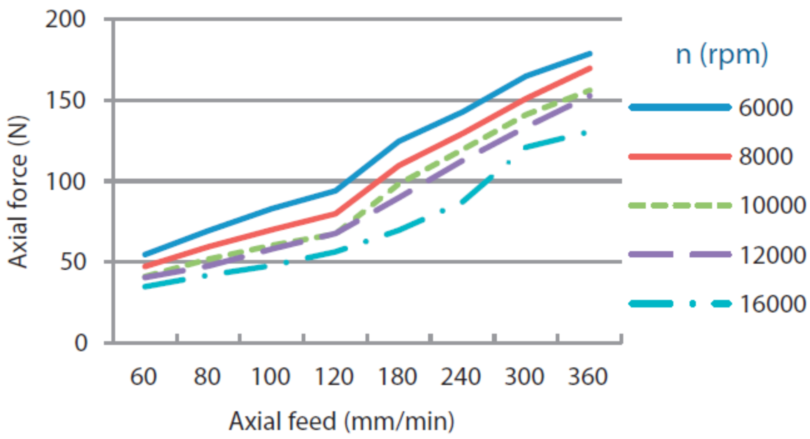

Figure 7-5: Axial thrust trend as a function of the feed speed as the spindle speed varies.

As for the temperatures related to the orbital drilling process, at the exit from the piece, the tool has a lower temperature of about 60% compared to traditional drilling carried out with a feed rate of 360 mm/min and a spindle speed of 6000 rpm.

The hole's geometry accuracy made Eh%, measured as the difference between the diameter of the hole obtained and the nominal one; for a traditional drilling process, it is characterized by values between ± 0.12% and ± 0.15%. In orbital drilling, these values still fail to be respected. At a fixed feed speed of 360 mm/min and low spindle speeds of 6000-8000 rpm, undersized holes are obtained, mainly due to the tip's deflection.

Positive differences in the accuracy of the hole begin to be obtained at high spindle speeds, as shown in Figure 7-8; this could be explained by the onset of a whirling phenomenon which the tool is subjected to high rotation speeds, but this hypothesis must be carefully verified. Furthermore, the breakage method must be checked, clearly showing the breakage signs due to whirling or reverse whirling if made of carbides [91].

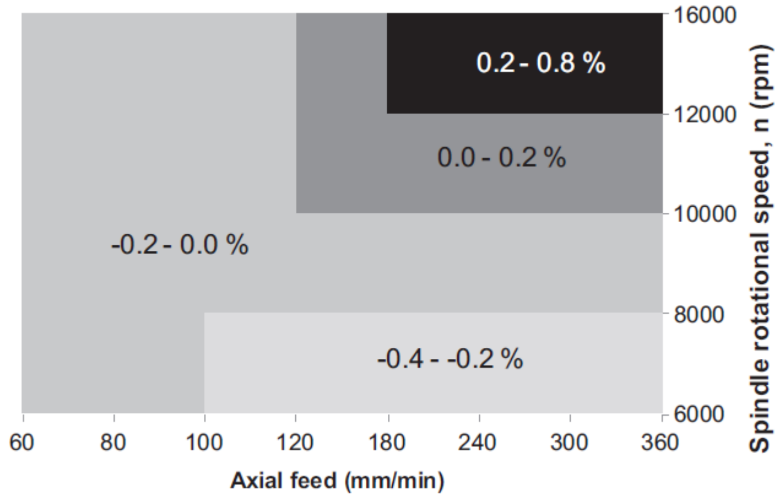

Figure 7-6: Hole accuracy as a function of axial load and spindle speed.

7.1 PROPOSED DRILL-MILLING PROCESS

As seen previously, tool geometry significantly affects the drilling [19],[92] . Designing new tools with better performance in terms of damage reduction, hole quality and cost; these factors are critical for drilling process optimisation [88]. Piquet et al. [93] analysed the effects of drilling tool geometry, comparing the results obtained with a specially designed cutting tool and traditional tool.

To reduce the delamination and thermal damage defects generated when drilling composites, a new process called orbital drilling (OD) has proposed. This process allows for obtaining holes with different diameters without replacing the tool. OD is a circular ramp machining process, composed of milling with a discontinuous peripheral cut and drilling with a continuous cut along the cutting-edge axis at the same time [89]. This technology involves simultaneous movement along a circular path (X, Y) and an axial feed (Z) with a pre-determined step [90].

In OD, the orthogonal thrust exerted on the surface is very low, resulting in a superior hole quality; this process is interesting, especially in the composite materials subject to delamination damage. This process is particularly suitable for applications in the aeronautical field, as it allows for a decrease of cutting forces and temperatures, which results in a reduction of polymer matrix damage [91].

Disadvantages of using the OD process are the difficulties in selecting the proper process parameters and vibration problems. OD operations are carried out by highly flexible machines, which exhibit severe forced vibrations that lead to a hole quality. Moreover, the thrust force responsible for delamination is reduced but still not eliminated with OD [92]. As shown in Figure 7-1, in traditional drilling, the axial loading consists of a concentrated load at the centre of the last ply of the laminate;

in orbital drilling, the axial loading is determined by an eccentric distributed load, which acts along the cutting-edge of the mill [91].

As an alternative to both traditional drilling and orbital drilling processes, an innovative hole making process for CFRP components is studying, where the hole was realised by a combination of drilling and peripheral milling, carried out using the same cutting tool. The objective is to reduce the process-induced delamination damage. For the particular process, an innovative drill-milling tool developed to perform the new combined drill-milling process is studying. The new drill-milling process performed under dry conditions in a green technology solution, with the advantages of the absence of cutting fluids and a lower environmental impact [94].

As studied by Hocheng et al. [36], [95], for traditional drilling, the axial load evaluation refers to a concentrated load at the centre of the last ply of the laminate.

Instead, for orbital drilling, an energy criterion characterised by applying an eccentric distributed load, which acts along the cutting-edge of the mill, is adopted. As reported in Figure 7-7 A-B, the OD means that the thrust force causing delamination is reduced but not eliminated [91].

To eliminate the drilling-induced delamination, a different original technique for CFRP hole making was proposed; in this technique, the hole was realised using a combination of drilling and peripheral milling processes. Figure 7-7 C illustrates two phases of the process; in the first phase, traditional drilling was employed to produce a smaller diameter than the final hole. In the second phase, the material around the first hole is removed by peripheral milling until the final diameter is achieved. These two phases were sequentially combined in a single process carried out using the same cutting tool.

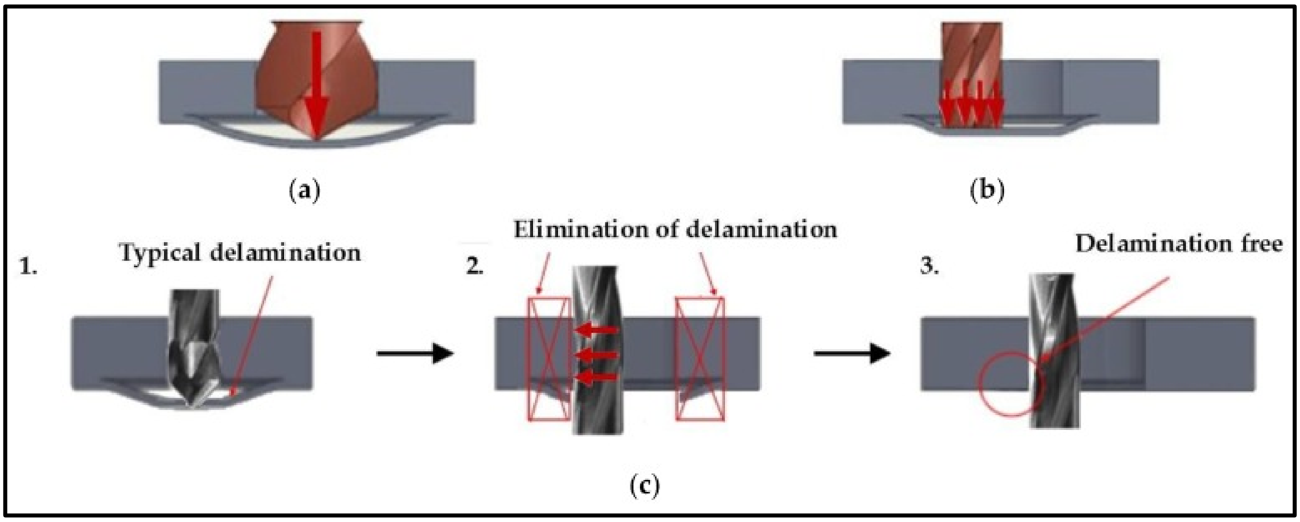

Figure 7-7: Representation of (a) traditional drilling; (b) orbital drilling [96],and (c) drill-milling processes.

An innovative drill-milling tool was designed and realised, and experimental cutting tests on CFRP laminates wereperformed to characterise the process.

7.2 DESIGN OF THE TOOL

Designing new tools that perform better in cost, damage reduction, and hole quality is a key factor in optimizing the drilling processes. With SolidWorks software, an innovative tool has been designed.

The paragraph reports the evaluations and considerations that led to the definition of new tool geometry. After choosing a traditional tool, we moved on to define the possible modifications to obtain an innovative and optimal tool for the type of bore-milling machining.

The tool studied differs from the traditional one, characterized by a double helix with two cutting edges. Figure 7-8 A and Figure 7-8 B shows it is possible to read the traditional tool with the hole-milling one.

To get to the type of geometry in Figure 7-8 B, starting from the traditional tool.

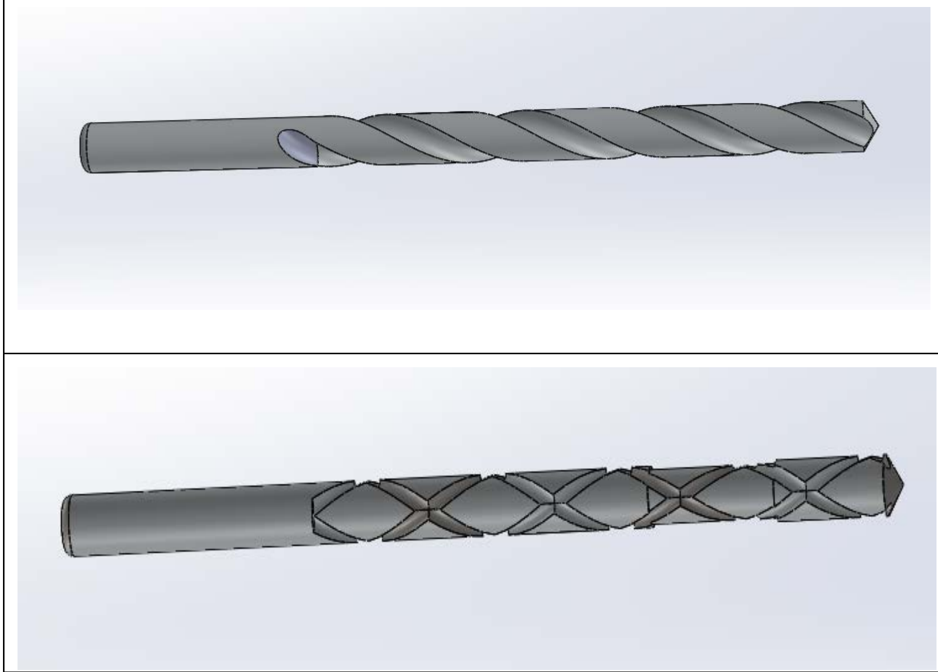

A

B

Figure 7-8: Traditional tool (A) for drilling operations and innovative tool (B) for drill milling operations of CFRP laminate.

In the new tool, it is possible to identify the first section, defined as a pilot drill, suitable for drilling, with a height of 15 mm and a maximum diameter of 6.35 mm and with an angle point of 118°, followed by a section of the same height but with a reduced diameter equal to 5.65 mm. Only 70 mm over a nominal height of 100 mm are involved in the processing.

The following steps describe the procedure to design the traditional tool from: the maximum dimensions (including nominal length), helix pitch, nominal diameter, number of helices and cutting angle.

It is started with creating a solid cylinder with a diameter of 6.35 mm and a nominal length of 100 mm. The helix is created by choosing the height/revolution ratio, setting a height equal to 70 mm and two revolutions in a clockwise direction. This resulted in a constant step of 35 mm (the step is the distance evaluated between two points in a mutually orthogonal position belonging to the helix). It is possible to vary the step by selecting the function that correlates step/height and determines the number of revolutions obtained. It is set a value of the channel through which the chip evacuation takes place by establishing, in an arbitrary way, a circumference equal to 4 mm, and with the help of the cut-sweep function, we obtained the first channel.

Subsequently, with the repetition-circular function, it was decided to obtain a total of two instances spread over 360° arranged one to the other at 180°.

Finally, with the aid of a centerline, an angle was constructed by employing a cut-revolution operation; by setting the value of the angle equal to 121°, the angle at which the cut takes place, it was possible to obtain the tip of the tool with a cutting angle, for complementarity with the removed one, equal to 118°.

Later, it was decided to make further changes to obtain a tool that would control and reduce the defects and the effects of delamination and optimize the production and assembly of the finished piece.

It started with a specimen with a nominal length of 100 mm. Two values of nominal diameter were set, differently from the traditional case (one only diameter). The first section has a length of 15 mm and a diameter of 6.35 mm that decrease to 0.70 mm, obtaining a nominal diameter of 5.65 mm. The second section has a length of 15 mm and a diameter of 6.35 mm. Finally, the remaining 70 mm were always maintained with a nominal diameter of 6.35 mm as well.

From **Figure 7-9,** it is possible to compare the starting tool and the modified one.

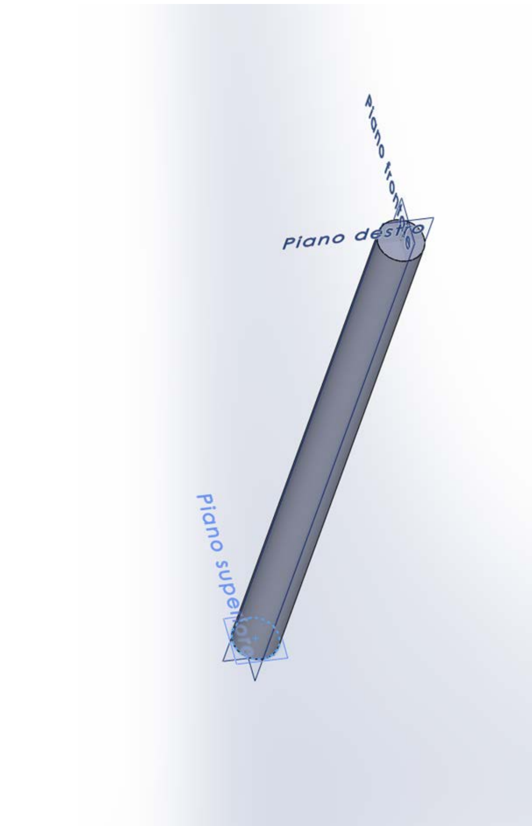	
A	**B**

Figure 7-9: Comparison between cylinder for design traditional tool (A) and changes made after the first step (B) for design the innovative tool.

Later it was decided to no longer have two clockwise but four helices with a clockwise-anti-clockwise alternation arranged at 90° from each other and distributed over 360°; thus, the first and third helices are clockwise while the second and fourth are anti-clockwise. It was also chosen to modify the function chosen to obtain the helix by setting step-height. The step was fixed at 30 mm, height 70 mm; helix repetition was obtained equal to 2.33 mm. Figure 7-10 A shows the construction of a clockwise helix at the top and a counterclockwise one at the bottom.

Once all four helices were made, it is moved to create the chip evacuation channel, fixing a smaller circumference equal to 2 mm. Compared to the previous one, it was impossible to create a single channel and then repeat it the other times, but it was necessary to create the channels one by one. In Figure 7-10 B, C, it is already possible to see the channel obtained from a clockwise helix that intersects with the one obtained from a counterclockwise helix (grey part in 3D).

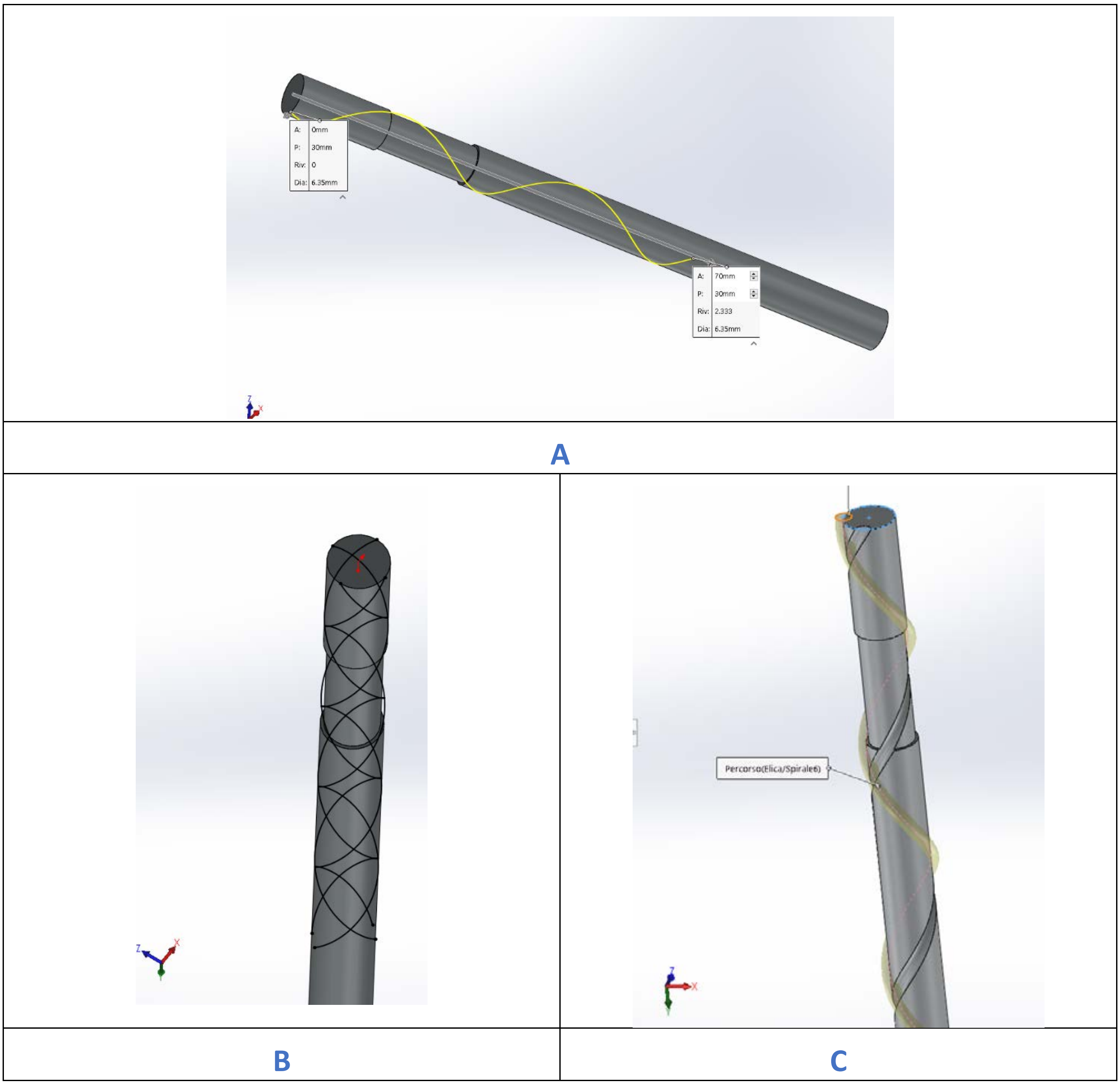

Figure 7-10: Construction of the alternating clockwise-counterclockwise helices with 90° arrangement (A) and the evacuation channels of the first and second helices, on the right (B-C).

Repeating the process for the other two helices, keeping the circumference value constant and applying the sweep-revolution operations as in the previous cases, we obtained the following result shown in Figure 7-11.

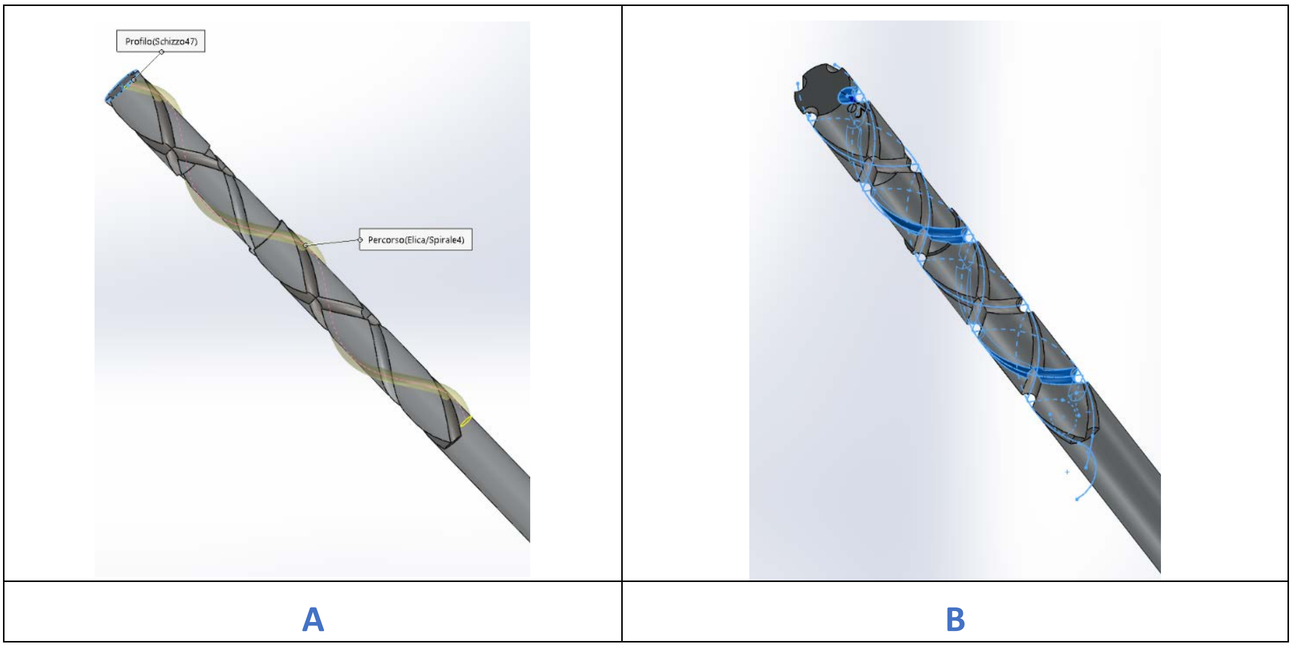

Figure 7-11: Realization of the last helix (A) sweep-revolution function (B).

7.3 EXPERIMENTAL TESTS: TOOL DIAMETER 4 MM

To examine the process, tests were carried out. The thrust force and radial force signals were detected through a sensor system to analyse the cutting forces occurring during the process.

For the study of this process, CFRP laminates different from the previous ones were used only for the lamination sequence, which in this case is [±45/0/±45/90/±45/0/−45/90/45/90]s.

The drill-milling tests were performed in dry conditions on a Cosmec Conquest 3200 NC five-axis machining centre. The system is equipped with a sensor system to detect the force signals generated during the process. The thrust force signals, Fz and radial force, Fx, were detected by a Kistler three-axis stationary dynamometer model 9257A, positioned under the workpiece fixing device. The sensor system is equipped with a Kistler 5007 charge amplifier model and a National Instruments 9239 data acquisition card model, which transforms the acquired signal into a processable electrical signal.

Through appropriate software, the signal was then acquired. During the tests, a signal acquisition speed of 10 kHz was used, and the post-processing phase was performed through the Matlab R2016 B Software; Figure 7-12 shows the geometries of the tools designed to study the new drilling process.

Once the pilot hole is realised, the tool follows a spiral milling path to increase the hole diameter by 0.10 mm per revolution, illustrated in Figure 7-12 B Figure 7-12 C up to the desired diameter. Finally, three boring revolutions at constant diameter are executed [96].

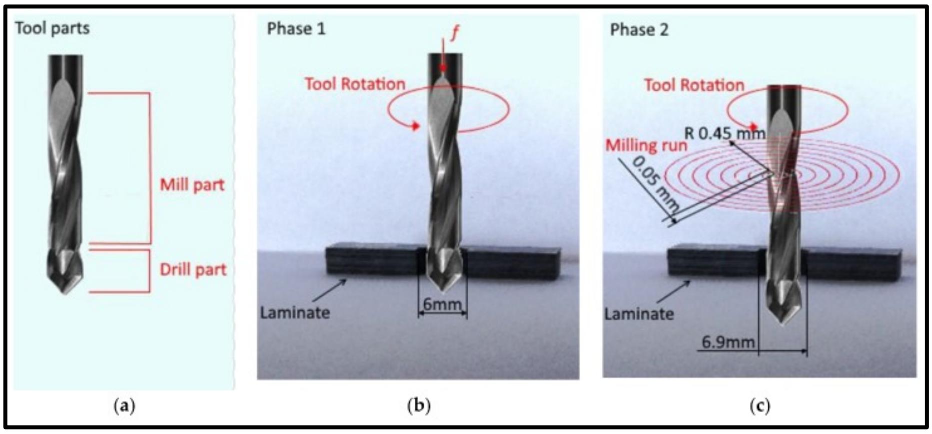

Figure 7-12: Representation of (a) tool parts and process steps: (b) drilling and (c) milling.

Drill-milling experimental analysis started setting the parameter of the drilling and milling process and changing only the tool's geometry.

The parameters used are a spindle speed of 10000 rpm and a feed rate of 625 mm/min during the drilling and milling phases.

Figure 7-13 (red box) shows the first type (twist tool) of the various tools, which differ from each other for the point angles dedicated to drilling and the helix part dedicated to milling.

Figure 7-13: Tool prototypes. The nominal diameter is 4 mm.

The tool is made of tungsten carbide (WC) and has a 4 mm diameter and 100 mm length; the drilling portion is 8 mm extended, and the milling portion is 18 mm and 2 flutes number. Table 7-1 compares the different geometry parameter for the first kind of prototype tools. The table shows the parameter related to point angle, helix angle and rank angle.

TWIST TOOL (4 MM)

IDENTIFY TOOL NUMBER	Point Angle	Helix Angle	Rank Angle
DM1	90°	25°	25°
DM2	90°	25°	20°
DM3	90°	15°	20°
DM4	90°	20°	20°
DM5	120°	25°	25°
DM6	120°	25°	20°
DM7	120°	15°	20°
DM8	120°	20°	20°
DM9	120°	10°	20°

Table 7-1: Comparison of newly developed drill-milling tools and milling portion geometry parameters.

Figure 7-14 (red box) shows the second type (rasp tool) and third type (helix + rasp) of the various tools, which differ from each other for the point angles dedicated to drilling and the helix part dedicated to milling.

Figure 7-14: Tool prototypes. The nominal diameter is 4 mm.

The tools are made of tungsten carbide (WC) and have a 4 mm diameter and 100 mm length; the second type of tool has 12 right helices and 10 left helices. The third type of tool, the drilling portion, is 8 mm extended, and the milling portion is 18 mm and 2 flutes number; the milling portion is made with a rasp on the single helices. Table 7-2 shows the different geometry parameter for the second and third kind of prototype tools.

Rasp Tool	
Identify Tool Number	**point angle**
RDM1	90°
RDM2	120°
Twist + Rasp tool	
Identify Tool Number	**point angle**
TRDM1	90°
TRDM2	120°

Table 7-2: Comparison of newly developed drill-milling tools and milling portion geometry parameters.

7.3.1 RESULTS OF THE PRELIMINARY TESTS

After the first tests, the results are reported in Table 7-3.

The first analysis was related to the hole's tolerance, the much faster evaluation method for the better choice of tool. Moreover, the roundness of the hole and the goodness of the signal were analysed. Signals with much noise caused by the drilling vibration are not acceptable. Then, the hole dimension with the analogic gauge along the four holes direction was analysed. The results are reported in Table 7-4 (where the final nominal size is 4.9 mm). All the signal recording during the drill-milling operation was reported in Appendix III.

TOOL	DIMENSIONAL TOLERANCE	ROUNDNESS	FZ	FX
DM1	Out Tolerance min	yes	Good	Sinusoidal
DM2	Out Tolerance max	yes	no sinusoidal	no sinusoidal
DM3	Accepted	Less a decimal	Good	Sinusoidal
DM4	Out Tolerance min	yes	Good	Sinusoidal
DM5	Out Tolerance max	yes	noise	noise
DM6	Out Tolerance max	no	noise	noise
DM7	Out Tolerance min	yes	Good	Sinusoidal
DM8	Out Tolerance min	no	Good	Sinusoidal

Table 7-3: Result obtained after the first hole, made with different tools.

NUMERO	0°	90°	45°	-45°
DM1	4.55	4.55	4.55	4.55
DM2	5.1	5.1	5.1	5.15
DM3	4.85	4.8	4.8	4.9
DM4	4.45	4.45	4.45	4.45
DM5	5.2	5.2	5.25	5.25
DM6	5.45	5.3	5.3	5.2
DM7	4.6	4.6	4.6	4.6
DM8	4.45	4.45	4.4	4.5

Table 7-4: Size analysis of the first hole made with the different tools.

7.3.2 TESTS TOOL DM3

After the first analysis, tool DM3 was chosen for the drill-milling operation. The aim was to determine the best parameters for the machining operation. 8 holes with different parameters for the milling part were executed. Concerning the drilling part, instead, a constant set of parameters was chosen, so as reported in the drilling paragraph. Their choose was made to limit the drilling-induced delamination damage, that is lower than the zone removed by the peripheral milling. In particular, the drilling spindle speed was set to 10000 rpm and the feed rate to 375 mm/min.

Table 7-5 reports the milling process parameter set with tool DM3 for the first 7 holes.

HOLE N.	RPM	MM/MIN	BORING ROTATION NUMBER
1	10000	625	5
2	10000	312.5	5
3	14000	312.5	5
4	14000	156.25	5
5	14000	312.5	3
6	16000	312.5	4
7	16000	312.5	3

Table 7-5: Parameter used during the milling process, made with tool 3 for the first 8 holes.

Successively, Fx and Fz signals were studied. Figure 7-15 shows the signal acquired to Fx, and Figure 7-16 shows the smooth signal to Fx, elaborated with the mobile average. Figure 7-17 shows the signal acquired to Fz, and Figure 7-18 shows the smooth signal to Fz, elaborated with the mobile average.

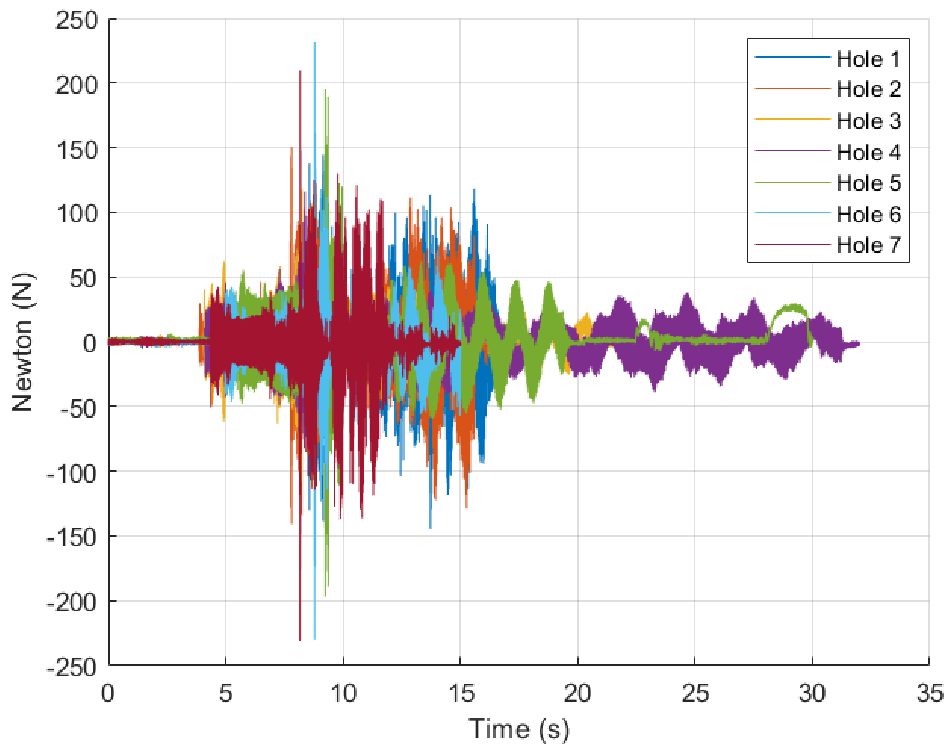

Figure 7-15: Fx signal acquired for the first 7 holes during the drill-milling process with DM3 and different parameters.

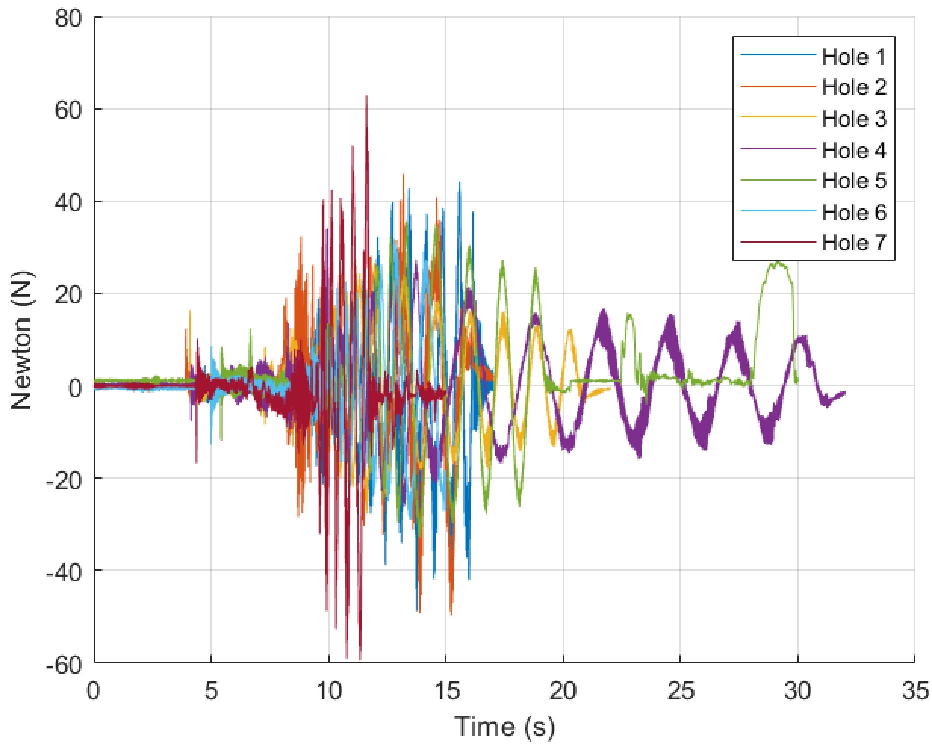

Figure 7-16: Fx signal elaborated with the mobile average for the first 7 holes during the drill-milling process DM3 and different parameters.

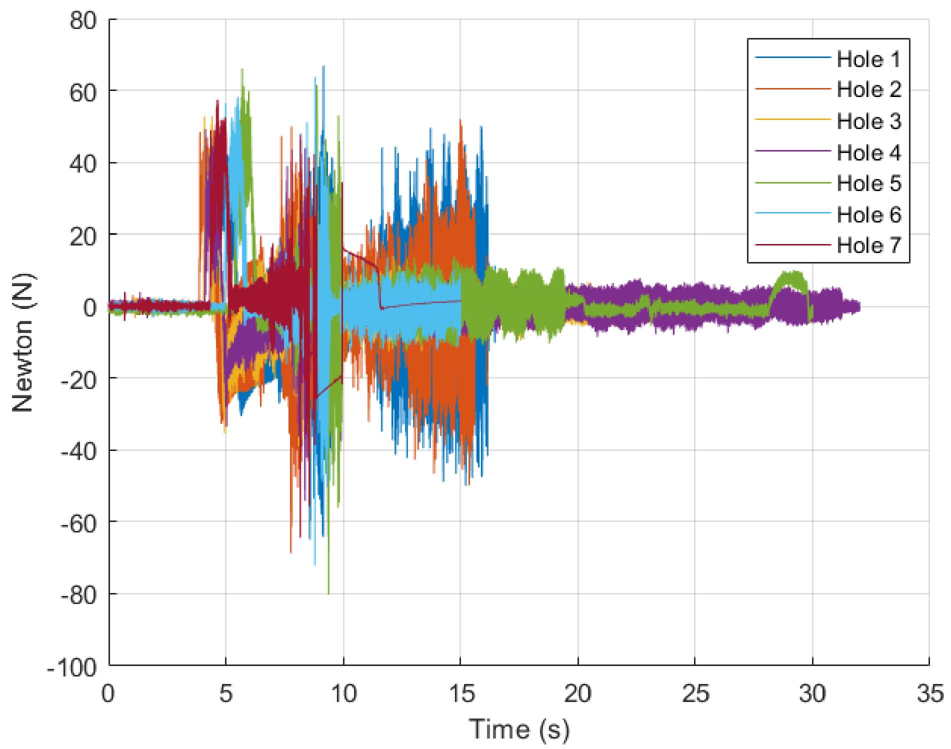

Figure 7-17: Fz signal acquired for the first 7 holes during the drill-milling process DM3 and different parameters.

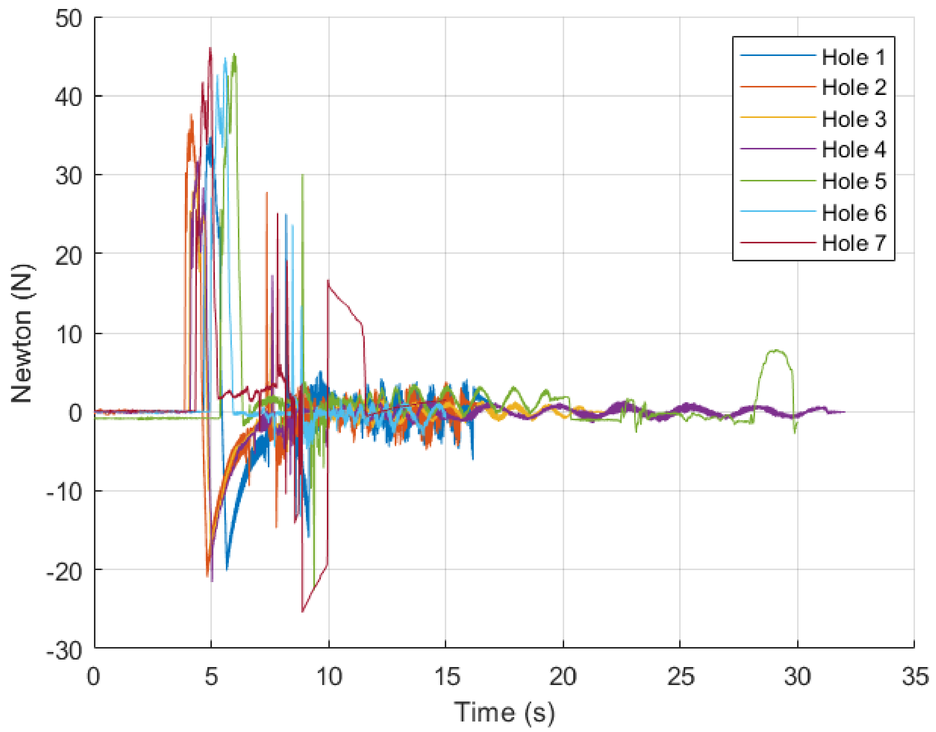

Figure 7-18: Fz signal elaborated with the mobile average for the first 7 holes during the drill-milling process DM3 and different parameters.

The hole size was checked to control the process's goodness; it was decided to use the milling parameter 16000 rpm - 312.5 mm/min by programming the machine tool with 5 boring passes.

With these parameters and the same tool used to make the 7 previous holes, the test campaign continued. We then arrived at the tenth hole made with the same parameters at which the tip broke.

Indeed, the signal are very unstable for the hole n. 7 and vibrations influence too much the acquired signal's accuracy and influence the tool breakage.

7.3.3 TESTS TOOL DM4

With the best parameters used for the previous tests, 16000 rpm - 312.5 mm/min and 3 bores, other specimens were drilled with tool DM4 (the drilling speed was set to 10000 rpm and the axial feed to 375 mm/min).

However, a break occurred after two holes due to the strong vibrations that caused the tool resonance during drilling, how is clear observing Figure 7-21 Figure 7-22 relative to Fx signal and Fx smooth signal and Figure 7-23 Figure 7-24 relative to Fz signal and Fz smooth signal.

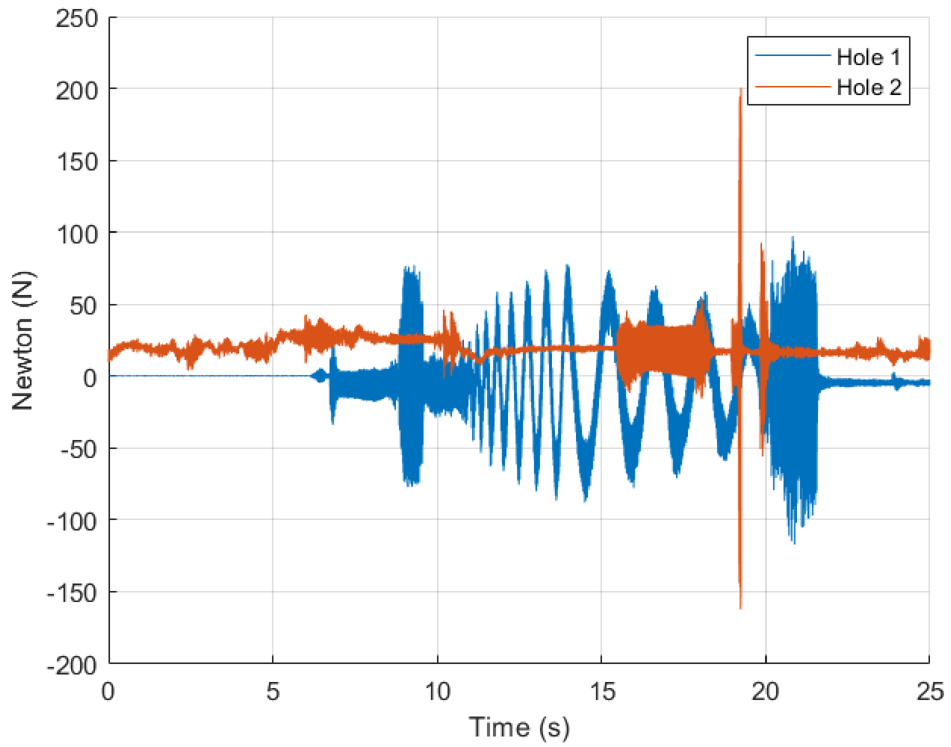

Figure 7-19: Fx signal acquired during the drill-milling process with DM4 and 16000 rpm - 312.5 mm/min and 3 bores parameters.

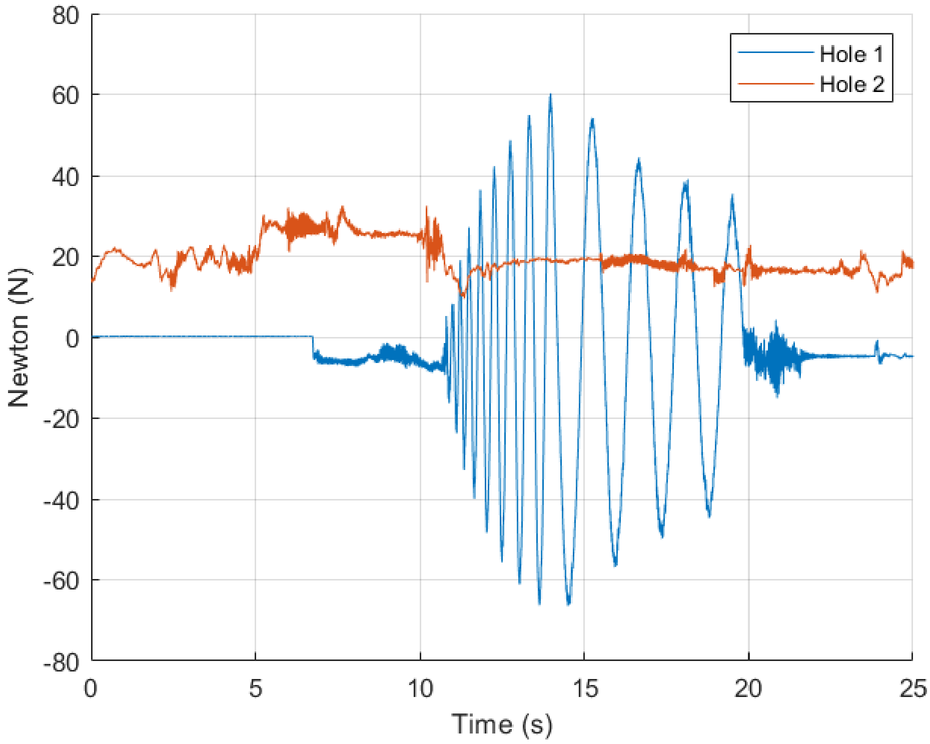

Figure 7-20: Fx signal elaborated with the mobile average for the first 2 holes during the drill-milling process with DM4 and 16000 rpm - 312.5 mm/min and 3 bores parameters.

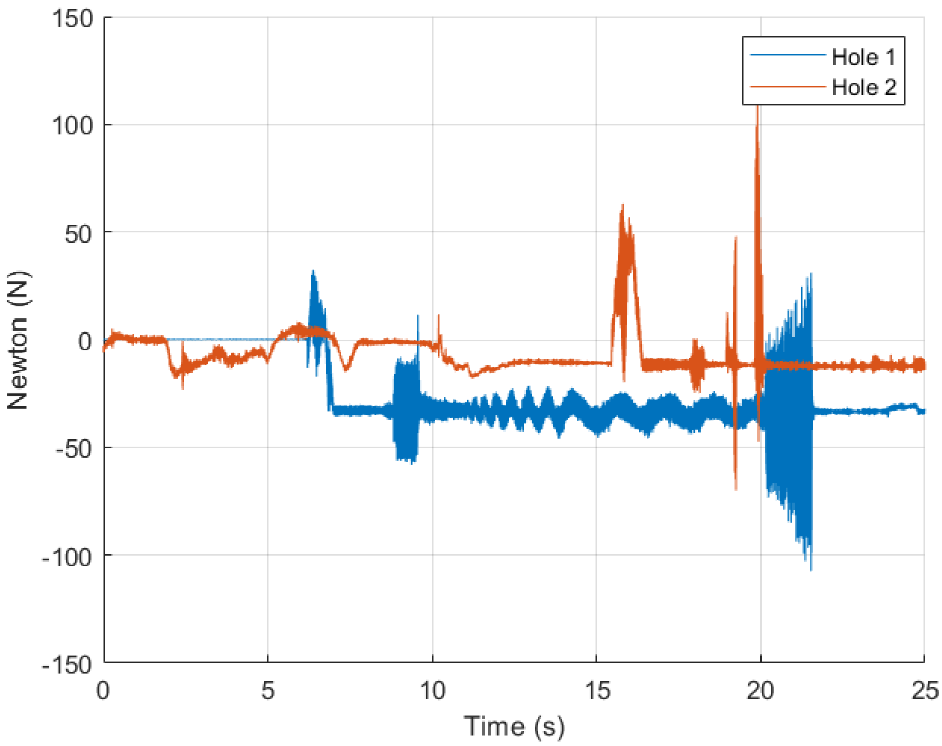

Figure 7-21: Fz signal acquired during the drill-milling process with DM4 and 16000 rpm - 312.5 mm/min and 3 bores parameters.

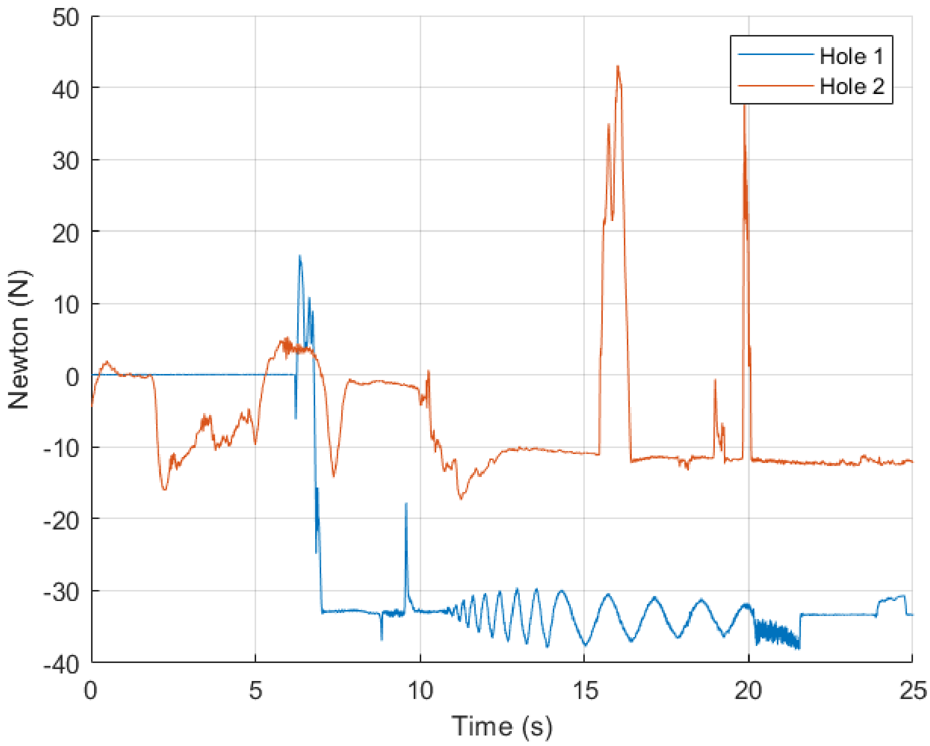

Figure 7-22: Fz signal elaborated with the mobile average for the first 2 holes during the drill-milling process with DM4 and 16000 rpm - 312.5 mm/min and 3 bores parameters.

7.3.4 TESTS TOOL DM9

With the best parameters, 14000 rpm - 312.5 mm/min and 3 bores, other specimens were drilled with tool DM9 (the drilling speed was set to 10000 rpm and the axial feed to 375 mm/min).

Figure 7-23 shows the Fx signal during the drilling process for no. 20 holes. Figure 7-24 shows the Fx signal elaborated with the mobile average for the first 20 holes during the drill-milling process.

Figure 7-25 shows the Fz signal during the drilling process for no. 20 holes. Figure 7-26 shows the Fz signal elaborated with the mobile average for the first 20 holes during the drill-milling process.

Subsequently, it was decided to modify the set of parameters; it was decided to increase the milling process's number of bores to improve the hole geometric features (16000 mm/rev - 312.5 mm/min and 5 bores). However, it was only reached hole no. 12, when the tool broke.

Figure 7-27 shows the Fx signal during the drilling process for no. 10 holes. Figure 7-28 shows the Fx signal elaborated with the mobile average for the first 10 holes during the drill-milling process.

Figure 7-29 shows the Fz signal during the drilling process for no. 10 holes. Figure 7-30 shows the Fz signal elaborated with the mobile average for the first 10 holes during the drill-milling process.

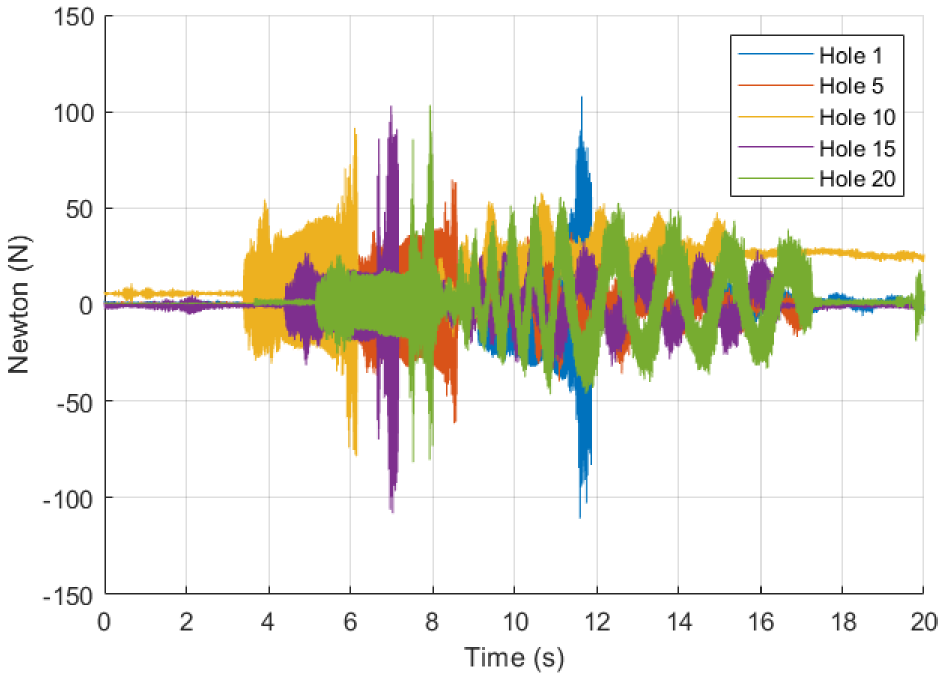

Figure 7-23: Fx signal acquired during the drill-milling process with DM9 and 14000 rpm - 312.5 mm/min and 3 bores parameters for the no. 20 holes.

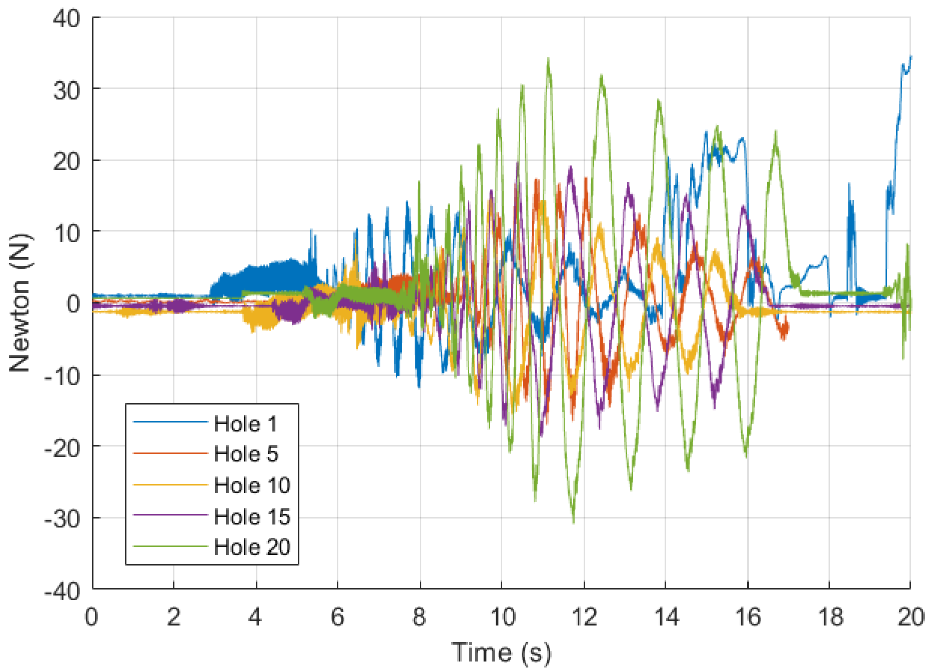

Figure 7-24: Fx signal elaborated with the mobile average for the holes no.1-5-10-15-20 during the drill-milling process with DM4 and 14000 rpm - 312.5 mm/min and 3 bores parameters.

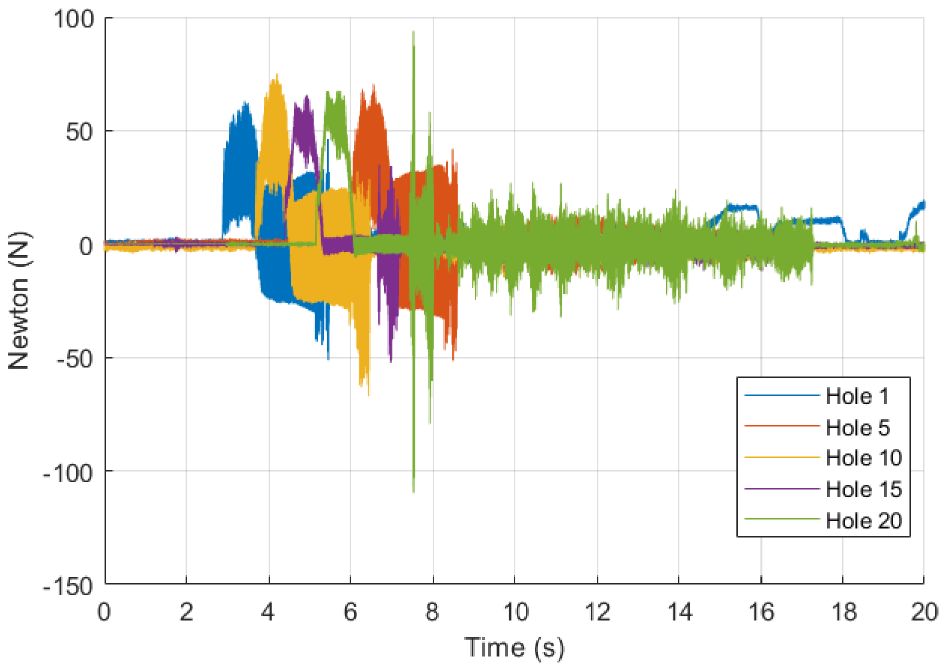

Figure 7-25: Fz signal acquired during the drill-milling process with DM4 and 14000 rpm - 312.5 mm/min and 3 bores parameters for the no. 20 holes.

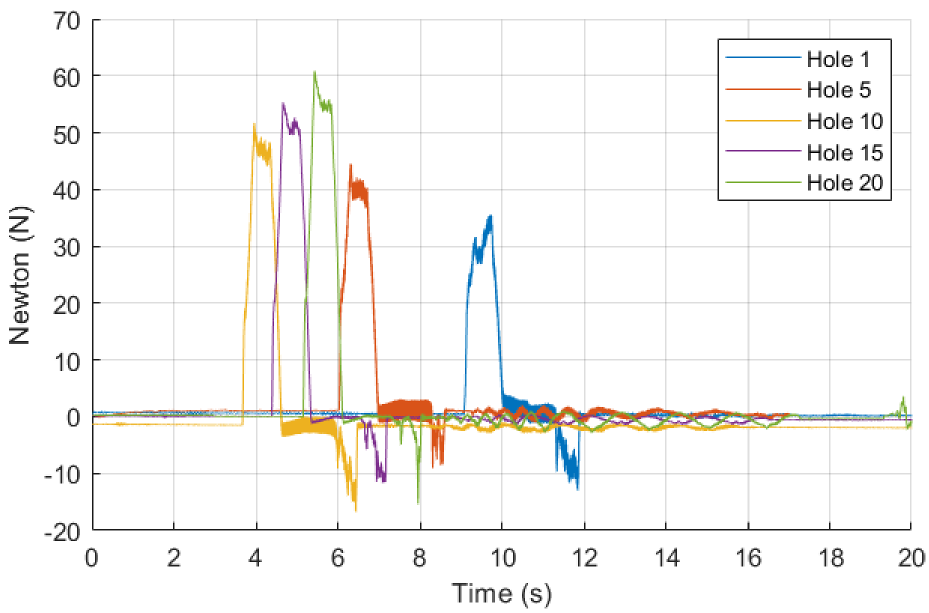

Figure 7-26: Fz signal elaborated with the mobile average for the holes no.1-5-10-15-20 during the drill-milling process with DM9 and 14000 rpm - 312.5 mm/min and 3 bores parameters.

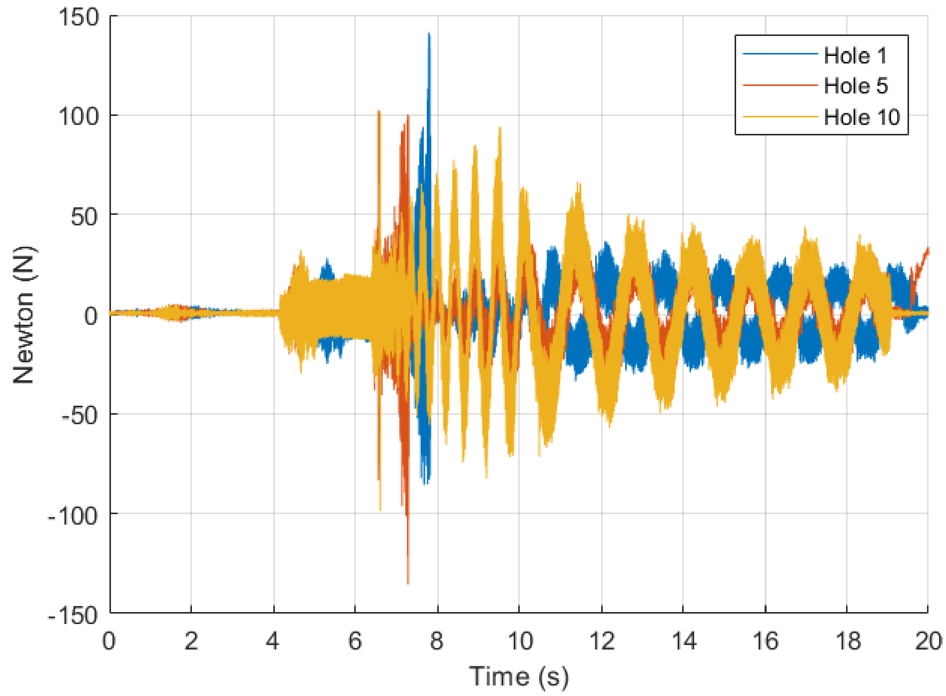

Figure 7-27: Fx signal acquired during the drill-milling process with DM9 and 16000 rpm - 312.5 mm/min and 5 bores parameters for the no. 12 holes.

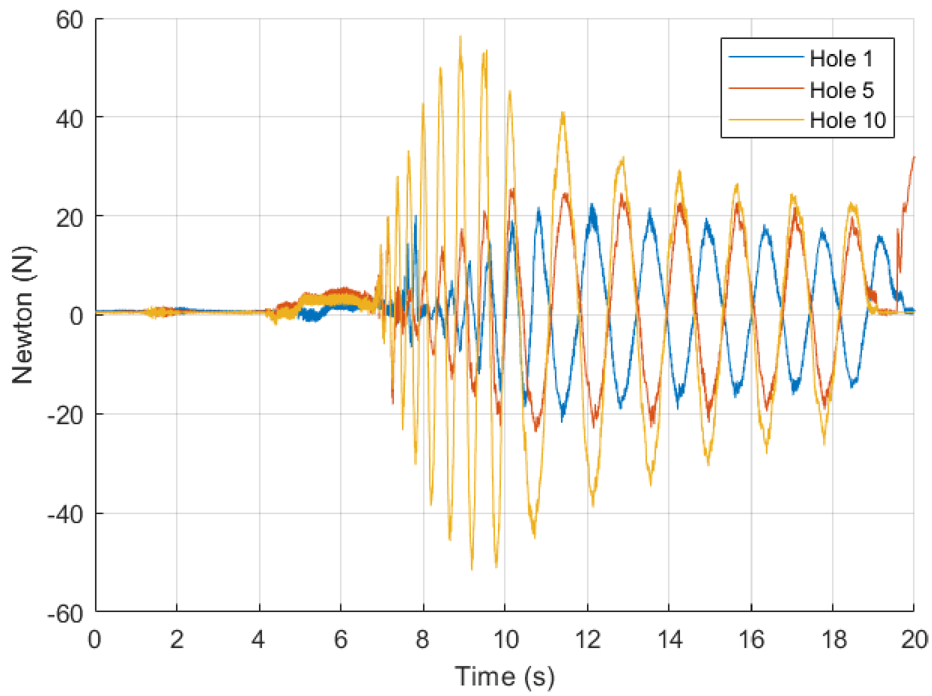

Figure 7-28: Fx signal elaborated with the mobile average for the holes no.1-5-10 during the drill-milling process with DM9 and 16000 rpm - 312.5 mm/min and 5 bores parameters.

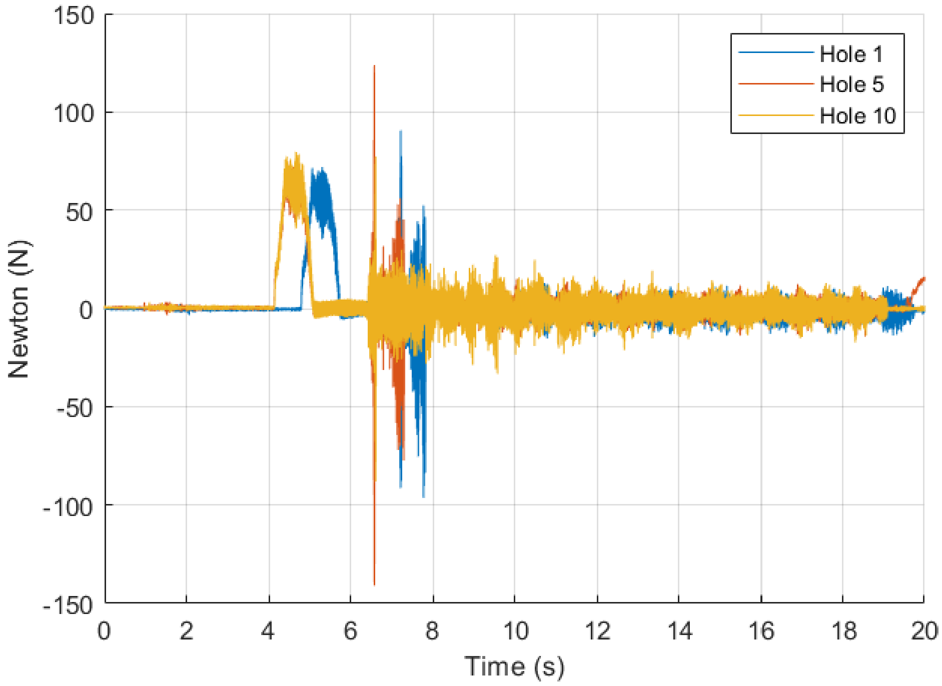

Figure 7-29: Fz signal acquired during the drill-milling process with DM9 and 16000 rpm - 312.5 mm/min and 5 bores parameters for the no. 12 holes.

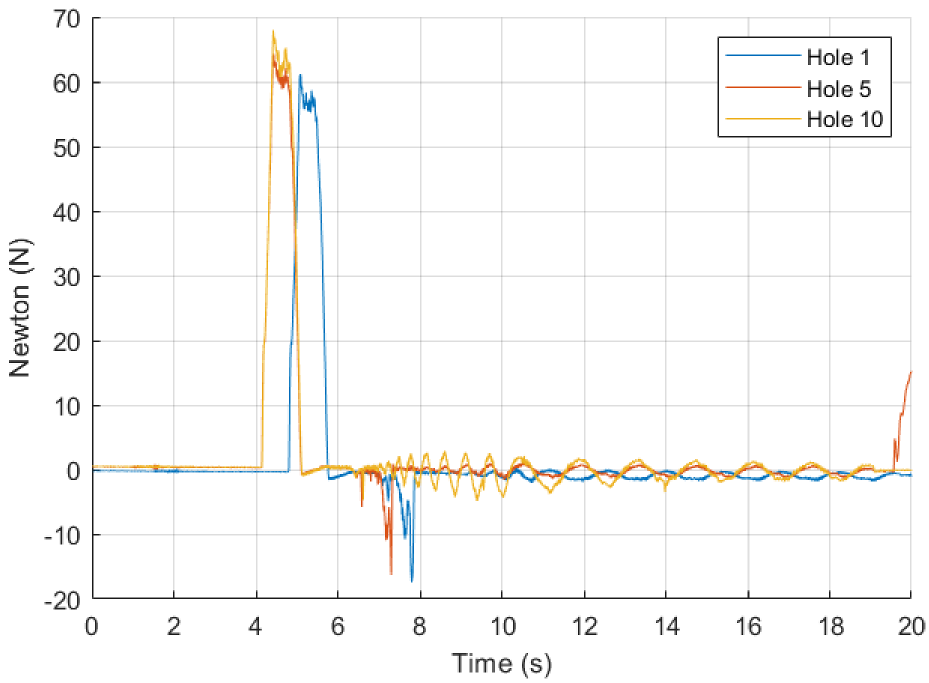

Figure 7-30: Fz signal elaborated with the mobile average for the holes no.1-5-10 during the drill-milling process with DM9 and 16000 rpm - 312.5 mm/min and 5 bores parameters.

7.3.5 TESTS TOOL RDM1

This new tool used the parameter 14000 rpm - 156.25 mm/min by programming the machine tool with 3 boring passes.

With this parameter, hole no. 9 was drilled before the tool breakage.

The test was interrupted here due to the non-tolerability of the hole dimensions.

Figure 7-31 shows the Fx signal during the drilling process for no. 1-5-9 holes. Figure 7-32 shows the Fx signal elaborated with the mobile average for the first 9 holes during the drill-milling process.

Figure 7-33 shows the Fz signal during the drilling process for no. 1-5-9 holes. Figure 7-34 shows the Fz signal elaborated with the mobile average for the first 9 holes during the drill-milling process.

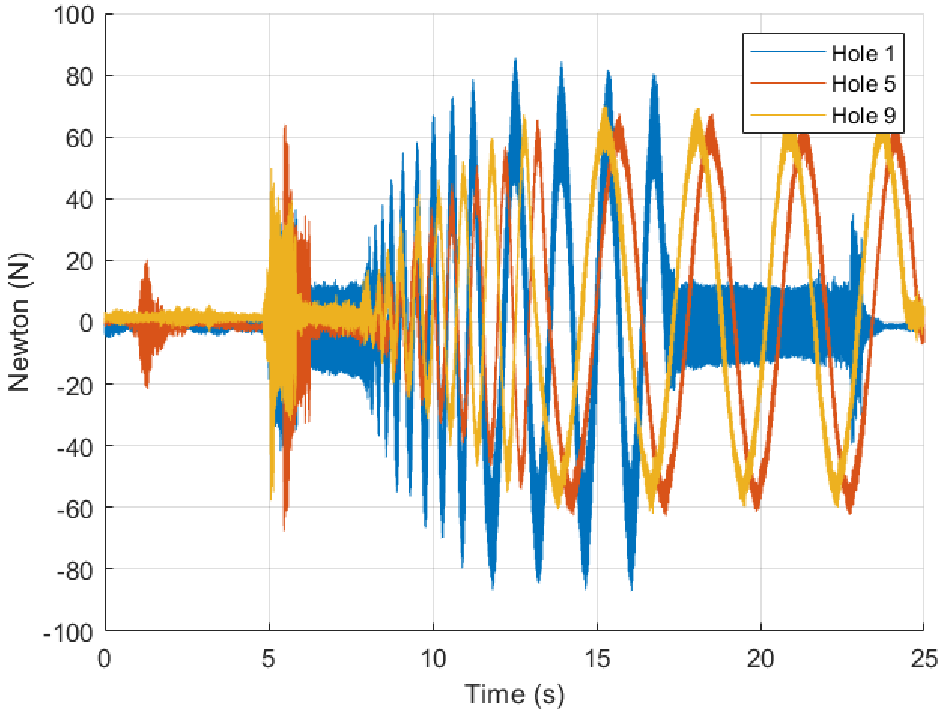

Figure 7-31: Fx signal acquired during the drill-milling process with RDM1 and 14000 rpm – 156.25 mm/min and 3 bores parameters for the no.1-5-9 holes.

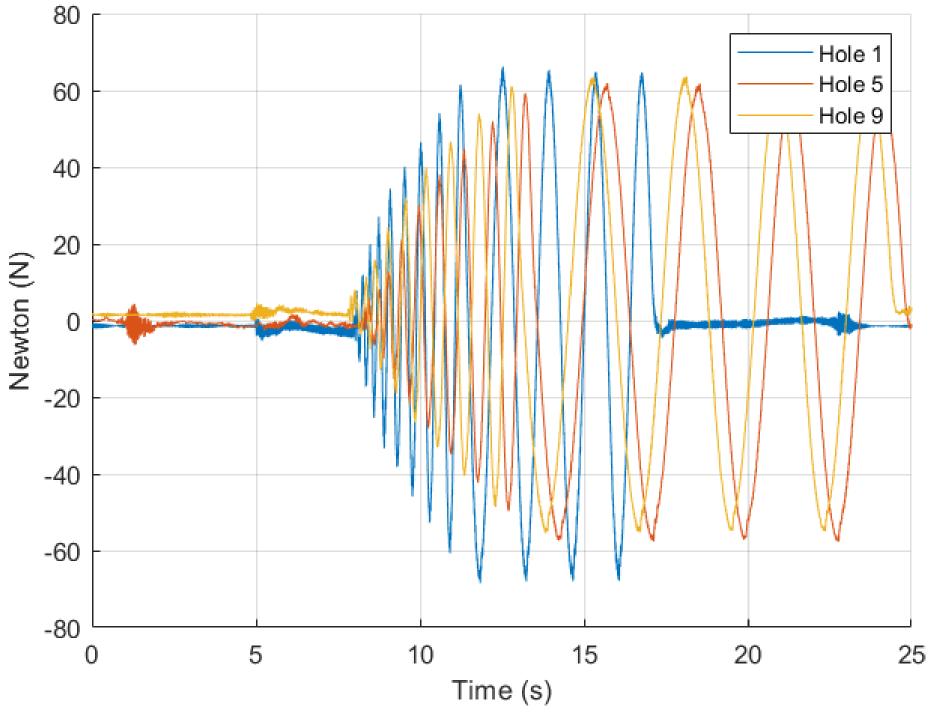

Figure 7-32: Fx signal elaborated with the mobile average for the no.1-5-9 holes during the drill-milling process with RDM1 and 14000 rpm - 156.25 mm/min and 3 bores parameters.

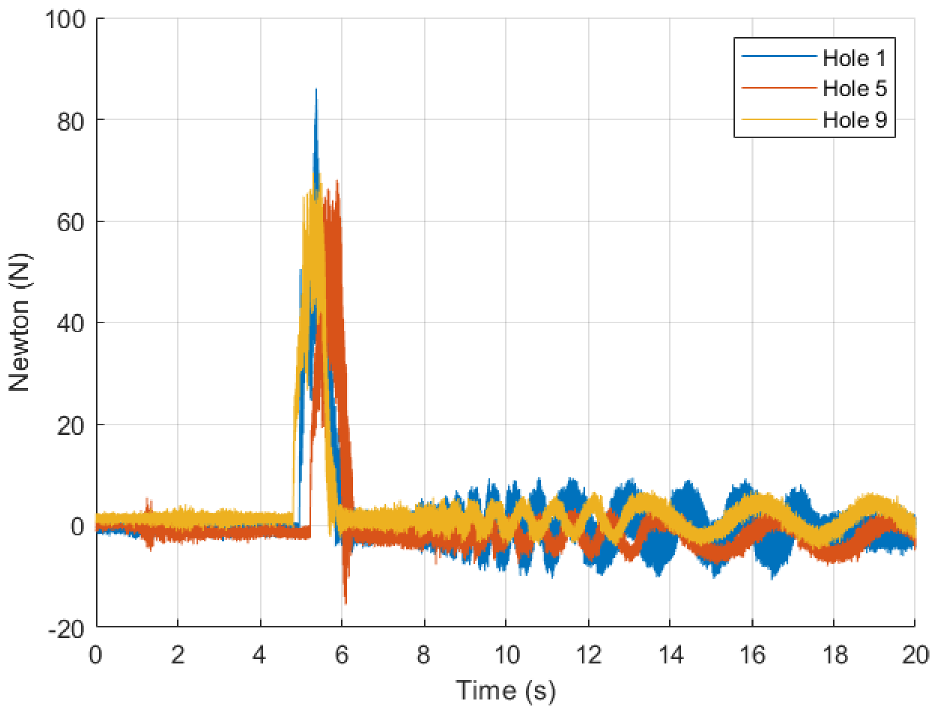

Figure 7-33: Fz signal acquired during the drill-milling process with RDM1 and 14000 rpm – 156.25 mm/min and 3 bores parameters for the no. 9 holes.

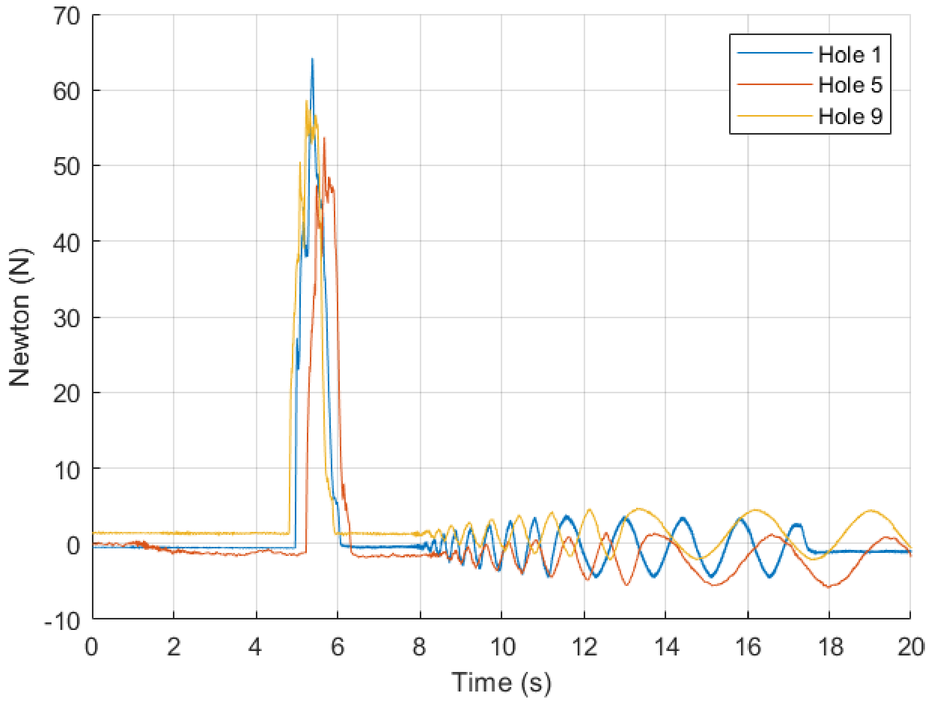

Figure 7-34: Fz signal elaborated with the mobile average for the no.1-5-9 holes during the drill-milling process with RDM1 and 14000 rpm - 156.25 mm/min and 3 bores parameters.

7.3.6 RESULTS FROM THE TOOL 4MM TESTS

After the second set of tests, it was decided to suspend the measurements made with the 4 mm tools since the holes did not meet the dimensional requirements as the tool was not able to mill such a high thickness. The tool often broke due to resonance during the tests.

7.4 TOOL DIAMETER 6 MM EXPERIMENTAL TESTS

The experimental campaign continued using tools with a larger diameter.

The tool was made of tungsten carbide (WC) and has a 6 mm diameter and 100 mm length; the drilling portion is 8 mm extended, with two cutting edges at a 120° point angle. Figure 7-35 shows the original tools.

Table 7-6 reports the geometrical features of the tools. In particular:

ha = helix angle;

ra= rake angle;
ca= clearance angle;
Z= flutes number.

The spindle speed was set to 10000 rpm and the feed rate to 375 mm/min, while the values of milling speed are reported in Table 7-6. For the study of this process, 60 holes were made with each type of tool.

Figure 7-35: Tool prototypes. The nominal diameter is 6 mm.

TOOL	GEOMETRY	RPM	MM/MIN
DM11	ha20ra10ca7 Z3	14000	375
DM12	ha20ra15ca7 Z3	14000	375
DM13	ha20ra10ca7 Z3	14000	250
DM14	ha20ra15ca7 Z3	14000	250
DM15	ha15ra10ca7 Z3	14000	375
DM16	ha15ra15ca7 Z3	14000	375
DM17	ha20ra10ca7 Z5	14000	375
DM18	ha15ra10ca7 Z5	14000	125
DM19	ha20ra15ca7 Z5	14000	187.5
DM20	ha15ra15ca7 Z5	14000	125

Table 7-6: Comparison of newly developed drill-milling tools (ha—helix angle; ra—rake angle; ca—clearance angle; Z—flutes number) and their drilling parameter.

Fx and Fz signals were acquired to analyse the cutting forces that develop during the hole-milling process. Fz is predominant in the first phase (drilling process), while Fx is predominant in the second phase, where it is possible to observe the characteristic sinusoidal trend of the peripheral milling process. Then, the signals were conditioned using the moving average method (with a window length of 200 samples, corresponding to 0.02 s). This operation aims to facilitate the extraction of the maximum values of force signals without taking into account high-frequency oscillations.

In this paragraph, the experimental results will be investigated by analyzing the roughness trends as a tool wear function. These trends were obtained by calculating the average roughness Ra values using a contact profilometer described in Paragraph 5.2. The measurement was performed with the same methods described above. Moreover, the geometric quality of the drilling holes was measured.

7.4.1 TESTS TOOL DM11

Figure 7-36 shows the maximum thrust force obtained during the drilling process with DM11, along, respectively, Z and X directions.

It is recorded a value of **Fzmax** to 118.75 N and a **Fxmax** to 147.95 N.

The Fzmax trend is comparable with the results obtained during the traditional drilling. Instead, Fxmax has a growing trend up to hole no. 25, and successively the trend is constant around the value of 140N.

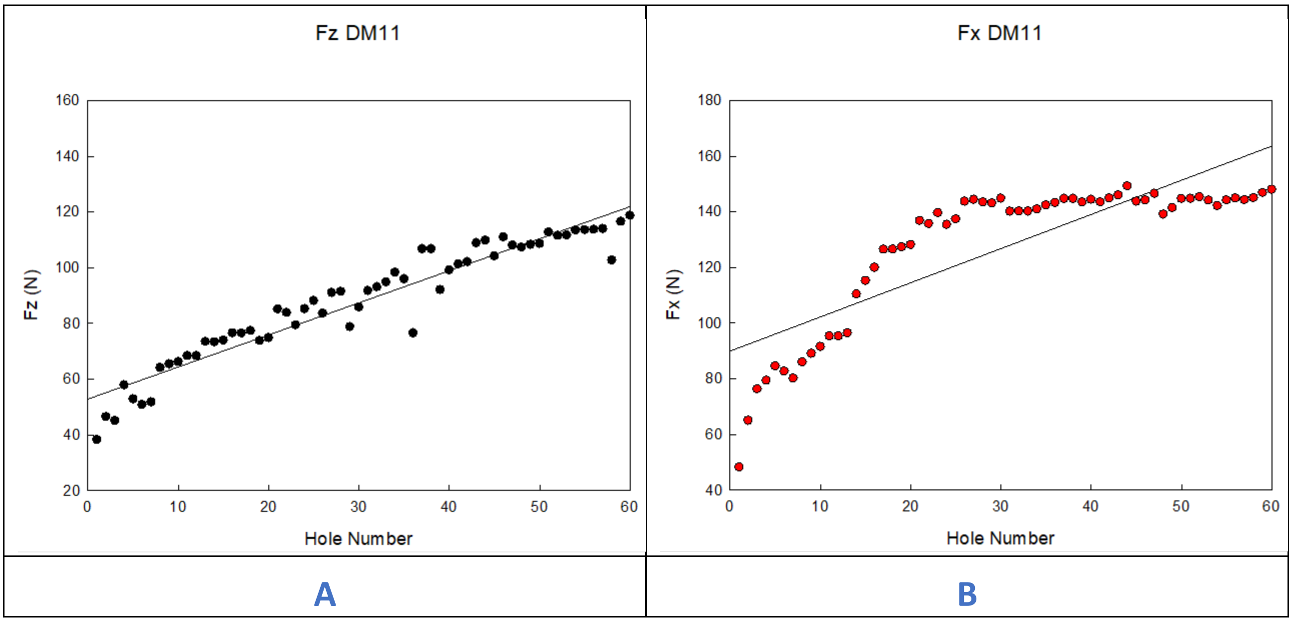

Figure 7-36: Maximum cutting force in the (A) X direction, Fxmax, and (B) Z direction, Fzmax, measured for tools DM11.

Figure 7-37 A shows the dimensional hole analysis, performed along with four directions of the single hole, and reports an average trend in the hole diameter from hole no. 1 to hole no. 60. The **Δdiameter** from hole no. 1 to hole no. 60 is 0.52 mm.

Figure 7-37 B shows the eccentricity from hole no. 1 to hole no. 60. All the holes are eccentric, except the last one.

Figure 7-38 reported the trend of the roughness variation with the progress of tool wear. The roughness value related to the single hole was an average value between three measurements. In particular, the analysis of the Ra was carried out for holes no. 1-10-20-30-40-50-60. The **Δroughness** from hole no. 1 to hole no. 60 is 1.40µm.

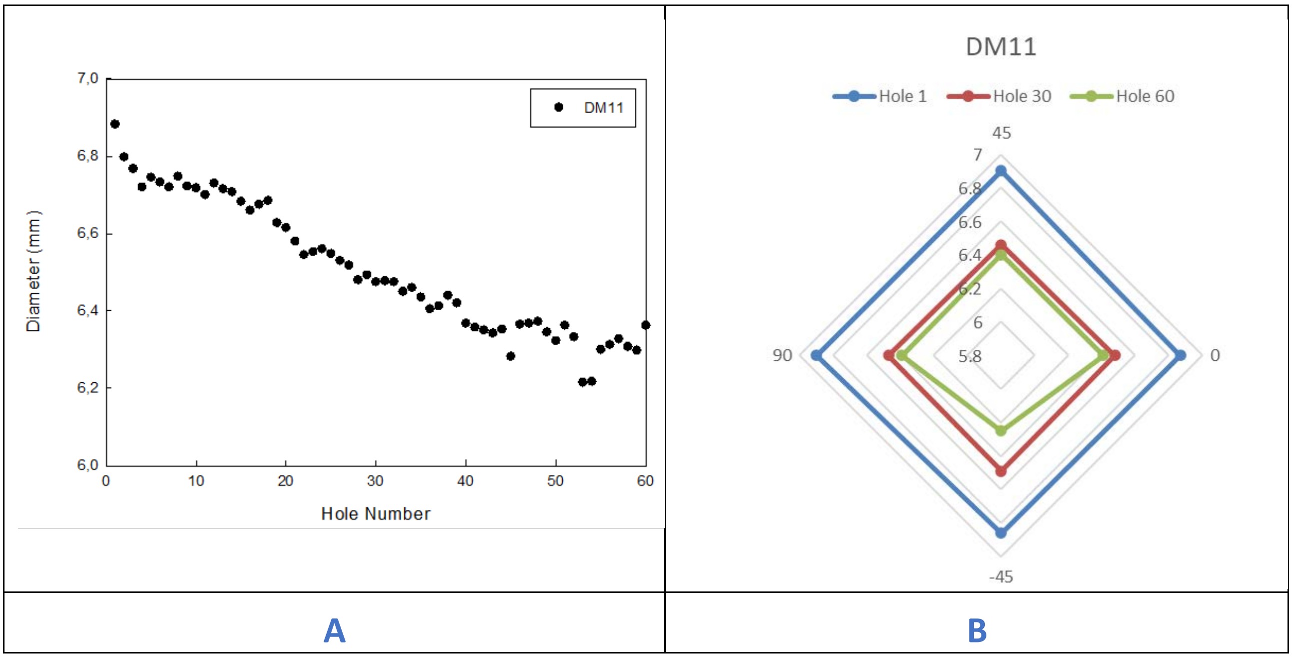

Figure 7-37: Hole diameter measured from hole no. 1 to no. 60 drilled by DM11 (A) and (B)dimensional analysis for the number of 1-15-30 holes for DM11 (unit of measure in mm).

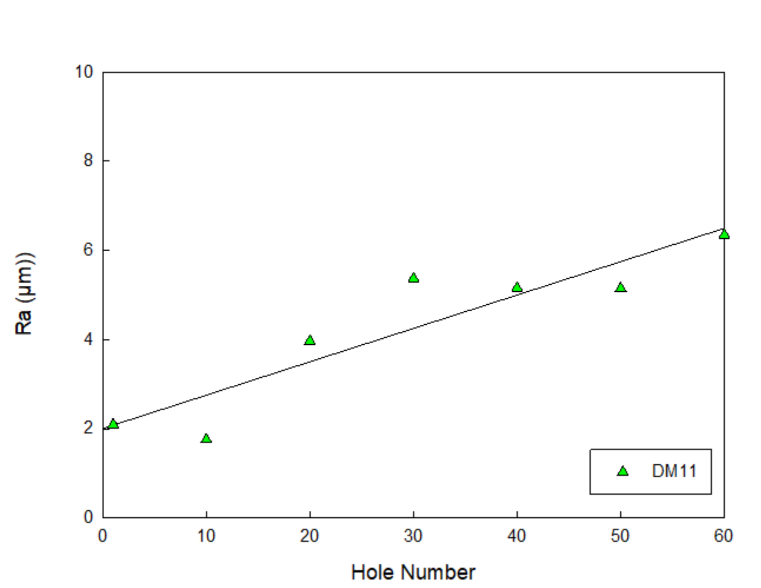

Figure 7-38: Values of Ra relative to the holes obtained with DM11.

7.4.2 TESTS TOOL DM12

Figure 7-39 shows the maximum thrust force obtained during the drilling process with DM12 along, respectively, Z and X directions.

It is recorded a value of **Fzmax** to 244.15 N and a **Fxmax** to 186.44 N.

The Fzmax and Fxmax have a growing trend.

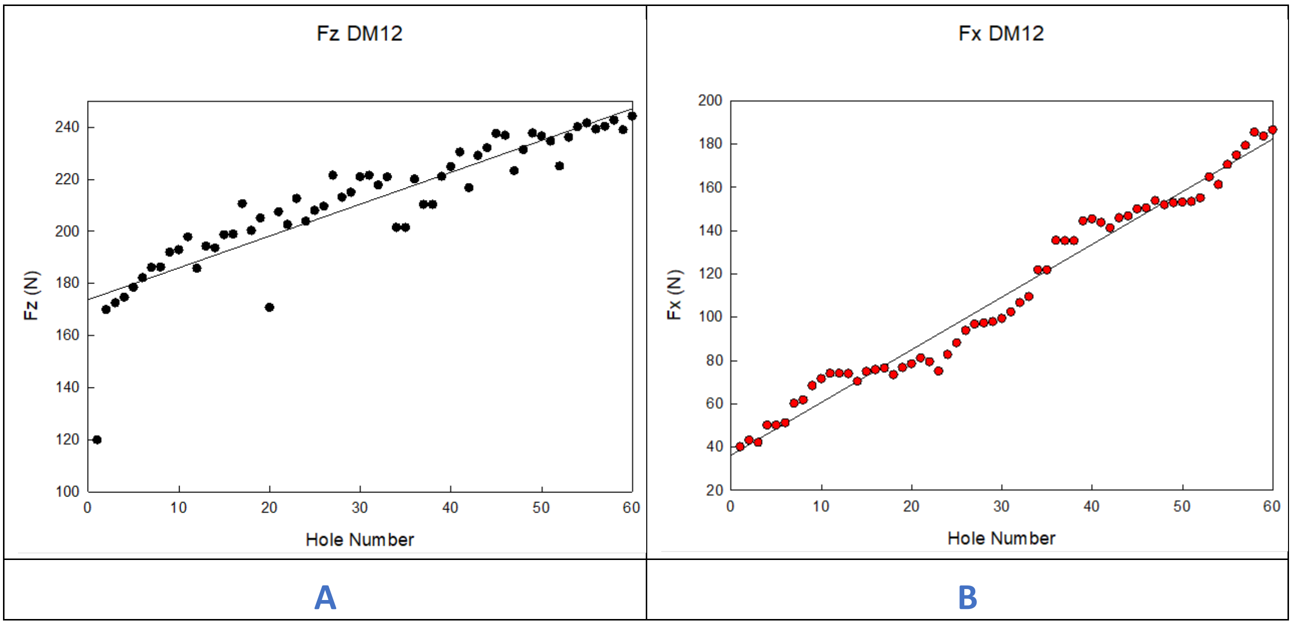

Figure 7-39: Maximum cutting force in the (A) X direction, Fxmax, and (B) Z direction, Fzmax, measured for tools DM12.

Figure 7-40 A shows the dimensional hole analysis, performed along with four directions of the single hole, and reports an average trend in the hole diameter from hole no. 1 to hole no. 60. The **Δdiameter** from hole no. 1 to hole no. 60 is 0.445 mm. Figure 7-40 B shows the eccentricity from hole no. 1 to hole no. 60.

Figure 7-41 reported the trend of the roughness variation with the progress of tool wear. The roughness value relating to the single hole was an average value between three measurements. In particular, the analysis of the Ra was carried out for holes no. 1-10-20-30-40-50-60. The **Δroughness** from hole no. 1 to hole no. 60 is 3.307µm.

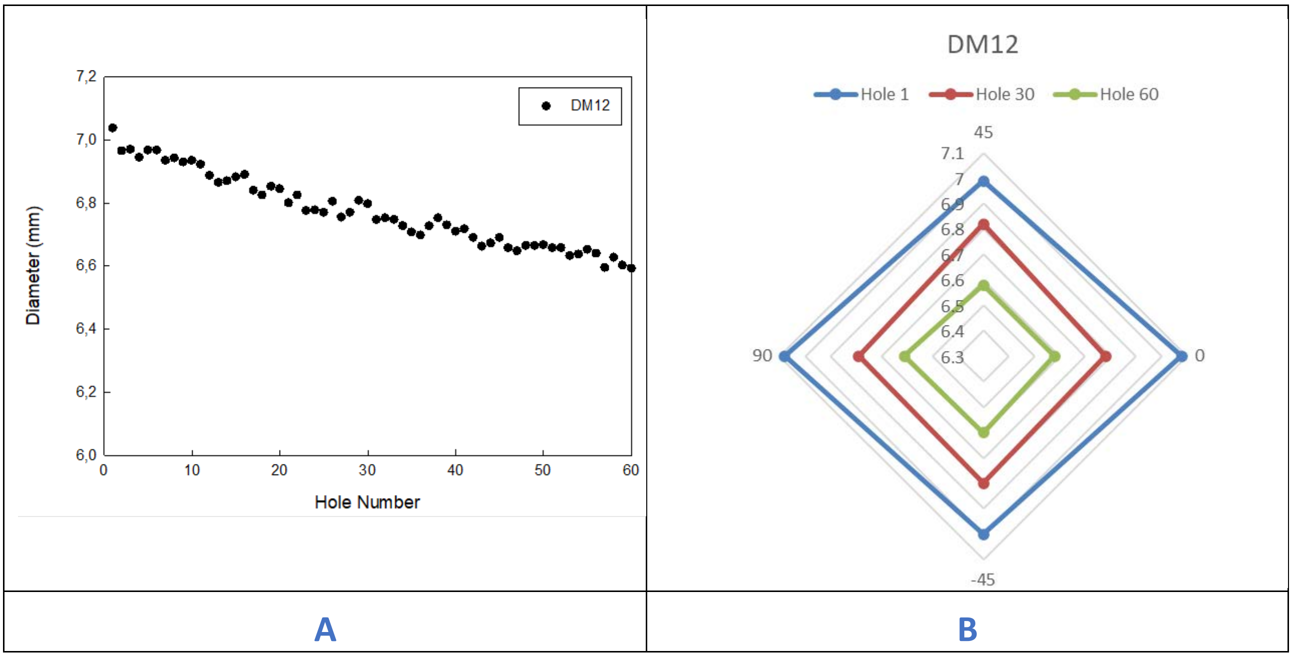

Figure 7-40: Hole diameter measured from hole no. 1 to no. 60 drilled by DM12 (A) and (B)dimensional analysis for the number of 1-15-30 holes for DM12 (unit of measure in mm).

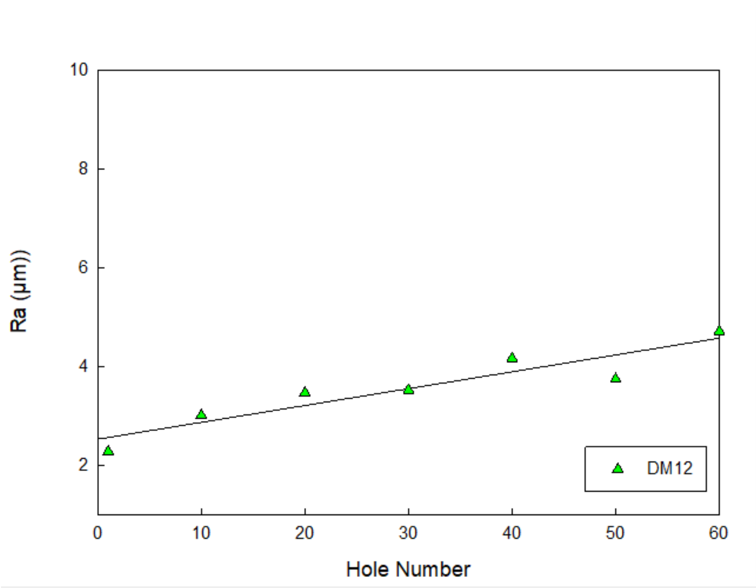

Figure 7-41: Values of Ra relative to the holes obtained with DM12.

7.4.3 TESTS TOOL DM13

Figure 7-42 shows the maximum thrust force obtained during the drilling process with DM13 along, respectively, Z and X directions.

It is recorded a value of **Fzmax** to 130.13 N and a **Fxmax** to 173.23 N.

The Fzmax trend is comparable with the results obtained during the traditional drilling. Instead, Fxmax has a growing trend up to hole no. 15, and successively the trend grows slower than the first hole. The trend after hole 45 is constant around the value of 170 N.

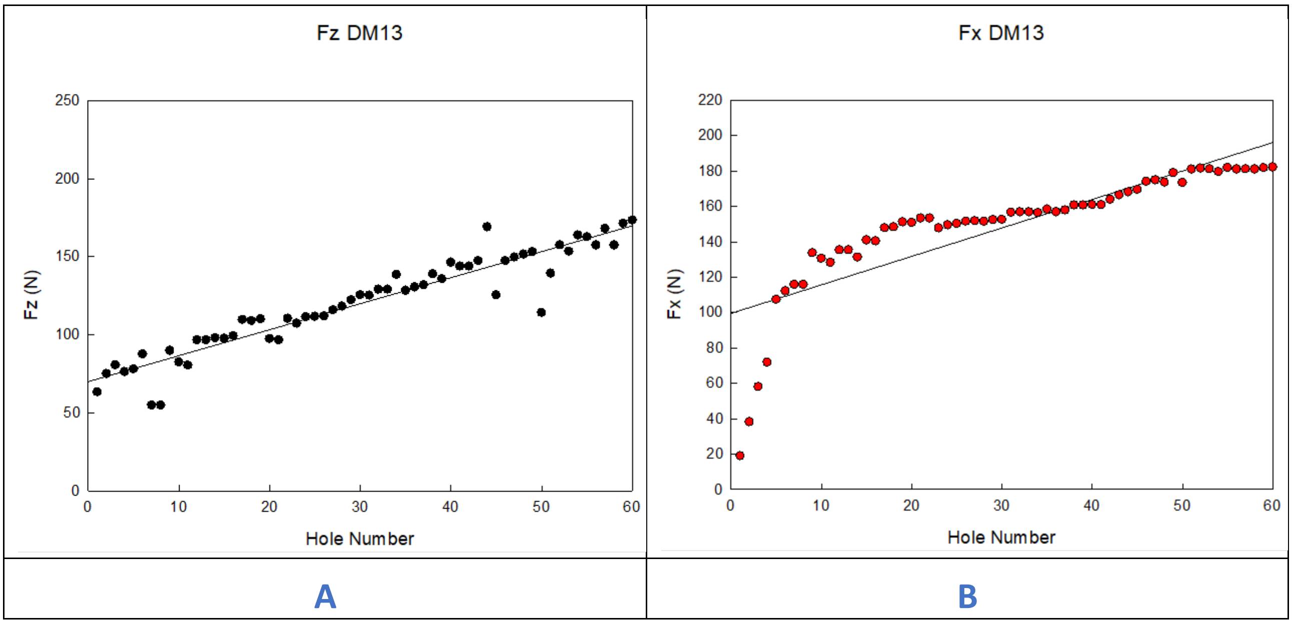

Figure 7-42: Maximum cutting force in the (A) X direction, Fxmax, and (B) Z direction, Fzmax, measured for tools DM13.

Figure 7-43 A shows the dimensional hole analysis, performed along with four directions of the single hole, and reports an average trend in the hole diameter from hole no. 1 to hole no. 60. The **Δdiameter** from hole no. 1 to hole no. 60 is 0.565 mm.

Figure 7-43 B shows the eccentricity from hole no. 1 to hole no. 60. An eccentric hole is observed, but with a quick reduction of diameter from hole no. 1 and hole no. 30.

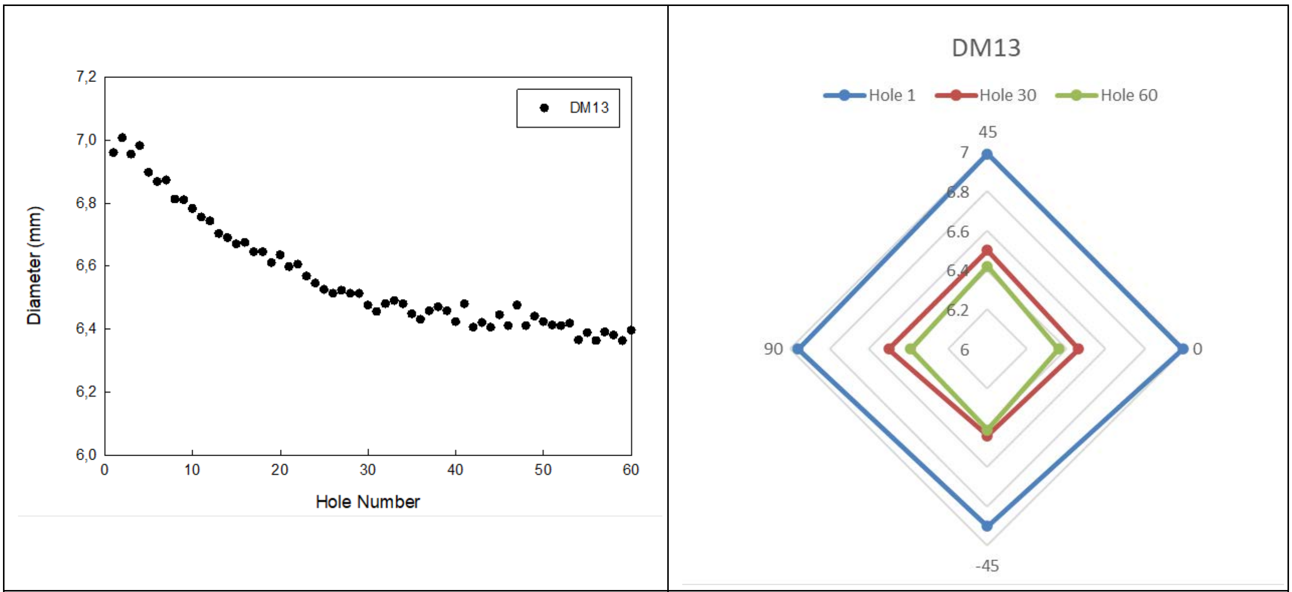

A | B

Figure 7-43: Hole diameter measured from hole no. 1 to no. 60 drilled by DM13 (A) and (B)dimensional analysis for the number of 1-15-30 holes for DM13 (unit of measure in mm).

Figure 7-44 reported the trend of the roughness variation with the progress of tool wear. The roughness value relating to the single hole was an average value between three measurements. In particular, the analysis of the Ra was carried out for holes no. 1-10-20-30-40-50-60. The **Δroughness** from hole no. 1 to hole no. 60 is 3.627µm.

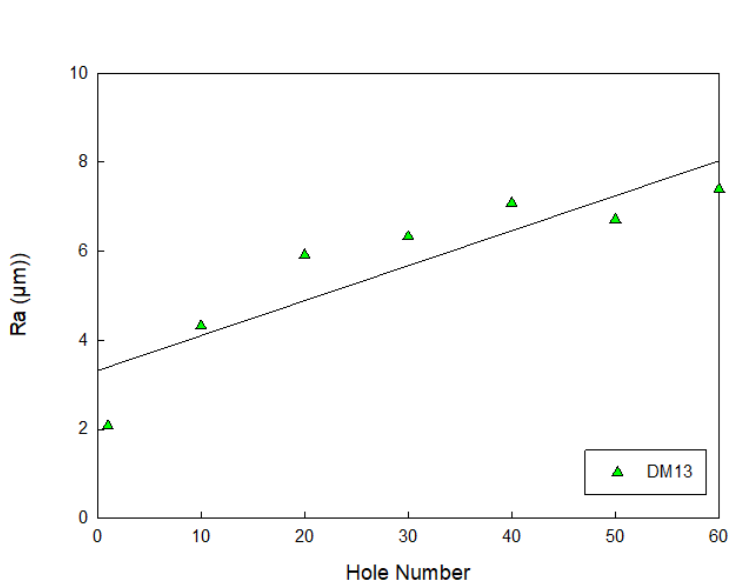

Figure 7-44: Values of Ra relative to the holes obtained with DM13.

7.4.4 TESTS TOOL DM14

Figure 7-45 shows the maximum thrust force obtained during the drilling process with DM14 along, respectively, Z and X directions.

It is recorded a value of **Fzmax** to 155.33 N, and a **Fxmax** to 161.59 N. Fzmax and Fxmax have a growing trend.

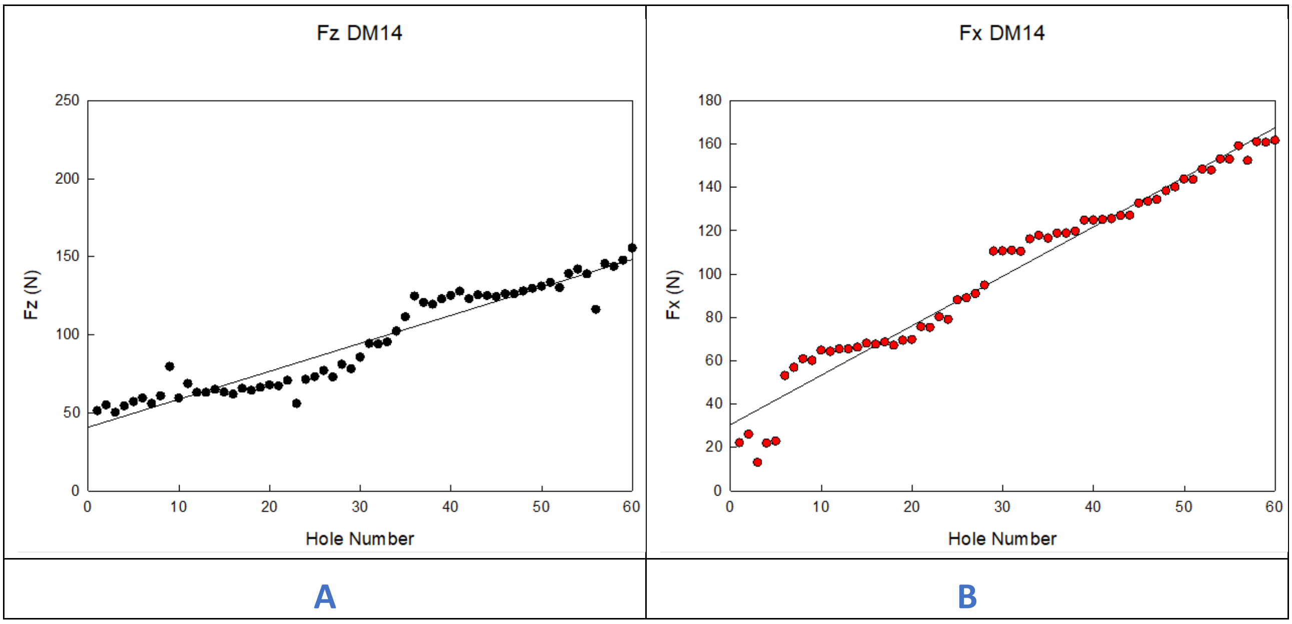

Figure 7-45: Maximum cutting force in the (A) X direction, Fxmax, and (B) Z direction, Fzmax, measured for tools DM14.

Figure 7-46 A shows the dimensional hole analysis, performed along with four directions of the single hole, and reports an average trend in the hole diameter from hole no. 1 to hole no. 60. The **Δdiameter** from hole no. 1 to hole no. 60 is 0.57 mm.

Figure 7-46 B shows the eccentricity from hole no. 1 to hole no. 60. An eccentric hole is observed.

Figure 7-47 shows the trend of the roughness variation with the progress of tool wear. The roughness value relating to the single hole was an average value between three measurements. In particular, the analysis of the Ra was carried out for holes no. 1-10-20-30-40-50-60. The **Δroughness** from hole no. 1 to hole no. 60 is 3.140μm.

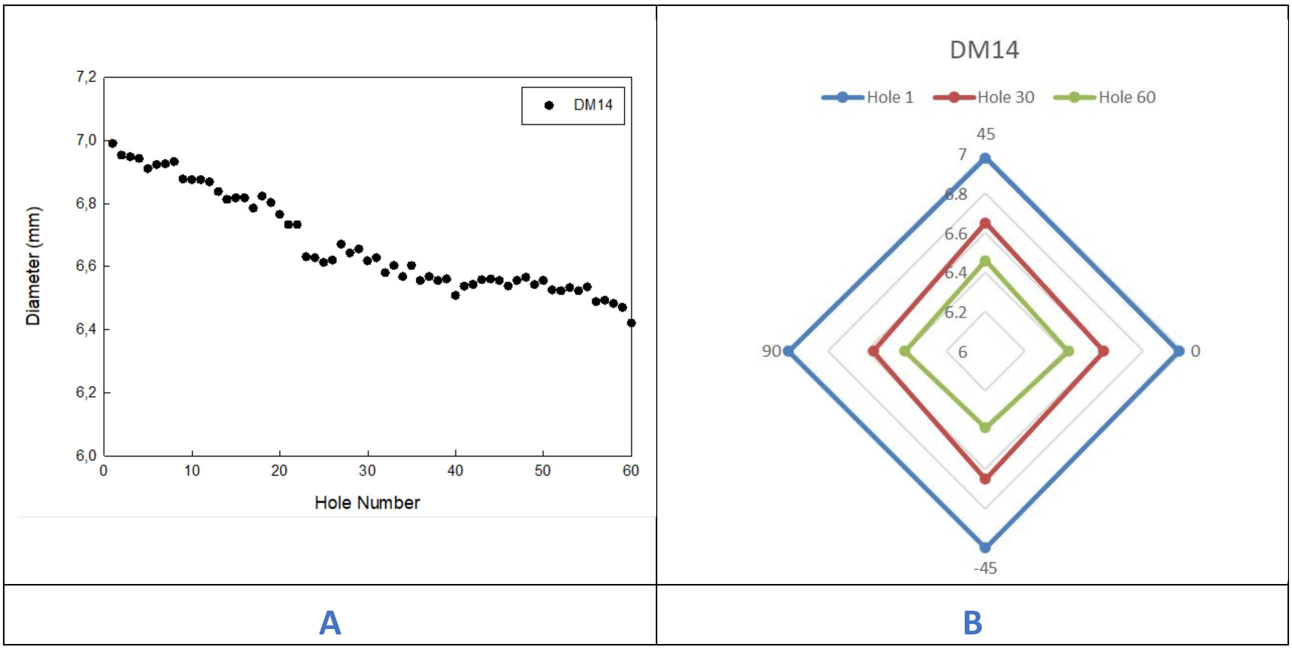

Figure 7-46: Hole diameter measured from hole no. 1 to no. 60 drilled by DM14 (A) and (B)dimensional analysis for the number of 1-15-30 holes for DM14 (unit of measure in mm).

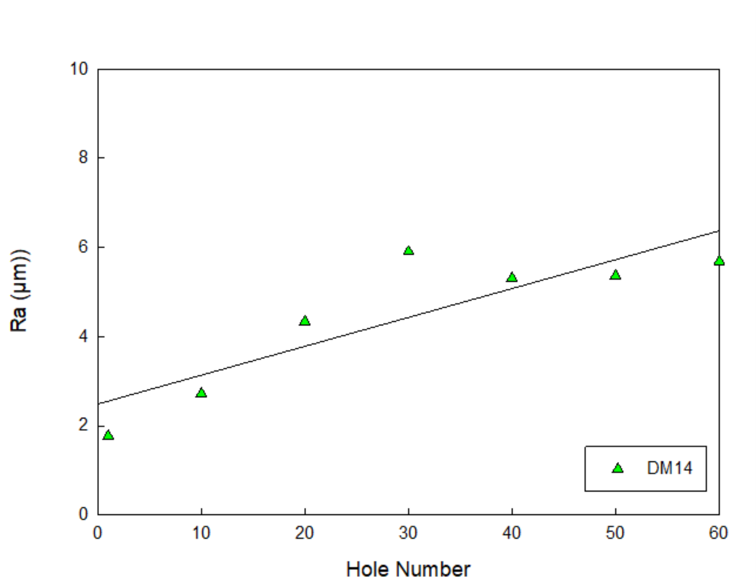

Figure 7-47: Values of Ra relative to the holes obtained with DM14.

7.4.5 TESTS TOOL DM15

Figure 7-48 shows the maximum thrust force obtained during the drilling process with DM15 along, respectively, Z and X directions.

It is recorded a value of **Fzmax** to 140.05 N and a **Fxmax** to 201.27 N.

Fxmax has a growing trend. Fzmax has a growth trend until hole no. 30, and successively the trend is constant around the value 120 N.

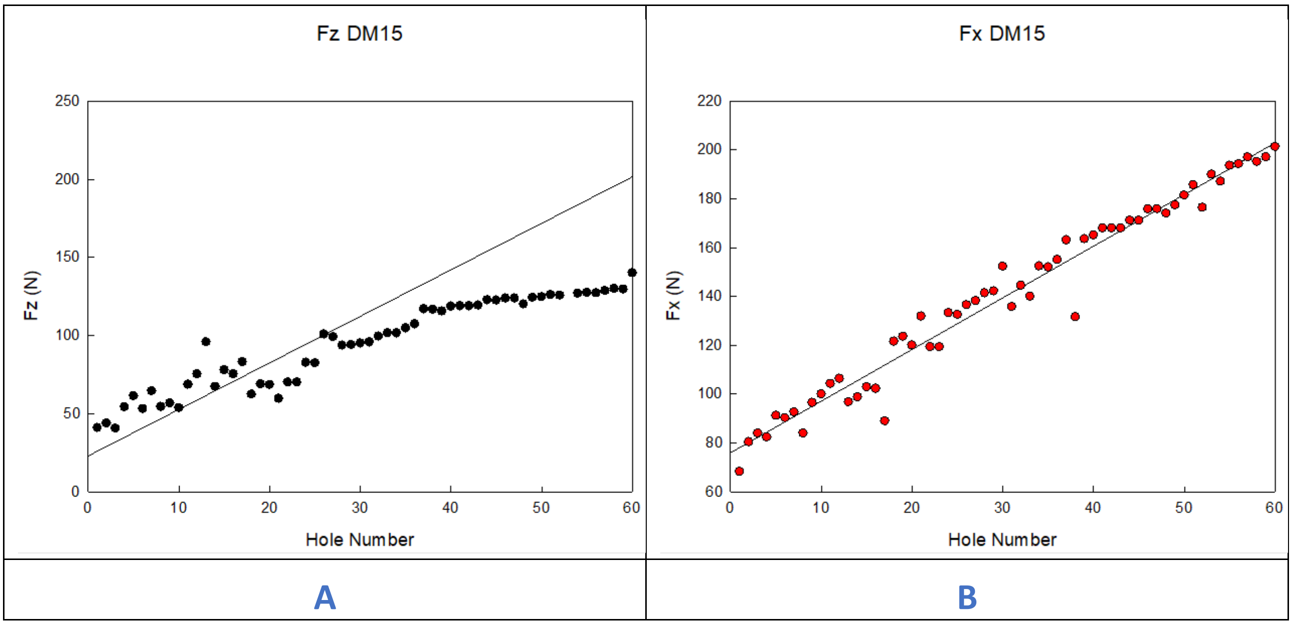

Figure 7-48: Maximum cutting force in the (A) X direction, Fxmax, and (B) Z direction, Fzmax, measured for tools DM15.

Figure 7-49 A shows the dimensional hole analysis, performed along with four directions of the single hole, and reports an average trend in the hole diameter from hole no. 1 to hole no. 60. The **Δdiameter** from hole no. 1 to hole no. 60 is 0.54 mm.

Figure 7-49 B shows the eccentricity from hole no. 1 to hole no. 60. An eccentric hole is observed, except for the last hole.

Figure 7-50 shows the trend of the roughness variation with the progress of tool wear. The roughness value relating to the single hole was an average value between three measurements. In particular, the analysis of the Ra was carried out for holes no. 1-10-20-30-40-50-60. The **Δroughness** from hole no. 1 to hole no. 60 is 3.240µm.

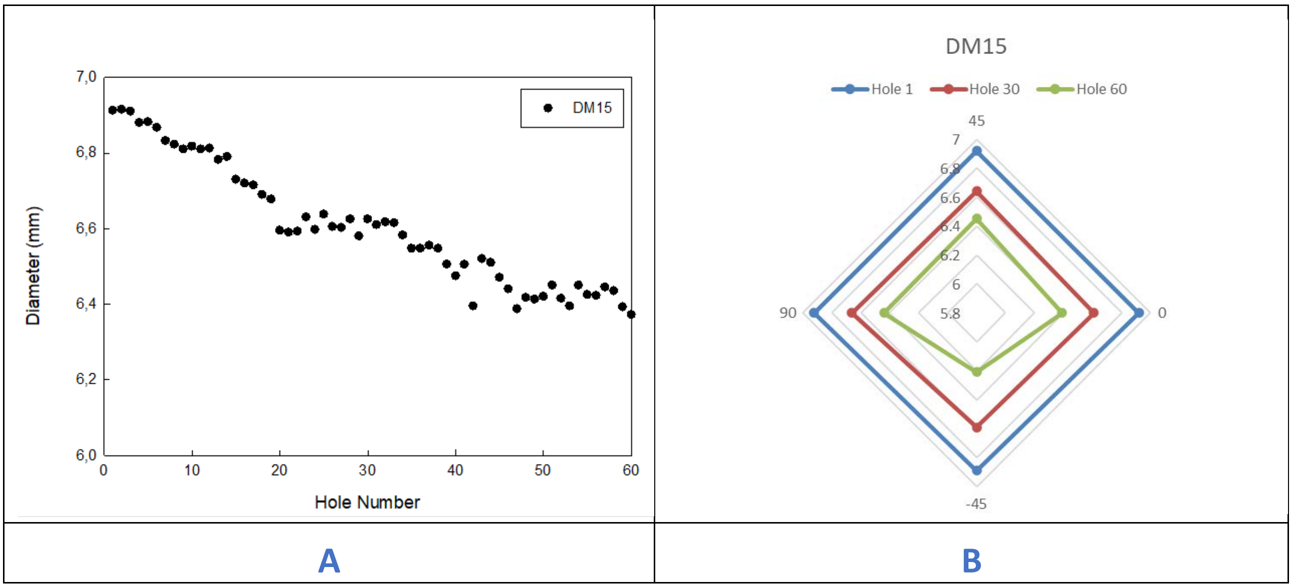

Figure 7-49: Hole diameter measured from hole no. 1 to no. 60 drilled by DM15 (A) and (B)dimensional analysis for the number of 1-15-30 holes for DM15 (unit of measure in mm).

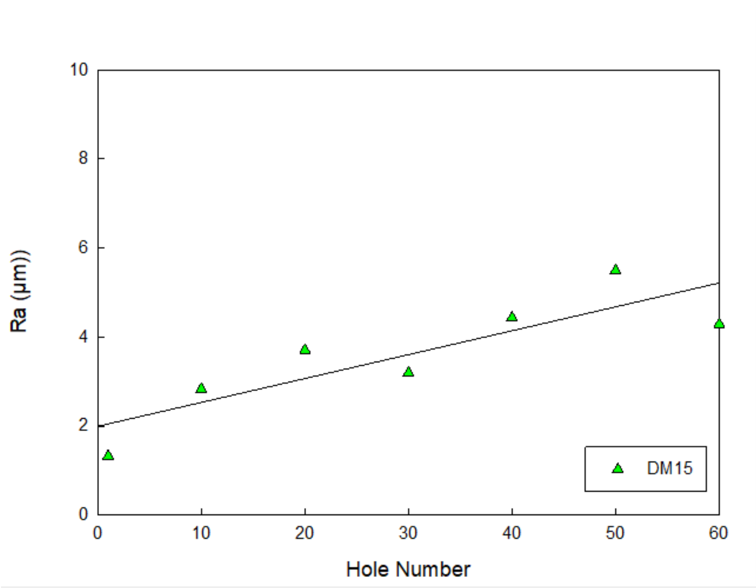

Figure 7-50: Values of Ra relative to the holes obtained with DM15.

7.4.6 TESTS TOOL DM16

Figure 7-51 shows the maximum thrust force obtained during the drilling process with DM16 along, respectively, Z and X directions.

It is recorded a value of **Fzmax** to 191.25 N and a **Fxmax** to 187.32 N.

The Fzmax and Fxmax have a growing trend.

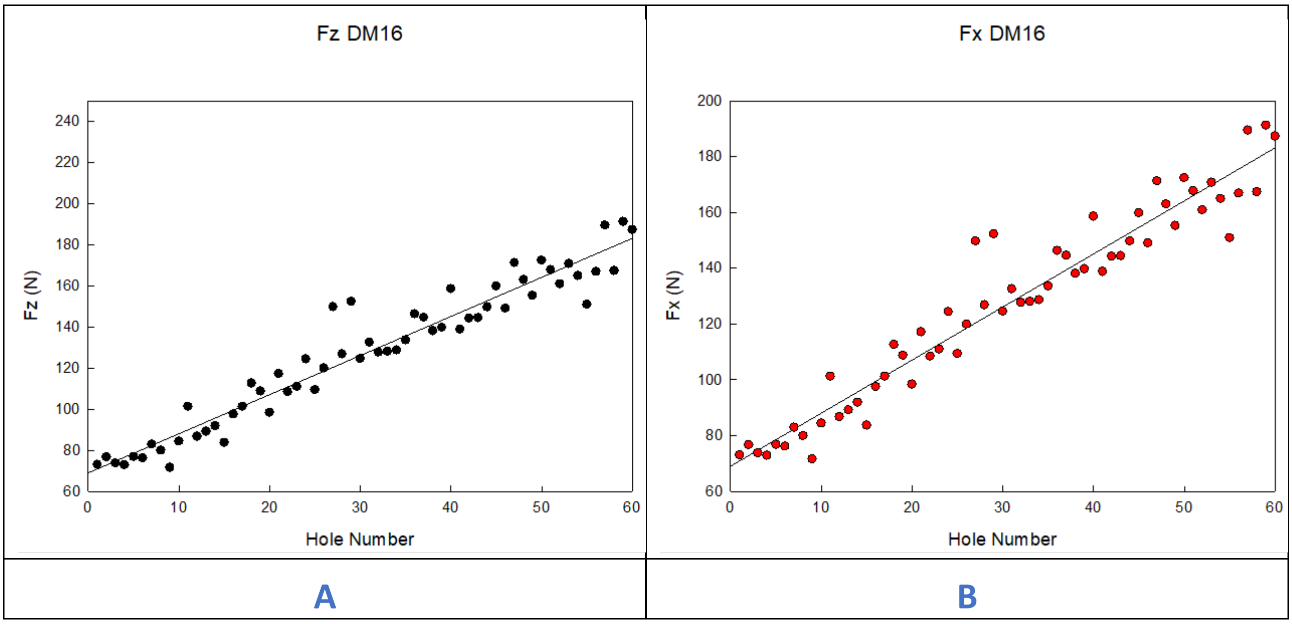

Figure 7-51: Maximum cutting force in the (A) X direction, Fxmax, and (B) Z direction, Fzmax, measured for tools DM16.

Figure 7-52 A shows the dimensional hole analysis, performed along with four directions of the single hole, and reports an average trend in the hole diameter from hole no. 1 to hole no. 60. The **Δdiameter** from hole no. 1 to hole no. 60 is 0.502 mm.

Figure 7-52 B shows the eccentricity from hole no. 1 to hole no. 60. An eccentric hole with a quick reduction of diameter from hole no. 1 and hole no. 30 was observed.

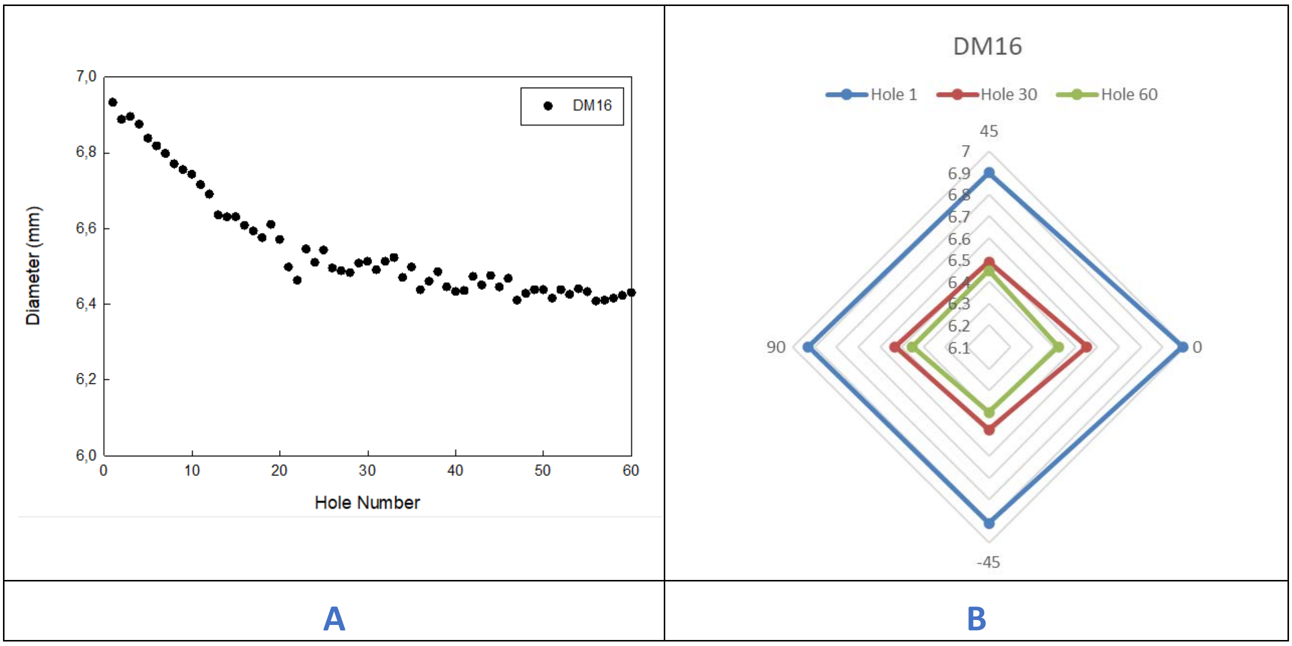

Figure 7-52: Hole diameter measured from hole no. 1 to no. 60 drilled by DM16 (A) and (B)dimensional analysis for the number of 1-15-30 holes for DM16 (unit of measure in mm).

Figure 7-53 shows the trend of the roughness variation with the progress of tool wear. The roughness value relating to the single hole was an average value between three measurements. In particular, the analysis of the Ra was carried out for holes no. 1-10-20-30-40-50-60. The **Δroughness** from hole no. 1 to hole no. 60 is 4.576 µm.

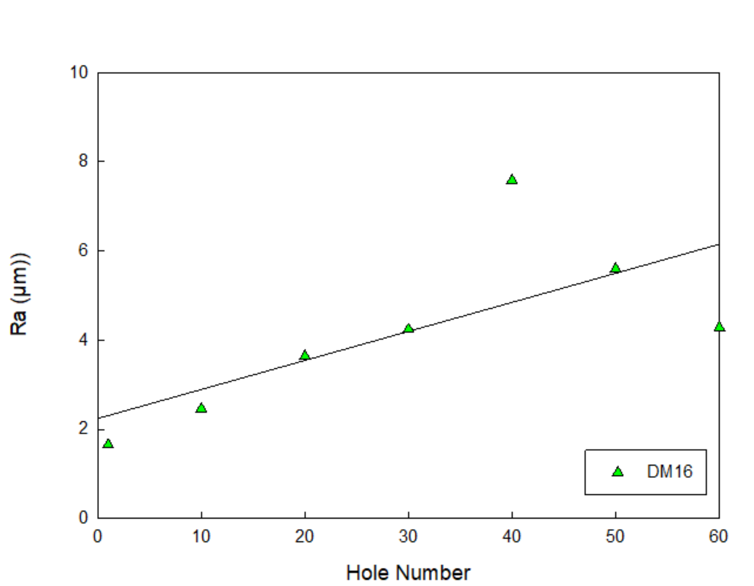

Figure 7-53: Values of Ra relative to the holes obtained with DM16.

Figure 7-54 shows the maximum thrust force obtained during the drilling process with DM17 along, respectively, Z and X directions.

It is recorded a value of **Fzmax** to 179.56 N and a **Fxmax** to 181.71 N.

Fxmax has a growing trend. Instead, Fzmax has a growing trend up to hole no. 10, and successively the trend grows slower than the first hole. The trend after hole 35 is constant around the value of 150 N.

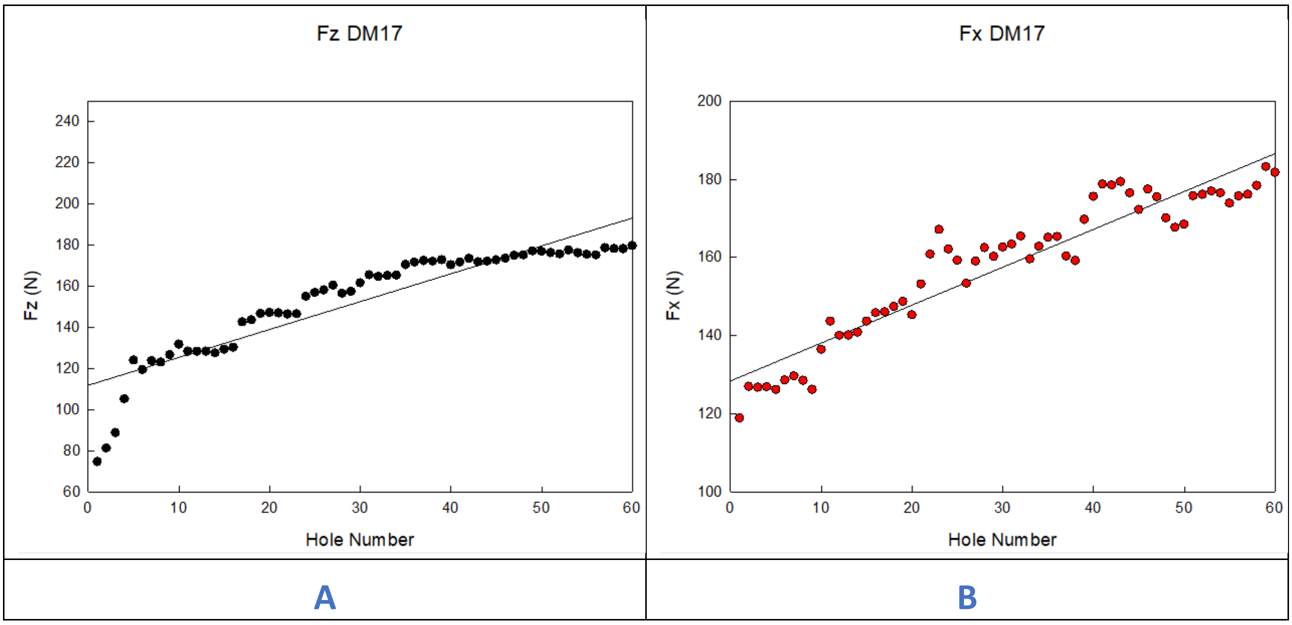

Figure 7-54: Maximum cutting force in the (A) X direction, Fxmax, and (B) Z direction, Fzmax, measured for tools DM17.

Figure 7-55 A shows the dimensional hole analysis, performed along with four directions of the single hole, and reports an average trend in the hole diameter from hole no. 1 to hole no. 60. The **Δdiameter** from hole no. 1 to hole no. 60 is 0.52 mm.

Figure 7-55 B shows the eccentricity from hole no. 1 to hole no. 60. An eccentric hole with a quick reduction of diameter from hole no. 1 and hole no. 30 was observed.

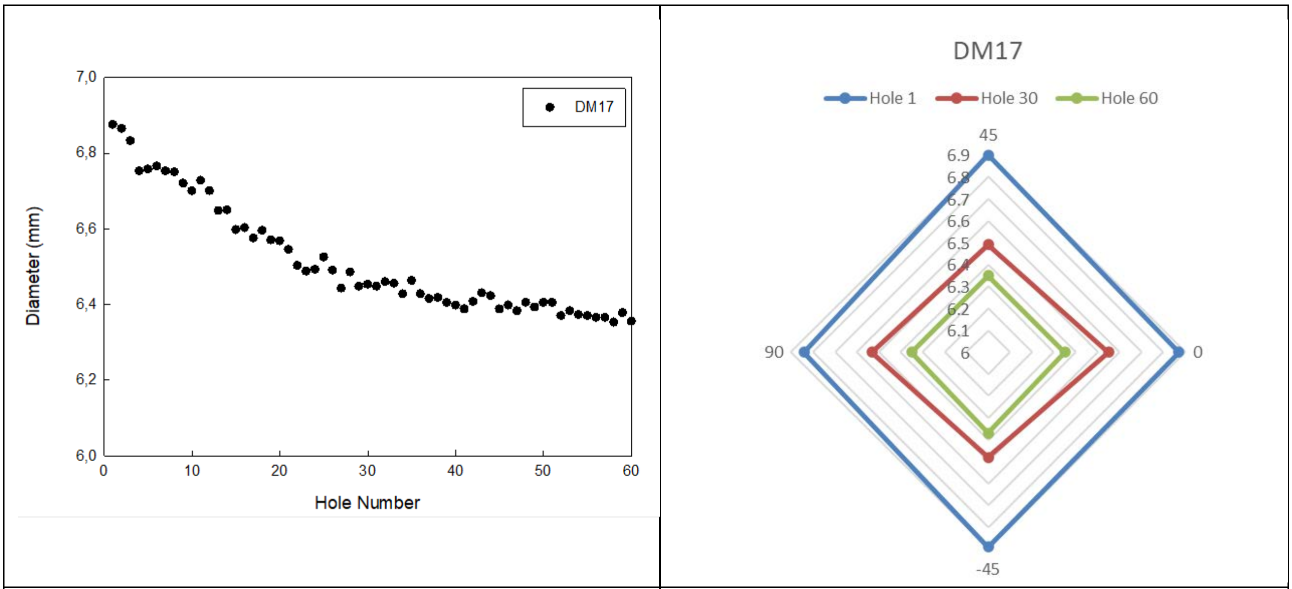

A	B

Figure 7-55: Hole diameter measured from hole no. 1 to no. 60 drilled by DM17 (A) and (B)dimensional analysis for the number of 1-15-30 holes for DM17 (unit of measure in mm).

Figure 7-56 reports the trend of the roughness variation with the progress of tool wear. The roughness value relating to the single hole was an average value between three measurements. In particular, the analysis of the Ra was carried out for holes no. 1-10-20-30-40-50-60. The **Δroughness** from hole no. 1 to hole no. 60 is 1.767µm.

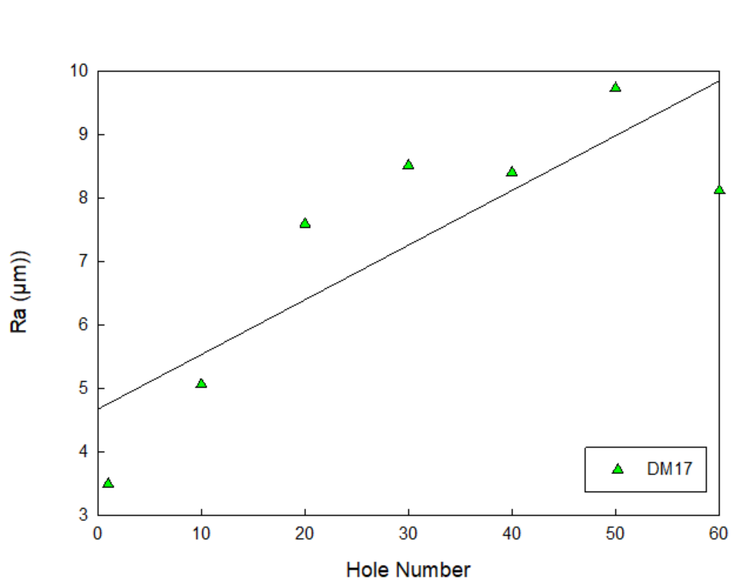

Figure 7-56: Values of Ra relative to the holes obtained with DM17.

7.4.8 TESTS TOOL DM18

With DM18, the tool broke at hole no. 20.

Figure 7-57 shows the maximum thrust force obtained during the drilling process with DM18 along, respectively, Z and X directions.

Figure 7-58 shows the dimensional hole analysis, performed along with four directions of the single hole, and reports an average trend in the hole diameter from hole no. 1 to hole no. 60.

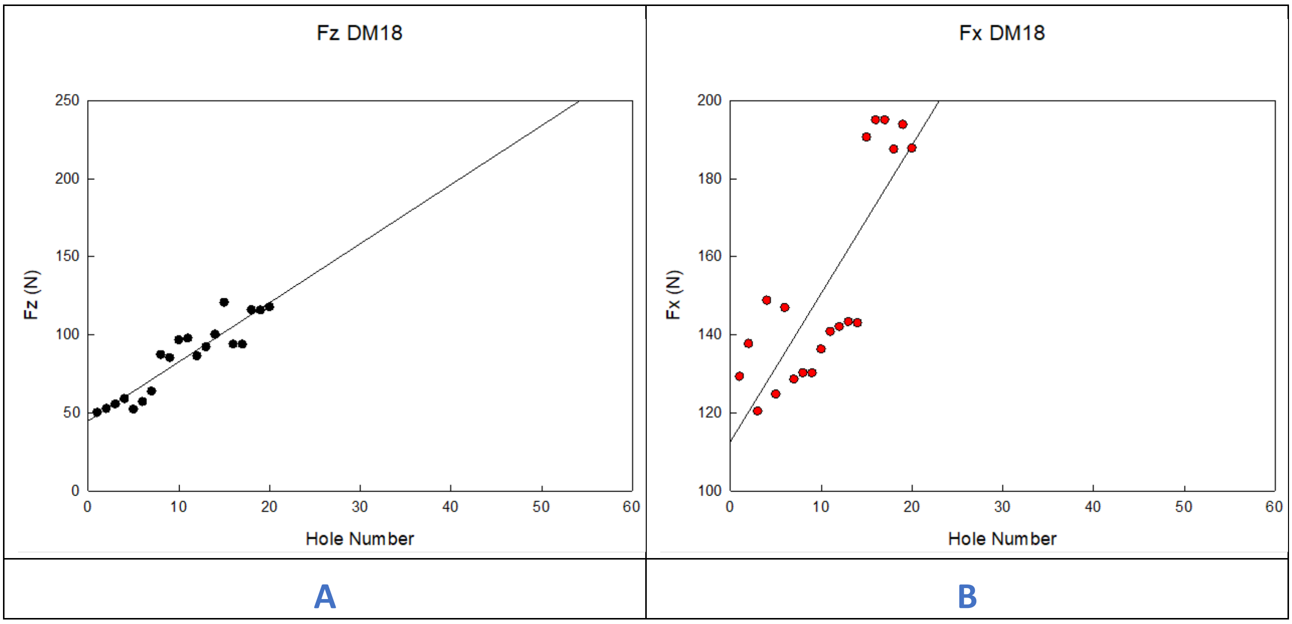

Figure 7-57: Maximum cutting force in the (A) X direction, Fxmax, and (B) Z direction, Fzmax, measured for tools DM18.

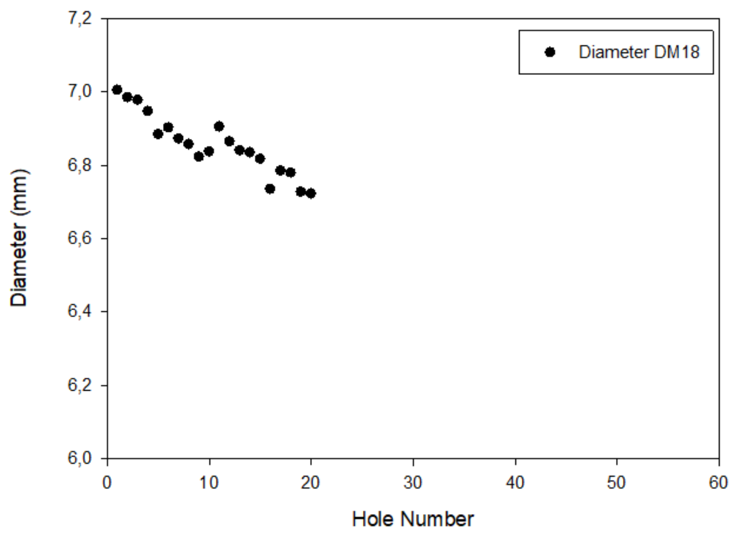

Figure 7-58: Hole diameter measured from hole no. 1 to no. 20 drilled by DM18.

7.4.9 TESTS TOOL DM19

With DM18, the tool broke at hole no. 20.

Figure 7-59 shows the maximum thrust force obtained during the drilling process with DM1 along, respectively, Z and X directions.

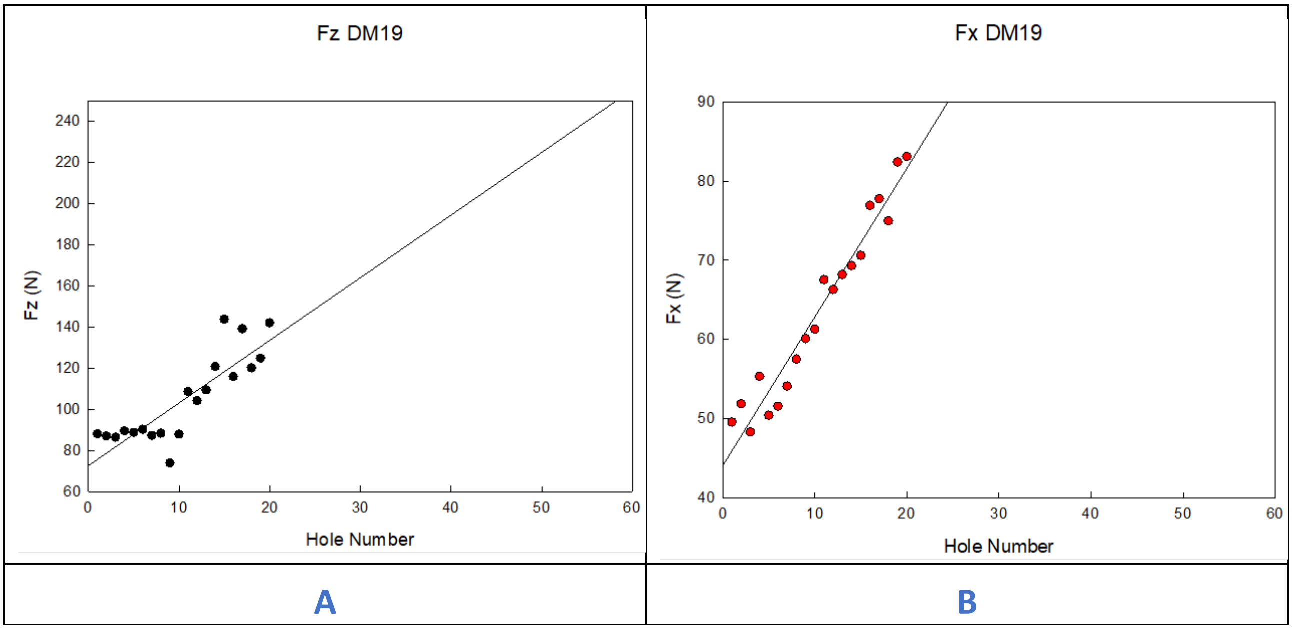

Figure 7-59: Maximum cutting force in the (A) X direction, Fxmax, and (B) Z direction, Fzmax, measured for tools DM19.

Figure 7-60 shows the dimensional hole analysis, performed along with four directions of the single hole, and reports an average trend in the hole diameter from hole no. 1 to hole no. 60.

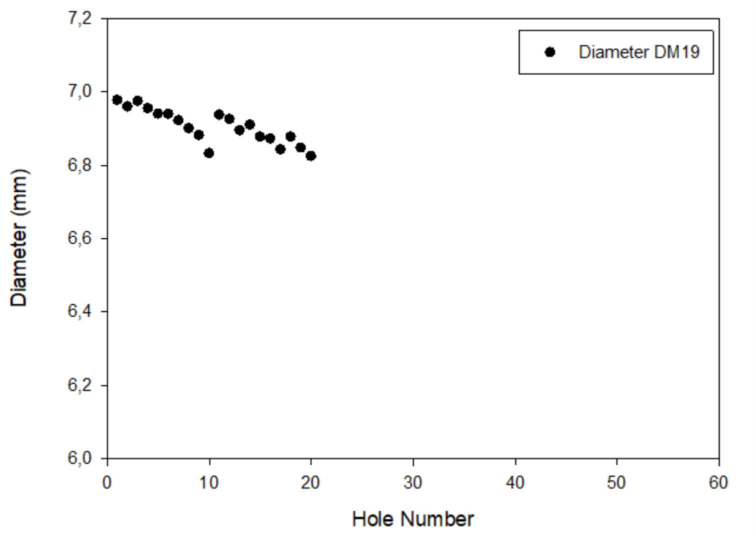

Figure 7-60: Hole diameter measured from hole no. 1 to no. 20 drilled by DM19.

7.4.10 TESTS TOOL DM20

With DM18, the tool broke at hole no. 20.

Figure 7-61 shows the maximum thrust force obtained during the drilling process with DM1 along, respectively, Z and X directions.

Figure 7-62 shows the dimensional hole analysis, performed along with four directions of the single hole, and reports an average trend in the hole diameter from hole no. 1 to hole no. 60.

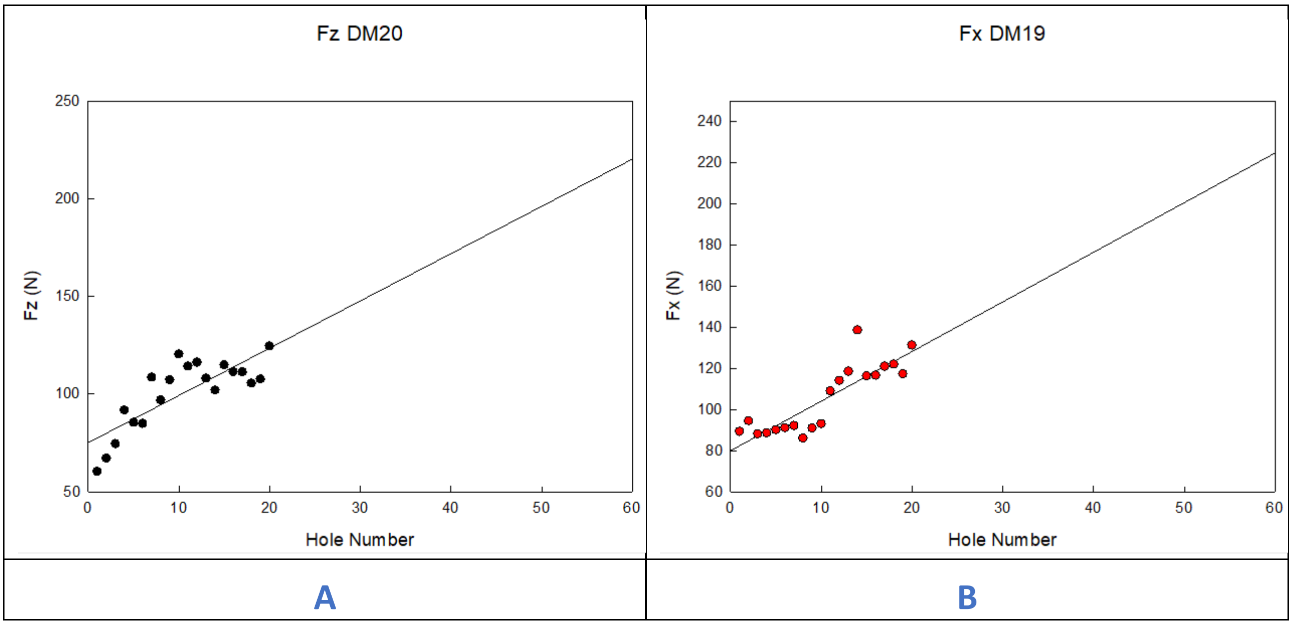

Figure 7-61: Maximum cutting force in the (A) X direction, Fxmax, and (B) Z direction, Fzmax, measured for tools DM20.

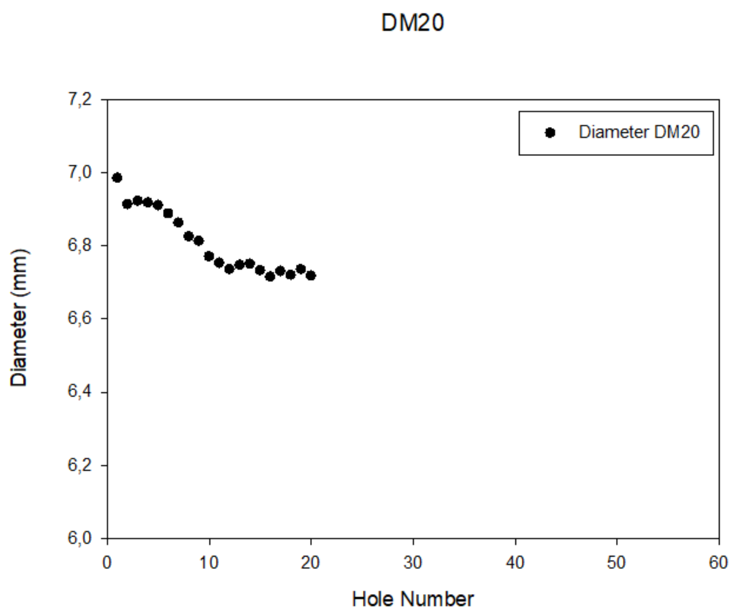

Figure 7-62: Hole diameter measured from hole no. 1 to no. 20 drilled by DM20.

7.5 THE FINAL RESULTS

Table 7-7 shows the results relative to the trust force acquired during the drill-milling process using the tool with a nominal diameter of 6 mm.

-DM11 and DM15 showed the lowest maximum forces.

-DM12 and DM16 showed the highest trust forces and were more subjected to vibrations during the drilling process.

TOOL	F_xMAX [N]	Δ F_xMAX [N]	F_zMAX [N]	Δ F_zMAX [N]	TOOL BREAKAGE
DM11	147.96	100.99	118.75	80.51	No
DM12	186.44	146.42	244.15	124.31	No
DM13	173.23	122.11	130.13	108.11	No
DM14	161.59	93.38	155.33	114.45	No
DM15	140.05	133.06	201.28	97.61	No
DM16	187.32	144.89	191.25	118.26	No
DM17	181.71	107.20	179.56	60.76	No
DM18					Hole no. 20
DM19					Hole no. 20
DM20					Hole no. 20

Table 7-7: Summary of the results of the forces exerted during drilling using 6 mm diameter tools.

Figure 7-63 shows the dimensional analysis elaborated during the drill-milling process using the tool with a nominal diameter of 6 mm.

-There was a rapid decrease in the diameter of the hole due to tool wear in all tools.

-All trends show a rapid decrease up to hole no. 30, and successively the graph decreases most slowly.

- The best results were found in DM12 and DM15, where there was a lower decrease in the diameter of the hole.

-DM18, DM19 and DM20 show a similar graph with the tool breakage at hole no. 20.

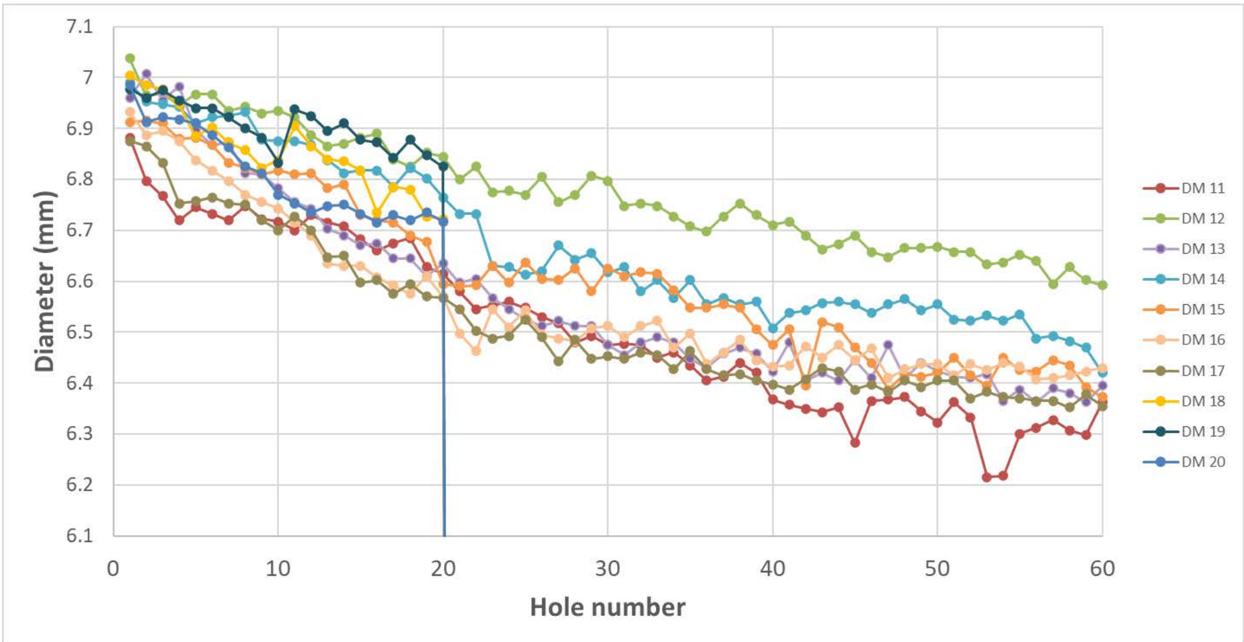

Figure 7-63: Summary of the dimensional analysis performed on the holes obtained after the drilling process using 6 mm diameter tools.

Figure 7-64 shows the roughness analysis elaborated during the drill-milling process using the tool with a nominal diameter of 6 mm.

- From the comparison of the reported roughness, it can be seen that the trends are all increasing as expected and that better results have also been found for the roughnesses for the holes made with DM12 and DM15.

-The high roughness values are due to the vibrations encountered during the process.

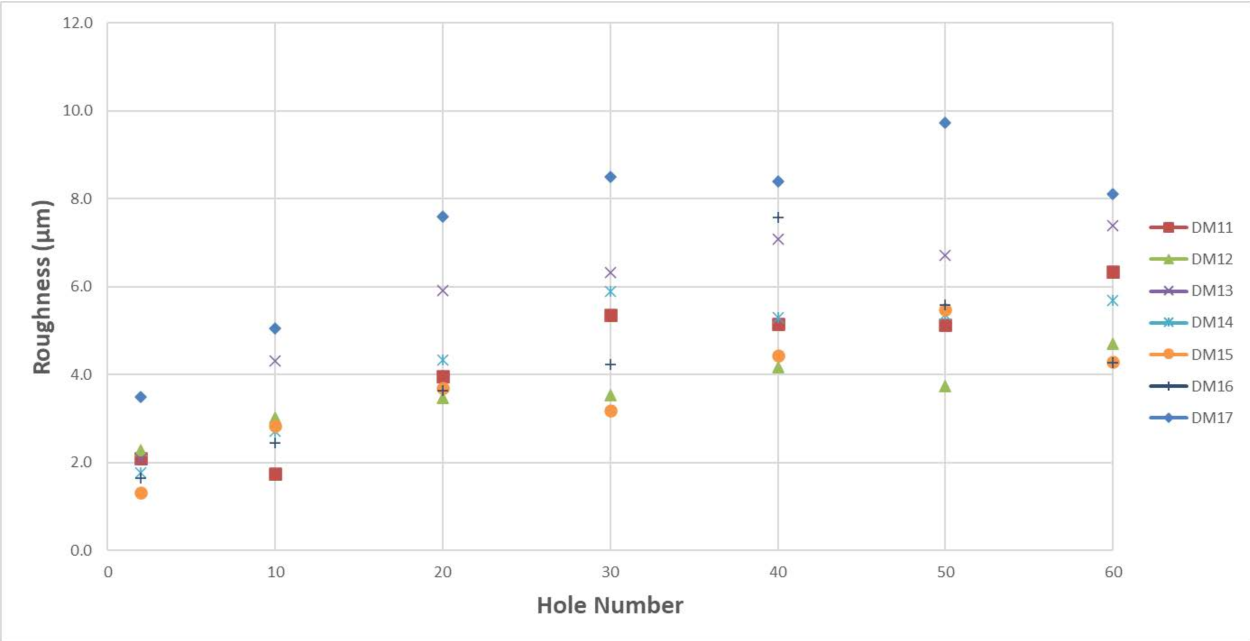

Figure 7-64: Summary of the roughness survey performed on the holes obtained after the drilling process using the 6 mm diameter tools.

Different path strategies will test to verify the potential benefits of hole quality and improved tool wear as future development.

It has, therefore, concluded that this process represents an interesting opportunity to reduce the delamination damage produced by traditional drilling. The advantages of this drilling process are the ease of programming the route and the absence of refrigerants with the benefits of green technology.

8 CONCLUSIONS

The purpose of this thesis concerns the drilling of polymer matrix fibrous composite materials. These materials are widely used for parts in the aerospace industry due to their high specific mechanical properties and low weight and require extensive drilling processes in order to allow for subsequent joining operations. Proper optimization of the drilling process can substantially improve the parts' quality, which may be affected by several types of faults generated during the machining process.

In order to provide an overview of the main relevant issues from different perspectives, several aspects were discussed in this thesis. In particular, the influence of tool geometry and technological parameters on thrust force, torque and tool wear was discussed, as well as their role in delamination. These aspects were illustrated with particular reference to the drilling of carbon fibre reinforced polymer (CFRP) composites, which are widely employed in the aerospace industry and have been extensively investigated in the scientific literature.

As regards the delamination damage, which is the most common and relevant fault occurring during CFRP drilling, it was explained how peel-up and push-out delamination takes place when the axial forces exerted by the drill bit overcome the interlaminar strength of the workpiece, and it was shown that the delamination damage grows with increasing cutting speed and feed rate, which increases the thrust force and causes an enlargement of the delamination damage at the hole exit. The role of tool wear development on delamination damage extent was also investigated through experimental studies, showing that progressive tool wear does not affect delamination at the hole entry (i.e. peel-up delamination). However, tool wear was shown to affect delamination at the hole exit (i.e. push-out delamination) as the delamination indices significantly increase with an increasing number of drilled holes. Moreover, a preferential orientation of push-out delamination can be identified, which is consistent with the fibre orientation of the most external plies of the CFRP laminate stacking sequence.

The geometry of the drilling tool, particularly the rake angle, has been shown to significantly affect delamination, as it determines the distribution of the cutting forces that the tool exerts on the workpiece. Different geometries, including twist drills and step drills, have been reported, showing different performance in terms of thrust force, torque and temperature generated on the CFRP parts, with consequent different results in terms of part output quality. The development of thrust force and torque during the drilling process was discussed and illustrated with reference to different tool geometries and under different drilling parameters, and it was related to the tool wear development, which is particularly rapid when machining the highly abrasive carbon fibres. Tool wear significantly affects the drilling process: an increase in tool wear results in increased thrust force and torque and reduces the overall quality of the drilling process. It was also shown that the increase in tool wear leads to an increase in the maximum temperature reached during drilling, which can cause matrix degradation and delamination damage.

Finally, alternative hole making technologies such as orbital drilling and an innovative drill-milling process were presented, showing how they can improve the drilling-induced delamination damage typically produced by traditional drilling.

9 BIBLIOGRAPHY

[1] G. Caprino, L. Santo, and L. Nele, "On the origin of cutting forces in machining unidirectional composite materials," in *American Society of Mechanical Engineers, Petroleum Division (Publication) PD*, 1996, vol. 75, no. 3, pp. 83–87.

[2] R. Teti, "Machining of composite materials," *CIRP Ann. - Manuf. Technol.*, vol. 51, no. 2, pp. 611–634, 2002, doi: 10.1016/S0007-8506(07)61703-X.

[3] A. Caggiano, "Machining of fibre reinforced plastic composite materials," *Materials (Basel).*, vol. 11, no. 3, 2018, doi: 10.3390/ma11030442.

[4] T. Reincke, S. Hartwig, and K. Dilger, "Improvement of the adhesion of continuously manufactured multi-material joints by application of thermoplastic adhesive film," *Int. J. Adhes. Adhes.*, vol. 93, p. 102321, 2019, doi: https://doi.org/10.1016/j.ijadhadh.2019.01.015.

[5] R. DON, L. Bastien, T. Jakobsen, and J. Gillespie, "Fusion bonding of thermoplastic composites by resistance heating," *SAMPE J.*, 1990.

[6] M. J. Troughton, Ed., "Chapter 11 - Induction Welding," in *Handbook of Plastics Joining (Second Edition)*, Second Edi., Boston: William Andrew Publishing, 2009, pp. 113–120.

[7] L. Nele and B. Palmieri, "Electromagnetic heating for adhesive melting in CFRTP joining: study, analysis, and testing," *Int. J. Adv. Manuf. Technol.*, vol. 106, no. 11–12, pp. 5317–5331, 2020, doi: 10.1007/s00170-019-04910-9.

[8] M. Dubé, P. Hubert, J. N. Gallet, D. Stavrov, H. E. Bersee, and A. Yousefpour, "Metal mesh heating element size effect in resistance welding of thermoplastic composites," *J. Compos. Mater.*, vol. 46, no. 8, pp. 911–919, Apr. 2012, doi: 10.1177/0021998311412986.

[9] J.-H. Kweon, J.-W. Jung, T.-H. Kim, J.-H. Choi, and D.-H. Kim, "Failure of carbon composite-to-aluminum joints with combined mechanical fastening and adhesive bonding," *Compos. Struct.*, vol. 75, no. 1–4, pp. 192–198, 2006.

[10] M. Mariam, M. Afendi, M. S. A. Majid, M. J. M. Ridzuan, and A. G. Gibson, "Tensile and fatigue properties of single lap joints of aluminium alloy/glass fibre reinforced composites fabricated with different joining methods," *Compos. Struct.*, vol. 200, pp. 647–658, 2018.

[11] E. R. Fotsing, F. Miron, Y. Eury, A. Ross, and E. Ruiz, "Bonding analysis of carbon/epoxy composites with viscoelastic acrylic adhesive," *Compos. Part B Eng.*, vol. 43, no. 5, pp. 2087–2093, Jul. 2012, doi: 10.1016/j.compositesb.2012.03.009.

[12] R. Haque and Y. Durandet, "Strength prediction of self-pierce riveted joint in cross-tension and lap-shear," *Mater. Des.*, vol. 108, pp. 666–678, Oct. 2016, doi: 10.1016/j.matdes.2016.07.029.

[13] K. Abhishek, S. Datta, and S. S. Mahapatra, "Optimization of thrust, torque, entry, and exist delamination factor during drilling of CFRP composites," *Int. J. Adv. Manuf. Technol.*, vol. 76, no. 1, pp. 401–416, 2015, doi: 10.1007/s00170-014-6199-3.

[14] L. Xie, H. Liu, W. Wu, D. Abliz, Y. Duan, and D. Li, "Fusion bonding of thermosets composite structures with thermoplastic binder co-cure and prepreg interlayer in electrical resistance welding," *Mater. Des.*, vol. 98, pp. 143–149, 2016, doi: 10.1016/j.matdes.2016.03.020.

[15] F. Lionetto, M. N. Morillas, S. Pappadà, G. Buccoliero, I. Fernandez Villegas, and A. Maffezzoli, "Hybrid welding of carbon-fiber reinforced epoxy based composites," *Compos. Part A Appl. Sci. Manuf.*, vol. 104, pp. 32–40, 2018, doi: 10.1016/j.compositesa.2017.10.021.

[16] W. Obande *et al.*, "Study of the influence of initiator content in the polymerization reaction

of a thermoplastic liquid resin for advanced composite manufacturing," *Compos. Part A Appl. Sci. Manuf.*, vol. 13, no. June, pp. 3579–3587, Dec. 2019, doi: 10.1002/adv.22142.

[17] S. K. Bhudolia, G. Gohel, and K. F. Leong, "Advances in Ultrasonic Welding of Thermoplastic Composites : A Review," 2020.

[18] B. Palmieri, L. Nele, and F. Galise, "Numerical modeling and experimental validation of thermoplastic composites induction welding," in *AIP Conference Proceedings*, 2018, vol. 050013, p. 050013, doi: 10.1063/1.5034886.

[19] V. Stokes, "Joining methods for plastics and plastic composites: an overview," *Polym. Eng. Sci.*, 1989.

[20] C. Ageorges, L. Ye, and M. Hou, "Advances in fusion bonding techniques for joining thermoplastic matrix composites: a review," *Compos. Part A Appl. Sci. Manuf.*, vol. 32, no. 6, pp. 839–857, Jun. 2001, doi: 10.1016/S1359-835X(00)00166-4.

[21] A. Yousefpour, M. Hojjati, and J.-P. Immarigeon, "Fusion Bonding/Welding of Thermoplastic Composites," *J. Thermoplast. Compos. Mater.*, vol. 17, no. 4, pp. 303–341, Jul. 2004, doi: 10.1177/0892705704045187.

[22] W. König, C. Wulf, P. Graß, and H. Willerscheid, "Machining of Fibre Reinforced Plastics," *CIRP Ann. - Manuf. Technol.*, vol. 34, no. 2, pp. 537–548, 1985, doi: 10.1016/S0007-8506(07)60186-3.

[23] G. Caprino and L. Nele, "Cutting Forces in Orthogonal Cutting of Unidirectional GFRP Composites," *J. Eng. Mater. Technol.*, vol. 118, no. 3, pp. 419–425, Jul. 1996, doi: 10.1115/1.2806829.

[24] D. Nayak, N. Bhatnagar, and P. Mahajan, "MACHINING STUDIES OF UD-FRP COMPOSITES PART 2: FINITE ELEMENT ANALYSIS," *Mach. Sci. Technol.*, vol. 9, no. 4, pp. 503–528, Dec. 2005, doi: 10.1080/10910340500398183.

[25] X. M. Wang and L. C. Zhang, "An experimental investigation into the orthogonal cutting of unidirectional fibre reinforced plastics," *Int. J. Mach. Tools Manuf.*, vol. 43, no. 10, pp. 1015–1022, 2003, doi: https://doi.org/10.1016/S0890-6955(03)00090-7.

[26] V. Lopresto, A. Caggiano, and R. Teti, "High Performance Cutting of Fibre Reinforced Plastic Composite Materials," *Procedia CIRP*, vol. 46, pp. 71–82, 2016, doi: https://doi.org/10.1016/j.procir.2016.05.079.

[27] F. Cepero-Mejias, J. L. Curiel-Sosa, K. Kerrigan, and V. A. Phadnis, "Chip formation in machining of unidirectional carbon fibre reinforced polymer laminates: FEM based assessment," *Procedia CIRP*, vol. 85, pp. 302–307, 2019, doi: https://doi.org/10.1016/j.procir.2019.09.005.

[28] G. Santhanakrishnan, R. Krishnamurthy, and S. K. Malhotra, "Investigation into the machining of carbon-fibre-reinforced plastics with cemented carbides," *J. Mater. Process. Technol.*, vol. 30, no. 3, pp. 263–275, 1992, doi: https://doi.org/10.1016/0924-0136(92)90219-I.

[29] L. C. Zhang, H. J. Zhang, and X. M. Wang, "A FORCE PREDICTION MODEL FOR CUTTING UNIDIRECTIONAL FIBRE-REINFORCED PLASTICS," *Mach. Sci. Technol.*, vol. 5, no. 3, pp. 293–305, 2001, doi: 10.1081/MST-100108616.

[30] P. S. Sreejith, R. Krishnamurthy, S. K. Malhotra, and K. Narayanasamy, "Evaluation of PCD tool performance during machining of carbon/phenolic ablative composites," *J. Mater. Process. Technol.*, vol. 104, no. 1, pp. 53–58, 2000, doi: https://doi.org/10.1016/S0924-0136(00)00549-5.

[31] J. Fleischer, R. Teti, G. Lanza, P. Mativenga, H. C. Möhring, and A. Caggiano, "Composite

materials parts manufacturing," *CIRP Ann.*, vol. 67, no. 2, pp. 603–626, 2018, doi: 10.1016/j.cirp.2018.05.005.

[32] W.-C. Chen, "Some experimental investigations in the drilling of carbon fiber-reinforced plastic (CFRP) composite laminates," *Int. J. Mach. Tools Manuf.*, vol. 37, no. 8, pp. 1097–1108, 1997, doi: 10.1016/S0890-6955(96)00095-8.

[33] D. Kumar, K. K. Singh, and R. Zitoune, "Experimental investigation of delamination and surface roughness in the drilling of GFRP composite material with different drills," *Adv. Manuf. Polym. Compos. Sci.*, vol. 2, no. 2, pp. 47–56, 2016, doi: 10.1080/20550340.2016.1187434.

[34] S. Jain and D. C. H. Yang, "Delamination-free drilling of composite laminates," *J. Eng. Ind.*, vol. 116, no. 4, pp. 475–481, 1994, doi: 10.1115/1.2902131.

[35] S. C. Lin and I. K. Chen, "Drilling carbon fiber-reinforced composite material at high speed," *Wear*, vol. 194, no. 1–2, pp. 156–162, 1996, doi: 10.1016/0043-1648(95)06831-7.

[36] H. Ho-Cheng and C. K. H. Dharan, "Delamination during drilling in composite laminates," *J. Eng. Ind.*, vol. 112, no. 3, pp. 236–239, 1990, doi: 10.1115/1.2899580.

[37] J. P. Davim and P. Reis, "Study of delamination in drilling carbon fiber reinforced plastics (CFRP) using design experiments," *Compos. Struct.*, vol. 59, no. 4, pp. 481–487, 2003, doi: 10.1016/S0263-8223(02)00257-X.

[38] H. Hocheng and C. C. Tsao, "The path towards delamination-free drilling of composite materials," *J. Mater. Process. Technol.*, vol. 167, no. 2–3, pp. 251–264, 2005, doi: 10.1016/j.jmatprotec.2005.06.039.

[39] D. Geng *et al.*, "Delamination formation, evaluation and suppression during drilling of composite laminates: A review," *Compos. Struct.*, vol. 216, pp. 168–186, May 2019, doi: 10.1016/J.COMPSTRUCT.2019.02.099.

[40] P. R. Babu and B. Pradhan, "Effect of damage levels and curing stresses on delamination growth behaviour emanating from circular holes in laminated FRP composites," *Compos. Part A Appl. Sci. Manuf.*, vol. 38, no. 12, pp. 2412–2421, 2007, doi: 10.1016/j.compositesa.2007.08.010.

[41] L. Durão, J. Tavares, V. de Albuquerque, J. Marques, and O. Andrade, "Drilling Damage in Composite Material," *Materials (Basel).*, vol. 7, no. 5, pp. 3802–3819, 2014, doi: 10.3390/ma7053802.

[42] K. Phapale, A. Ahire, and R. Singh, "Experimental characterization and finite element modeling of critical thrust force in cfrp drilling," *Mach. Sci. Technol.*, vol. 22, no. 2, pp. 249–270, 2018, doi: 10.1080/10910344.2017.1337134.

[43] K. B. Karpat Y, Bahtiyar O, Deger B, "A mechanistic approach to investigate drillingof UD-CFRP laminates with PCD drills," *CIRP Ann. - Manuf. Technol.*, vol. 63, pp. 81–84, 2014.

[44] Y. Karpat and O. Bahtiyar, "Energy Based Investigation of Process Parameters while Drilling Carbon Fiber Reinforced Polymers," *Procedia CIRP*, vol. 46, pp. 59–62, 2016, doi: 10.1016/j.procir.2016.03.185.

[45] A. Caggiano, F. Napolitano, L. Nele, and R. Teti, "Multiple Sensor Monitoring for Tool Wear Forecast in Drilling of CFRP/CFRP Stacks with Traditional and Innovative Drill Bits," *Procedia CIRP*, vol. 67, pp. 404–409, 2018, doi: https://doi.org/10.1016/j.procir.2017.12.233.

[46] M. H. Hassan and J. Abdullah, "Drilling of fiber-reinforced composites: An innovative tool design," *Hole-Making Drill. Technol. Compos.*, pp. 47–62, Jan. 2019, doi: 10.1016/B978-0-08-102397-6.00004-0.

[47] A. Caggiano, R. Angelone, and R. Teti, “Image Analysis for CFRP Drilled Hole Quality Assessment,” *Procedia CIRP*, vol. 62, pp. 440–445, Jan. 2017, doi: 10.1016/J.PROCIR.2017.03.045.

[48] J. P. Davim, J. C. Rubio, and A. M. Abrao, “A novel approach based on digital image analysis to evaluate the delamination factor after drilling composite laminates,” *Compos. Sci. Technol.*, vol. 67, no. 9, pp. 1939–1945, Jul. 2007, doi: 10.1016/J.COMPSCITECH.2006.10.009.

[49] R. Angelone, A. Caggiano, I. Improta, L. Nele, and R. Teti, “Temperature Measurements for the Tool Wear and Hole Quality Assessment during Drilling of CFRP/CFRP Stacks,” in *Procedia CIRP*, 2018, vol. 67, pp. 416–421, doi: 10.1016/j.procir.2017.12.235.

[50] M. Giuseppe and A. Devices, “U niversit à degli S tudi di N apoli F ederico II Facoltà di Ingegneria Corso : Integrated Photonic,” no. May, 2015.

[51] E. Dei Processi Industriali, R. Teti, and I. Alberto Bottillo Giuseppe Mensitieri, “DOTTORATO DI RICERCA IN INGEGNERIA DEI PRODOTTI Advanced 3D Ultrasonic Non-destructive Evaluation Technique for CFRP aeronautical applications PHD PROJECT SUPERVISOR PHD CANDIDATE PHD PROGRAM COORDINATOR.”

[52] T. Segreto, A. Bottillo, A. Caggiano, R. Teti, and F. Ricci, “Full-volume Ultrasonic Technique for 3D Thickness Reconstruction of CFRP Aeronautical Components,” *Procedia CIRP*, vol. 67, pp. 434–439, 2018, doi: 10.1016/j.procir.2017.12.238.

[53] N. Geier, J. P. Davim, and T. Szalay, “Advanced cutting tools and technologies for drilling carbon fibre reinforced polymer (CFRP) composites: A review,” *Compos. Part A Appl. Sci. Manuf.*, vol. 125, p. 105552, Oct. 2019, doi: 10.1016/J.COMPOSITESA.2019.105552.

[54] L. Lizzul, M. Sorgato, R. Bertolini, A. Ghiotti, and S. Bruschi, “Influence of additive manufacturing-induced anisotropy on tool wear in end milling of Ti6Al4V,” *Tribol. Int.*, vol. 146, p. 106200, Jun. 2020, doi: 10.1016/J.TRIBOINT.2020.106200.

[55] D. Samuel Raj and L. Karunamoorthy, “Performance of cryogenically treated WC drill using tool wear measurements on the cutting edge and hole surface topography when drilling CFRP,” *Int. J. Refract. Met. Hard Mater.*, vol. 78, pp. 32–44, Jan. 2019, doi: 10.1016/J.IJRMHM.2018.08.011.

[56] J. Fernández-Pérez, J. L. Cantero, J. Díaz-Álvarez, and M. H. Miguélez, “Tool wear and induced damage in CFRP drilling with step and double point angle drill bits,” *Procedia Manuf.*, vol. 41, pp. 610–617, Jan. 2019, doi: 10.1016/J.PROMFG.2019.09.049.

[57] D. Nguyen, M. S. Bin Abdullah, R. Khawarizmi, D. Kim, and P. Kwon, “The effect of fiber orientation on tool wear in edge-trimming of carbon fiber reinforced plastics (CFRP) laminates,” *Wear*, vol. 450–451, p. 203213, Jun. 2020, doi: 10.1016/J.WEAR.2020.203213.

[58] A. Hrechuk, V. Bushlya, R. M’Saoubi, and J.-E. Ståhl, “Experimental investigations into tool wear of drilling CFRP,” *Procedia Manuf.*, vol. 25, pp. 294–301, Jan. 2018, doi: 10.1016/J.PROMFG.2018.06.086.

[59] R. Angelone, A. Caggiano, I. Improta, and L. Nele, “Temperature Measurements for the Tool Wear and Hole Quality Assessment During Drilling of CFRP/CFRP Stacks,” *Procedia CIRP*, vol. 67, pp. 416–421, Jan. 2018, doi: 10.1016/J.PROCIR.2017.12.235.

[60] D. Kim, M. Ramulu, and X. Doan, “Influence of consolidation process on the drilling performance and machinability of PIXA-M and PEEK thermoplastic composites,” *J. Thermoplast. Compos. Mater.*, vol. 18, no. 3, pp. 195–217, 2005, doi: 10.1177/0892705705044556.

[61] M. Bono and J. Ni, “The effects of thermal distortions on the diameter and cylindricity of dry

drilled holes," *Int. J. Mach. Tools Manuf.*, vol. 41, no. 15, pp. 2261–2270, 2001, doi: https://doi.org/10.1016/S0890-6955(01)00047-5.

[62] S. A. Ashrafi, P. W. Miller, K. M. Wandro, and D. Kim, "Characterization and effects of fiber pull-outs in hole quality of carbon fiber reinforced plastics composite," *Materials (Basel).*, vol. 9, no. 10, pp. 1–12, 2016, doi: 10.3390/ma9100828.

[63] V. Chandrasekharan, S. G. Kapoor, and R. E. DeVor, "A Mechanistic Model to Predict the Cutting Force System for Arbitrary Drill Point Geometry," *J. Manuf. Sci. Eng.*, vol. 120, no. 3, pp. 563–570, Aug. 1998, doi: 10.1115/1.2830160.

[64] M. Shah Mohammadi, M. Ghani, M. Komeili, B. Crawford, and A. S. Milani, "The effect of manufacturing parameters on the surface roughness of glass fibre reinforced polymer moulds," *Compos. Part B Eng.*, vol. 125, pp. 39–48, 2017, doi: 10.1016/j.compositesb.2017.05.028.

[65] V. N. Gaitonde, S. R. Karnik, J. C. Rubio, A. M. Abrão, A. E. Correia, and J. P. Davim, "Surface roughness analysis in high-speed drilling of unreinforced and reinforced polyamides," *J. Compos. Mater.*, vol. 46, no. 21, pp. 2659–2673, 2012, doi: 10.1177/0021998311431640.

[66] El-Hoffy and H. Abdel-Gawad, *Fundementals of machining processes : conventional and nonconventional processes*. 2013.

[67] J. Sheikh-Ahmad and J. P. Davim, "Tool wear in machining processes for composites," in *Machining Technology for Composite Materials: Principles and Practice*, 2011.

[68] ASTM E2758 − 15a, "Standard Guide for Selection and Use of Wideband, Low Temperature Infrared Thermometers," *ASTM Int. West Conshohocken, PA, 2015*, pp. 1–17, 2015.

[69] R. Yang and Y. He, "Polymer-matrix composites carbon fibre characterisation and damage inspection using selectively heating thermography (SeHT) through electromagnetic induction," *Compos. Struct.*, vol. 140, pp. 590–601, 2016, doi: 10.1016/j.compstruct.2016.01.006.

[70] C. Canturri, E. S. Greenhalgh, S. T. Pinho, and J. Ankersen, "Delamination growth directionality and the subsequent migration processes - The key to damage tolerant design," *ECCM 2012 - Compos. Venice, Proc. 15th Eur. Conf. Compos. Mater.*, no. June, pp. 24–28, 2012.

[71] "PII_ S0890-6955(96)00095-8 _ Elsevier Enhanced Reader.pdf." .

[72] N. P. Avdelidis, P. I. Nicholson, and P. Wallace, "Pulsed thermography in the investigation of PCBs for defect detection & analysis," no. November 2014, 2006, doi: 10.21611/qirt.2006.048.

[73] A. T. Marques, L. M. Durão, A. G. Magalhães, J. F. Silva, and J. M. R. S. Tavares, "Delamination analysis of carbon fibre reinforced laminates: Evaluation of a special step drill," *Compos. Sci. Technol.*, vol. 69, no. 14, pp. 2376–2382, 2009, doi: 10.1016/j.compscitech.2009.01.025.

[74] R. Melentiev, P. C. Priarone, M. Robiglio, and L. Settineri, "Effects of Tool Geometry and Process Parameters on Delamination in CFRP Drilling: An Overview," *Procedia CIRP*, vol. 45, pp. 31–34, 2016, doi: 10.1016/j.procir.2016.02.255.

[75] V. N. Gaitonde, S. R. Karnik, J. C. Rubio, A. M. Abrão, A. E. Correia, and J. P. Davim, "Surface roughness analysis in high-speed drilling of unreinforced and reinforced polyamides," *J. Compos. Mater.*, vol. 46, no. 21, pp. 2659–2673, 2012, doi: 10.1177/0021998311431640.

[76] J. Kundrak, K. Gyani, and V. Bana, "Roughness of ground and hard-turned surfaces on the

basis of 3D parameters," *Int. J. Adv. Manuf. Technol.*, vol. 38, no. 1, pp. 110–119, 2008, doi: 10.1007/s00170-007-1086-9.

[77] S. A. Hussain, V. Pandurangadu, and K. Palanikumar, "Surface roughness analysis in machining of GFRP composites by carbide tool (K20)," *Eur. J. Sci. Res.*, vol. 41, no. 1, pp. 84–98, 2010.

[78] M. Ramesh, J. Nehru, R. P. Elvin, S. Sai, and R. Engineering, "International Journal of Applied Research in Mechanical Engineering Surface Roughness Optimization Of Machining Parameters In Machining Of Composite Materials Surface Roughness Optimization Of Machining Parameters In Machining Of Composite Materials," vol. 1, no. 1, 2011.

[79] K. Palanikumar, L. Karunamoorthy, and N. Manoharan, "Mathematical model to predict the surface roughness on the machining of glass fiber reinforced polymer composites," *J. Reinf. Plast. Compos.*, vol. 25, no. 4, pp. 407–419, 2006, doi: 10.1177/0731684405060568.

[80] L. M. P. Durão, D. J. S. Gonçalves, J. M. R. S. Tavares, V. H. C. de Albuquerque, A. Aguiar Vieira, and A. Torres Marques, "Drilling tool geometry evaluation for reinforced composite laminates," *Compos. Struct.*, vol. 92, no. 7, pp. 1545–1550, 2010, doi: 10.1016/j.compstruct.2009.10.035.

[81] A. D'Orazio, M. El Mehtedi, A. Forcellese, A. Nardinocchi, and M. Simoncini, "Tool wear and hole quality in drilling of CFRP/AA7075 stacks with DLC and nanocomposite TiAlN coated tools," *J. Manuf. Process.*, vol. 30, pp. 582–592, Dec. 2017, doi: 10.1016/J.JMAPRO.2017.10.019.

[82] S. L. M. Ribeiro Filho, C. H. Lauro, A. H. S. Bueno, and L. C. Brandão, "Influence cutting parameters on the surface quality and corrosion behavior of Ti–6Al–4V alloy in synthetic body environment (SBF) using Response Surface Method," *Measurement*, vol. 88, pp. 223–237, Jun. 2016, doi: 10.1016/J.MEASUREMENT.2016.03.047.

[83] N. S. Mohan, A. Ramachandra, and S. M. Kulkarni, "Influence of process parameters on cutting force and torque during drilling of glass–fiber polyester reinforced composites," *Compos. Struct.*, vol. 71, no. 3–4, pp. 407–413, Dec. 2005, doi: 10.1016/J.COMPSTRUCT.2005.09.039.

[84] C. K. H. Dharan and M. S. Won, "Machining parameters for an intelligent machining system for composite laminates," *Int. J. Mach. Tools Manuf.*, vol. 40, no. 3, pp. 415–426, 2000, doi: https://doi.org/10.1016/S0890-6955(99)00065-6.

[85] N. P. Avdelidis, D. P. Almond, A. Dobbinson, B. C. Hawtin, C. Ibarra-Castanedo, and X. Maldague, "Aircraft composites assessment by means of transient thermal NDT," *Prog. Aerosp. Sci.*, vol. 40, no. 3, pp. 143–162, 2004, doi: https://doi.org/10.1016/j.paerosci.2004.03.001.

[86] J. R. Figueira, S. Greco, V. Mousseau, and R. Słowiński, "Interactive multiobjective optimization using a set of additive value functions," *Lect. Notes Comput. Sci. (including Subser. Lect. Notes Artif. Intell. Lect. Notes Bioinformatics)*, vol. 5252 LNCS, no. October, pp. 97–119, 2008, doi: 10.1007/978-3-540-88908-3_4.

[87] S. Greco, M. Ehrgott, and J. Figueira, "Multiple criteria decision analysis: state of the art surveys," *Oper. Res. Manag. Sci.*, 2005.

[88] L. M. P. Durão, D. J. S. Gonçalves, J. M. R. S. Tavares, V. H. C. de Albuquerque, A. Aguiar Vieira, and A. Torres Marques, "Drilling tool geometry evaluation for reinforced composite laminates," *Compos. Struct.*, vol. 92, no. 7, pp. 1545–1550, 2010, doi: 10.1016/j.compstruct.2009.10.035.

[89] R. Voss, M. Henerichs, and F. Kuster, “Comparison of conventional drilling and orbital drilling in machining carbon fibre reinforced plastics (CFRP),” *CIRP Ann.*, vol. 65, no. 1, pp. 137–140, Jan. 2016, doi: 10.1016/J.CIRP.2016.04.001.

[90] R. Lindqvist, I. Eriksson, and M. Wolf, “Orbital drilling of sandwich constructions for space applications,” *SAE Tech. Pap.*, 2001, doi: 10.4271/2001-01-2571.

[91] A. Sadek, M. Meshreki, and M. H. Attia, “Characterization and optimization of orbital drilling of woven carbon fiber reinforced epoxy laminates,” *CIRP Ann. - Manuf. Technol.*, vol. 61, no. 1, pp. 123–126, 2012, doi: 10.1016/j.cirp.2012.03.089.

[92] O. M. Ozturk, Z. M. Kilic, and Y. Altintas, “Mechanics and dynamics of orbital drilling operations,” *Int. J. Mach. Tools Manuf.*, vol. 129, pp. 37–47, 2018, doi: 10.1016/j.ijmachtools.2018.03.001.

[93] R. Piquet, B. Ferret, F. Lachaud, and P. Swider, “Experimental analysis of drilling damage in thin carbon/epoxy plate using special drills,” *Compos. Part A Appl. Sci. Manuf.*, vol. 31, no. 10, pp. 1107–1115, 2000, doi: 10.1016/S1359-835X(00)00069-5.

[94] L. M. P. Durão, J. M. R. S. Tavares, V. H. C. de Albuquerque, J. F. S. Marques, and O. N. G. Andrade, “Drilling damage in composite material,” *Materials (Basel).*, vol. 7, no. 5, pp. 3802–3819, 2014, doi: 10.3390/ma7053802.

[95] H. Hocheng and C. C. Tsao, “Comprehensive analysis of delamination in drilling of composite materials with various drill bits,” *J. Mater. Process. Technol.*, vol. 140, no. 1-3 SPEC., pp. 335–339, 2003, doi: 10.1016/S0924-0136(03)00749-0.

[96] A. Caggiano, I. Improta, and L. Nele, “Characterization of a new dry drill-milling process of Carbon Fibre Reinforced Polymer laminates,” *Materials (Basel).*, vol. 11, no. 8, 2018, doi: 10.3390/ma11081470.

APPENDIX

APPENDIX I

The analysis of the parameters is fundamental for the visual analysis of the 3D images since, by integrating these images into the collected data, it is possible to have a much clearer view of each test.

Figure 0-1(Appendix I) shows all 3D surfaces obtained; images with the same feed rate were compared. Furthermore, it was found that the internal roughness depends much more on the feed rate than spindle speed; in fact, parameters with the same number of revolutions have surfaces similar to each other.

	HOLE 1	HOLE 5	HOLE 10	HOLE 15	HOLE 20	HOLE 25	HOLE 30
T 1	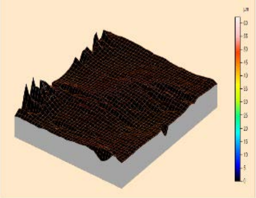	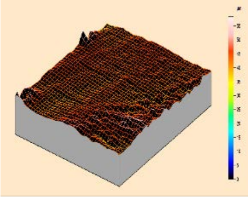	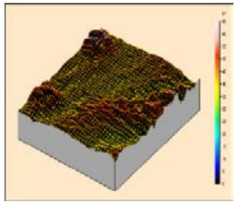	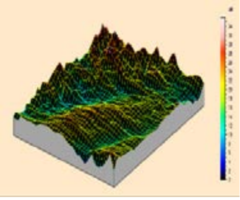	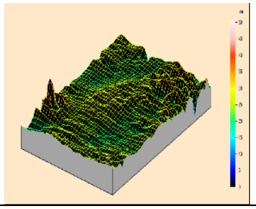	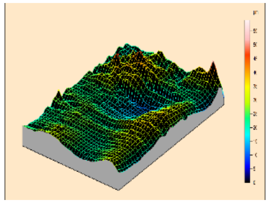	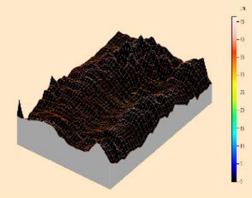
T 2	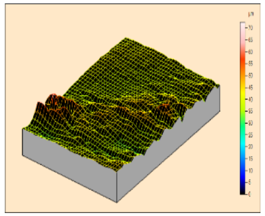	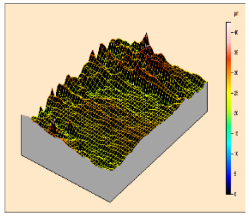	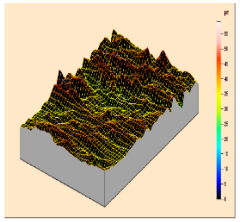	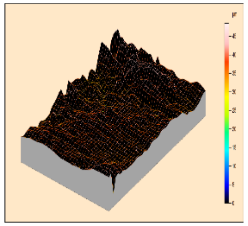	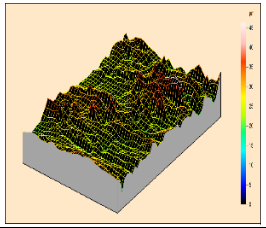	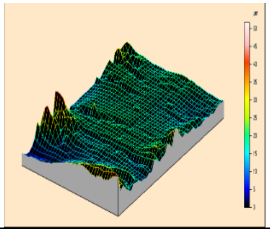	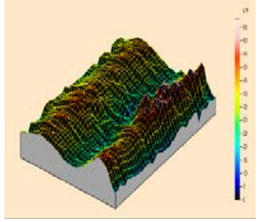

Appendix II

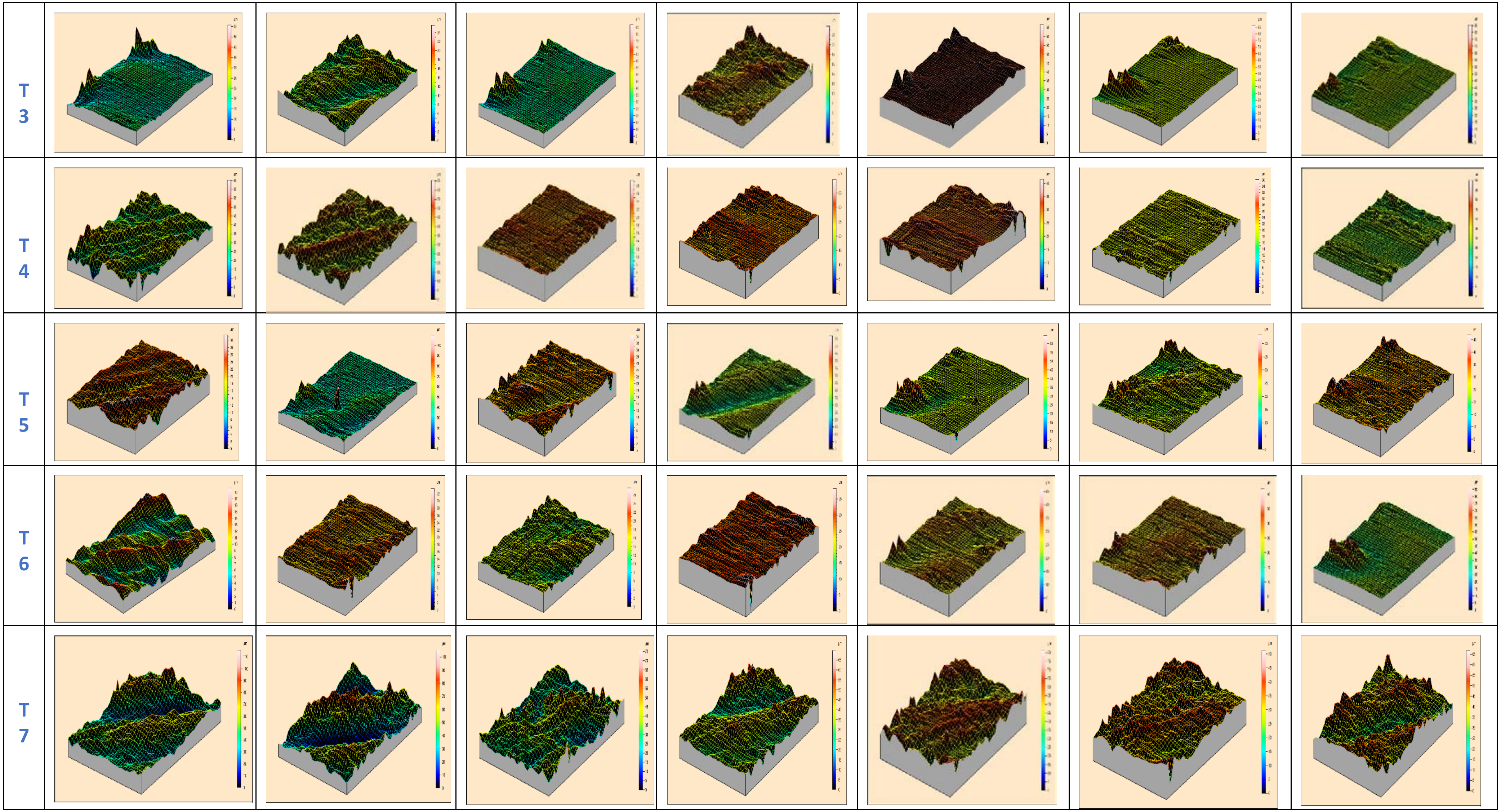

Figure 0-1 (Appendix I): 3D Image analysis of roughness test for holes no. 1, 5, 10, 15, 20, 25 and 30.

APPENDIX II

Figure 0-2 shows all 2D surfaces obtained; images with the same feed rate were compared. Furthermore, it was found that the internal roughness depends much more on the feed rate than spindle speed; in fact, parameters with the same number of revolutions have surfaces similar to each other.

Appendix II

	HOLE 1	HOLE 5	HOLE 10	HOLE 15	HOLE 20	HOLE 25	HOLE 30
T1	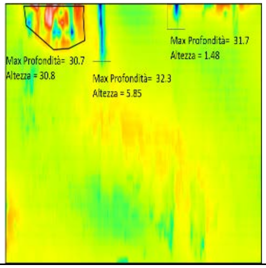	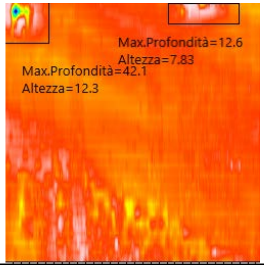	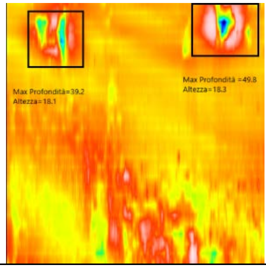	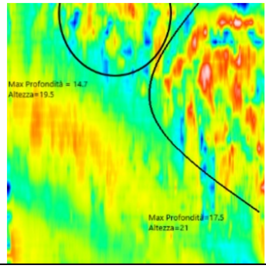	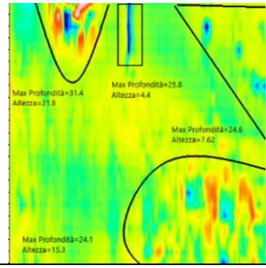	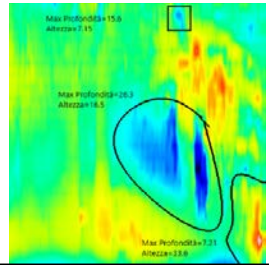	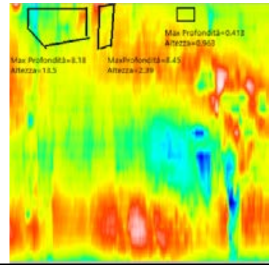
T2	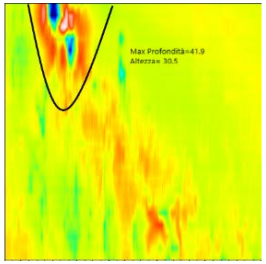	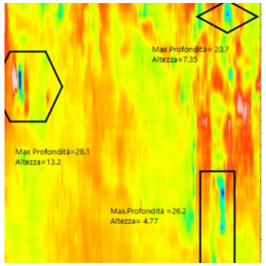	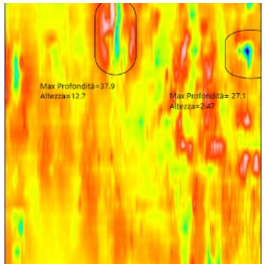	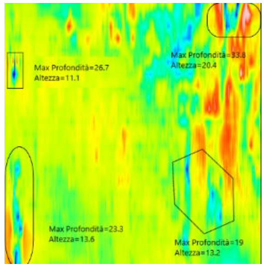	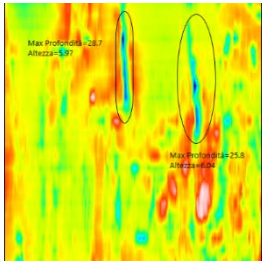	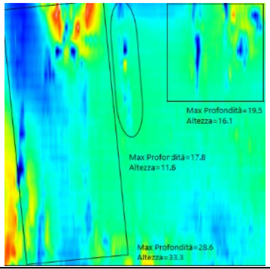	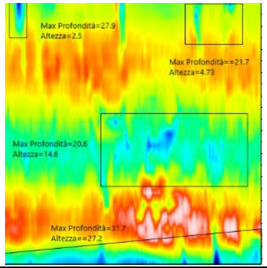
T3	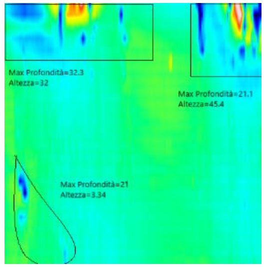	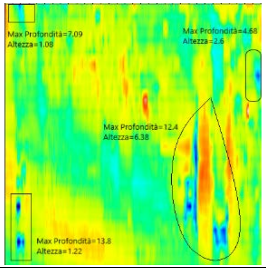	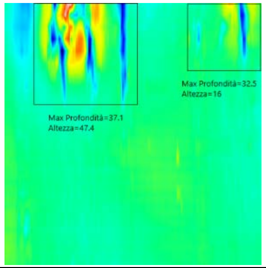	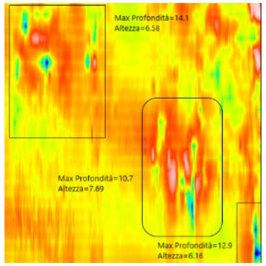	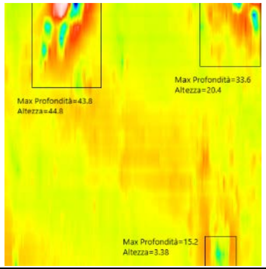	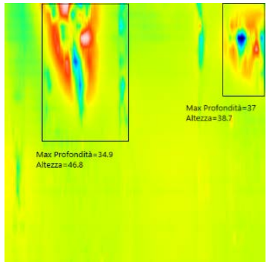	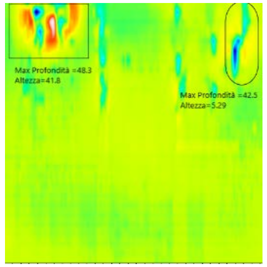
T4	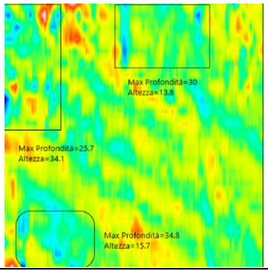	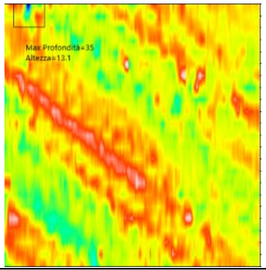	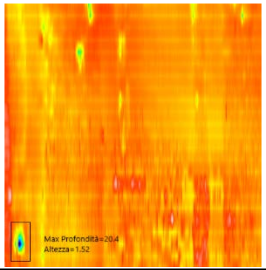	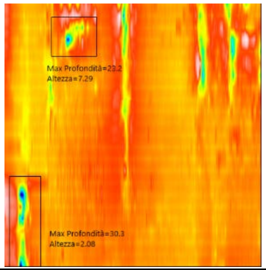	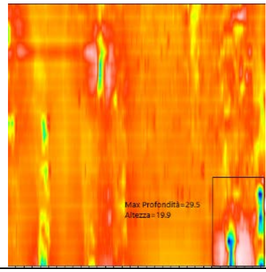	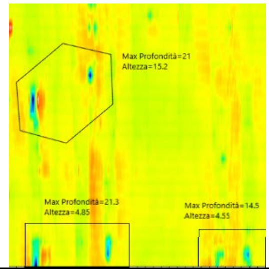	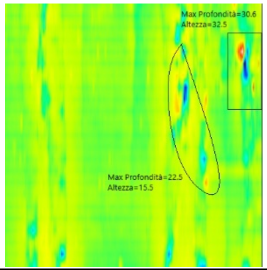

Appendix II

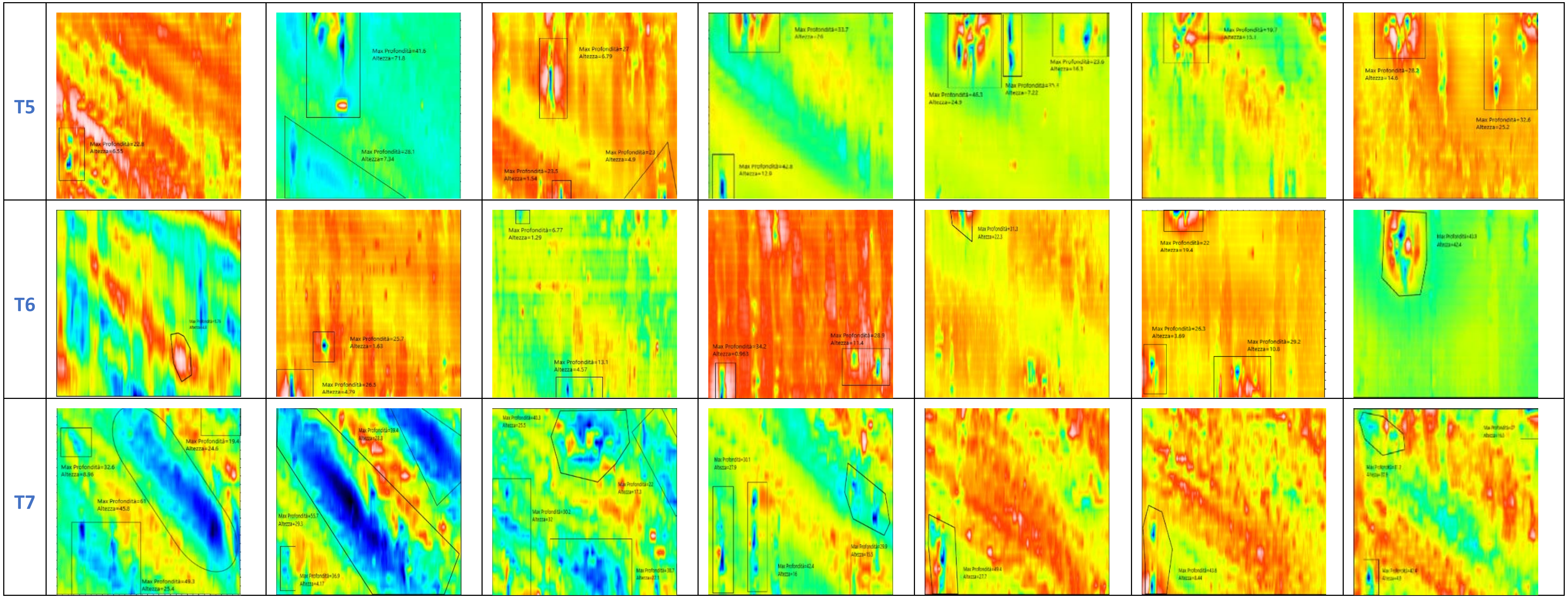

Figure 0-2(Appendix II): 2D Image analysis of roughness test for holes no. 1, 5, 10, 15, 20, 25 and 30.

APPENDIX III

Figure 0-3 (Appendix III) shows the DM1 tool signal of Fx and Fz recording.

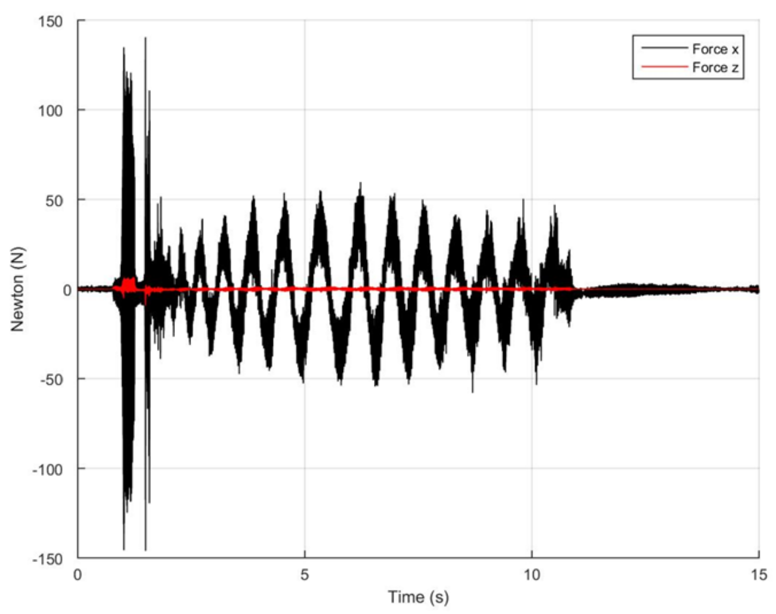

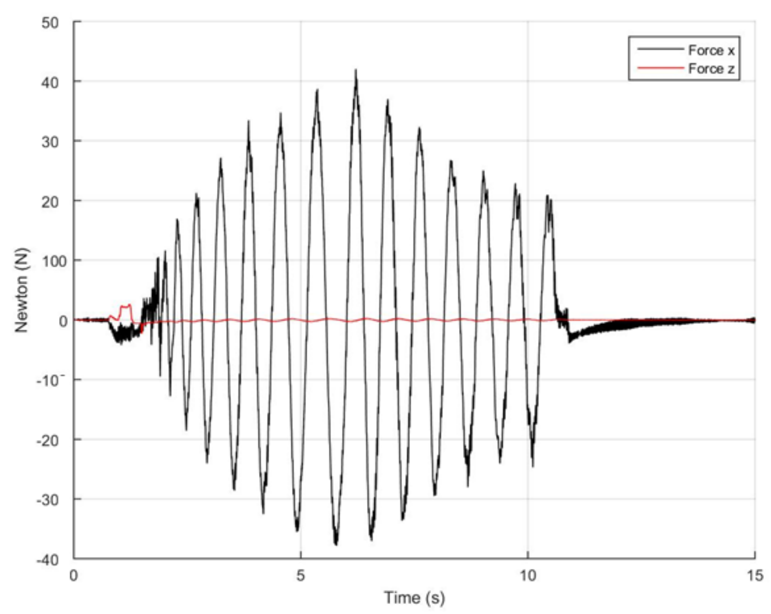

A	B

Figure 0-3(Appendix III): Signal Fx (black signal) and Fz (red signal) (A) recording during the drill-milling process with DM1 and (B) signal Fx (black signal) and Fz (red signal) elaborate with the mobile average by hole no. 1.

Figure 0-4(Appendix III) shows the DM2 tool signal of Fx and Fz recording.

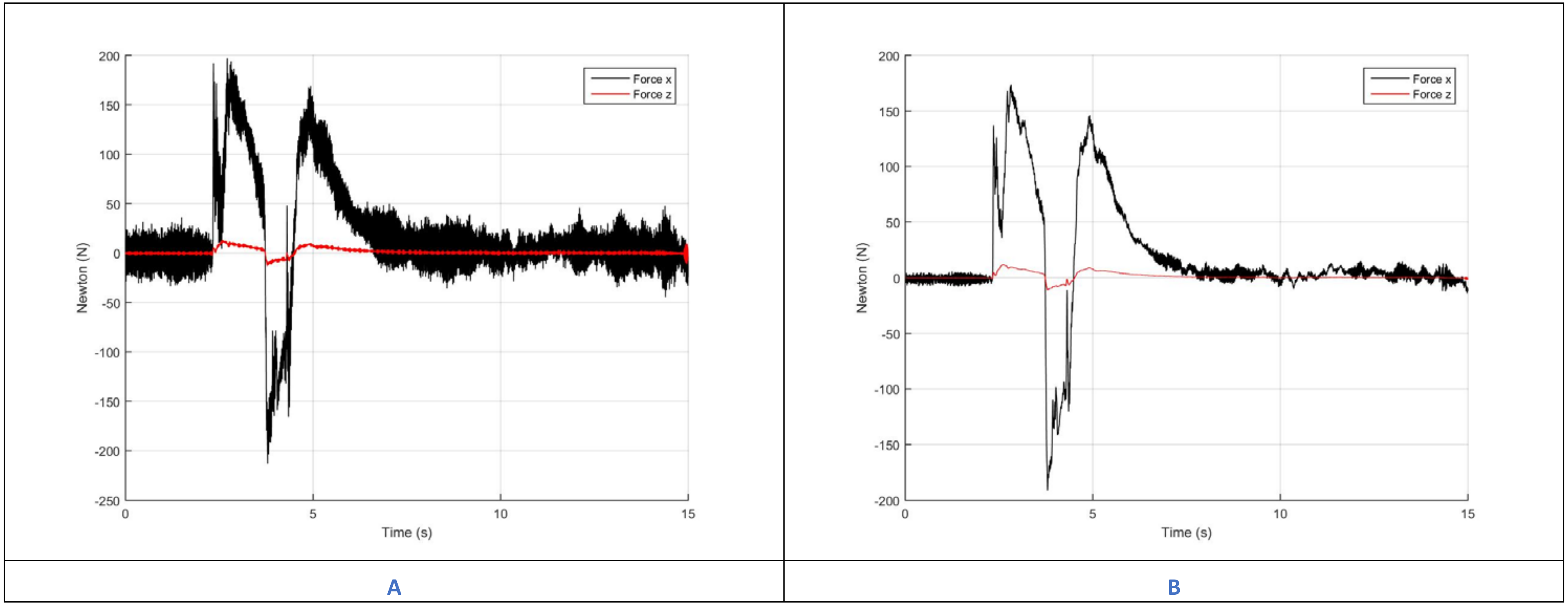

Figure 0-4(Appendix III): Signal Fx (black signal) and Fz (red signal) (A) recording during the drill-milling process with DM2 and (B) signal Fx (black signal) and Fz (red signal) elaborate with the mobile average by hole no. 1.

Figure 0-5 (Appendix III) shows the DM3 tool signal of Fx and Fz recording.

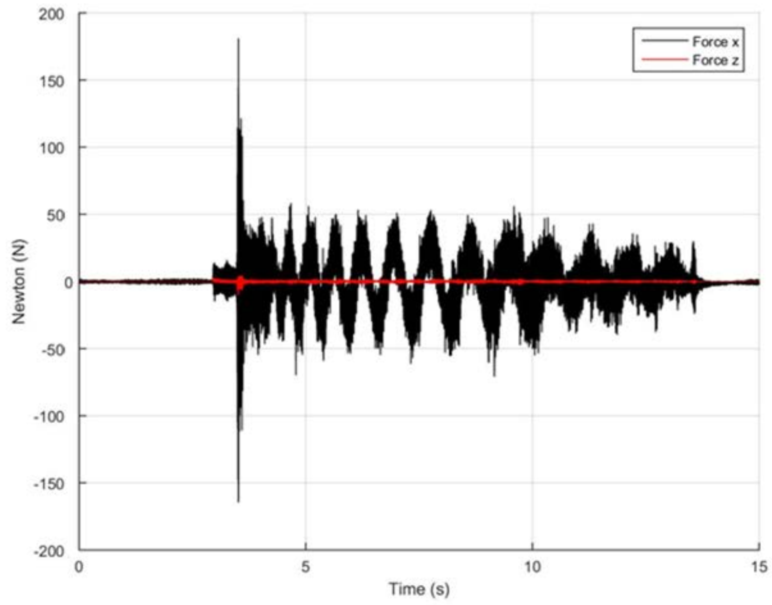

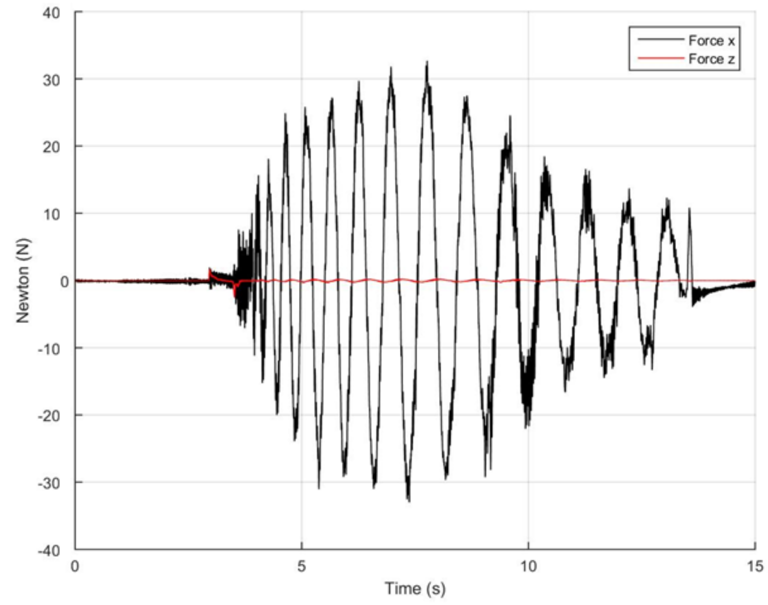

A	B

Figure 0-5(Appendix III): Signal Fx (black signal) and Fz (red signal) (A) recording during the drill-milling process with DM3 and (B) signal Fx (black signal) and Fz (red signal) elaborate with the mobile average by hole no. 1.

Figure 0-6 (Appendix III) shows the DM4 tool signal of Fx and Fz recording.

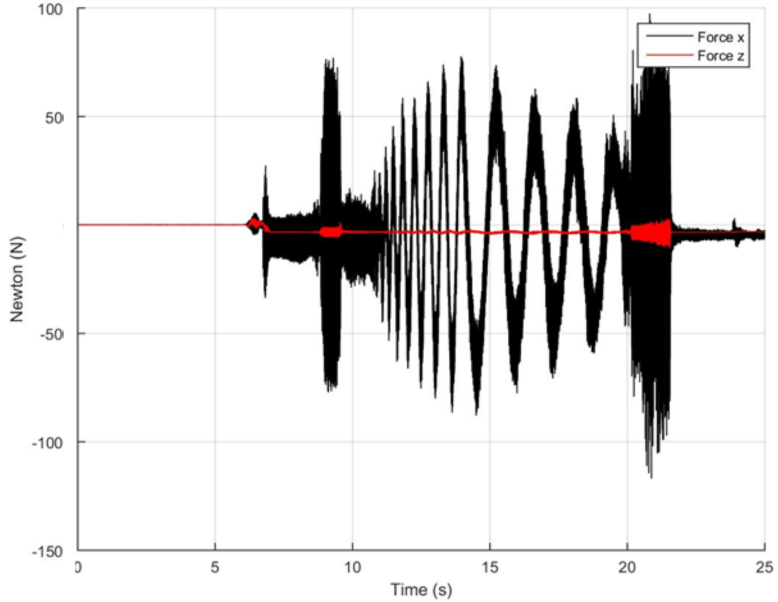

A

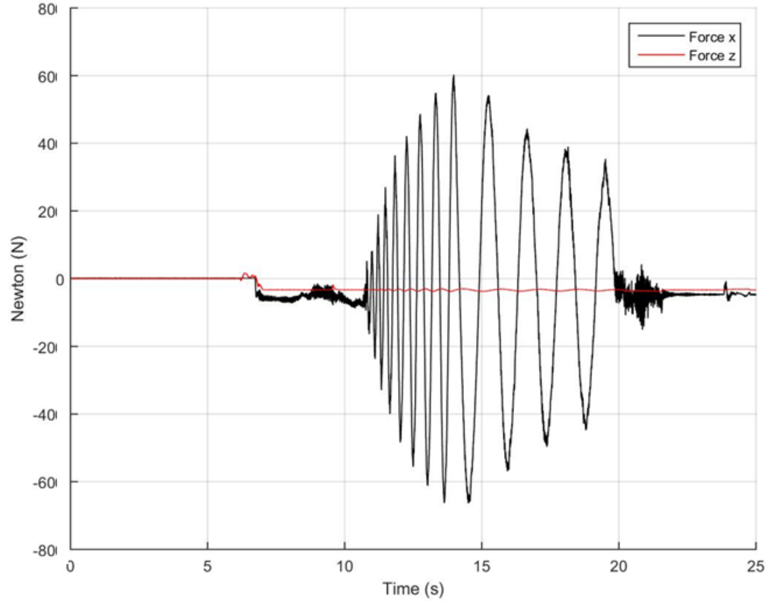

B

Figure 0-6(Appendix III): Signal Fx (black signal) and Fz (red signal) (A) recording during the drill-milling process with DM4 and (B) signal Fx (black signal) and Fz (red signal) elaborate with the mobile average by hole no. 1.

Figure 0-7 (Appendix III) shows the DM5 tool signal of Fx and Fz recording.

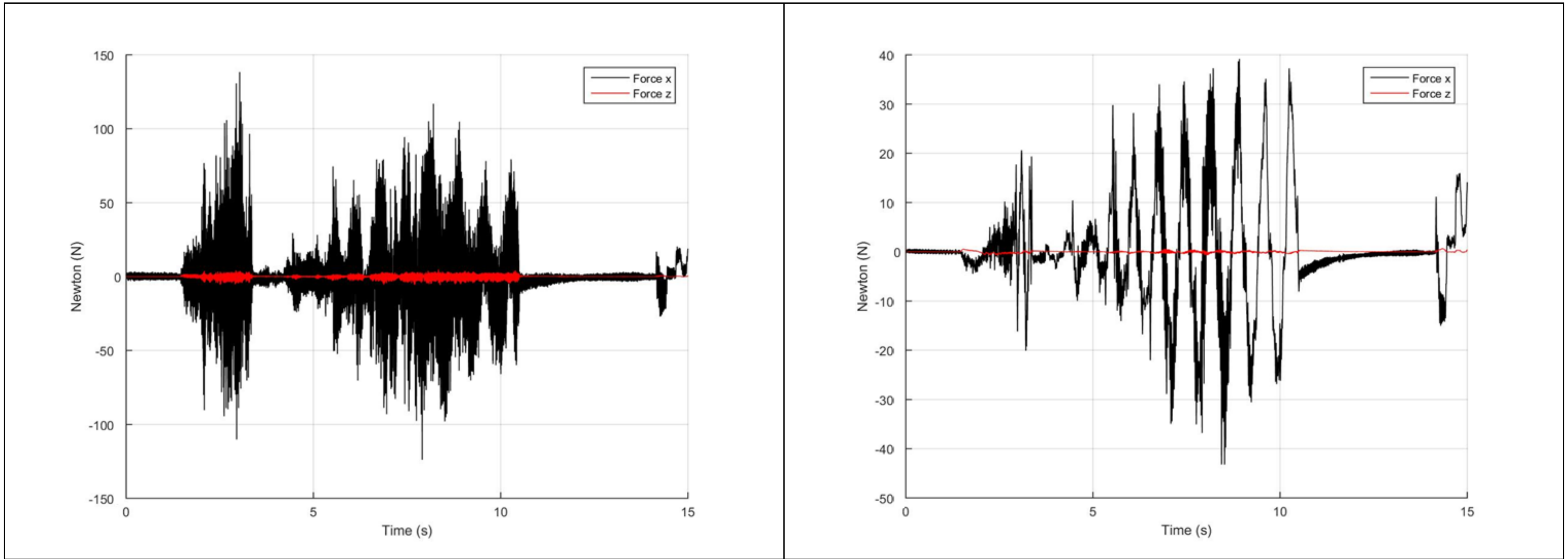

A	B

Figure 0-7(Appendix III): Signal Fx (black signal) and Fz (red signal) (A) recording during the drill-milling process with DM5 and (B) signal Fx (black signal) and Fz (red signal) elaborate with the mobile average by hole no. 1.

Figure 0-8 (Appendix III) shows the DM6 tool signal of Fx and Fz recording.

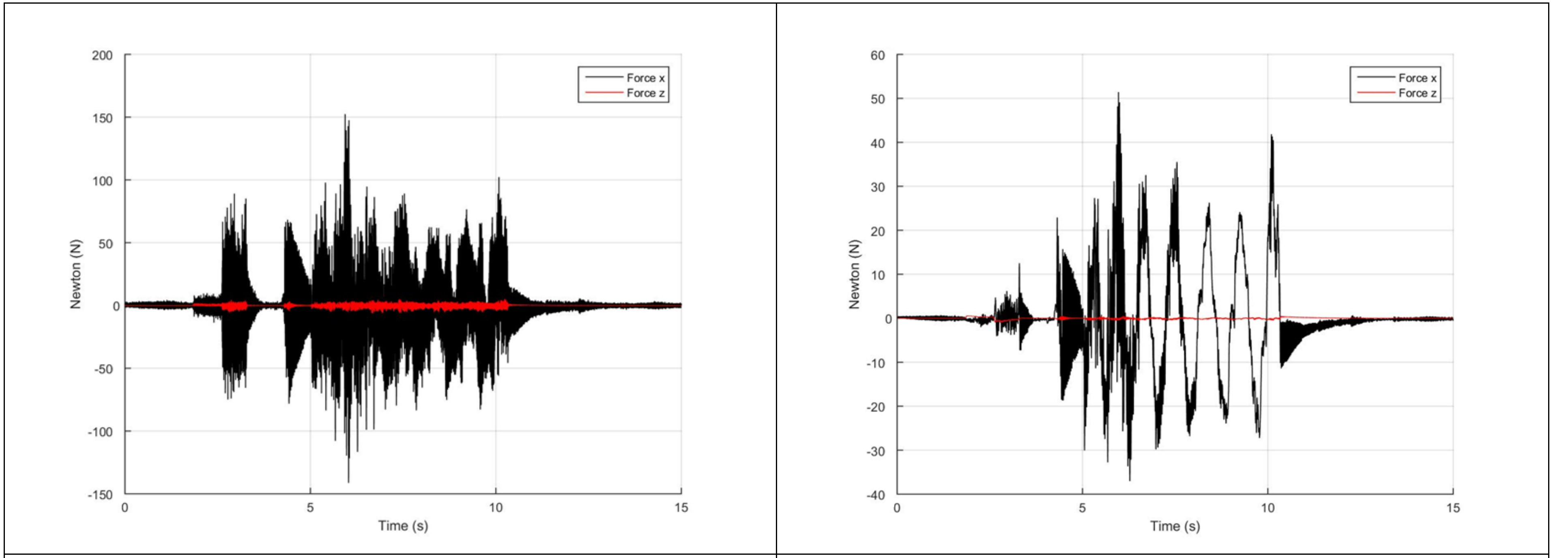

A	B

Figure 0-8(Appendix III): Signal Fx (black signal) and Fz (red signal) (A) recording during the drill-milling process with DM6 and (B) signal Fx (black signal) and Fz (red signal) elaborate with the mobile average by hole no. 1.

Figure 0-9 (Appendix III) shows the DM7 tool signal of Fx and Fz recording.

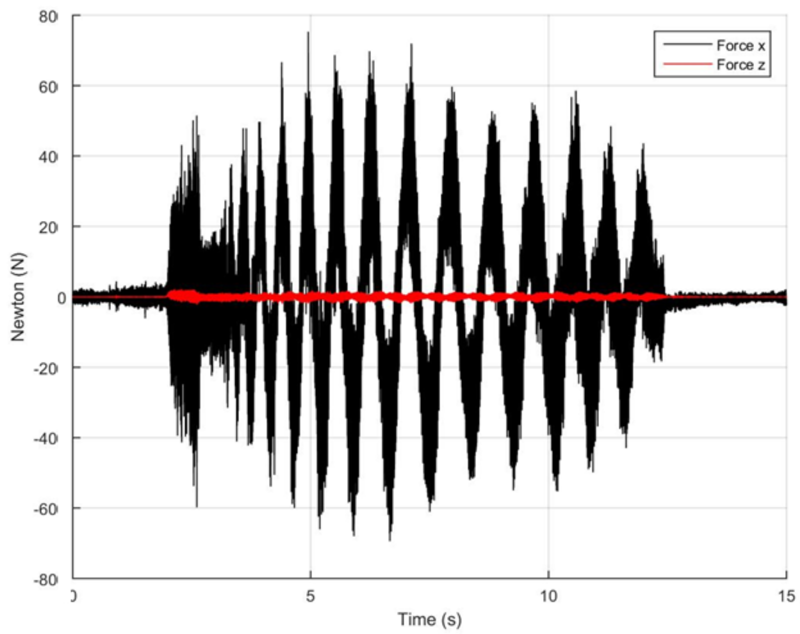

A

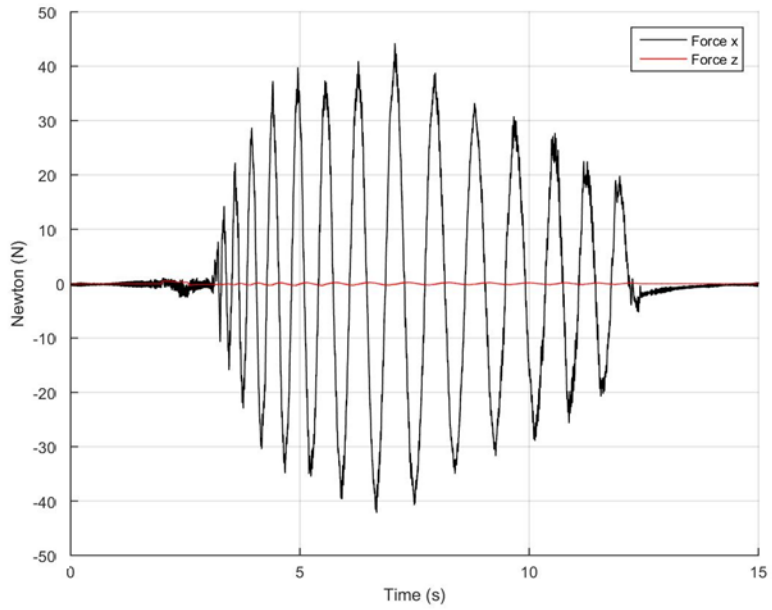

B

Figure 0-9(Appendix III): Signal Fx (black signal) and Fz (red signal) (A) recording during the drill-milling process with DM7 and (B) signal Fx (black signal) and Fz (red signal) elaborate with the mobile average by hole no. 1.

Figure 0-10 (Appendix III) shows the DM8 tool signal of Fx and Fz recording.

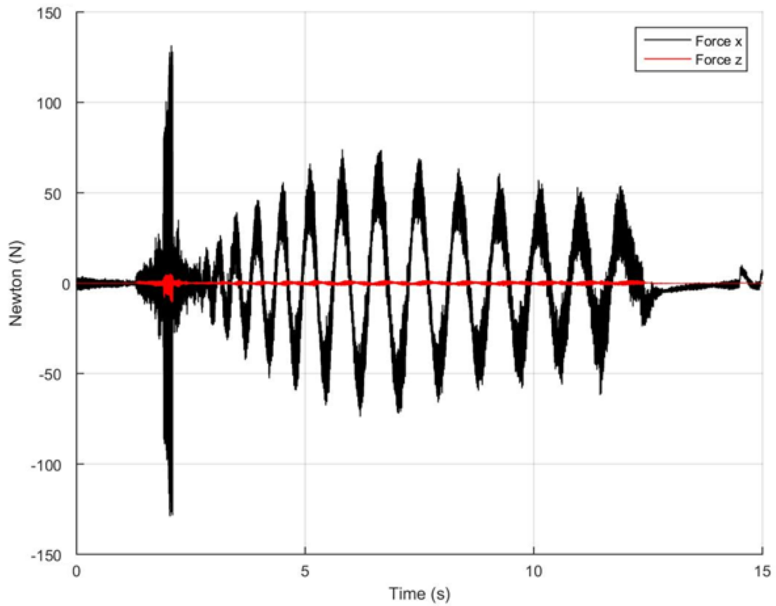

A

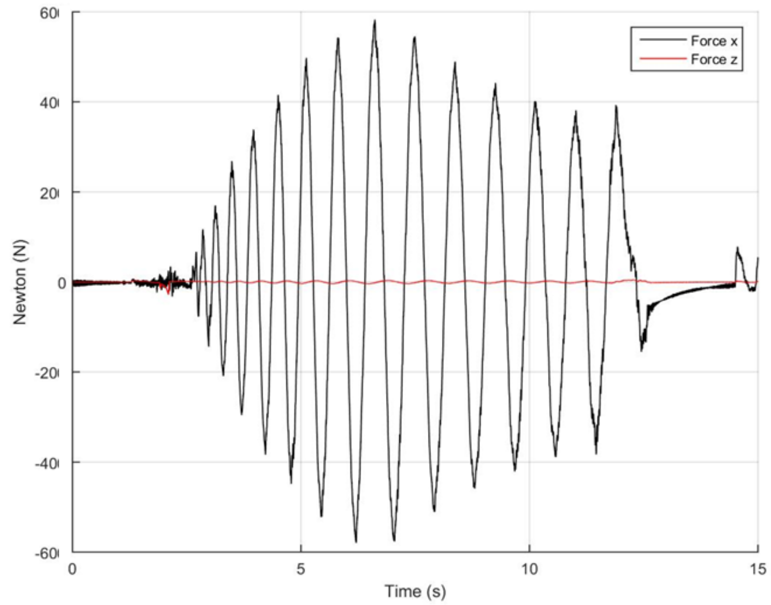

B

Figure 0-10(Appendix III): Signal Fx (black signal) and Fz (red signal) (A) recording during the drill-milling process with DM8 and (B) signal Fx (black signal) and Fz (red signal) elaborate with the mobile average by hole no. 1.

APPENDIX IV

Figure 0-11(Appendix IV) shows the DM11 tool wear picture.

Hole no. 60	Drilling		Milling (3Z)
Front	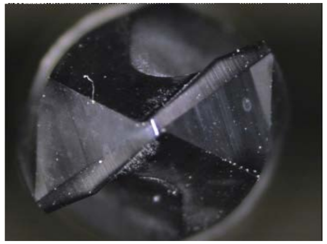		
Edge Right		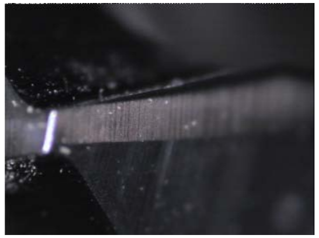	
Edge Left		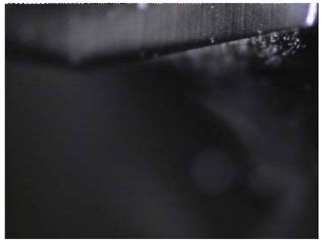	
First cutting edge			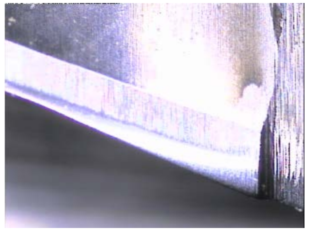

Second cutting edge			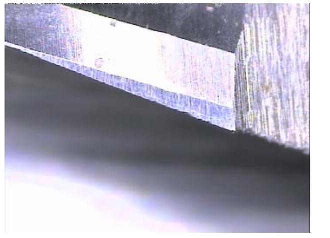
Third cutting edge			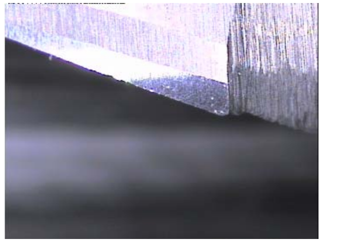

Figure 0-11(Appendix IV): DM11 tool wear picture by hole no. 60.

Figure 0-12 (Appendix IV) shows the DM12 tool wear picture.

Hole no. 60	Drilling		Milling (3Z)
Front	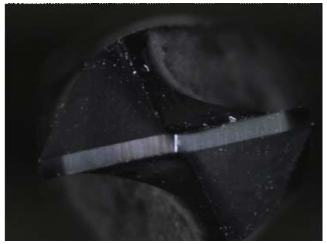		
Edge Right	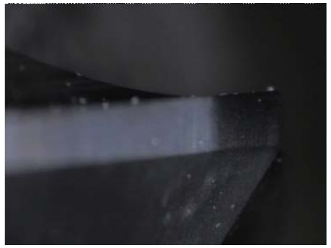	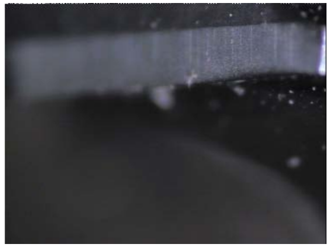	
Edge Left			
First cutting edge			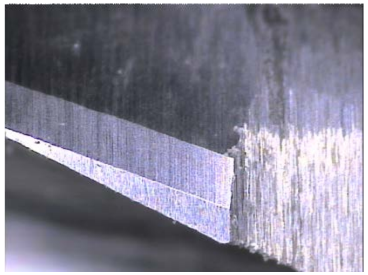

Second cutting edge			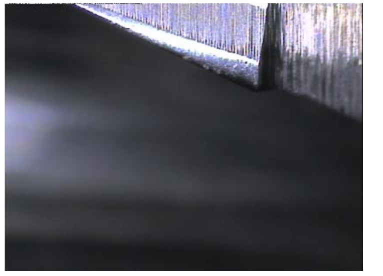
Third cutting edge			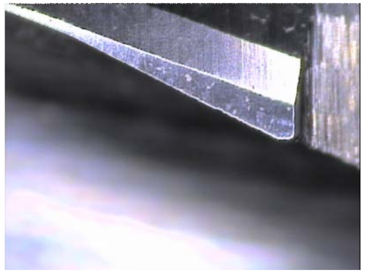

Figure 0-12(Appendix IV): DM12 tool wear picture by hole no. 60.

Figure 0-13 (Appendix IV) shows the DM13 tool wear picture.

Hole no. 60	Drilling		Milling (3Z)
Front	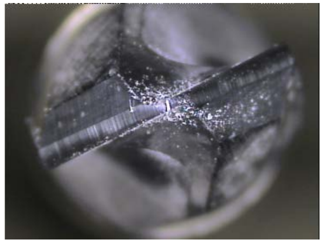		
Edge Right		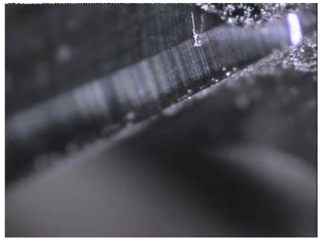	
Edge Left	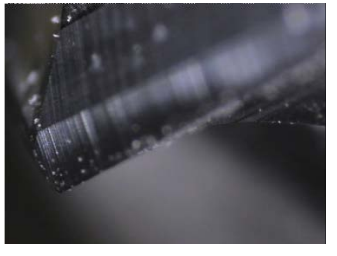		
First cutting edge			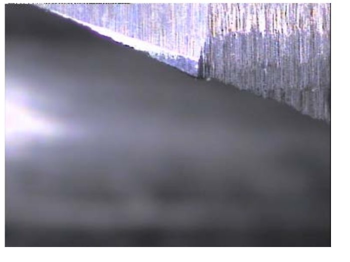

Second cutting edge			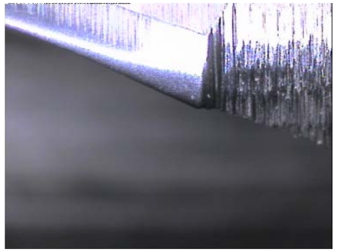
Third cutting edge			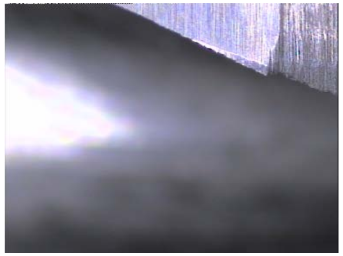

Figure 0-13(Appendix IV): DM13 tool wear picture by hole no. 60.

Figure 0-14 (Appendix IV) shows the DM14 tool wear picture.

Hole no. 60	Drilling		Milling (3Z)
Front	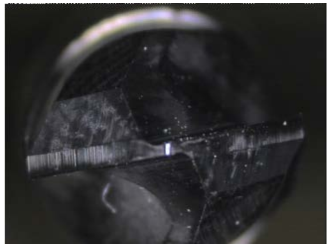		
Edge Right			
Edge Left	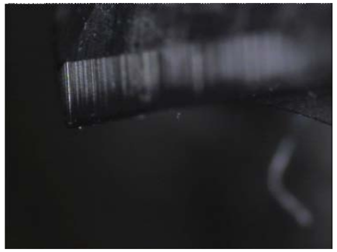		
First cutting edge			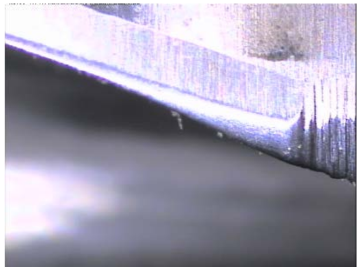

Second cutting edge			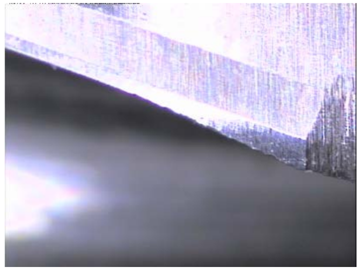
Third cutting edge			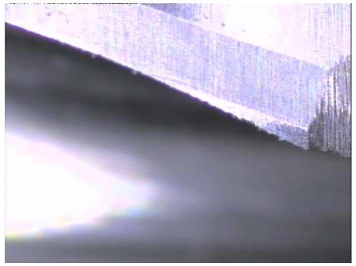

Figure 0-14(Appendix IV): DM14 tool wear picture by hole no. 60.

Figure 0-15 (Appendix IV) shows the DM15 tool wear picture.

Hole no. 60	Drilling		Milling (3Z)
Front	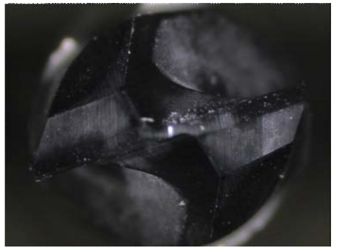		
Edge Right			
Edge Left			
First cutting edge			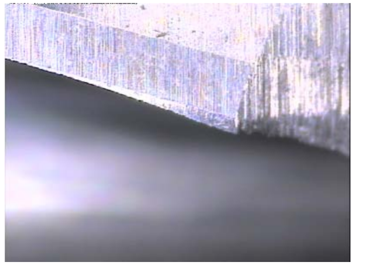

Second cutting edge			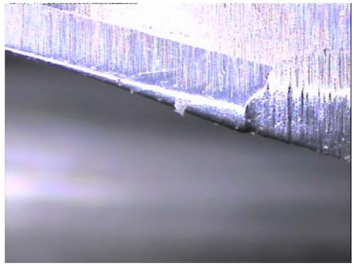
Third cutting edge			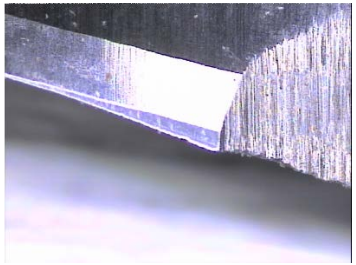

Figure 0-15(Appendix IV): DM15 tool wear picture by hole no. 60.

Figure 0-16 (Appendix IV) shows the DM16 tool wear picture.

Hole no. 60	Drilling		Milling (3Z)
Front	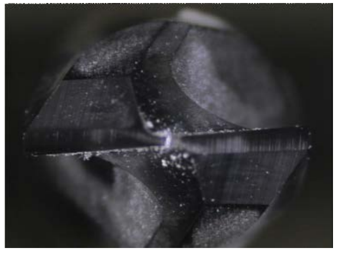		
Edge Right		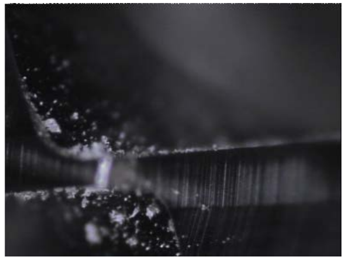	
Edge Left	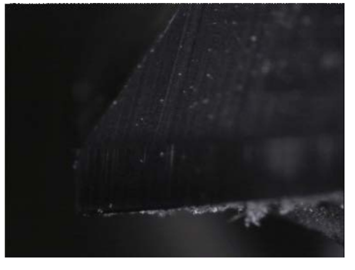		
First cutting edge			

Second cutting edge			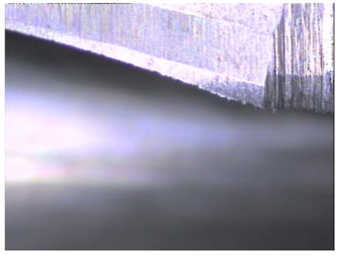
Third cutting edge			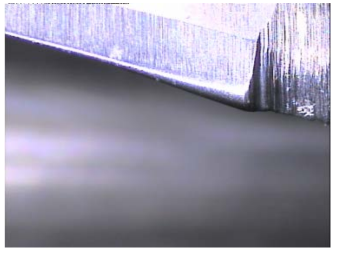

Figure 0-16(Appendix IV): DM16 tool wear picture by hole no. 60.

Figure 0-17 (Appendix IV) shows the DM17 tool wear picture.

Hole no. 60	**Drilling**		**Milling (5Z)**
Front	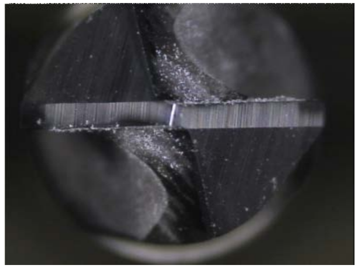		
Edge Right	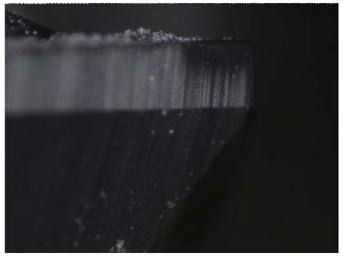	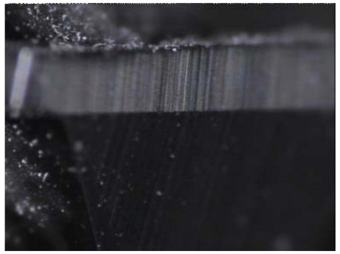	
Edge Left	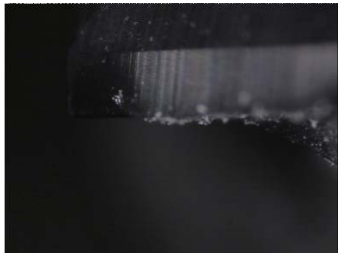	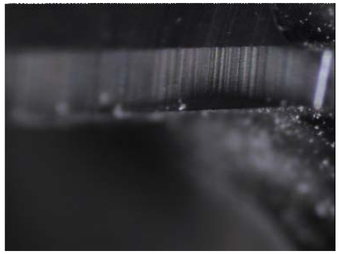	
First cutting edge			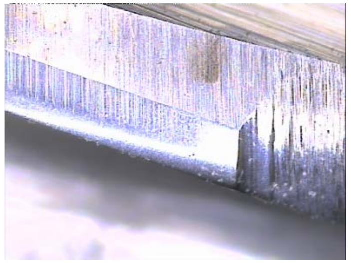

Second cutting edge			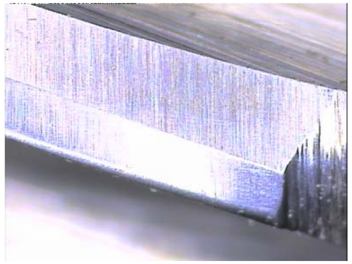
Third cutting edge			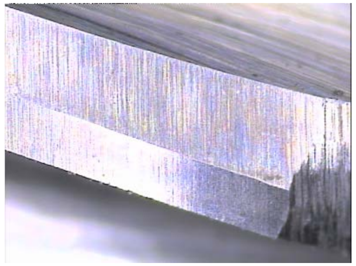
Fourth cutting edge			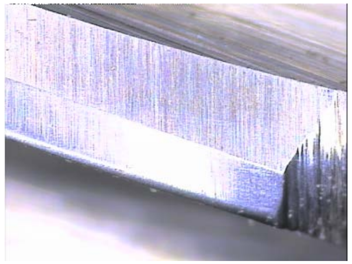
Fifth cutting edge			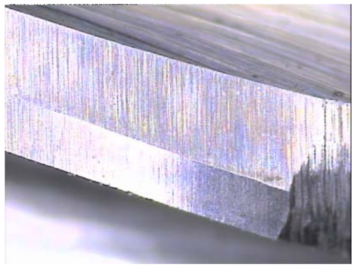

Figure 0-17(Appendix IV): DM17 tool wear picture by hole no. 60.